Czech Technical University in Prague
Faculty of Civil Engineering
Department of Mechanics

Bayesian probabilistic models in civil engineering problems

by
Tomáš Janda

Habilitation Thesis

December 2024

Acknowledgements

First and foremost, I would like to express my heartfelt gratitude to my family for providing the perfect balance of unwavering support and much-needed occasional distractions throughout the process of writing this thesis.

I am also deeply thankful to my colleagues for their valuable discussions and advice, with special thanks to Prof. Michal Šejnoha, Prof. Jan Zeman, Dr. Alena Zemanová, Prof. Jan Vorel, Doc. Jan Sýkora and Dr. Lucie Keřková Kucíková.

My deepest gratitude goes to Prof. Jiří Šejnoha, who introduced me to the fascinating world of Bayesian statistics. Without his guidance and inspiration, I might have missed the adventure of exploring this captivating field of study.

Contents

Abstract

This thesis consolidates advancements in the application of Bayesian statistical methods to address uncertainties and variability in material behavior and structural responses across diverse civil engineering problems. A theoretical introduction to principles of Bayesian inference and Markov Chain Monte Carlo (MCMC) sampling methods precedes the individual studies, providing a robust foundation for their application.

Five distinct studies form the core of the research:

Soil Mechanics A hierarchical probabilistic model was developed to quantify the uncertainty of hypoplastic material parameters for clay, demonstrating the influence of laboratory data selection on parameter variability. This framework encourages stochastic simulations even with limited data available for a particular soil.

Tunnel Excavation Bayesian updating methods improved the predictions of ground settlements during tunnel excavation. By integrating numerical modeling and in situ measurements, the study demonstrated iterative model refinement for better alignment with real-world data.

Fire-Exposed Timber Beams The behavior of glued laminated timber beams exposed to fire was examined through experimental and numerical analyses. Bayesian inference identified temperature-dependent material parameters, enabling enhanced charring rate predictions and facilitating fully stochastic structural fire analysis.

Elastic Properties of Laminated Timber A stochastic hierarchical model was formulated to capture the variability and uncertainty of the elastic properties of laminated timber beams. Bayesian inference combined experimental data with finite element simulations, yielding improved material property estimations and a refined formula for longitudinal elastic modulus.

Micromechanics of Wood A Bayesian framework was designed to link micromechanics, computational homogenization, and experimental measurements to estimate uncertainties in the macroscopic elastic properties of wood, accounting for microstructural randomness and experimental error.

Collectively, these studies highlight the power of Bayesian statistics in quantifying uncertainties, improving parameter estimation, and enhancing predictive capabilities across engineering problems. They underscore the value of integrating computational models

with experimental data and general prior knowledge to achieve more reliable designs and analyses.

Chapter 1

Introduction

Virtually all physical processes that are of interest in the field of civil engineering are controlled by deterministic laws of nature. When starting from the same state, the deterministic systems will always evolve in the same way and end up in the same state. No random effects influence their output. The omnipresence and undisputed validity of deterministic physical laws motivate engineers and researchers to formulate mathematical models that describe the observed phenomena to great detail. With the help of numerical methods for solving system of differential equations at hand, a vast range of processes with different geometries and material properties can be simulated. The types of simulations range from static or dynamic mechanical analysis, fluid dynamics, and transport processes to coupled multiphysics simulations.

When engineers apply complex simulations to real-word systems, they face a problem of specifying an initial state and parameters of the system. In mechanics of solids, for example, the input includes parameters of material models, an initial stress state, loading, or even geometry. Many of these inputs cannot be measured directly. They are either measured indirectly or estimated from previous observations. In any case, the inputs are often uncertain. Unfortunately, there is no generally accepted way for engineering problems to quantify uncertainties of model parameters or to propagate them through the deterministic model. Instead, there is a number of different ways.

The approaches to the problem of uncertain inputs entering a deterministic engineering model range from very simple and straightforward ones to rather convoluted and academical ones. The simplest approach typically chooses some adverse but possible values of the input parameters and ensures that the solution obtained for these parameters is still satisfactory. A more advanced family of approaches is the Monte Carlo method, which relies on multiple deterministic simulations performed with a representative ensemble of input values. Another approach is the stochastic finite element method, which relies on a numerical solution of stochastic differential equations. However, this approach typically requires reformulation or reimplementation of the deterministic model.

All of the above approaches share one feature: they require the input parameters to be specified in a probabilistic manner. The parameters are often not directly observable, and their values need to be estimated from the observed data. The approaches to pa-

rameter estimation also vary. Two dominant approaches are referred to as frequentist and Bayesian. The frequentist approach proposes a single value of the desired parameter and relies on hypothesis testing to justify it. The Bayesian approach, on the other hand, primarily searches for the joint probability distribution of the parameters.

The goal of this thesis is to outline the principles of Bayesian inference and to provide examples of its application to several different problems in the field of civil engineering.

Bayesian inference is a statistical method that allows us to combine a prior general knowledge about the model with observed data to arrive at the joint posterior distribution of the model parameters. From the perspective of a typical user of Bayesian inference, i.e., a researcher or engineer with a limited training in statistics, the method may be perceived as two fold. On one hand, the main creative part when using Bayesian inference – the formulation of the data generating statistical model and definition of its parameters – is relatively intuitive and typically requires only basic knowledge of probability theory. On the other hand, there are a number of concepts and technicalities that the user should understand to be able to reason about how and why the method works and identify and resolve potential problems in the inference.

The text of this theses consists of two parts. The first part briefly summarizes the principles of Bayesian inference, related concepts, and the technicalities associated to sampling. The second part is a collection of previously published journal papers presenting the applications of Bayesian inference and predictions to selected engineering problems.

The first part is by no means a complete and rigorous introduction to Bayesian statistics. Instead, it is meant to be a brief overview of the principles, terminology, and topics that aspiring user of Bayesian inference might want to study. It also provides some reference to technical details and intuition behind the Markov chain Monte Carlo, the method that makes Bayesian inference possible for complex models. Note, however, that a detailed and rigorous introduction of probability theory and various Markov Chain Monte Carlo samplers is completely outside the scope and extent of this text.

The second, more extensive part of the thesis is a collection of already published journal articles that focuses on the application of Bayesian inference to civil engineering problems. The articles are:

- Janda, T.; Pavelcová, V.; Zemanová, A.; Šejnoha, M., Uncertainty in calibration of hypoplastic model for clay attributed to limited number of laboratory tests, Computers and Structures. 2024, 295 ISSN 1879-2243.

- Janda, T.; Šejnoha, M.; Šejnoha, J., Applying Bayesian approach to predict deformations during tunnel construction, International Journal for Numerical and Analytical Methods in Geomechanics. 2018, 42(15), 1765-1784. ISSN 0363-9061.

- Kucíková, L.; Janda, T.; Sýkora, J.; Šejnoha, M.; Marseglia, G., Experimental and numerical investigation of the response of GLT beams exposed to fire, Construction and Building Materials. 2021, 299 1-18. ISSN 1879-0526.

- Šejnoha, M.; Janda, T.; Melzerová, L.; Nežerka, V.; Šejnoha, J., Modeling glulams

in linear range with parameters updated using Bayesian inference, Engineering Structures. 2017, 138 293-307. ISSN 0141-0296.

- Šejnoha, M.; Janda, T.; Vorel, J.; Kucíková, L.; Padevět, P.; Hrbek, V., Bayesian inference as a tool for improving estimates of effective elastic parameters of wood, Computers and Structures. 2019, 218 94-107. ISSN 0045-7949.

The papers share one characteristic: they focus on structures or processes involving natural materials such as soil or wood. The inferred properties of these materials are inherently uncertain for two reasons. The first source of uncertainty is their natural spatial and structural variability. This source of inherent aleatoric uncertainty is irreducible and should always be considered. The second, principally different source of uncertainty of the material properties is attributed to the inaccuracy of the measuring process and the limited amount of available data. In contrast, this epistemic uncertainty depends on the data acquisition process and might be controlled. Bayesian inference naturally takes both sources of uncertainty into account and in most cases quantifies them separately.

Chapter 2

Principles of Bayesian inference

Bayesian inference is a statistical method that allows us to reason about data and probabilistic models in a natural, coherent way. Its appeal comes from its broad applicability and consistent methodology in a wide range of problems. The principles and workflow of the inference remain the same regardless of the specific application.

For example, Bayesian inference can be used to determine credible intervals for basic statistics, such as the mean and standard deviation of a dataset. It can also be applied to estimate parameters in various regression models. In hierarchical probabilistic models, Bayesian inference helps to estimate credible intervals of not directly observable latent variables. Furthermore, it can calculate credible ranges for the expected value of a variable, even when the number of observations is limited. In addition, Bayesian methods can be used to compare the predictive performance of different probabilistic models. Although the range of problems to which Bayesian inference can be applied is vast, the core of the Bayesian workflow remains the same across all these problems.

First, a probabilistic model is formulated and its likelihood function is defined. Next, the prior distribution of the model parameters is specified. By combining the prior distribution with the likelihood, the posterior distribution is obtained. This posterior distribution is then explored using Markov chain Monte Carlo (MCMC) sampling techniques.

While the practical steps of Bayesian inference are relatively straightforward, and some of them can even be automated, a deeper understanding of the method is desirable. Understanding the principles and numerical techniques related to Bayesian inference is crucial especially when one needs to identify and fix a problem in the model that is typically manifested by non-converging MCMC chains of samples.

This chapter provides a basic understanding of how and why Bayesian inference works. The text does not aim to be comprehensive or particularly rigorous. Instead, it should serve as a brief overview of the topics with examples and references to several comprehensive but accessible classic works on the topic.

2.1 Probability

Probability theory plays a central role in Bayesian inference. The inference of parameters is carried out for a *probabilistic* model of the observed data and the inferred parameters are treated as *random* variables. Understanding the basics of probability theory to at least the level outlined in this theoretical section is therefore the stepping stone to Bayesian modeling.

2.1.1 What is probability

Consider an action that randomly results in one of several possible outcomes. This action is referred to as a trial of a random experiment. By convention, each possible outcome is categorized as a success or a failure.

The most intuitive way to define the probability of success is by considering proportions. Specifically, probability is defined as the ratio of the number of successes to the total number of trials, assuming that the number of trials is sufficiently large.

However, despite its simplicity, this definition has two notable limitations. First, it assumes the feasibility of conducting a large number of trials, which may not always be practical or possible. Second, it provides little insight into how the probability might change if we alter our classification of outcomes, redefining which are considered successes and which failures. Therefore, a more rigorous definition of probability and its relation to possible outcomes of the random experiment is needed.

2.1.2 Notion and axioms of probability

Consider a *random experiment* such as rolling a dice or measuring atmospheric pressure at a certain place and time. The experiment results in *outcome* ω. In case of the dice-rolling experiment, the outcome can be dice landing with one of its sides up. In case of atmospheric pressure measurement, the outcome is the value of the pressure value represented by a real number. The set of all possible outcomes is the experiment's *sample space* Ω. The results are denoted as *elementary events*. The sample space of six-sided dice is the set $\Omega = \{1, 2, 3, 4, 5, 6\}$. The sample space of the atmospheric pressure contains positive real numbers $\Omega = \mathbb{R}^+$. Note that the elements of the sample space, i.e., the outcomes, do not have to be numbers. They are merely something that we observe when the random experiment is executed.

Now, it would be tempting to assign some value (probability) to each of the possible outcomes to indicate how often we observe this particular outcome. While this approach would work with the dice experiment, it would be problematic for the infinity of possible outcomes of a continuous quantity such as the atmospheric pressure.

Therefore, the probability is assigned not to the elements of the sample space but rather to the elements of *event space* $\mathcal{F}$. The event space is a set of *events*. An event is a subset of the sample space. The event space $\mathcal{F}$ must satisfy the following three properties:

- It is closed under complements. This means that if an event A, that is, some set of outcomes, is present in $\mathcal{F}$ the complement of A to Ω denoted as $\overline{A}$ is also present in $\mathcal{F}$.
- It is closed under unions. This means that if two events A and B are present in $\mathcal{F}$, then their union is also present in $\mathcal{F}$.
- The event space $\mathcal{F}$ always contains the entire sample space Ω.

A set F constructed from another set Ω and satisfying the above properties is called a σ-algebra on the set Ω.

For example, for a coin that lands either heads (H) or tails (T), the sample space is $\Omega = \{\mathrm{H}, \mathrm{T}\}$ and the event space is $\mathcal{F} = \{\{\}, \{\mathrm{H}\}, \{\mathrm{T}\}, \{\mathrm{H}, \mathrm{T}\}\}$. The sample space of a six-sided dice is $\Omega = \{1, 2, 3, 4, 5, 6\}$. One possible event space is the set of all subsets of the event space denoted as $\mathcal{F} = 2^{\Omega}$. Another possible even space could be $\mathcal{F} = \{\{\}, \{3, 6\}, \{1, 2, 4, 5\}, \Omega\}$. With such event space we consider only two nontrivial events: dice landing up with a number evenly divisible by three and dice landing up with the other numbers.

Two events are trivially present in the event space $\mathcal{F}$: an empty set denoted as *impossible event* and the entire sample space Ω denoted in this context as the *sure event*.

A probability $P(A)$ of an event A is mapping from event space F onto real numbers. The mapping must satisfy the following axioms:

- For any event, the probability is nonnegative.
- Probability of certain event is one, $P(\Omega) = 1$
- Probability of the union of any two mutually exclusive events is the sum of their probabilities, $P(A \cup B) = P(A) + P(B)$ for any A and B satisfying $A \cap B = \emptyset$.

A surprisingly large number of properties can be derived for probability from these axioms. For example, the probability of a complementary event is calculated as

$$P(\overline{A}) = 1 - P(A) \tag{2.1}$$

Additional relationships, particularly those relevant in the context of Bayesian inference, are discussed in the following sections.

One particular property of probability should be highlighted: Depending on the formulation of the event space, the probability may, but *does not have to*, be assigned to the elements of the sample space, that is, to the elementary events that are observed. This is particularly important in the case of a continuous random quantity where the individual observed values are not part of the event space and therefore do not have a probability, as pointed out in Section 2.2.2.

Also note that this axiomatic definition of probability, unlike the naive approach, does not rely on the number of observed failures or the total number of performed trials. All properties of probability derived from these axioms remain valid, whether the probability reflects the relative frequency of an observable event or whether it represents our belief about the state of an unobservable system.

2.1.3 Conditional probability

Probability of the event A given that event B happened is termed *conditional probability* and is denoted as $P(A \mid B)$. It is defined as

$$P(A|B) = \frac{P(A \cap B)}{P(B)} \tag{2.2}$$

Conditional probability ranges from zero to one. When $P(A|B) = P(A)$ then the events A and B are *independent*. Note that the probability of an intersection of two independent events follows

$$P(A \cap B) = P(A)P(B) \tag{2.3}$$

while the probability of the intersection of two dependent events features the conditional probability

$$P(A \cap B) = P(A \mid B)P(B) = P(A)P(B \mid A) \tag{2.4}$$

2.1.4 Chain rule of probability

The probability of an intersection of more than two events (either mutually dependent or not) is expressed according to the *chain rule* of probability

$$P(A_1 \cap A_2 \cap \cdots \cap A_n) = P(A_1 \mid A_2 \cap \cdots \cap A_n)P(A_2 \cap \cdots \cap A_n) = \tag{2.5}$$

$$= P(A_1 \mid A_2 \cap \cdots \cap A_n)P(A_2 \mid A_3 \cap \cdots \cap A_n) \cdot \ldots \cdot P(A_{n-1} \mid A_n)P(A_n) \tag{2.6}$$

2.1.5 Law of total probability

The *law of total probability* states that the probability of an event A can be expressed as a sum of probabilities of intersections of A with elements of mutually exclusive and complete system of events B_i, $i = 1 \ldots n$. The partitioning of the sample space into events B_i together with the event A is conceptually shown in Figure 2.1. The probability of A can be written as

$$P(A) = \sum_{i=1}^{n} P(A \cap B_i) = \sum_{i=1}^{n} P(A|B_i)P(B_i) \tag{2.7}$$

where $B_1 \cup B_2 \cup \ldots \cup B_n = \Omega$ and $B_i \cap B_j = \emptyset$ for any $i = 1 \ldots n$, $j = 1 \ldots n$ with $i \neq j$.

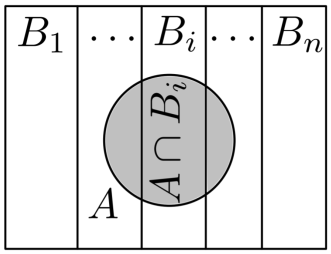

Figure 2.1: Events appearing in the law of total probability, Equation (2.7). Events B_i (the columns) represent the complete and mutually exclusive partitioning of the entire sample space Ω (the rectangle). The circle represents the event A.

2.1.6 Bayes' theorem for probabilities

The *Bayes' theorem* in its most succinct form

$$P(B \mid A) = \frac{P(A \mid B)P(B)}{P(A)} \tag{2.8}$$

follows directly from Eq. (2.4). Expanding the denominator according to Eq. (2.7) gives a slightly more intuitive form

$$P(B_i \mid A) = \frac{P(A \mid B_i)P(B_i)}{\sum_{j=1}^{n} P(A \mid B_j)P(B_j)} \tag{2.9}$$

that expresses the probability of B_i, i.e., that a randomly chosen point is contained in the i-th column in Figure (2.1), given that A happened, i.e., given an information that the point was found in the circle.

A special mutually exclusive and complete system of events is the event B and its complement to Ω denoted as $\overline{B}$. For such partitioning of Ω the Bayes theorem reduces to

$$P(B \mid A) = \frac{P(A \mid B)P(B)}{P(A \mid B)P(B) + P(A \mid \overline{B})P(\overline{B})} \tag{2.10}$$

Note that the Bayes' theorem can be informally seen as a rule to swap the arguments in the conditional probabilities. Its consequence is illustrated in the following example.

2.1.7 Example: Recognizing defective products

A factory produces batteries. An expert in quality control inspects each battery and labels it as good or defective. He recognizes a good battery with probability 0.98 and a defective battery with probability 0.99. On average, 95% of the batteries produced are good. Our goal is to calculate the probability that a battery *labeled* by the expert as defective really *is* defective.

The real condition of the battery is denoted in lowercase letters: g and d denote a good and defective battery, respectively. The battery condition reported by the quality-control expert is denoted in upper case letters: G resp. D. The three problem statements are written in terms of (conditional) probabilities as

$$P(G \mid g) = 0.98 \tag{2.11}$$

$$P(D \mid d) = 0.99 \tag{2.12}$$

$$P(g) = 0.95 \tag{2.13}$$

and the goal is to calculate conditional probability $P(d \mid D)$. Note that events g and d are complementary. Therefore, $P(d) = 1 - P(g) = 0.05$. The events G and D are also complementary and $P(D \mid g) = 1 - P(G \mid g) = 0.02$ and $P(G \mid d) = 1 - P(D \mid d) = 0.01$ therefore holds. The Bayes rule used to express the desired conditional probability $P(d \mid D)$ is written as

$$P(d \mid D) = \frac{P(D \mid d)P(d)}{P(D \mid d)P(d) + P(D \mid g)P(g)} = \frac{0.99 \times 0.05}{0.99 \times 0.05 + 0.02 \times 0.95} \approx 0.723 \tag{2.14}$$

A battery labeled as defective really is defective only with probability around 0.723. The probability of a complementary event, that is, the probability that the battery labeled as defective is actually good, is again calculated as $P(g \mid D) = 1 - P(d \mid D) \approx 0.277$. The following intuition helps to justify the relative high rate of good batteries labeled as defective: If defective batteries were extremely scarce, the expert would inspect mostly good batteries and, of course, label some of them incorrectly. Several good batteries could therefore be labeled as defective before a really defective battery is even inspected.

2.2 Random variable

A special case of a random experiment – but very common in engineering problems – is one that results in random values of some quantity. The experiment is then viewed as a *random variable*. Depending on the sample space, i.e., the possible values that the random experiment generates, the random variable is either discrete or continuous. The mathematical description of how the probabilities are assigned to particular values of a random variable is called *probability distribution*.

2.2.1 Discrete random variable

The sample space of a discrete random variable is a subset of integers $\Omega \in \mathbb{N}$. If the sample space of a random experiment is a finite or a countable set, it can be treated as a discrete random variable simply by mapping its outcomes to a subset of $\mathbb{Z}$. For example, the two elements of the sample space of a coin-flipping experiment, i.e., *Heads* and *Tails*, can be mapped to 0 and 1, respectively.

The probability of particular values of the continuous variable X is given by the *probability mass function* (PMF) p. It is defined as

$$p(x) = P(X = x) \tag{2.15}$$

where $p(x)$ denotes the probability mass function evaluated at a given value x and $P(X = x)$ is the probability of an event $X = x$. PMF is therefore a function mapping the possible values of X to their probabilities. The probability mass function sums to one

$$\sum_{\Omega_X} p(x) = 1 \tag{2.16}$$

Since any value of the probability mass function *is* a probability, the relations presented in Section 2.1.2 apply analogically to it. This is shown in the following subsections.

2.2.1.1 Multivariate discrete distribution

Consider a random experiment that produces n discrete values on a single trial. The experiment defines n potentially dependent discrete random variables. Putting the random variables in a vector $\boldsymbol{X} = [X_1, \ldots, X_n]$ gives *random vector*. The *multivariate discrete distribution* of a random vector is completely determined by the *joint* probability mass function defined as

$$p_{\boldsymbol{X}}(\boldsymbol{x}) = p_{X_1,\ldots,X_n}(x_1, \ldots, x_n) = P(X_1 = x_1 \cap \cdots \cap X_n = x_n) \tag{2.17}$$

The subscript of the function p specifies the random variable or the random vector in question while the argument specifies concrete values for which the probability is evaluated.

2.2.1.2 Marginal and conditional probability mass function

Consider a multivariate discrete distribution of a random vector $\boldsymbol{Z}$ with elements conceptually separated into two parts

$$\boldsymbol{Z} = [\boldsymbol{X}, \boldsymbol{Y}] = [X_1, \ldots, X_m, Y_1, \ldots, Y_n] \tag{2.18}$$

Its joint probability mass function is denoted by

$$p_{\boldsymbol{X},\boldsymbol{Y}}(\boldsymbol{x}, \boldsymbol{y}) = p_{X_1,\ldots,X_m,Y_1,\ldots,Y_n}(x_1, \ldots, x_m, y_1, \ldots, y_n) \tag{2.19}$$

Now we can define two useful probability distributions for X: the *marginal* distribution and the *conditional* distribution. The marginal distribution is sufficiently defined by the marginal probability mass function

$$p_{\boldsymbol{X}}(x_1, \ldots, x_m) = \sum_{i_1} \cdots \sum_{i_n} p_{\boldsymbol{X},\boldsymbol{Y}}(x_1, \ldots, x_m, y_{1,i_1}, \ldots, y_{n,i_n}) \tag{2.20}$$

where the index i_k in $\sum_{i_k}$ indexes all possible values of a random variable Y_k each denoted y_{k,i_k}.

The conditional probability mass function is written as

$$p_{\boldsymbol{X}|\boldsymbol{Y}=\boldsymbol{y}}(x_1, \ldots x_m) = \frac{p_{\boldsymbol{X},\boldsymbol{Y}}(x_1, \ldots, x_m, y_1, \ldots, y_n)}{p_{\boldsymbol{Y}}(y_1, \ldots, y_n)} \tag{2.21}$$

where $p_{\boldsymbol{Y}}(y_1, \ldots, y_n)$ is the marginal distribution of $\boldsymbol{Y}$. It is calculated according to Eq. (2.20) but the sums are calculated over all possible values of the random vector $\boldsymbol{X}$.

Note that the marginal and conditional distributions are both distributions of the $\boldsymbol{X}$-part of the $\boldsymbol{Z}$ random vector but they are conceptually different. The marginal distribution of $\boldsymbol{X}$ merely ignores the $\boldsymbol{Y}$ part, while the conditional distribution assigns probabilities to all possible values of $\boldsymbol{X}$ in the case when the values of $\boldsymbol{Y}$ are known to be $\boldsymbol{y}$.

2.2.1.3 Simplified notation

When the random vector $\boldsymbol{Z}$ is evident from context, a simplified notation $p(\boldsymbol{z}) = p(\boldsymbol{x}, \boldsymbol{y}) = p_{\boldsymbol{X},\boldsymbol{Y}}(\boldsymbol{x}, \boldsymbol{y}) = p_{\boldsymbol{Z}}(\boldsymbol{z})$ is used for the joint probability mass function, $p(\boldsymbol{x}) = p(x_1, \ldots, x_m) = p_{\boldsymbol{X}}(\boldsymbol{x})$ is used for the marginal distribution, and $p(\boldsymbol{x} \mid \boldsymbol{y}) = p(x_1, \ldots, x_m \mid y_1, \ldots, y_n) = p_{\boldsymbol{X},\boldsymbol{Y}=\boldsymbol{y}}(\boldsymbol{x})$ is used for the conditional probability mass function. The simplified notation also highlights an important detail about the conditional probability mass function. Although $p(\boldsymbol{x} \mid \boldsymbol{y})$ is typically seen as a function of $\boldsymbol{x}$ while $\boldsymbol{y}$ is kept fixed, from a technical point of view, it is still function of both arguments. It is completely legal to fix $\boldsymbol{x}$ and treat it as a function of $\boldsymbol{y}$. In this case, however, the function looses the properties of probability mass function. For example $\sum_{\Omega_{\boldsymbol{y}}} p(\boldsymbol{x} \mid \boldsymbol{y})$ is generally not equal to 1.

2.2.1.4 Chain rule for probability mass function

In analogy to Eq. (2.6), the joint probability mass function is composed of conditional probability mass functions. Using the simplified notation, the joint probability mass function is written as

$$p(x_1, \ldots, x_n) = p(x_1 \mid x_2, \ldots x_n)p(x_2 \mid x_3, \ldots x_n) \ldots p(x_{n-1} \mid x_n)p(x_n) \tag{2.22}$$

2.2.1.5 Bayes' theorem in terms of probability mass functions

Bayes' theorem is written in terms of probability mass functions as

$$p(\boldsymbol{x} \mid \boldsymbol{y}) = \frac{p(\boldsymbol{y} \mid \boldsymbol{x})p(\boldsymbol{x})}{p(\boldsymbol{y})} = \frac{p(\boldsymbol{y} \mid \boldsymbol{x})p(\boldsymbol{x})}{\sum_{\Omega_{\boldsymbol{x}}} p(\boldsymbol{y} \mid \boldsymbol{x})p(\boldsymbol{x})} \tag{2.23}$$

Note that the denominator is a marginal probability mass function of Y, i.e., the joint probability mass function *marginalized* over all possible values of $\boldsymbol{X}$. Therefore, the denominator is *independent* of $\boldsymbol{x}$.

2.2.1.6 Example: Dice and dots in corners

Consider the following random experiment that results in two discrete values x and y. The experiment involves rolling standard western-style six-sided dice and randomly selecting one of the four corners of the top face. The first result $x \in \{1, 2, \ldots 6\}$ is the number of dots on the top face. The second result $y \in \{0, 1\}$ is the number of dots in the randomly selected corner of the top face. For this setup, we want to express

the probability mass function for x conditioned on $y = 1$. In other words, we want to calculate the probabilities that the dice landed with $1, 2, \ldots, 6$ at the top face when we know that there *was* a dot in the randomly selected corner of that face.

Solution: Due to its symmetries, a fair six-sided dice has a constant marginal probability mass function $p(x) = \frac{1}{6}$ for $x \in \{1, 2, \ldots, 6\}$. By examining the patterns of the dots on western-style six-sided dice, we learn that a) at the face with one dot no corners are occupied by a dot, b) the faces with two and three dots have two out of four corners occupied by a dot, and c) faces with four, five, and six dots have all corners occupied by a dot. Since the corner is selected randomly, this can be written as $p(y = 1 \mid x = 1) = 0$, $p(y = 1 \mid x = 2) = p(y = 1 \mid x = 3) = \frac{1}{2}$, and $p(y = 1 \mid x = 4) = p(y = 1 \mid x = 5) = p(y = 1 \mid x = 6) = 1$. Because there are only two possible values of y, the conditional probability mass function evaluated for $y = 0$ is $p(y = 0 \mid x) = 1 - p(y = 1 \mid x)$ for all possible values of $x \in 1, 2, \ldots, 6$. The probability mass function for y conditioned by x is expressed using the Bayes' rule as

$$p(x \mid y) = \frac{p(y \mid x)p(x)}{p(y)} \tag{2.24}$$

The denominator is the marginal probability mass function for Y which, contrary to the marginal probability mass function for X, is not directly known. It is therefore calculated by marginalizing the joint probability mass function , i.e., summing it over all possible values of X

$$p(y) = \sum_{\Omega_x} p(y, x) \tag{2.25}$$

Using the chain rule we rewrite the joint probability mass function in terms of conditional probability mass function and arrive at

$$p(y) = \sum_{\Omega_x} p(y \mid x)p(x) \tag{2.26}$$

To evaluate $p(y)$ at $y = 1$ we expand the sum to individual summands as

$$p_Y(1) = p_{Y|X=1}(1)p_X(1) + p_{Y|X=2}(1)p_X(2) + \cdots + p_{Y|X=6}(1)p_X(6) \tag{2.27}$$

$$= 0 \cdot \frac{1}{6} + \frac{1}{2} \cdot \frac{1}{6} + \frac{1}{2} \cdot \frac{1}{6} + 1 \cdot \frac{1}{6} + 1 \cdot \frac{1}{6} + 1 \cdot \frac{1}{6} = \frac{2}{3} \tag{2.28}$$

The marginal probability mass function evaluated at $y = 1$ is the probability that we observe a dot on a randomly selected corner of a random face of the dice. Note that for a fair dice the probability can be calculated as a ratio of the number of face corners with dots to the number of all face corners. However, this approach would not be applicable to an unfair dice.

The probability of *not* observing a dot in the randomly selected corner on a randomly selected face is $p(y = 0) = 1 - p(y = 1) = \frac{1}{3}$.

The conditional probability mass function $p(x \mid y)$ follows from Eq. (2.24). For example, the probability that the dice lands with *one* dot on the top face when we *observe*, resp. do *not* observe a dot in a random face corner is

$$p(x=1 \mid y=1) = \frac{p(y=1 \mid x=1)p(x=1)}{p(y=1)} = \frac{0 \cdot \frac{1}{6}}{\frac{2}{3}} = 0 \tag{2.29}$$

$$p(x=1 \mid y=0) = \frac{p(y=0 \mid x=1)p(x=1)}{p(y=0)} = \frac{1 \cdot \frac{1}{6}}{\frac{1}{3}} = \frac{1}{2} \tag{2.30}$$

respectively. The probability that the dice lands with *two* dots on the top face when we *observe*, resp. do *not* observe a dot in a random face corner is

$$p(x=2 \mid y=1) = \frac{p(y=1 \mid x=2)p(x=2)}{p(y=1)} = \frac{\frac{1}{2} \cdot \frac{1}{6}}{\frac{2}{3}} = \frac{1}{8} \tag{2.31}$$

$$p(x=2 \mid y=0) = \frac{p(y=0 \mid x=2)p(x=2)}{p(y=0)} = \frac{\frac{1}{2} \cdot \frac{1}{6}}{\frac{1}{3}} = \frac{1}{16} \tag{2.32}$$

respectively. Finally, we express the probability that the dice lands with *four* dots on the top face when we *observe*, resp. do *not* observe a dot in a random face corner is

$$p(x=4 \mid y=1) = \frac{p(y=1 \mid x=4)p(x=4)}{p(y=1)} = \frac{1 \cdot \frac{1}{6}}{\frac{2}{3}} = \frac{1}{4} \tag{2.33}$$

$$p(x=4 \mid y=0) = \frac{p(y=0 \mid x=4)p(x=4)}{p(y=0)} = \frac{0 \cdot \frac{1}{6}}{\frac{1}{3}} = 0 \tag{2.34}$$

respectively. Obviously, due to the same number of corner dots on faces 2 and 3 and faces 4, 5, and 6 we have $p(x=2 \mid y) = p(x=3 \mid y)$ and $p(x=4 \mid y) = p(x=5 \mid y) = p(x=6 \mid y)$.

2.2.2 Continuous random variable

The sample space of a continuous random variable is a subset of real numbers, $\Omega \in \mathbb{R}$, and is used to represent a random experiment with outcomes that can be assigned to this subset. For example, the value of atmospheric pressure or temperature measured at a chosen time results in a real number representing the value of the measured quantity. The quantity can be treated as a continuous random variable.

2.2.2.1 Probability density function

In the case of a continuous random variable, the probability is assigned to infinitesimal intervals around particular values. In particular, the probability that the random variable is in interval $(x, x+dx)$ with dx being small is

$$P(x < X < x + dx) = f_X(x)dx \tag{2.35}$$

where the positive function $f_X(x)$ is the *probability density function*. Note that this is in contrast to a discrete random variable for which the probability mass function assigns probabilities directly to particular values. The continuous random variable is also an example of probability triplet $(\Omega, \mathcal{F}, P)$ in which the event space $\mathcal{F}$ does not contain individual elements of the sample space Ω.

The probability density function is nonnegative and integrates to one

$$\int_{-\infty}^{\infty} f_X(x)dx = 1 \tag{2.36}$$

2.2.2.2 Multivariate continuous distribution

A random process that generates n results in a single trial, each assigned to a subset of real numbers, is denoted a *random vector*. The random vector consists of individual random continuous variables $\boldsymbol{X} = [X_1, \ldots, X_n]$. The *multivariate continuous distribution* of the random vector is completely determined by *joint* probability density function which defines a probability that each random variable is in small interval around some point $\boldsymbol{x}$

$$f_{\boldsymbol{X}}(\boldsymbol{x}) = \frac{P(x_1 < X_1 < x_1 + dx_1 \cap \cdots \cap x_n < X_n < x_n + dx_n)}{dx_1 \cdot \ldots \cdot dx_n} \tag{2.37}$$

Again, the subscript $\boldsymbol{X}$ of the function f specifies the random vector in question while the argument $\boldsymbol{x} = \{x_1, x_2, \ldots, x_n\}$ specifies a concrete point at which the probability density is evaluated.

In analogy to the univariate case, the joint probability density function is nonnegative and integrates to one over its domain. When the domain of $f_{\boldsymbol{X}}$ is only some subset Ω of $\mathbb{R}^n$, the function $f_{\boldsymbol{x}}$ can be formally extended to $\boldsymbol{x} \in \mathbb{R}^n$ by defining $f_{\boldsymbol{X}}(\boldsymbol{x}) = 0$ for all $\boldsymbol{x} \in \mathbb{R}^n \setminus \Omega$. Then we can write

$$\int_{-\infty}^{\infty} \cdots \int_{-\infty}^{\infty} f_{\boldsymbol{X}}(x_1, \cdots, x_n)dx_1 \cdots dx_n = 1 \tag{2.38}$$

2.2.2.3 Marginal and conditional probability density function

Again, in analogy to the discrete case we consider a random vector $\boldsymbol{Z}$ whose elements are conceptually separated into two parts

$$\boldsymbol{Z} = [\boldsymbol{X}, \boldsymbol{Y}] = [X_1, \ldots, X_m, Y_1, \ldots, Y_n] \tag{2.39}$$

This random vector has some continuous probability distribution defined by the joint probability density function

$$f_{\boldsymbol{X},\boldsymbol{Y}}(\boldsymbol{x}, \boldsymbol{y}) = f_{X_1,\ldots,X_m,Y_1,\ldots,Y_n}(x_1, \ldots, x_m, y_1, \ldots, y_n) \tag{2.40}$$

The marginal distribution of $\boldsymbol{X}$ defined by the marginal probability density function

$$f_{\boldsymbol{X}}(x_1, \ldots, x_m) = \int_{-\infty}^{\infty} \cdots \int_{-\infty}^{\infty} f_{\boldsymbol{X},\boldsymbol{Y}}(x_1, \ldots, x_m, y_{1,i_1}, \ldots, y_{n,i_n})dy_1 \cdots dy_n \tag{2.41}$$

A useful intuition behind the marginal distribution is that it is the distribution of $\boldsymbol{X}$ when the outcomes of $\boldsymbol{Y}$ are *ignored*.

The conditional distribution of $\boldsymbol{X}$ is defined by the conditional probability density function defined as

$$f_{\boldsymbol{X}|\boldsymbol{Y}=\boldsymbol{y}}(x_1, \dots x_m) = \frac{f_{\boldsymbol{X},\boldsymbol{Y}}(x_1, \dots, x_m, y_1, \dots, y_n)}{f_{\boldsymbol{Y}}(y_1, \dots, y_n)} \tag{2.42}$$

where $f_{\boldsymbol{Y}}(y_1, \dots, y_n)$ is the marginal probability density function of $\boldsymbol{Y}$. The conditional distribution is the distribution of $\boldsymbol{X}$ when the values of $\boldsymbol{Y}$ are *known and fixed*.

Recall that when $f_{\boldsymbol{X},\boldsymbol{Y}=\boldsymbol{y}}(\boldsymbol{x}) = f_{\boldsymbol{X}}(\boldsymbol{x})$ for all $\boldsymbol{x}$ and $\boldsymbol{y}$ the random vectors $\boldsymbol{X}$ and $\boldsymbol{Y}$ are *independent*.

2.2.2.4 Simplified notation

The simplified notation also applies to the continuous probability density functions. The subscripts of the function's name is left out and the function is recognized by the names of its arguments

$$f_X(x) = f(x) \tag{2.43}$$
$$f_{X|Y=y}(x) = f(x \mid y) \tag{2.44}$$

and for function evaluated or conditioned at certain known point a and b we write

$$f_X(a) = f(x = a) \tag{2.45}$$
$$f_{X|Y=b}(a) = f(x = a \mid y = b) \tag{2.46}$$

2.2.2.5 Chain rule for probability density function

The chain rule also applies to probability density functions. The joint probability density is written as a product of conditional and marginal probability density function as

$$f(x_1, \dots, x_n) = f(x_1 \mid x_2, \dots x_n) f(x_2 \mid x_3, \dots x_n) \dots f(x_{n-1} \mid x_n) f(x_n) \tag{2.47}$$

Note then when the variables are independent, the marginal and conditional densities are identical and the joint probability density function becomes a product of individual density functions. This is written as

$$f(x_1, \dots, x_n) = \prod_{i=1}^{n} f(x_i) \tag{2.48}$$

2.2.2.6 Bayes' theorem in terms of probability density functions

Bayes' theorem can be written in terms of probability densities as

$$f(\boldsymbol{x} \mid \boldsymbol{y}) = \frac{f(\boldsymbol{y} \mid \boldsymbol{x}) f(\boldsymbol{x})}{f(\boldsymbol{y})} = \frac{f(\boldsymbol{y} \mid \boldsymbol{x}) f(\boldsymbol{x})}{\int_{\Omega_x} f(\boldsymbol{y} \mid \boldsymbol{x}) f(\boldsymbol{x}) d\boldsymbol{x}} \tag{2.49}$$

At this point, it is useful to emphasize that both sides of the equation are typically assumed to be functions of $\boldsymbol{x}$ while $\boldsymbol{y}$ is considered to be fixed and known. This might be counterintuitive especially at the right-hand side term $f(\boldsymbol{y} \mid \boldsymbol{x})$ because the conditional probability density function is being evaluated at the fixed $\boldsymbol{y}$ while it is conditioned on the free variable $\boldsymbol{x}$.

2.2.2.7 Example: Two-stage exam

Consider the following two-stage system of student's examination:

- In the first stage, students can score from 0 to 10 points.
- Students who scored less than 5 points in the first stage can obtain between 0 and 100 points in the second stage of the exam.
- Students who scored 5 or more points in the first stage can obtain between 50 and 100 points in the second stage.
- In both stages, the points scored are uniformly distributed between the possible limits.

For this setup, we want to find the probability density function of x conditioned on y, that is, to find the distribution of the points obtained in the first stage of the exam when we know the points obtained in the second stage.

Solution: The marginal probability density for the points gained in the first stage x is constant on closed interval $[0, 10]$ and zero elsewhere. It is written as

$$f(x) = \begin{cases} \frac{1}{10} & \text{for } x \in [0, 10] \\ 0 & \text{elsewhere} \end{cases} \tag{2.50}$$

The probability density for the points gained in the second stage y is also constant. However, it is conditioned on the points obtained in the first stage. This is written as

$$f(y \mid x) = \begin{cases} \frac{1}{100} & \text{for } y \in [0, 100] \text{ and } x < 5 \\ \frac{1}{50} & \text{for } y \in [50, 100] \text{ and } x \geq 5 \\ 0 & \text{elsewhere} \end{cases} \tag{2.51}$$

Using the chain rule we write the marginal probability density function for y as follows

$$f(y) = \int_{-\infty}^{\infty} f(y \mid x) f(x) dx \tag{2.52}$$

The integration over x is performed separately for $y \in [0, 50)$ and $y \in [50, 100]$ resulting in

$$f(y) = \begin{cases} \frac{1}{100} \cdot \frac{1}{10} \cdot 5 + 0 \cdot \frac{1}{10} \cdot 5 = \frac{1}{200} & \text{for } y \in [0, 50) \\ \frac{1}{100} \cdot \frac{1}{10} \cdot 5 + \frac{1}{50} \cdot \frac{1}{10} \cdot 5 = \frac{3}{200} & \text{for } y \in [50, 100] \\ 0 & \text{elsewhere} \end{cases} \tag{2.53}$$

The probability density function for x conditioned on $y \in [0, 50)$ then reads

$$f(x \mid y \in [0,50)) = \begin{cases} \frac{\frac{1}{100}\cdot\frac{1}{10}}{\frac{1}{200}} = \frac{1}{5} & \text{for } x \in [0,5) \\ \frac{0\cdot\frac{1}{10}}{\frac{1}{200}} = 0 & \text{for } x \in [5,10] \\ 0 & \text{elsewhere} \end{cases} \tag{2.54}$$

This density can be interpreted as follows: *When we learn that a student obtained less than 50 points in the second stage of the exam, we know that in the first stage he/she received between 0 and 5 points and all the values in this range are equally likely.*

When the probability density function for x is conditioned on $y \in [50, 100]$ it becomes

$$f(x \mid y \in [50,100]) = \begin{cases} \frac{\frac{1}{100}\cdot\frac{1}{10}}{\frac{3}{200}} = \frac{1}{15} & \text{for } x \in [0,5) \\ \frac{\frac{1}{50}\cdot\frac{1}{10}}{\frac{3}{200}} = \frac{2}{15} & \text{for } x \in [5,10] \\ 0 & \text{elsewhere} \end{cases} \tag{2.55}$$

Note that the probability density function is now piecewise constant. It can be interpreted as follows: *When we learn that a student obtained more than 50 points in the second stage of the exam, we know that in the first stage he/she received between 0 and 10 points and any value greater than 5 is twice as likely than any value less than 5.*

Also note that the conditional probability density function $f(x \mid y)$ integrate to one regardless of the value of y:

$$\int_{-\infty}^{\infty} f(x \mid y \in [0,50))dx = \frac{1}{5}\cdot 5 = 1 \tag{2.56}$$

$$\int_{-\infty}^{\infty} f(x \mid y \in [50,100])dx = \frac{1}{15}\cdot 5 + \frac{2}{15}\cdot 5 = 1 \tag{2.57}$$

2.2.3 Collection of discrete and continuous variables

In the previous sections the multivariate distribution and the marginal/conditional probability mass/density functions were defined for vectors of either discrete or continuous variables. However, this is not necessary, and a multivariate distribution can be defined for a collection of random variables of mixed types. As the basic example, consider a discrete random variable x with the probability mass function $p(x)$ and the sample space Ω_x and a continuous random variable y with the probability density function $f(y)$ and sample space Ω_y. Bayes' theorem for these two variables is written as

$$p(x \mid y) = \frac{f(y \mid x)p(x)}{f(y)} = \frac{f(y \mid x)p(x)}{\sum_{x\in\Omega_x} f(y \mid x)p(x)} \tag{2.58}$$

or

$$f(y \mid x) = \frac{p(x \mid y)f(y)}{p(x)} = \frac{p(x \mid y)f(y)}{\int_{y\in\Omega_y} p(x \mid y)f(y)dy} \tag{2.59}$$

2.3 Bayesian inference

A statistical inference is the process of finding the values of the parameters of a probabilistic model given the observed data generated by the random quantity of interest. The concepts of probabilistic model, model parameters, and observed data are introduced in the following sections.

2.3.1 Probabilistic model

When a single trial of a random experiment results in an integer value, a real value, or a collection of these, it can be described by a *probabilistic model*. The model describes how the outcome values are distributed and how they depend on each other. In the simple case, the model of a random variable is just some *probability distribution* defined by the probability mass function or the probability density function. Most common probability distributions use some parameters. These are numbers that appear in the probability mass/density function. When they are fixed, the probability mass function or probability density function becomes an expression of the variable x only. As an example, when the continuous random variable X is uniformly distributed in the interval $(1, 2)$, which is written as $X \sim \mathcal{U}(1, 2)$, then its model is a uniform distribution and the lower and upper bounds are its parameters and the values 1 and 2 are their values. Two completely different random variables may be described by the same model but may have different values of its parameters. For example, two random variables may both have a uniform distribution, but each with different ranges.

In a more general case, the probabilistic model is a system of probabilistic and deterministic relations that describe how the random values are generated. The system described in Section 2.2.1.6 that generates a pair of integers and the system described in Section 2.2.2.7 that generates a pair of real numbers also represent two probabilistic models. The limits of the uniform distributions in the latter model are the model parameters.

2.3.2 Probability as a measure of credibility

In the classical sense, a probability of a value generated by a random experiment is a relative frequency of that value. This means that probability is used to describe something for which we can perform *trials*. The execution of trials is also known as *sampling* from a random experiment or *drawing samples*.

Bayesian approach to probability extends its application to variables that we cannot sample. In particular, probability is used to express a *credibility* of possible events or values of a certain process or variable. Note that the distinction is subtle and rather philosophical. For example, if we say "There is 80% probability that Beatrice will arrive at our wedding." we use probability to describe credibility of an event rather than a relative frequency of that event. We presumably will not be able to sample Beatrice's presence more than once.

Note that from a mathematical point of view it is irrelevant in which of these two contexts the probability is used.

2.3.3 Bayes' theorem in context of statistical inference

The Bayesian inference assigns probability not only to the observed values that were sampled from a random system but also to the parameters of its model. When the data are observed, the Bayes theorem is used to express the credibility of the model parameters. It is customary to denote the *observed data* as $\boldsymbol{y}$ and the model *parameters* as $\boldsymbol{\theta}$. In context of statistical inference the Bayes theorem, here written in terms of probability density functions, reads

$$f(\boldsymbol{\theta} \mid \boldsymbol{y}) = \frac{f(\boldsymbol{y} \mid \boldsymbol{\theta}) f(\boldsymbol{\theta})}{f(\boldsymbol{y})} = \frac{f(\boldsymbol{y} \mid \boldsymbol{\theta}) f(\boldsymbol{\theta})}{\int_{\Omega_{\boldsymbol{\theta}}} f(\boldsymbol{y} \mid \boldsymbol{\theta}) f(\boldsymbol{\theta}) d\boldsymbol{\theta}} \tag{2.60}$$

The term $f(\boldsymbol{\theta} \mid \boldsymbol{y})$ is referred to as the probability density function of the *posterior distribution* of the model parameters, or simply as the *posterior density*. It represents the distribution of credit for the possible values of the model parameters $\boldsymbol{\theta}$ *after* the random data $\boldsymbol{y}$ were generated from the random system in question.

The term $f(\boldsymbol{y} \mid \boldsymbol{\theta})$ is referred to as the *likelihood* of the model parameters. It is essential to understand that the probability density of the data $\boldsymbol{y}$ and the likelihood of the parameters $\boldsymbol{\theta}$ are technically the same functions. When the parameters are fixed and the function is evaluated for different values of $\boldsymbol{y}$, it is referred to as the probability density function. When the data $\boldsymbol{y}$ are fixed at some observed values and the function is evaluated for different values or parameters $\boldsymbol{\theta}$, the function is termed likelihood. In this case, it returns the credibility of these parameter values given the observed data.

The term $f(\boldsymbol{\theta})$ represents the probability density function of *prior distribution* of the model parameters, or simply *prior distribution*. It specifies the distribution of the credibility of the possible parameter values before any random data was observed. As such, it represents general prior knowledge of the system. For example, the information that some values of the model parameters are physically meaningless can be incorporated into the inference by choosing a prior distribution with zero probability density for these values.

The term $f(\boldsymbol{y}) = \int_{\Omega_{\boldsymbol{\theta}}} f(\boldsymbol{y} \mid \boldsymbol{\theta}) f(\boldsymbol{\theta}) d\boldsymbol{\theta}$ is referred to as *evidence*. It does not depend on $\boldsymbol{\theta}$. The evidence merely scales the numerator so that the resulting posterior density satisfies

$$\int_{\Omega_{\boldsymbol{\theta}}} f(\boldsymbol{\theta} \mid \boldsymbol{y}) d\boldsymbol{\theta} = 1 \tag{2.61}$$

The evidence term is not of high importance in practical applications of Bayesian inference of complex probabilistic models because the posterior density is typically explored by *sampling* the model parameters. Section 2.5 describes the commonly used algorithms that can sample from the posterior distribution using only the product of likelihood and prior density $f(\boldsymbol{y} \mid \boldsymbol{\theta}) f(\boldsymbol{\theta})$ without requiring that the function is properly scaled by $f(\boldsymbol{y})$.

2.3.4 Example: inferring the probability of a coin landing heads or tails

Variations of the following example appear commonly in various texts on Bayesian inference. The example nicely illustrates the roles of prior distribution, likelihood, and evidence to obtain the posterior distribution of a single model parameter.

Consider a slightly deformed coin. When flipped, the coin can land on one of its two sides, denoted as *heads* and *tails*. It cannot land on its edge because these are rounded. The coin is not symmetric, so it may or may not be fair. We want to determine the probability of the coin landing heads.

A single flip of the coin is a random experiment that results in two possible events. We label Heads $= 1$ and Tails $= 0$. By such an assignment, the random experiment becomes a discrete random variable Y with sample space $\Omega_Y = \{0, 1\}$.

We further assume that the coin has some inherent probability that is the same for all flips and that the outcomes of a series of flips are independent of each other, i.e., the coin has no memory. Such samples are referred to as being independent and identically distributed (i.i.d). We *choose* the probability of the coin landing heads being the model's *parameter* θ. The model therefore *defines* its parameter θ as

$$p(y = 1) = \theta \tag{2.62}$$

The prior distribution expresses our belief in different values of θ. Since θ is a probability, it ranges between 0 and 1. The case $\theta = 0$ represents a coin which *never* lands heads, $\theta = 1$ represents a coin which *always* lands heads, $\theta = 0.5$ represents a fair coin, theta $\theta = 0.42$ represents a coin slightly biased towards tails, etc. If we have no prior knowledge about the coin, it is natural to assume all values between 0 and 1 are equally likely. This is expressed by a uniform distribution for θ. The probability density function reads

$$f(\theta) = \begin{cases} 1 & \text{for } \theta \in [0, 1] \\ 0 & \text{otherwise} \end{cases} \tag{2.63}$$

The likelihood function is simply the probability of observing heads with some value of θ which is

$$p(y = 1 \mid \theta) = \theta \tag{2.64}$$

and the probability of observing tails with θ is

$$p(y = 0 \mid \theta) = 1 - \theta \tag{2.65}$$

Now suppose that we flipped the coin once and observed it landed *heads*. The posterior distribution obtained via the Bayes theorem is

$$f(\theta \mid y = 1) = \frac{p(y = 1 \mid \theta) f(\theta)}{\int_{\theta=0}^{1} p(y = 1 \mid \theta) f(\theta)} = \begin{cases} \frac{\theta \cdot 1}{\int_{\theta=0}^{1} \theta \cdot 1 d\theta} = 2\theta & \text{for } \theta \in [0, 1] \\ 0 & \text{otherwise} \end{cases} \tag{2.66}$$

The function describes how we redistributed our belief in particular values of θ after we observed $y = 1$. Several things are to be taken into account in the probability density $f(\theta \mid y = 1)$. We now tend to favor higher values of θ. The value $\theta = 0$ has zero posterior density. Although we *a priori* considered the possibility that the coin could land on tails only, the *posterior* density at $\theta = 0$ is zero, which naturally rules out this scenario. Also note that the posterior probability density function is properly scaled so it integrates to 1.

Now suppose that we flipped the coin again and observed heads again. Now, the data are heads twice, simply denoted as $y = \{1, 1\}$. Since the coin flips are independent, the probability of observing heads twice is a product of the probabilities of the individual outcomes rendering

$$p(y = \{1, 1\} \mid \theta) = p(y = 1 \mid \theta)p(y = 1 \mid \theta) \tag{2.67}$$

This gives the posterior density in form

$$f(\theta \mid y = \{1, 1\}) = \frac{p(y = \{1, 1\} \mid \theta)f(\theta)}{\int_{\theta=0}^{1} p(y = \{1, 1\} \mid \theta)f(\theta)} = \begin{cases} \frac{\theta \cdot \theta \cdot 1}{\int_{\theta=0}^{1} \theta \cdot \theta \cdot 1 d\theta} = 3\theta^2 & \text{for } \theta \in [0, 1] \\ 0 & \text{otherwise} \end{cases} \tag{2.68}$$

Our belief in possible values of θ shifted even more towards 1. Low values of θ are very unlikely, suggesting that we almost surely do not deal with a coin highly biased towards tails.

The final coin flip resulted in tails. The probability of observing heads twice and tails once is again a product of probabilities of individual events

$$p(y = \{1, 1, 0\} \mid \theta) = p(y = 1 \mid \theta)p(y = 1 \mid \theta)p(y = 0 \mid \theta) \tag{2.69}$$

The posterior density then reads

$$f(\theta \mid y = \{1, 1, 0\}) = \begin{cases} \frac{\theta \cdot \theta \cdot (1-\theta) \cdot 1}{\int_{\theta=0}^{1} \theta \cdot \theta \cdot (1-\theta) \cdot 1 d\theta} = 12\theta^2(1 - \theta) & \text{for } \theta \in [0, 1] \\ 0 & \text{otherwise} \end{cases} \tag{2.70}$$

With this posterior probability density function it holds not only $f(\theta = 0 \mid y = [1, 1, 0]) = 0$ but also $f(\theta = 1 \mid y = [1, 1, 0]) = 0$, meaning that the prior possibility that the coin lands only heads is ruled out given the observed data. As shown in Figure 2.2, the density begins to form a peak that shows the range of the most credible values of θ.

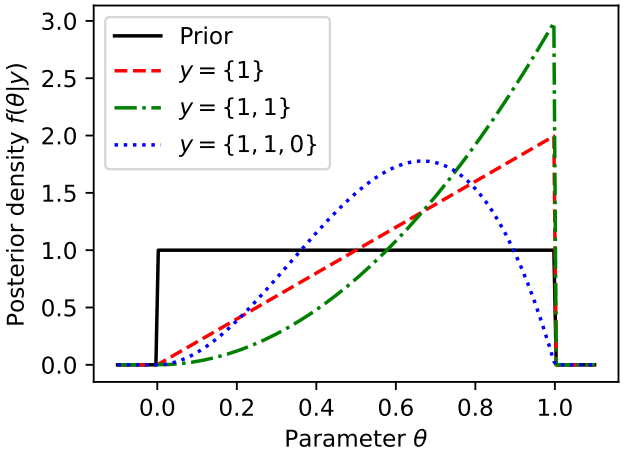

Figure 2.2: Prior density and posterior densities of parameter θ obtained for 1, 2 and 3 coin tosses.

The posterior distribution of θ resulting from this example is actually the Beta distribution. This distribution is typically formulated using two parameters α and β and its probability density function is

$$f(x) = \frac{x^{\alpha-1}(1-x)^{\beta-1}}{B(\alpha, \beta)} \tag{2.71}$$

where B is the Beta function which for positive integers is provided by

$$B(m, n) = \frac{(m-1)!(n-1)!}{(m+n-1)!} \tag{2.72}$$

2.3.5 Prior predictive and posterior predictive distributions

It was demonstrated in the previous example that Bayesian inference does not result in a single value of the model parameter but rather in a posterior distribution of all possible values. One might ask how to use this result to predict values of yet-unobserved data. The unobserved data are traditionally denoted as $\overline{y}$ and *posterior predictive distribution* given the already observed data y is generally written as

$$f(\overline{\boldsymbol{y}} \mid \boldsymbol{y}) = \int_{\Omega_\theta} f(\overline{\boldsymbol{y}} \mid \boldsymbol{\theta}) f(\boldsymbol{\theta} \mid \boldsymbol{y}) d\boldsymbol{\theta} \tag{2.73}$$

Note that the posterior predictive probability density function can be seen as weighted average of the density function $f(\overline{\boldsymbol{y}} \mid \boldsymbol{\theta})$ with the weights being the posterior distribution $f(\boldsymbol{\theta} \mid \boldsymbol{y})$. Analogous to the concept of posterior predictive distribution is the *prior predictive distribution* defined as average distribution of the data weighted by the prior

distribution of the model parameters

$$f(\overline{\boldsymbol{y}}) = \int_{\Omega_\theta} f(\overline{\boldsymbol{y}} \mid \boldsymbol{\theta}) f(\boldsymbol{\theta}) d\boldsymbol{\theta} \tag{2.74}$$

The prior predictive distribution of data $\overline{\boldsymbol{y}}$ characterizes what the probabilistic model together with our choice of the prior distribution of its parameters imply on the data. It shows our assumption on how the data are distributed *before* any data were observed.

2.3.6 Example: Predicting the outcome of a coin flip

Consider the previous example of a potentially unfair coin tossed three times. The prior distribution for its parameter θ was uniform in $\theta \in [0, 1]$. The prior probability of observing heads is given by the prior probability mass function evaluated at $\overline{y} = 1$ which is

$$p(\overline{y} = 1) = \int_{\Omega_\theta} p(y = 1 \mid \theta) f(\theta) d\theta = \int_0^1 \theta \cdot 1 d\theta = \frac{1}{2} \tag{2.75}$$

Obviously the prior probability of observing tails is $p(\overline{y} = 0) = 1 - p(\overline{y} = 1) = \frac{1}{2}$. The result can be interpreted as follows: if we consider all possible properties of the coin, i.e., a fair one, one biased towards heads, one biased towards tail, etc., the resulting "averaged" coin would be fair.

When heads were observed for the first time, the posterior distribution was $f(\theta \mid y = 1) = 2\theta$. The posterior predictive probability mass function evaluated for heads then reads

$$p(\overline{y} = 1 \mid y = 1) = \int_0^1 \theta \cdot 2\theta d\theta = \frac{2}{3} \tag{2.76}$$

This result tells us that if we have an unbiased uniform distribution of our credit over all possible properties of the coin and observe heads after single coin toss, we should expect observing heads again with probability $\frac{2}{3}$.

After observing two heads, the posterior probability density function was $f(\theta \mid y = \{1, 1\}) = 3\theta^2$. The posterior predictive distribution is in this case given by the probability

$$p(\overline{y} = 1 \mid y = \{1, 1\}) = \int_0^1 \theta \cdot 3\theta^2 d\theta = \frac{3}{4} \tag{2.77}$$

The coin seems to land heads quite often and therefore the probability of observing heads as the next result increases to $\frac{3}{4}$.

Finally, after observing heads twice and tails once, the posterior probability density of θ was $f(\theta \mid y = \{1, 1, 0\}) = 12\theta^2(1 - \theta)$. The posterior predictive distribution is in this case given by the mass function

$$p(\overline{y} = 1 \mid y = \{1, 1, 0\}) = \int_0^1 \theta \cdot 12\theta^2(1 - \theta) d\theta = \frac{3}{5} \tag{2.78}$$

$$p(\overline{y} = 0 \mid y = \{1, 1, 0\}) = 1 - p(\overline{y} = 1 \mid y = \{1, 1, 0\}) = \frac{2}{5} \tag{2.79}$$

By observing tails the probability of observing heads in the next toss decreased to $\frac{3}{5}$.

In summary, the parameters of a Bayesian model are always expressed in the form of their probability distributions. The initial general knowledge about the parameter values before the data are observed is expressed as a prior distribution. The result of Bayesian inference is the posterior distribution. When a prediction of new data needs to be made, the posterior predictive distribution is constructed from the posterior distribution of the model parameters.

2.4 Hierarchical Bayesian models

The power of Bayesian inference arises from its ability to work with more complex probabilistic models than the coin example shown in the previous section. When the relations between the data and parameters have several levels and a graph-like structure, the models are referred to as *hierarchical* or *graphical* Bayesian models or *Bayesian networks*.

2.4.1 Declarative notation for probabilistic model

The growing complexity of hierarchical models calls for some way to separate the model declaration from the process of deriving the likelihood function. For structuring the probabilistic relationships within the model, the notation $X \sim \mathcal{A}(\alpha, \beta)$ is used. This means that a random variable X is distributed according to the distribution $\mathcal{A}$ with parameters α and β. This is a shorter way of writing $P(x < X < x + dx) = f_X(x; \alpha, \beta)dx$ with $f_X(x; \alpha, \beta)$ being the probability density function of the distribution $\mathcal{A}$. A deterministic relation between variables or parameters is traditionally denoted as $A = f(B, C)$ where f is some known deterministic function.

The tradition of denoting random variables in upper case letters is often abandoned in the Bayesian hierarchical model declaration. The type of symbol, whether it represents a random quantity of fixed value, usually follows from the context.

2.4.2 Example - tensile test on wood specimens

Consider a series of m displacement-controlled tensile tests on spruce wood specimens. A series of n_i strains is applied to each i-th specimen. Thus, e_{ij} denotes the axial strain prescribed to the i-th specimen in the j-th loading step. The corresponding axial stress s_{ij} is measured for each strain step. Note that the symbols e and s are used for the strain and stress instead of the common symbols ε and σ to prevent confusion with a standard deviation and an error term in regression models.

Our goal is to determine Young's modulus for each specimen, the mean, and standard deviation of Young's moduli among the samples. All these parameters will be determined by means of Bayesian inference, i.e., in the form of their posterior joint probability distribution.

We start from formulating the probabilistic model of the data. The model describes how we believe the data are generated in a situation where the values of the model

parameters are known. Therefore, the probabilistic model is also referred to as *forward model.*

Since the measured stress depends on strain non-deterministically, the probabilistic model is a regression model with the strain $e_{ij},\ i = 1 \dots N,\ j = 1 \dots M_i$ being the known predictor variable and the stress $s_{ij},\ i = 1 \dots N,\ j = 1 \dots M_i$ being the response variable. The response variable represents the data that we are going to predict. In the model, we assume that the measured stress is normally distributed around some mean value $\bar{s}_{ij}$ with standard deviation σ_s representing a measurement error. This is written declaratively as

$$s_{ij} \sim \mathcal{N}(\mu = \bar{s}_{ij}, \sigma = \sigma_s) \tag{2.80}$$

The mean value of stress $\bar{s}_{ij}$ depends deterministically on strain according to Hooke's law

$$\bar{s}_{ij} = E_i e_{ij} \tag{2.81}$$

Two things are of interest in these relations. First, there are N values of Young's moduli, each attributed to an individual wood specimen and indexed by i. Second, the relations (2.80) and (2.81) can be equivalently written as

$$s_{ij} = E_i e_{ij} + \varepsilon \tag{2.82}$$

$$\varepsilon \sim \mathcal{N}(\mu = 0, \sigma = \sigma_s) \tag{2.83}$$

which is a more common form in standard regression models. However, in the context of Bayesian models, the first approach seems to be more natural, because it directly specifies the probability density function of the observed data s_{ij}.

The individual Young moduli are not completely independent values. They originate from a population of possible Young's moduli on spruce wood specimens, and therefore they share some probability distribution. Here we assume that they are also normally distributed

$$E_i \sim \mathcal{N}(\mu = \mu_E, \sigma = \sigma_E) \tag{2.84}$$

where μ_E and σ_E are the mean Young's modulus observed on tensile test specimens and its standard deviation.

Note the two levels of the model hierarchy. The lower level describes the uncertain process of measurement that occurs in an individual specimen. The upper level describes the differences in properties within a group of individual wood specimens.

The parameters of the model are E_i, σ_s, μ_E and σ_E, but of these only E_i has the probability distribution already specified by Eq. (2.84). We further specify the uniform probability distribution of σ_s, μ_E and σ_E *a priori.* The prior distribution is therefore written as

$$\sigma_s \sim \mathcal{U}(a, b) \tag{2.85}$$

$$\mu_E \sim \mathcal{U}(c, d) \tag{2.86}$$

$$\sigma_E \sim \mathcal{U}(e, f) \tag{2.87}$$

where $x \sim \mathcal{U}(a, b)$ means that x is uniformly distributed between a and b. The parameters of the prior distributions are fixed and known *a priori*. They are called *hyper parameters* and their values are based on general knowledge of the domain or expert judgement. This completes the specification of the model in a declarative way. We proceed by deriving the posterior density functions from these probabilistic relations.

The posterior distribution is given by the probability density function of *all unknown* model parameters, i.e., excluding hyperparameters, conditioned on known values of the data. Assembling all Young's moduli and all observed values of stress into a vectors $\boldsymbol{E} = \{E_1 \ldots, E_N\}$ and $\boldsymbol{s} = \{s_{11}, \ldots, s_{N,M_N}\}$ and using Bayes' theorem we write

$$f(\boldsymbol{E}, \mu_E, \sigma_E, \sigma_s \mid \boldsymbol{s}) = \frac{f(\boldsymbol{s} \mid \boldsymbol{E}, \mu_E, \sigma_E, \sigma_s) f(\boldsymbol{E}, \mu_E, \sigma_E, \sigma_s)}{f(\boldsymbol{s})} \tag{2.88}$$

As will be shown in later sections, the posterior density will be analyzed by drawing samples from it. The samplers used in the Bayesian context require the posterior density function to be defined up to multiplication of some positive constant. In other words, it is not necessary to calculate the evidence term $f(\boldsymbol{s})$. The posterior density function is *proportional* to the product of likelihood and prior density

$$f(\boldsymbol{E}, \mu_E, \sigma_E, \sigma_s \mid \boldsymbol{s}) \propto f(\boldsymbol{s} | \boldsymbol{E}, \mu_E, \sigma_E, \sigma_s) f(\boldsymbol{E}, \mu_E, \sigma_E, \sigma_s) \tag{2.89}$$

Considering that a) the data $\boldsymbol{s}$ depend on $\boldsymbol{E}$ and σ_s, b) taking into account that $\boldsymbol{E}$ depends on μ_E and σ_E and c) the parameters σ_s, μ_s and σ_E are mutually independent *a priori*, we write

$$f(\boldsymbol{E}, \mu_E, \sigma_E, \sigma_s \mid \boldsymbol{s}) \propto f(\boldsymbol{s} | \boldsymbol{E}, \sigma_s) f(\boldsymbol{E} | \mu_E, \sigma_E) f(\mu_E) f(\sigma_E) f(\sigma_s) \tag{2.90}$$

Since the individual errors in s_{ij} are mutually independent and the same holds for Young's moduli E_i, their joint probability density function is a product of individual densities. This brings us to the posterior probability density function in the final form

$$\begin{aligned} f(\boldsymbol{E}, \mu_E, \sigma_E, \sigma_s \mid \boldsymbol{s}) \propto & \prod_{i=1}^{N} \prod_{j=1}^{M_i} f_N(s_{ij}, E_i \cdot e_{ij}, \sigma_s) \\ & \cdot \prod_{i=1}^{N} f_N(E_i, \mu_E, \sigma_E) f_U(\mu_E, c, d) f_U(\sigma_E, e, f) f_U(\sigma_s, a, b) \end{aligned} \tag{2.91}$$

where $f_N(x, \mu, \sigma)$ is the probability density function of the normal distribution

$$f_N(x, \mu, \sigma) = \frac{1}{\sqrt{2\pi\sigma^2}} \exp\left(\frac{(x-\mu)^2}{2\sigma^2}\right) \tag{2.92}$$

and $f_U(x, a, b)$ is the probability density function of the uniform distribution

$$f_U(x, a, b) = \begin{cases} \frac{1}{b-a} & \text{if } x \in [a, b] \\ 0 & \text{otherwise} \end{cases} \tag{2.93}$$

Note that because the strain values e_{ij}, the stress values s_{ij} and the hyper parameters $a, b, \ldots, e$ are fixed and known, the right-hand side of the equation is a function of the model parameters $\boldsymbol{E}$, μ_E,σ_E and σ_s only.

2.4.3 Log-likelihood

Calculating the products such as those in Eq. (2.91) is impractical. Instead the posterior density is expressed as a sum of logarithms of the individual likelihood terms. For example, Eq. (2.91) is written as

$$\begin{aligned}\ln(f(\boldsymbol{E}, \mu_E, \sigma_E, \sigma_s \mid \boldsymbol{s})) = &\sum_{i=1}^{N}\sum_{j=1}^{M_i} \ln(f_N(s_{ij}, E_i \cdot e_{ij}, \sigma_s)) \\ &+ \sum_{i=1}^{N} \ln(f_N(E_i, \mu_E, \sigma_E)) \\ &+ \ln(f_U(\mu_E, c, d)) \ln(f_U(\sigma_E, e, f)) \ln(f_U(\sigma_s, a, b)) \\ &+ const. \end{aligned} \tag{2.94}$$

where the constant is independent on the function's arguments. Such expression is referred to as the *log-likelihood*. In practical applications only the *ratio* of the posterior density function expressed at two different points is of importance. This is equivalent to expressing a *difference* of log-likelihoods at different points. Therefore, the constant term in Eq (2.94) can be ignored.

2.5 Markov chain Monte Carlo sampling methods

The posterior joint probability density function of the model parameters does not provide much insight *per se*. However, it is used to calculate quantities that provide useful information such as the probability that some parameter is greater than or less than a chosen value. Calculating *credible intervals* or expressing the posterior predictive distribution of the data yet unobserved are other examples of useful results that are calculated from the posterior density function. All these calculations involve *integration* of the density function. As the example on Young's modulus estimation showed, the probability density function is often *multivariate* and the number of its arguments can reach hundreds or even thousands [1]. Closed forms of the integrals are often unknown or overly complex, and calculating the integrals by common quadrature rules is inefficient due to the high dimensionality. The Bayesian inference therefore resorts to Monte Carlo integration.

The Monte Carlo analysis of the posterior distribution is based on drawing samples of the model parameters from it. The particularly useful family of samplers in the context of Bayesian inference are *Markov chain Monte Carlo sampling* methods. These methods share the same property. The probability distribution of the value of the next sample depends only on the previous sample and therefore the sequence of generated values consists of a *Markov chain*. The common feature of the sampling algorithms briefly described in the following sections is that they keep track of the last returned sample and use this value when generating the next sample.

Another property of the sampling algorithms is that they do not need the *proper* posterior density function which integrates to 1 but they work also with a function

proportional to the density function. This means that when sampling from the posterior distribution, only the product of likelihood and prior density is necessary to evaluate, and the evidence term in the denominator is irrelevant. The discovery of effective sampling algorithms not requiring the proper scaling of the probability density functions is what made the Bayesian inference applicable to many complex statistical models.

2.5.1 Metropolis-Hastings algorithm

Consider generating values of discrete or continuous multidimensional random variables $\boldsymbol{X}$ with a probability mass function $p_{\boldsymbol{X}}(\boldsymbol{x})$ or a probability density function $f_{\boldsymbol{X}}(\boldsymbol{x})$. In addition, assume that we only know a function $g(\boldsymbol{x})$ *proportional* to $p_{\boldsymbol{X}}(\boldsymbol{x})$ or $f_{\boldsymbol{X}}(\boldsymbol{x})$. The sequence of the samples starts with some initial value $\boldsymbol{x}_0$. A candidate point is drawn from a multivariate *proposal* distribution that is symmetric around $\boldsymbol{x}_0$ and typically has a lower standard deviation than the *target* distribution. Then the ratio of the target probability density function at the candidate point to the current point is calculated, that is, $r = \frac{g(\boldsymbol{x}_{candidate})}{g(\boldsymbol{x}_{current})}$. If the ratio is greater than 1, which implies that the proposed point is more probable than the current point, the candidate point is accepted. When the ratio is less than 1, the proposed point is accepted only with the probability equal to the ratio r. If the candidate point is accepted, it is added to the sequence of the samples and used in the next step as the current point. If the candidate point is *not* accepted, the current point is added to the sequence of samples *again* and used as the current point in the next step.

2.5.1.1 Analogy with presidential candidate

A nice illustration of the principles of Metropolis-Hastings was presented in [2]. The illustration provides an easy-to-comprehend intuition and covers most of the essential components of the algorithm, and it is worth rephrasing here.

Consider a presidential candidate running for the office in a state made of a single row of many small islands. The strategy for the election campaign is to stay on each island proportionally to its population. The mayor of each island knows the island's population and will report it to the candidate when asked. Nevertheless, there are so many islands that no one wants to take the effort to ask all mayors of all islands and calculate the total population of the island state. The presidential candidate proceeds in the following way. He starts campaigning on a randomly selected island. He asks the mayor about the island's population. At the end of the day, he chooses one of the two neighboring islands based on the toss of a fair coin. Before moving to the chosen island, he asks the mayor of that proposed island about its population. If the population of the chosen island is greater than the population of the current island, he moves overnight and starts campaigning on this new island the next day. If the population of the chosen island is smaller, he moves there only with the probability given by the ratio of the proposed island's population to the current island's population. This is achieved by calculating the ratio and comparing it to the uniformly distributed random number between 0 and 1. If the random number is less than the ration, he moves to the chosen island. If the

random number is greater than the ration, he stays on the current island and campaigns there one more day.

If this strategy is exercised for a long period, the days spent on each island will be proportional to its population.

2.5.1.2 Why Metropolis-Hastings algorithm works

A Markov chain of a continuous random variable is completely defined by the *transition probability density*, here denoted as $f(x_{i+1} \mid x_i)$. It is the probability density of the new value x_{i+1} in the chain conditioned on the last value in the chain x_i. Generally, a Markov chain may or may not have a *stationary distribution*. The stationary distribution is the distribution of the values when sufficiently many values were generated so they are no longer influenced by the initial value of the chain. A sufficient condition for the existence of the stationary distribution is the condition of *detailed balance*. This condition states that the stationary distribution $f(x)$ has to satisfy the equation

$$f(x_j \mid x_i)f(x_i) = f(x_i \mid x_j)f(x_j) \tag{2.95}$$

for all pairs of x_i and x_j. This means that a probability density of the stationary distribution of x_i multiplied by the density of the transition from x_i to x_j equals the same expression expressed for the other direction, i.e., the probability density of the stationary distribution expressed at x_j and multiplied by the density of the transition from x_j to x_i. When sampling, the target distribution is given and should be identical to the stationary distribution. The natural way to go is to design the transition probability density so that the detailed balance condition is satisfied. A common choice of the transition distribution in Metropolis-Hastings samplers can be viewed as a mixture of two distributions. In particular, the transition probability density is a weighted average of some proposal distribution and the Dirac delta function

$$f(x_j \mid x_i) = P_{x_j,x_i} \cdot f_{prop}(x_j \mid x_i) + (1 - P_{x_j,x_i})\delta(x_j - x_i) \tag{2.96}$$

This is the probability density of a variable x_j that is drawn from the distribution with density $f_{prop}(x_j \mid x_i)$ and accepted only with the probability P_{x_j,x_i} while being exactly x_i in the remaining cases, i.e., with the probability $1 - P_{x_j,x_i}$. For further discussion note that for $x_i = x_j$ the detailed balance condition is satisfied trivially due to its symmetry. For the remaining cases when $x_i \neq x_j$ it holds $\delta(x_j - x_i) = \delta(x_i - x_j) = 0$. Plugging the above equation into detailed balance equation while omitting the terms with the Dirac delta function we arrive at

$$P_{x_j,x_i} f_{prop}(x_j \mid x_i)f(x_i) = P_{x_i,x_j} f_{prop}(x_i \mid x_j)f(x_j) \tag{2.97}$$

The task now is to determine what is the acceptance probability when x_j is proposed from the current value x_i, here denoted as P_{x_j,x_i}, so that the above equation is satisfied. It turns out that an convenient choice is

$$P_{x_j,x_i} = \min\left(\frac{f_{prop}(x_i \mid x_j)f(x_j)}{f_{prop}(x_j \mid x_i)f(x_i)}, 1\right) \tag{2.98}$$

Consider for example the case when the *fraction* in the above formulation of P_{x_j,x_i} is less than one and the probability P_{x_j,x_i} itself will equal this fraction. Obviously, the fraction in the formulation P_{x_i,x_j} will be greater than one and the value of P_{x_i,x_j} itself will equal one. Plugging this back to Equation (2.97) shows us that with such a choice of the acceptance probability the detailed balance equation is satisfied independently from the actual form of target distribution or the choice of the proposal distribution.

2.5.2 Gibbs sampling

Another sampling algorithm widely used in the context of Bayesian inference is the *Gibbs sampler* [3]. The algorithm is built around the fact that even a complex posterior probability density function is composed of simpler conditional densities, from which it is relatively easy to sample. The simplest form of the algorithm is as follows. Consider a multivariate posterior probability function denoted as $f(x_1, x_2, \ldots, x_n)$ and the initial vector $(x_1^{(k=0)}, x_2^{(k=0)}, \ldots, x_n^{(k=0)})$. The creation of the next sample of the random vector $\boldsymbol{x}$ involves sampling each component of the vector individually from the conditional distribution. The first component of the new vector, denoted as x_1^{k+1}, is drawn from a conditional distribution with the probability density function $f(x_1^{(k+1)} \mid x_2^{(k)}, \ldots, x_n^{(k)})$. The second component of the new vector is also drawn form a univariate conditional distribution, but this time it is conditioned on the new value of x_1, i.e., on $x_1^{(k+1)}$. The conditional probability density is therefore $f(x_2^{(k+1)} \mid x_1^{(k+1)}, x_3^{(k)}, \ldots, x_n^{(k)})$. The i-th component of the new vector is drawn from $f(x_i^{(k+1)} \mid x_1^{(k+1)}, \ldots, x_{i-1}^{(k+1)}, x_{i+1}^{(k)}, \ldots, x_n^{(k)})$.

The advantage of Gibbs sampling is the absence of sampler parameters and a minimum of other sampler settings. Compare this, for example, with the necessity of setting up the proposal distribution in the Metropolis-Hastings algorithm.

On the other hand, there are probability density functions for which the Gibbs sampling is inefficient or even fails completely. Consider, for example, a probability density function of two variables x_1 and x_2 whose graph is a long, diagonally oriented ridge above the $x_1 \times x_2$ plane. Also consider a point on the ridge but far from the ridge's peak. Sampling along the ridge's axis towards its peak is difficult because it requires moving the current value x_1 off the ridge, i.e., to a region with low probability, and only then to move the point in the x_2 direction back to the ridge. When the ridge is narrow, these steps are small and sampling is inefficient. Nevertheless, most reasonably parametrized models with a limited number of parameters define posterior probability density that works well with Gibbs sampling. In fact, the Gibbs sampling gave the name of early software projects focused on Bayesian inference such as the BUGS (Bayesian inference Using the Gibbs Sampling) [4] and its successor projects WinBUGS and OpenBUGS. JAGS (Just Another Gibbs Sampler) also acknowledges the Gibbs sampling algorithm in its name even when it offers a variety of different sampling algorithms [5].

2.5.3 Hamiltonian Monte Carlo

Both sampling algorithms mentioned in the previous section, i.e., the Metropolis-Hastings algorithm and the Gibbs sampling, show inefficient mixing for posterior densities with large number of parameters. This is caused by the fact that a point in high-dimensional space has a neighborhood with significantly larger volume compared to low-dimensional spaces. Therefore, the high-dimensional space is more difficult to explore. To illustrate the problem, consider a k-dimensional hypercube domain. When k is large, it is impossible to generate chains containing values from all its 2^k hyperoctants. When samples from this volume are generated with a wide proposal distribution, the proposed samples are likely to have low density and, therefore, to be rejected. Due to the high rejection rate, the chain would contain long sequences of the same values. On the other hand with narrow proposal distribution the acceptance rate would be high; nevertheless, the new values would not differ much from the previous ones. Both scenarios represent inefficient mixing.

The goal here is to propose *distant* points with a similar probability density. When the points have similar density, the acceptance rate will be high, and when the proposed points are distant, the mixing will be efficient.

One class of methods that sample efficiently from high-dimensional posterior distributions is the Hamiltonian Monte Carlo.

Similarly to the other Markov chain Monte Carlo methods, the algorithm requires the probability density function $f(\boldsymbol{x})$ to be specified up to a multiplicative constant only. The k-dimensional space of the random variables $\boldsymbol{x}$ is enhanced by the same number of *momentum* variables denoted as $\boldsymbol{m}$. This $2k$-dimensional space is sometimes termed a *phase* space. A joint probability density function over the phase space is defined in the form

$$f(\boldsymbol{x}, \boldsymbol{m}) = f(\boldsymbol{x}) f(\boldsymbol{m}) \tag{2.99}$$

where $f(\boldsymbol{m})$ is typically the probability density function of normal distribution with zero mean vector and the covariance matrix $\boldsymbol{\Sigma}$ being a parameter of the algorithm. Note that the above form of the joint probability density function $f(\boldsymbol{x}, \boldsymbol{m})$ guarantees that the *marginal* distribution of $\boldsymbol{x}$ has the probability density function $f(\boldsymbol{x})$. Therefore, when the pairs of $\boldsymbol{x}$ and $\boldsymbol{m}$ are sampled from $f(\boldsymbol{x}, \boldsymbol{m})$ and the values of $\boldsymbol{m}$ are discarded, we have samples of $\boldsymbol{x}$ that are distributed according to $f(\boldsymbol{x})$. Recall that the initial goal is to propose a sample x^* *distant* from the current value $\boldsymbol{x}$ but at the same time the value of the density function at the proposed point is similar to that at the current point. The trick is to do just this, but in the phase space of $\boldsymbol{x}$ and $\boldsymbol{m}$ with the joint probability density $f(\boldsymbol{x}, \boldsymbol{m})$.

An auxiliary function $H(\boldsymbol{x}, \boldsymbol{m})$ is defined in the form

$$\begin{aligned} H(\boldsymbol{x}, \boldsymbol{m}) &= -\ln(f(\boldsymbol{x}, \boldsymbol{m})) && (2.100) \\ &= -\ln(f(\boldsymbol{x})) - \ln(f(\boldsymbol{m})) && (2.101) \\ &= U(\boldsymbol{x}) + V(\boldsymbol{m}) && (2.102) \end{aligned}$$

The structure of $H(\boldsymbol{x}, \boldsymbol{m})$ is identical to the Hamiltonian known from classical mechanics. Here the function $U(\boldsymbol{x})$ is the potential energy and depends only on the moving particle position $\boldsymbol{x}$ and the function $V(\boldsymbol{m})$ is the kinetic energy and depends on the moving particle momentum. The evolution of the system in time is driven by Hamilton's equations

$$\frac{d\boldsymbol{x}}{dt} = \frac{dH}{d\boldsymbol{m}} \tag{2.103}$$

$$\frac{d\boldsymbol{m}}{dt} = -\frac{dH}{d\boldsymbol{x}} \tag{2.104}$$

which can be solved numerically using symplectic integrators, typically the leapfrog integration scheme. Note that the value of the Hamiltonian is conserved as the system evolves.

A typical Hamiltonian Monte Carlo sampling starts from some initial point $\boldsymbol{x}^{(0)}$. The vector of momentum $\boldsymbol{m}^{(0)}$ is sampled from the multivariate normal distribution. The Hamilton equations are then solved using the leapfrog integrator essentially simulating a frictionless motion of a point mass from the initial state $(\boldsymbol{x}^{(0)}, \boldsymbol{m}^{(0)})$ to a new state $(\boldsymbol{x}, \boldsymbol{m})$ to which the point gets at time t. The time t for which the point travels is a parameter of the algorithm and must be reasonably tuned. The detailed balance equation written for the Markov chain of $(\boldsymbol{x}, \boldsymbol{m})$ pairs becomes

$$f(\boldsymbol{x}, \boldsymbol{m} \mid \boldsymbol{x}^{(0)}, \boldsymbol{m}^{(0)}) f(\boldsymbol{x}^{(0)}, \boldsymbol{m}^{(0)}) = f(\boldsymbol{x}^{(0)}, \boldsymbol{m}^{(0)} \mid \boldsymbol{x}, \boldsymbol{m}) f(\boldsymbol{x}, \boldsymbol{m}) \tag{2.105}$$

Following the approach outlined in Section 2.5.1.2 we arrive at the probability of accepting proposal $(\boldsymbol{x}, \boldsymbol{m})$ from state $(\boldsymbol{x}^{(0)}, \boldsymbol{m}^{(0)})$ to be in the form

$$P_{\boldsymbol{x}^{(0)}, \boldsymbol{x}} = \min \left(\frac{f(\boldsymbol{x}, \boldsymbol{m} \mid \boldsymbol{x}^{(0)}, \boldsymbol{m}^{(0)})}{f(\boldsymbol{x}^{(0)}, \boldsymbol{m}^{(0)} \mid \boldsymbol{x}, \boldsymbol{m})} \frac{f(\boldsymbol{x}, \boldsymbol{m})}{f(\boldsymbol{x}^{(0)}, \boldsymbol{m}^{(0)})}, 1 \right) \tag{2.106}$$

Since the Hamiltonian proposal step with fixed time t and step size is deterministic, the probability of obtaining $(\boldsymbol{x}, \boldsymbol{m})$ from $(\boldsymbol{x}^{(0)}, \boldsymbol{m}^{(0)})$ is equal to one. On the other hand, the probability of obtaining $(\boldsymbol{x}^{(0)}, \boldsymbol{m}^{(0)})$ from $(\boldsymbol{x}, \boldsymbol{m})$ practically zero. To make the proposal symmetric, the momentum is reversed at the end of integration. This modified proposal can be described as: Integrate the Hamilton equation by the symplectic integrator to time t and reverse the momentum vector obtained.

Since the value of the Hamiltonian H is conserved along the trajectory, the probability density of point $f(\boldsymbol{x}, \boldsymbol{m})$ at time t denoted as $f(\boldsymbol{x}, \boldsymbol{m})$ equals the probability density function at the initial point $f(\boldsymbol{x}^{(0)}, \boldsymbol{m}^{(0)})$.

An accessible introduction to principles of the Hamiltonian Monte Carlo are described in greater detail in [6, 7].

2.5.3.1 Parameters of Hamiltonian Monte Carlo

Drawing samples from a multivariate distribution using the Hamiltonian Monte Carlo method comes with the challenge of tuning the sampler parameters. The two key parameters of the deterministic transition step based on Hamiltonian mechanics are the

number of steps and the step size of the symplectic integrator. The parameters together influence the length and precision of the point's trajectory in the phase space.

If the trajectory is short, the point does not move into distant areas of the phase space and the produced samples are highly correlated. This is colloquially known as slow mixing. On the other hand, a long trajectory typically results in some sort of loop in the area where the probability density is high. Naturally, having the point traveling in a loop makes it return from distant areas back to the area close to its initial position. This wastes computational resources and worsens the inter-sample autocorrelation.

The size of the integration step influences the calculated trajectory in different ways. The numerical integration through the leap-frog integrator involves errors. Being symplectic, the leap-frog integrator does not *accumulate* errors when integrating the Hamiltonian equations. Nevertheless, some errors are still present and the calculated points are off the theoretical trajectory. This is manifested in the slight fluctuation of the Hamiltonian expressed at the calculated points. Recall that the Hamiltonian is related to the probability density in question and should be constant along the trajectory. If the leapfrog integration was accurate, the Hamiltonian would not change from the initial point to the proposed point, and the probability of accepting the proposed point would be equal to 1. Nevertheless, in real case integration error typically increases with a growing step size, fluctuations of the Hamiltonian become more pronounced, and the acceptance rate decreases. With a low acceptance rate, the produced samples are highly correlated, and their mixing is again inefficient. Consequently, the choice of integration step size results in a trade-off between a high acceptance rate requiring small steps and a computationally effective evaluation of the proposed point requiring larger steps. Empirical studies suggest keeping the acceptance rate between 0.65 and 0.95 [8, 9].

2.5.4 No U-Turn Sampler

There are different strategies to tune the parameters of the Hamiltonian Monte Carlo Sampler. The No U-Turn Sampler (NUTS) is a state-of-the-art sampling strategy based on the principles of the Hamiltonian Monte Carlo method. It uses a tuning period at the beginning of sampling during which it optimizes the parameters of the sampling method. In particular,it determines the covariance matrix $\boldsymbol{M}$ of the momentum variables and the step size of the leap-frog integrator. The samples from the tuning period are discarded.

Instead of optimizing the trajectory length, NUTS creates a series of candidate points by integrating the trajectory forward and backward. The choice among the candidate points is then done in a way that maintains the detailed balanced condition for the Markov process transition. Details on NUTS sampler are described in [10] and in the documentation of Stan statistical framework, in which it is a default sampler.

2.5.5 Convergence checks

All sampling methods introduced in the previous sections, i.e., the Metropolis-Hastings algorithm, the Gibbs sampling, the Hamiltonian Monte Carlo and the NUTS sampler, are special cases of the Markov chain Monte Carlo. In theory, the stationary distribution of

a sampler based on the Markov chain converges to the target distribution. Nevertheless, the rate of this convergence is not generally defined and the number of samples necessary for reaching convergence has to be estimated from the chain itself.

The process of examining the chain and determining whether the samples can be used as an approximation to the posterior density is known as *chain diagnostics*.

When the number of inferred parameters allows it, the simple convergence check includes visual inspection of the generated chains. A chain corresponding to variable θ is represented as a sequence of values drawn from its target distribution. In the context of Bayesian inference, the target distribution is typically the posterior distribution of the parameter θ or the posterior predictive distribution of an unobserved variable $\tilde{y}$. Two types of plot are usually created for each Markov chain: a histogram of the values that occur in the chain and an evolution of the value during sampling. The former plot tells us *what* has been inferred while the latter *how* it was inferred. Examples of non-converging and well-converging chains of a variable θ are shown in Figure 2.3 and Figure 2.4, respectively.

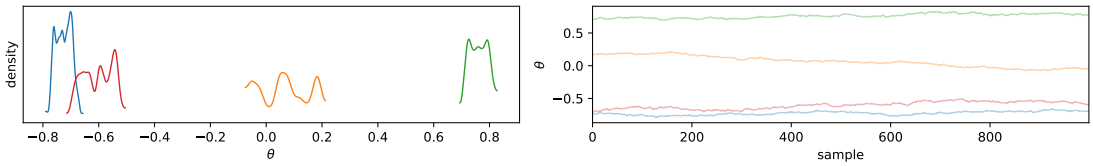

Figure 2.3: Example of non-converting Markov chains of parameter θ. Four chains each of 1000 samples were generated after a burn-in period of 4000 samples. Posterior densities estimated from each chain are plotted on the left. The four chains are plotted on the right.

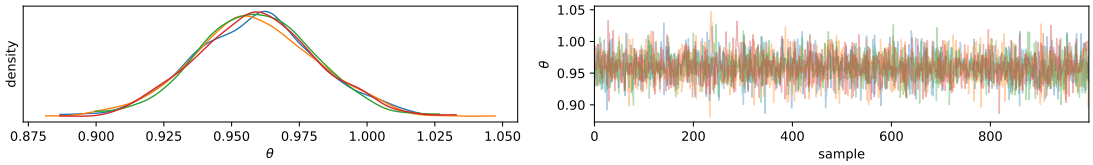

Figure 2.4: Example of well converting Markov chains of parameter θ. Four chains each of 1000 samples were generated after a burn-in period of 4000 samples. Posterior densities estimated from each chain are plotted on the left. The four chains are plotted on the right.

In both cases, four chains of samples of the parameter θ starting from different initial points were drawn using the NUTS sampler. In the non-converging case, we can observe that the values from each of the four chains center around different means. In addition, each mean evolves as the sampling progresses. The estimated posterior densities, here plotted from the chains as smoothed histograms by the mean of *kernel density* functions,

are completely different for each chain. Their multimodality is only accidental and does not represent the true nature of the parameter. On the other hand, the four chains in Figure 2.4 seem to share the mean value and also the dispersion. This is supported by the kernel density graph on the left. The slight discrepancies in the plotted kernel densities are a consequence of a relatively small number of samples. The results of the same inference with 10 times more samples are shown in Figure 2.5.

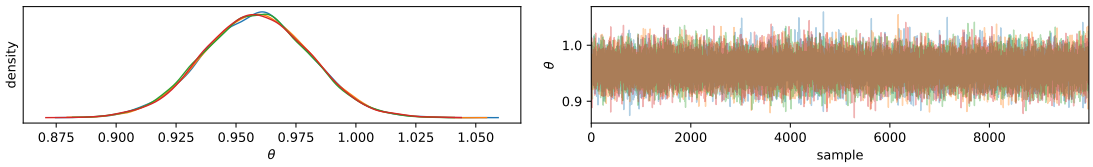

Figure 2.5: Example of well converting Markov chains of parameter θ. Four chains each of 10000 samples.

More rigorous approaches to chain diagnostics include z-scores proposed by Geweke [11] and Gelman-Rubin statistics [12]. The former approach compares the mean values and the standard deviations calculated from different sections of a single examined chain. The latter approach compares the variance within the chain with the variance between the chains. For inefficiently mixed, highly correlated chains, the generated samples are less dispersed then they should be and therefore the within-chain variance is underestimated. The Gelman-Rubin statistics reads

$$\hat{R} = \sqrt{\frac{\hat{\mathrm{Var}}(\theta \mid y)}{W}} \tag{2.107}$$

where $\hat{\mathrm{Var}}(\theta \mid y)$ is the estimated variance of all generated samples while W is the variance estimated within the chains. Values $\hat{R} > 1.1$ are typically considered to indicate poor convergence.

Another measure indicating inefficient mixing and high autocorrelation between samples within a single chain or among different chains is *effective sample size*. It is calculated from the generated samples as

$$\hat{n}_{\mathrm{eff}} = \frac{mn}{1 + \sum_{t=1}^{T} \hat{\rho}_t} \tag{2.108}$$

where m is the number of chains, n is the number of samples in each chain, $\hat{\rho}_t$ is the estimated autocorrelation between samples with lag t and T is the maximum lag possible in the chain. Note that for zero estimated correlations for all lags, the effective sample size is equal to the number of all samples in all chains. More details on the effective sample size can be found in [13], Section 11.5.

Bibliography

[1] S. Banerjee, B. P. Carlin, A. E. Gelfand, Hierarchical Modeling and Analysis for Spatial Data, 2nd Edition, Chapman and Hall/CRC, New York, 2014. doi:10.1201/b17115.

[2] J. Kruschke, Doing Bayesian Data Analysis, Elsevier, 2015. doi:10.1016/B978-0-12-405888-0.09999-2.

[3] S. Geman, D. Geman, Stochastic Relaxation, Gibbs Distributions, and the Bayesian Restoration of Images, IEEE Transactions on Pattern Analysis and Machine Intelligence PAMI-6 (6) (1984) 721–741. doi:10.1109/TPAMI.1984.4767596.

[4] D. Lunn, D. Spiegelhalter, A. Thomas, N. Best, The BUGS project: Evolution, critique and future directions, Statistics in Medicine 28 (25) (2009) 3049–3067. doi:10.1002/sim.3680.

[5] M. Plummer, JAGS Version 4.3.0 user manual (2017).

[6] Steve Brooks, Andrew Gelman, Galin L. Jones, Xiao-Li Meng, Handbook of Markov Chain Monte Carlo, Chapman & Hall, 2011. arXiv:1206.1901, doi:10.1201/b10905.

[7] M. Betancourt, A Conceptual Introduction to Hamiltonian Monte Carlo (Jul. 2018). arXiv:1701.02434.

[8] R. M. Neal, MCMC using Hamiltonian dynamics (Jun. 2012). arXiv:1206.1901.

[9] A. Honkela, Chapter 13 Hamiltonian Monte Carlo (HMC) | Computational Statistics I, 2020.

[10] M. D. Hoffman, A. Gelman, The No-U-Turn Sampler: Adaptively Setting Path Lengths in Hamiltonian Monte Carlo, Journal of Machine Learning Research 15 (2014) 1593–1623. doi:10.48550/arXiv.1111.4246.

[11] J. Geweke, Evaluating the accuracy of sampling-based approaches to the calculation of posterior moments, Staff Report (148) (1991).

[12] A. Gelman, D. B. Rubin, A Single Series from the Gibbs Sampler Provides a False Sense of Security, in: J. M. Bernardo, J. O. Berger, P. Dawid, A. F. M. Smith (Eds.), Bayesian Statistics 4, Oxford University PressOxford, 1992, pp. 625–632. doi:10.1093/oso/9780198522669.003.0038.

[13] A. Gelman, J. Carlin, H. Stern, D. Dunson, A. Vehtari, D. Rubin, Bayesian Data Analysis, Third Edition, Chapman & Hall/CRC Texts in Statistical Science, Taylor & Francis, 2013.

Chapter 3

Uncertainty in calibration of hypoplastic model for clay attributed to limited number of laboratory tests

This chapter presents the preprint version of the journal paper

> Janda, T.; Pavelcová, V.; Zemanová, A.; Šejnoha, M., Uncertainty in calibration of hypoplastic model for clay attributed to limited number of laboratory tests, Computers and Structures. 2024, 295 ISSN 1879-2243.

reformatted to align with the style of the thesis.

3.1 Abstract

The paper quantifies the uncertainty of material parameters of the hypoplastic model for clay resulting from the experimenter's choice about what laboratory data are utilised in the calibration process. The results of several 1D compression tests and undrained triaxial shear tests performed on twenty different fine-grained soils are considered in various combinations to yield a scattered set of material parameters for each soil. A hierarchical probabilistic model separating the variations and correlations of parameters within one soil from variations and correlations among different soils is formulated. The posterior distribution of the probabilistic model parameters is obtained by means of the Bayesian inference. The results allow for stochastic simulations on a structural level even when only point estimates of material parameters are available.

fine-grained soil, hypoplasticity, constitutive model, material parameters, calibration, uncertainty, Bayesian inference, hierarchical stochastic model, posterior distribution, credible intervals

3.2 Introduction

One of the key components of a finite element analysis of most geotechnical structures is the choice of a suitable constitutive model for the soil and the determination of its parameters. In contrast to the majority of other, typically man-made, structural materials the soil differs from one construction site to another and the soil properties are not guaranteed. For each site the mechanical properties of soils are determined by means of a geotechnical survey including field and laboratory testing. The results of laboratory tests are then used in a calibration process to obtain the material model parameters.

Uncertainties from different sources arise in the process of material model calibration and subsequent simulation of a geotechnical construction [1]. Common source of soil properties uncertainty is their spatial variability. It influences both the material model calibration for sands [2] and clays [3] and subsequent simulation at a structural level [4]. Another source of uncertainty relates to the variety of available experimental methods, ranging from basic field tests to advanced laboratory testing [5, 6]. A variety of approaches to identify the soil properties uncertainty are being utilised including machine learning [7] or sensitivity analysis [8, 9]. Another approach is to incorporate the stochastic nature of the material directly into the constitutive model [10].

Once quantified, the uncertainty of soil parameters can be taken into account in simulations at the structural level. This is commonly achieved by stochastic simulations based on the Monte-Carlo method [2, 11, 12], Latin hypercube sampling [13] method, random sets [14], Bayesian surrogate models [15, 16] or polynomial chaos expansion [17, 18]. The uncertainty of structural behaviour resulting from the possible use of different constitutive models in the context of FEM simulations can be assessed by a direct comparison of results [19].

Calibrating the soil from the results of differently executed laboratory tests, e.g. a 1D compression test with different maximal loading stress or a triaxial shear test executed with different cell pressures, gives different material parameters. Although a reasonable setup of a laboratory test falls within some generally recommended ranges, its exact choice is somewhat arbitrary and thus making the material parameters uncertain.

The key goal of this study is to quantify the uncertainty of material parameters arising from the fact that the results of only limited number of laboratory tests, each with somewhat arbitrary setup, enter the calibration process. To have a practical impact, the uncertainty is formulated in the form that can be incorporated into a stochastic finite element simulation even when only a point estimate of the material parameters is available for a given soil. In particular, the paper aims at inferring the standard deviations of all material parameters and their mutual correlation coefficients, applicable to the material model fitted to laboratory data of a general fine grained soil. This means that a user of the material model can superpose the uncertainty inferred in this study to any set of optimised material parameters and run Monte-Carlo stochastic simulations at a structural level.

The paper is organised as follows. The methodology including a brief overview of the material model and its parameters, the laboratory tests and the calibration process is

summarised in Section 3.3. The data utilised in the statistical analysis are introduced in Section 3.3.8 and the hierarchical probabilistic model on top of these data is formulated in Section 3.3.9. Section 3.4 shows the posterior distributions of the probabilistic model parameters obtained by means of the Bayesian inference. The results are discussed in Section 3.5. The principal result potentially applicable in follow up studies are summarised in Section 3.6.

3.3 Methods

3.3.1 Material model

The material model utilised in this study is the hypoplastic material model for clay. The model builds on principles of hypoplasticity [20] and takes into account the phenomena observed in the stress-strain relationship of fine grained soils. These are mainly the stress dependent stiffness, the hardening or softening depending on the current soil density and the existence of critical density to which the soil arrives after sufficiently long shearing. The original formulation [21] has been revised to explicitly define the asymptotic response [22, 23]. The material model is available in several commercial finite element programs [24, 25, 26] and has been utilised in various FEM simulations [19, 27, 28, 29, 30, 31, 32, 33] .

3.3.2 Material parameters

This section provides a brief overview of the five material parameters employed in the hypoplastic model for clay. The stress-strain relation is defined for isotropic loading and assumes different stiffness for primary loading and unloading/reloading. In both cases the stiffness increases with increasing compressive mean stress. For primary isotropic compression the stress-strain relationship is described in terms of the void ratio e and the mean effective compressive stress p by

$$\ln(1+e) = N - \lambda^* \ln\left(\frac{p}{p_{ref}}\right) \tag{3.1}$$

where N and λ^* are material parameters. The reference mean stress is assumed $p_{ref} = 1\,\mathrm{kPa}$. Thus λ^* is the slope of the primary compression line plotted in $\ln(p) \times \ln(1+e)$ space and the intercept N relates to the value of the void ratio for primary consolidated soil at $p = 1$ kPa according to

$$e_0 = \exp(N) - 1 \tag{3.2}$$

For unloading and reloading conditions the soil follows

$$\ln(1+e) = const. - \kappa^* \ln\left(\frac{p}{p_{ref}}\right) \tag{3.3}$$

where κ^* is the material parameter controlling the stiffness upon unloading/reloading. The constant in Eq. (3.3) depends on the loading history and is in fact irrelevant because the hypoplastic model is formulated in a rate form and only derivatives of the equation define the stress-strain relationship. The role of the parameters λ^*, κ^* and N is shown in the diagram of the primary loading and unloading in Figure 3.1.

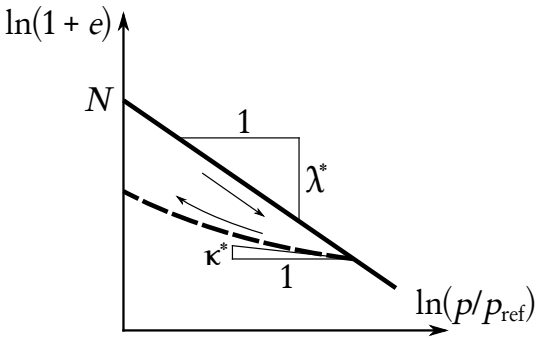

Figure 3.1: Diagram of isotropic primary loading (solid line) and subsequent unloading/reloading (dashed line) showing the role of parameters λ^*, κ^* and N.

Note that with exception of being written in $\ln(p) \times \ln(1+e)$ space, the above stress-strain relation is identical to that of the Modified Cam clay constitutive model [34] defined in $\ln(p) \times e$ space.

The shear strength of the model is controlled by the critical angle of internal friction φ_c representing the mobilised angle of internal friction in critical state

$$\sin^2 \varphi_c = \frac{9I_3 + I_1 I_2}{I_3 + I_1 I_2} \tag{3.4}$$

where I_1, I_2 and I_3 are the first, second and third invariants of the stress tensor at the critical state, respectively.

The parameter ν controls the ratio of the tangent shear modulus to the tangent bulk modulus derived from Eqs. (3.1) and (3.3). Its role is analogous to that of the Poisson ratio in a linear elastic material.

The five material parameters of the hypoplastic model for clay are φ_c, λ^*, κ^*, N and ν, see Figure 3.2. For complete formulation of the hypoplastic model for clay and the detailed definition of its parameters we refer the reader to [22], Sections 6 and 7. An example of realistic parameters of two different fine grained soils and the results of simulated oedometer tests are shown in Figure 3.2.

3.3.3 Laboratory tests

A common practice for observing the deformation behaviour of soil under various loading conditions is to perform a set of suitably chosen laboratory tests. Two types of common laboratory tests are prominent in the context of constitutive model calibration: the

one-dimensional constrained compression test also known as the oedometer test and the triaxial shear test. This is because these two laboratory tests are relatively easily performed and still maintain – at least in theory – a homogeneous stress field within the soil sample. This is in contrast to other laboratory tests such as the direct shear test or virtually any field test for which the stress field spatially varies.

The oedometer test (denoted as OED) mainly provides the data from which the stiffness characteristics are calibrated. In common OED test setup, the soil sample is subjected to an increasing one-dimensional strain and the corresponding normal stress is recorded. The soil sample is typically exposed to at least one loading and one unloading stage.

The undrained shear test with the measured pore pressure (denoted as CIUP) provides the data from which the shear stiffness and the soil strength are calibrated. The soil sample is first subjected to a certain effective isotropic stress that consolidates the soil to a given level. In the following stage the laterally unconstrained soil sample is loaded by increasing the deviatoric stress while keeping the undrained conditions. The evolution of vertical stress, strain, and excess pore pressure is monitored.

3.3.4 Automatic calibration application ExCalibre

A necessary step for using a material model within a finite element method (FEM) simulation is to determine the values of its parameters. This process is referred to as the calibration of the material model.

In the case of the hypoplastic model for clay, the calibration is quite tedious task requiring to tune several parameters simultaneously. An online calibration application ExCalibre [35, 36] was developed to make this task as easy as possible. The calibration algorithm combines a direct evaluation of the measured data and single element simulations of the laboratory tests [37, 38].

The user prepares a laboratory protocol in a predefined format. For a fine-grained soil the protocol must contain the united soil classification system (USCS) soil class, gradation curve data and Atterberg limits and most importantly the data of at least one oedometer (OED) and one undrained triaxial test with pore pressure measurements (CIUP). The user then uploads the laboratory protocols to the ExCalibre website and selects the material model to calibrate. After the calibration, the user is presented with the automatically determined parameters and several line charts showing how the laboratory tests simulated with these parameters correspond to the uploaded experimental data.

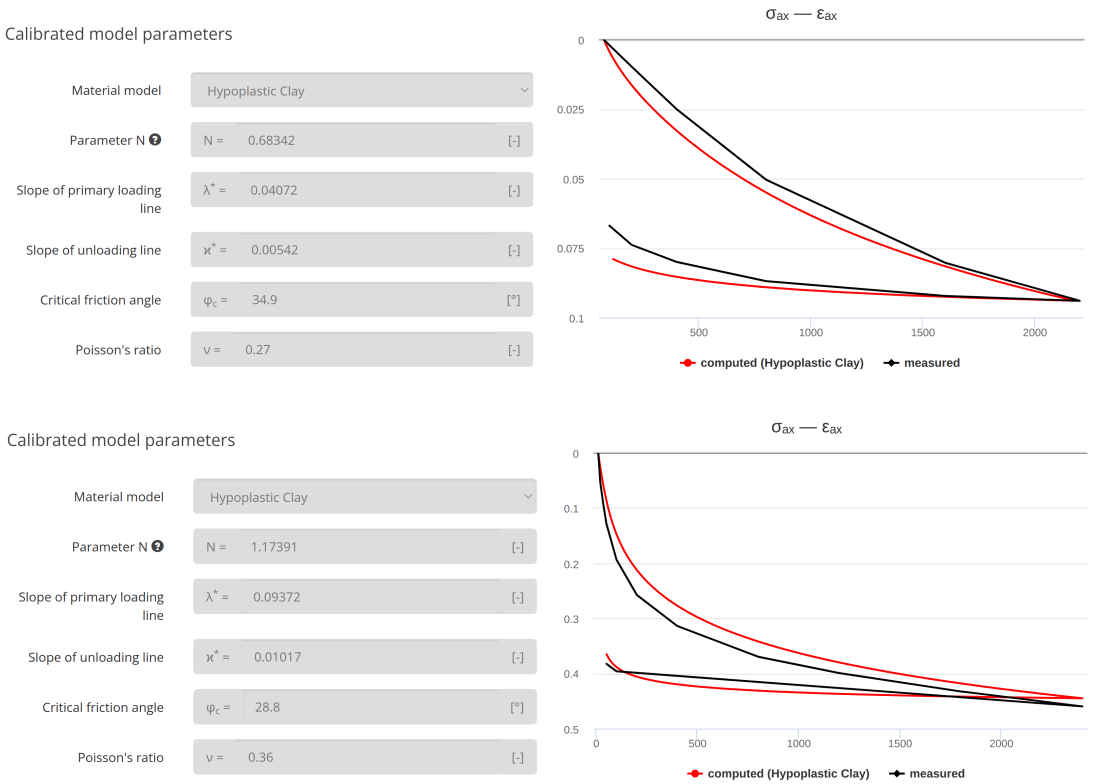

Figure 3.2: Example of an output from the ExCalibre application for two different soils: the application displays the optimised parameters and a list of plots comparing the simulated laboratory tests to the measured data. These examples show the dependence of axial strain ε_{ax} [–] on prescribed axial stress σ_{ax} [kPa] upon loading and unloading.

3.3.5 Data sources

Being available to the geotechnical community since 2018, more than two thousand laboratory protocols of various soils have been uploaded to ExCalibre. In compliance with the ExCalibre's user agreement, the data from the laboratory protocols uploaded to the ExCalibre database can be used anonymously for research purposes. The laboratory protocols of different fine grained soils from several locations including the United States, China, Thailand, United Kingdom, Germany, Finland, and the Czech Republic were utilised in this study. The protocols contained standard index parameters, soil gradation curves and the results of the oedometer and the undrained triaxial shear tests. Both the oedometer and triaxial tests were performed on either undisturbed or reconstituted soil samples.

3.3.6 Data preparation

The laboratory protocol contains all data available for a given soil and serves as the sole input for the calibration procedure. Recall that the laboratory protocol can contain more than one OED test and more than one CIUP test. In such a case, all the available data are used in the calibration process simultaneously and the calibration procedure optimises the material parameters to fit all provided laboratory tests as close as possible.

The following statistical analysis focuses on the uncertainty in the calibrated parameters attributed to the fact that arbitrary number of laboratory tests can enter the calibration. The laboratory protocols used in the present study were selected based on the following criteria:

- The protocol contains the data of at least two oedometer tests and at least two undrained triaxial shear tests.
- The soil is classified within USCS as a clay with low (CL) or high (CH) liquid limit.
- The protocol data are neither duplicate nor similar to the laboratory data in another protocol.

Twenty unique laboratory protocols of different fine-grained soils were selected for further processing according to these criteria. These protocols are referred to as the *base* protocols.

Several additional protocols were then created out of each base protocol by leaving out some of the available laboratory tests. The newly created protocols thus contained only a subset of the available laboratory tests. These protocols therefore simulate the situation when the experimenter provides the results of fewer laboratory tests. These artificially created protocols are referred to as *trimmed* protocols. The base laboratory protocols together with the trimmed protocols yield together 652 laboratory protocols grouped by the soils. Each group contained 1 base protocol and between 8 and 48 trimmed protocols. Table 3.1 shows the number of OED and CIUP laboratory tests available in the base protocol for each soil and the numbers of the laboratory protocols (base and trimmed) available for the soils.

3.3.7 Calibration

The deterministic calibration algorithm implemented in ExCalibre application was utilised in this study. The algorithm evaluates the parameters λ^* and N directly as the slope and the intercept of the primary loading branch of an oedometer test and optimises the remaining parameters κ^*, φ_c and ν so that the simulated laboratory tests fit the supplied data. The details of the calibration algorithm for the hypoplastic model for clay are described in [36].

The calibration algorithm was run for each of the 652 laboratory protocols described in the previous section. For different laboratory protocols the execution times of the calibration procedure varied. Most calibrations lasted about several seconds but in rare cases the execution time exceeded several minutes. For this reason the execution time

Soil number i	**1**	**2**	**3**	**4**	**5**	**6**	**7**	**8**	**9**	**10**
Num. of OED tests	2	2	2	2	3	2	2	2	2	2
Num. of CIUP tests	4	4	4	4	3	4	2	4	4	4
Num. of protocols	45	45	45	45	49	45	9	45	45	45
Num. of par. sets $n_{set,i}$	45	45	42	41	46	42	9	41	45	42
Soil number i	**11**	**12**	**13**	**14**	**15**	**16**	**17**	**18**	**19**	**20**
Num. of OED tests	2	2	2	2	2	2	2	2	2	2
Num. of CIUP tests	4	3	2	4	4	3	3	2	2	2
Num. of protocols	45	21	9	45	45	21	21	9	9	9
Num. of par. sets $n_{set,i}$	45	21	9	45	45	21	20	9	9	9

Table 3.1: Overview of the data available for each of the 20 soils. First row of the is the soil's index i. The second and the third row provide the number of OED and CIUP test available in the base protocol. The fourth row provide the number of all protocols available, i.e. the original base protocol and the additionally created trimmed protocols. The last row shows the number of successful calibration runs, i.e. number of material parameter sets.

was limited to 120 s and the calibrations running longer were cancelled. The successful calibrations resulted in 631 sets of five material parameters grouped by the 20 soils. The last row of in Table 3.1 shows the number of parameters sets belonging to each soil. The distribution of the material parameters for each soil is displayed in Figure 3.3. Figure 3.4 provides another view to the same data. It shows the histograms of all parameters and scatter plots that visually indicate the correlations between the material parameters.

Recall that the calibration algorithm is deterministic and for the same input data always returns the same optimal parameters. However, it does not provide any information on the credibility of these parameters. This study neither questions the accuracy of the calibration algorithm nor the fitness of the hypoplastic model for clay itself. It focuses solely on the uncertainty arising from the fact that the calibration of one soil can be preformed on data sets of various sizes leading to potentially different values of material parameters.

3.3.8 Transformed data

A brief overview of the scattered material parameters in Figure 3.4 suggests that some of the parameters might be correlated. In particular, there is a clear positive correlation between parameters λ^* and N.

A statistical description of the correlated quantities assumes that they follow some joint probability distribution. Owing to its simplicity, the multivariate normal distribution would be a useful choice to describe the variability of the material parameters. The multivariate normal distribution of n variables has a support of $\mathbb{R}^n$. This means that even negative values would have nonzero probability. This clearly conflicts with the fact that all the material parameters are positive and the parameter ν also has an upper

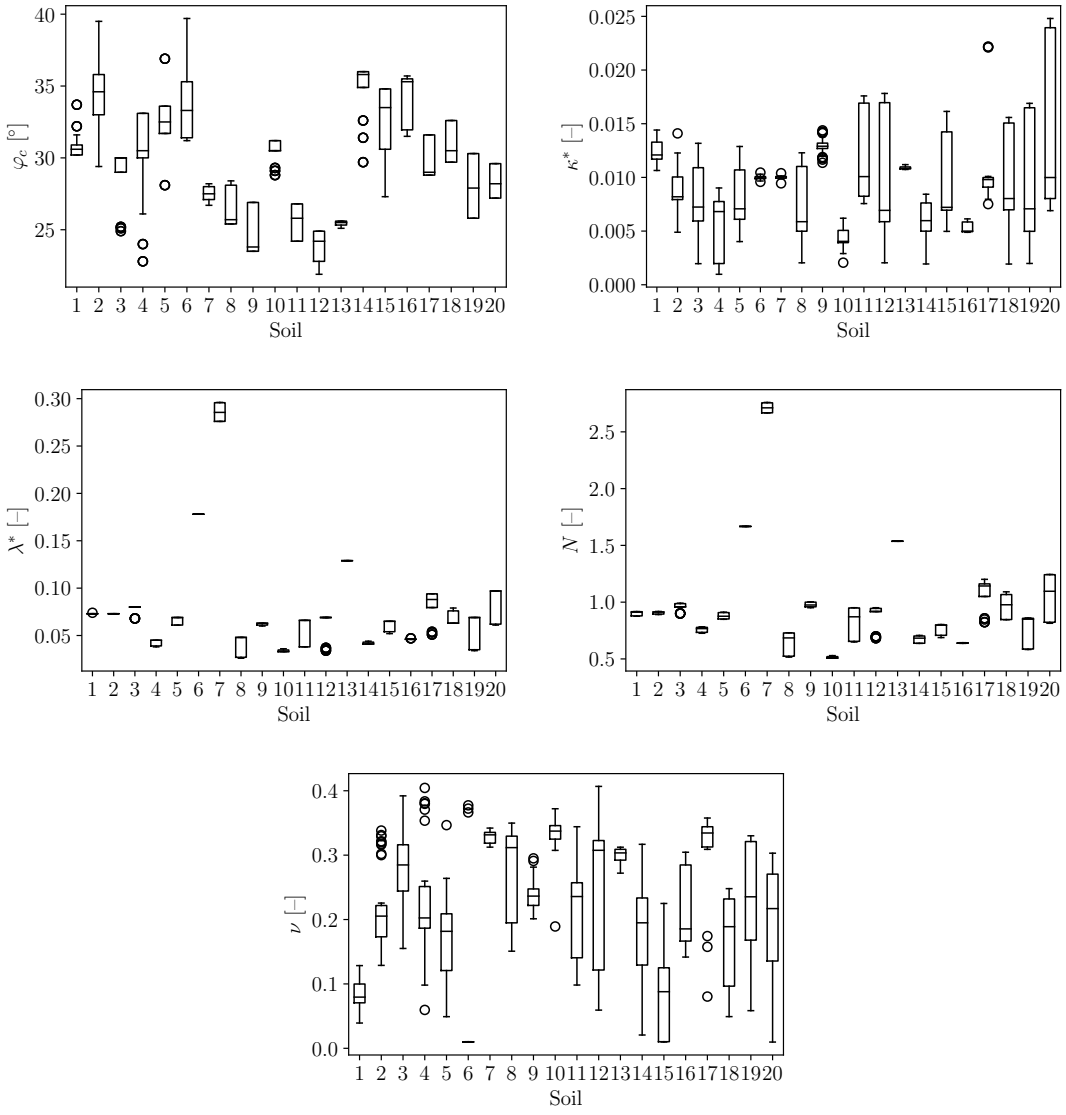

Figure 3.3: Distribution of material parameters grouped by soil samples 1 – 20

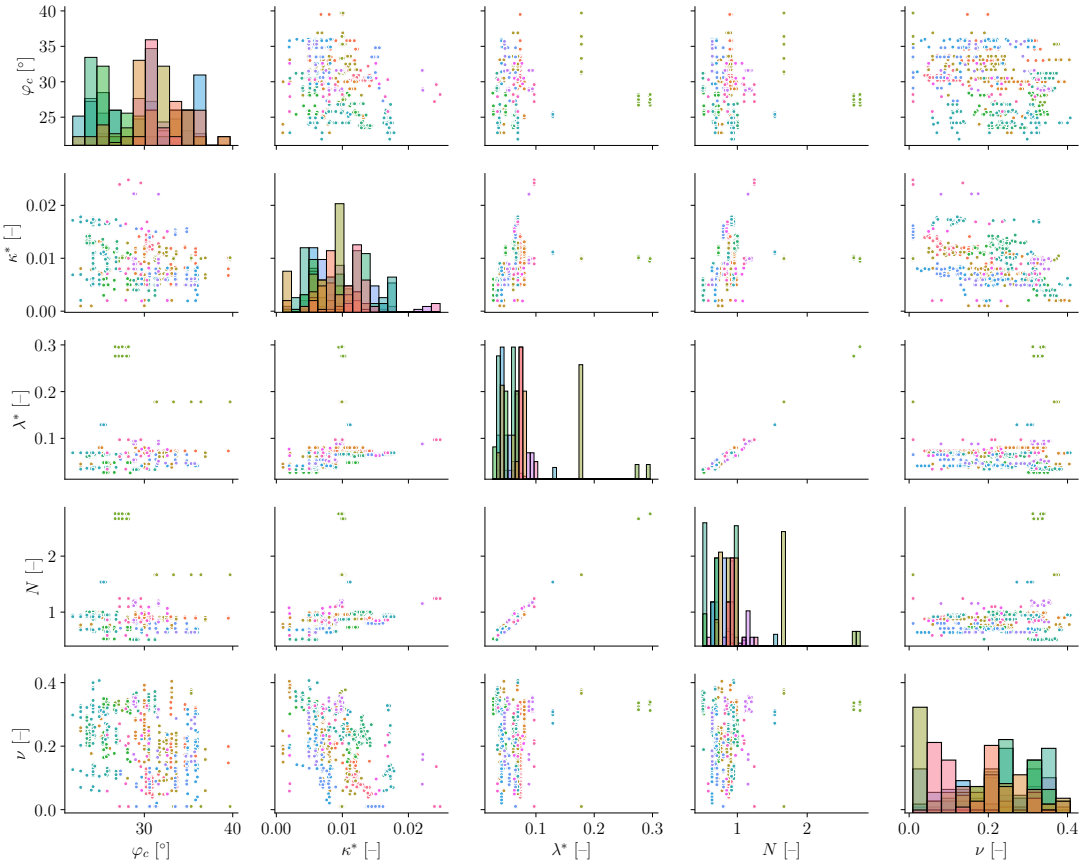

Figure 3.4: Pair plot showing correlations between material parameters. The colours indicate different soils.

bound of 0.5.

For this reason, it is not the vector of the parameters $\boldsymbol{z} = \{\varphi_c, \kappa^*, \lambda^*, N, \nu\}$ but rather its transformation $\boldsymbol{y} = \{y_{\varphi_c}, y_{\kappa^*}, y_{\lambda^*}, y_N, y_\nu\} \in \mathbb{R}^{n_{par}}$, $n_{par} = 5$, what is assumed to follow a multivariate normal distribution. The transformation is

$$y_{\varphi_c} = \text{softplus}_2^{-1}(\varphi_c, \beta = 1) \tag{3.5}$$

$$y_{\kappa^*} = \text{softplus}_2^{-1}(\kappa^*, \beta = 0.001) \tag{3.6}$$

$$y_{\lambda^*} = \text{softplus}_2^{-1}(\lambda^*, \beta = 0.01) \tag{3.7}$$

$$y_N = \text{softplus}_2^{-1}(N, \beta = 0.1) \tag{3.8}$$

$$y_\nu = \text{softclip}_2^{-1}(\nu, \beta = 0.1) \tag{3.9}$$

where functions softplus_2^{-1} and softclip_2^{-1} are inverse to functions softplus_2 and softclip_2 defined in 3.7.1 and plotted in Figures 3.12 and 3.13, respectively. The values of the parameter β were chosen such that the transformation functions are close to identity for most of the observed values.

Note that the variable φ_c is treated as not bounded from above despite the existence of a theoretical upper limit of 90°. This choice, however, does not cause problems because the observed values of φ_c are far below the upper limit. On the other hand, some observations of the parameter ν are close to its bounds and therefore the inverse CDF of standard normal distribution was applied to transform its range from $(0, 0.5)$ to $\mathbb{R}$ so that it can be described by a multivariate normal distribution.

3.3.9 Hierarchical model

An intuitive way to define a hierarchical model is to describe how the observed data are distributed. In this analysis, the observed data are the transformed material parameters stored in vectors $\boldsymbol{y}_{obs,ij} = \{y_{\varphi_c}, y_{\kappa^*}, y_{\lambda^*}, y_N, y_\nu\}_{ij}$, $i = 1, \ldots, n_{soil}$, $j = 1, \ldots, n_{set,i}$. The vector $\boldsymbol{y}_{obs,ij}$ thus collects the transformed material parameters φ_c, κ^*, λ^*, N and ν of the i-th soil obtained from the calibration algorithm for the j-th protocol. The number $n_{soil} = 20$ denotes the number of soils and the number $n_{set,i}$ denotes the number of protocols available for the i-th soil sample, i.e. the number of trimmed protocols plus one base protocol.

The following stochastic and deterministic relations form the hierarchical stochastic model. Each observed vector of the five standardised material parameters $\boldsymbol{y}_{obs,ij}$ is distributed according to the multivariate normal distribution with the vector of mean values $\boldsymbol{\mu}_{L,i}$ and the covariance matrix $\boldsymbol{\Sigma}_L$. This is written as

$$\boldsymbol{y}_{obs,ij} \sim N(\boldsymbol{\mu} = \boldsymbol{\mu}_{L,i}, \boldsymbol{\Sigma} = \boldsymbol{\Sigma}_L) \quad i = 1, \ldots, n_{soil}, \quad j = 1, \ldots, n_{set,i} \tag{3.10}$$

The index i in $\boldsymbol{\mu}_{L,i}$ indicates that different mean values are assumed for different soils. On the contrary, the covariance matrix, which characterises the variations and mutual correlations between the material parameters of a certain soil, is assumed identical for all soils. This is an intentional modelling choice that allows us to quantify the typical

dispersion of the observed material parameters of an arbitrary soil due to the different sets of laboratory data entering the calibration. The subscript L stands for "local" to individual soils.

The vector of the mean values for the i-th soil is itself also distributed according to the multivariate normal distribution with the mean vector $\boldsymbol{\mu}_G$ and the covariance matrix $\boldsymbol{\Sigma}_G$

$$\boldsymbol{\mu}_{L,i} \sim N(\boldsymbol{\mu} = \boldsymbol{\mu}_G, \boldsymbol{\Sigma} = \boldsymbol{\Sigma}_G) \quad i = 1, \ldots, n_{soil} \tag{3.11}$$

The subscript G stands for "global" or "general" to all soils. The global mean vector $\boldsymbol{\mu}_G$ thus describes the mean value of the transformed material parameters over all n_{soil} soils in question. The global covariance matrix $\boldsymbol{\Sigma}_G$ characterises the variance and correlations of material parameters amongst the soils.

The hierarchical stochastic model is now completed with the definitions of prior distributions for all top-level parameters, i.e. $\boldsymbol{\mu}_G$, $\boldsymbol{\Sigma}_G$ and $\boldsymbol{\Sigma}_L$.

A flat prior distribution over $\mathbb{R}$ was assumed for each component of $\boldsymbol{\mu}_G$. Symbolically, this is written as

$$\mu_{G,k} \sim \text{Flat}(), \quad k = 1, \ldots, n_{par} \tag{3.12}$$

This distribution has a constant probability density and is often denoted as improper distribution because it does not integrate to 1 over its support. The flat prior distribution is uninformative as it assigns the same prior credibility to all possible values of $\mu_{G,k}$.

Although the inverse Wishart distribution is the conjugate prior for the covariance matrix of multivariate normal distribution, it often fails to be efficient within an inference based on the Markov chain Monte-Carlo (MCMC) method. This is attributed to both the requirement of the symmetry and positive definiteness of the covariance matrix and the heavy tails of the Wishart distribution. Therefore, the covariance matrix $\boldsymbol{\Sigma}_G$ is assembled from the correlation matrix $\boldsymbol{\rho}_G$ and the vector of standard deviations $\boldsymbol{\sigma}_G$ element-wise according to

$$\Sigma_{G,kl} = \rho_{G,kl}\sigma_{G,k}\sigma_{G,l} \quad k = 1, \ldots, n_{par}, \quad l = 1, \ldots, n_{par} \tag{3.13}$$

The Lewandowski-Kurowicka-Joe (LKJ) method [39] was utilised do define the prior distribution of the global correlation matrix

$$\boldsymbol{\rho}_G \sim \text{LKJ}(\eta = 1) \tag{3.14}$$

with the parameter $\eta = 1$ implying a uniform prior distribution over the space of all correlation matrices. This in fact corresponds to the non-diagonal elements of the correlation matrix being beta-distributed, see Eq. (3.34) in 3.7.2, according to

$$\rho_{G,kl} \sim \text{Beta}\left(\alpha = \frac{n_{par}}{2}, \beta = \frac{n_{par}}{2}\right) \quad k = 1, \ldots, n_{par}, \quad l = 1, \ldots, n_{par} \tag{3.15}$$

The prior distribution of the standard deviations is assumed exponential with the rate parameter $\lambda = 1$

$$\sigma_{G,k} \sim \text{Exp}(\lambda = 1) \quad k = 1, \ldots, n_{par} \tag{3.16}$$

This can also be seen as weakly informative prior distribution that prescribes similar credibility to all possible values of the standard deviations.

The prior distribution of the *local* covariance matrix $\boldsymbol{\Sigma}_L$ is constructed analogously as

$$\Sigma_{L,kl} = \rho_{L,kl}\sigma_{L,k}\sigma_{L,l} \quad k = 1, \ldots, n_{par}, \quad l = 1, \ldots, n_{par} \tag{3.17}$$

$$\boldsymbol{\rho}_L \sim \mathrm{LKJ}(\eta = 1) \tag{3.18}$$

$$\sigma_{L,k} \sim \mathrm{Exp}(\lambda = 1) \quad k = 1, \ldots, n_{par} \tag{3.19}$$

The independent parameters of the stochastic model stored symbolically in vector $\boldsymbol{\theta}$ are $\boldsymbol{\theta} = (\boldsymbol{\mu}_{L,1}, \ldots, \boldsymbol{\mu}_{L,n_{soil}}, \boldsymbol{\sigma}_L, \boldsymbol{\rho}_L, \boldsymbol{\mu}_G, \boldsymbol{\sigma}_G, \boldsymbol{\rho}_G)$. Out of these, only the parameters $\boldsymbol{\sigma}_L$, $\boldsymbol{\rho}_L$, $\boldsymbol{\mu}_G$, $\boldsymbol{\sigma}_G$ and $\boldsymbol{\rho}_G$ are the *top-level* parameters (also called *sources* in the directed graph terminology) and have the prior distribution directly prescribed. The remaining parameters $\boldsymbol{\mu}_{L,1}, \ldots, \boldsymbol{\mu}_{L,n_{soil}}$ are *internal* parameters and their prior distribution is inferred from the prior distributions of their direct predecessors. Nevertheless, the joint posterior density is formulated for all of these parameters and all these parameters are sampled together. An alternative way is inferring the local parameters $\boldsymbol{\mu}_{L,1}, \ldots, \boldsymbol{\mu}_{L,n_{soil}}$, $\boldsymbol{\sigma}_L$ and $\boldsymbol{\rho}_L$ in the first step and then inferring the global parameters $\boldsymbol{\mu}_G$, $\boldsymbol{\sigma}_G$ and $\boldsymbol{\rho}_G$ in the second step while using the the previously obtained mean values $\boldsymbol{\mu}_{L,1}, \ldots, \boldsymbol{\mu}_{L,n_{soil}}$ as the data. This staggered approach, however, would require specifying the prior distribution for $\boldsymbol{\mu}_{L,1}, \ldots, \boldsymbol{\mu}_{L,n_{soil}}$ which is not necessary with the hierarchical model utilised in this study.

3.3.10 Bayesian inference

The joint posterior probability density of parameters $\boldsymbol{\theta}$ of a hierarchical model obtained through the Bayes rule is written as

$$f(\boldsymbol{\theta} \mid \boldsymbol{y}_{obs}) \propto f(\boldsymbol{y}_{obs} \mid \boldsymbol{\theta}) f(\boldsymbol{\theta}) \tag{3.20}$$

where $f(\boldsymbol{\theta} \mid \boldsymbol{y}_{obs})$ denotes the posterior density, $f(\boldsymbol{y}_{obs} \mid \boldsymbol{\theta})$ is the likelihood of $\boldsymbol{\theta}$ expressed for fixed data $\boldsymbol{y}_{obs}$ and $f(\boldsymbol{\theta})$ is the prior distribution. The likelihood is constructed from the relationship (3.10) while the prior distribution of $\boldsymbol{\theta}$ is derived from relationships (3.11)–(3.19). The symbol $\propto$ indicates that $f(\boldsymbol{\theta} \mid \boldsymbol{y}_{obs})$ seen as a function of $\boldsymbol{\theta}$ is proportional to the right hand side expression up to the multiplication by a certain unknown constant. The formulation of the posterior probability density function (PDF) together with a directed graph representing the model hierarchy is given in 3.7.2.

The inference was done by means of the MCMC sampling. In particular, the No-U-Turn sampler (NUTS) [40] based on principles of Hamiltonian Monte Carlo methods [41] combined with variational Bayesian inference [42] was utilised within the PyMC [43] framework to generate the samples from the joint posterior distribution of the probabilistic model parameters.

3.4 Results

This section presents the results of the Bayesian inference of the hierarchical stochastic model described in Section 3.3.9. Since the posterior distribution is explored by means of the MCMC sampling, the immediate results are the chains of samples drawn from the posterior distribution. In particular, two independent chains each of 2000 samples were generated. To generate more than one chain is a common practice allowing for a quick check that the generated samples converge to the same distribution. Through this section, the posterior distributions obtained from the first and the second chain are plotted by solid and dotted line.

Conceptually, the distributions of two types of quantities are explored: posterior distribution of the hierarchical model parameters $\boldsymbol{\theta}$ and posterior predictive distribution of the unobserved data.

3.4.1 Posterior distribution of statistical model parameters

The posterior distribution of individual *local* means $\boldsymbol{\mu}_{L,i}$, $i = 1 \dots n_{par}$, and standard deviations $\boldsymbol{\sigma}_L$, recall Eq. (3.10), extracted from the chains are plotted in Figure 3.5 in the form of their kernel densities. Note that the mean values plotted on the left differ for each examined soil while the standard deviation within each soil is just one, shared between all soils.

Figure 3.6 shows the posterior distribution of all *local* correlation coefficients of interest in the form of 95 % highest density intervals with the central points representing the posterior mean value estimates. The intervals are plotted in pairs, each line for each independent chain.

Similarly, the posterior distribution of the *global* means and standard deviations are displayed in Figure 3.7.

The correlation coefficients corresponding to the *global* covariance matrix $\boldsymbol{\Sigma}_G$ are plotted in Figure 3.8.

3.4.2 Posterior predictive distribution of material model parameters

Posterior predictive distribution describes how the observed data are distributed under the assumption that the stochastic model parameters follow their posterior distribution. Recall Eq. (3.10) that indicates how the *transformed* material parameters y_{obs} are distributed. Clearly, these values are not guaranteed to be within the theoretical limits of the material parameters, i.e. positive and in case of ν also less than 0.5. Therefore, the values in the chains are transformed back to the appropriate ranges, i.e. to interval $(0, 0.5)$ in case of ν and to interval $(0, \infty)$ in case of the other variables, by the

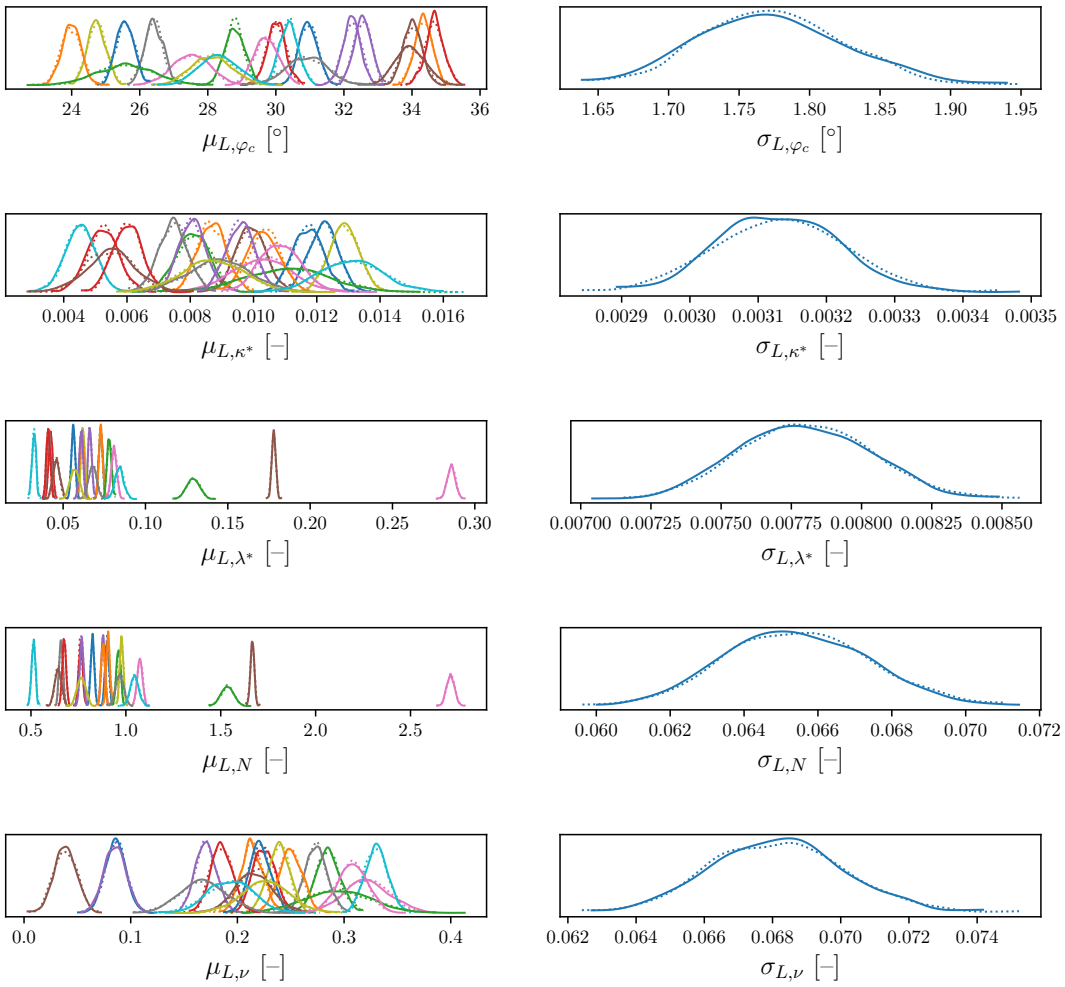

Figure 3.5: Posterior distribution of the *local* (i.e. within each soil) means ($\boldsymbol{\mu}_{L,i}$) and *local* standard deviations ($\boldsymbol{\sigma}_L$) of the material parameters for each soil. The distributions of the means of different soils are plotted in different colours.

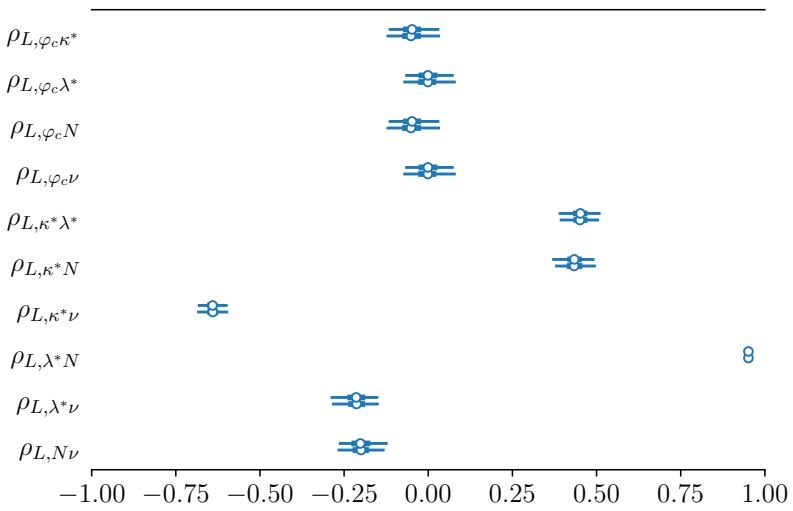

Figure 3.6: Posterior distribution of *local* (i.e. within each soil) correlation coefficients ($\boldsymbol{\rho}_L$) between material parameters

transformations

$$\varphi_c = \text{softplus}_2(y_{obs,1}, \beta) \tag{3.21}$$
$$\kappa^* = \text{softplus}_2(y_{obs,2}, \beta) \tag{3.22}$$
$$\lambda^* = \text{softplus}_2(y_{obs,3}, \beta) \tag{3.23}$$
$$N = \text{softplus}_2(y_{obs,4}, \beta) \tag{3.24}$$
$$\nu = 0.5\text{softclip}_2(2y_{obs,5}, \beta) \tag{3.25}$$

Note however, that this transformation is rather formal because for typical values the transformation function is close to identity. The posterior kernel density plots of the material parameters are in Figure 3.9.

One additional variable defined as $\boldsymbol{y}_{ex} = \{\varphi_{c,ex}, \kappa^*_{ex}, \lambda^*_{ex}, N_{ex}, \nu_{ex}\}$ and being normally distributed according to

$$\boldsymbol{y}_{ex} \sim N(\boldsymbol{\mu} = \boldsymbol{\mu}_{ex}, \boldsymbol{\Sigma} = \boldsymbol{\Sigma}_L) \tag{3.26}$$

was added into the stochastic model for illustration. It represents a normally distributed set of material parameters with a fixed mean of $\boldsymbol{\mu}_{ex} = \{30, 0.01, 0.1, 1, 0.3\}$. The sole purpose of this variable is to show how the observation are dispersed around this arbitrary mean due to the covariance matrix $\boldsymbol{\Sigma}_L$ calculated from $\boldsymbol{\sigma}_L$ and $\boldsymbol{\rho}_L$, which are itself inferred with limited certainty. The resulting posterior distribution of $\varphi_{c,ex}$, κ^*_{ex}, λ^*_{ex}, N_{ex} and ν_{ex} is plotted in Figure 3.10 in the form of kernel densities and also in Figure 3.11 in the form of pairwise scatter plots. Due to the properties of normal distribution the result can be seen in two ways. First, it shows how the material parameters that the

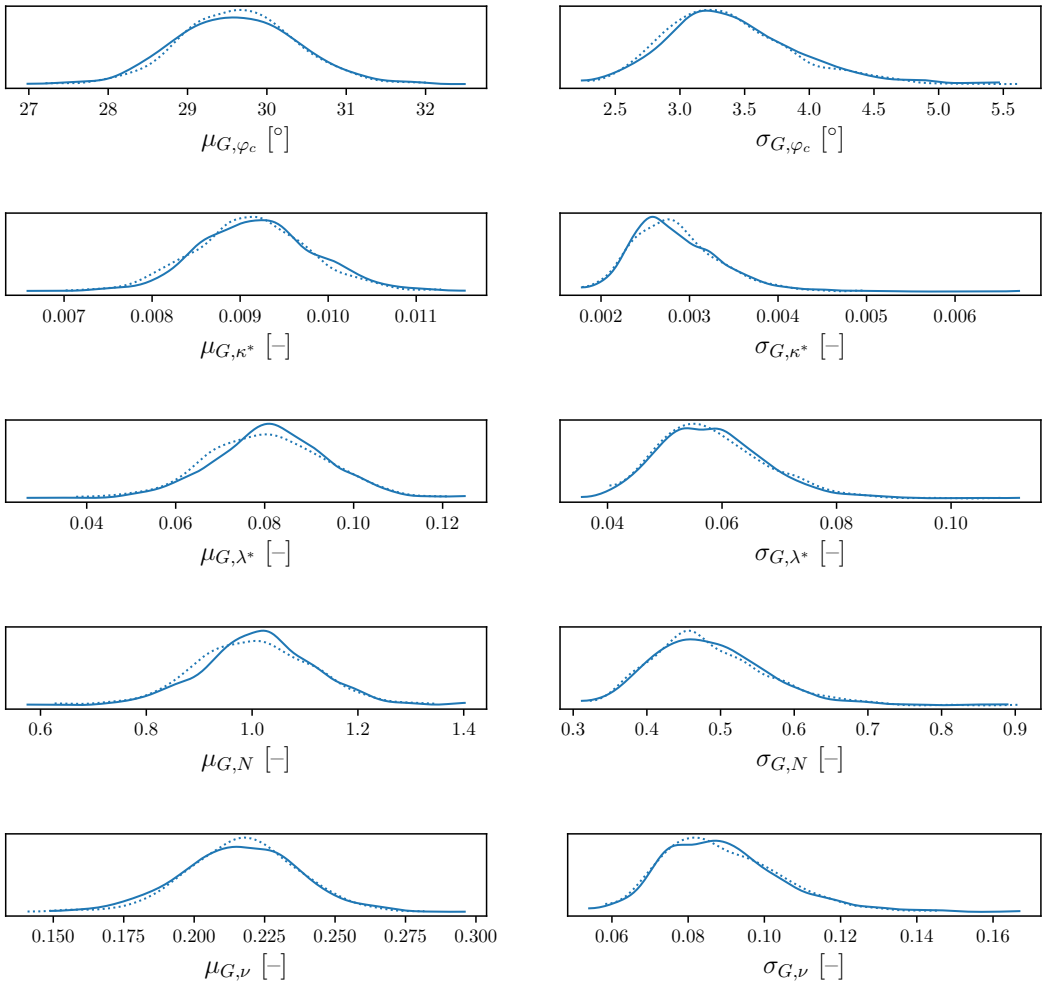

Figure 3.7: Posterior distribution of *global* (i.e. among the analysed soils) means ($\boldsymbol{\mu}_G$) and standard deviations ($\boldsymbol{\sigma}_G$) of the material parameters

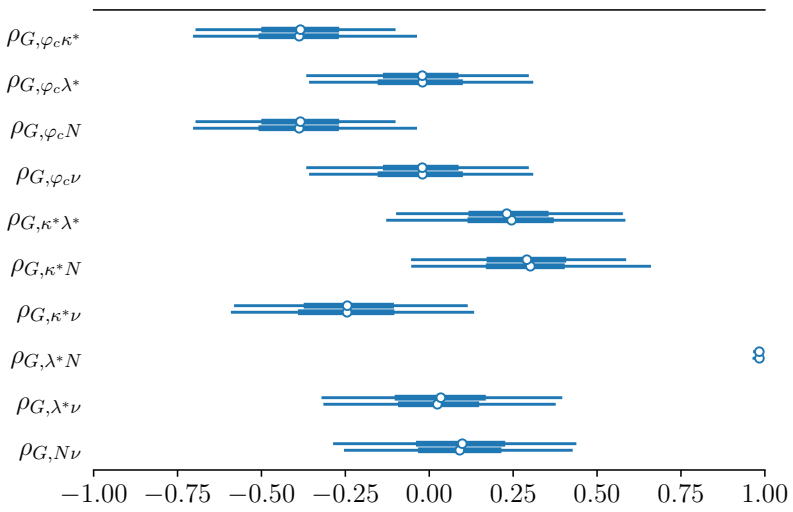

Figure 3.8: Posterior distribution of *global* (i.e. among the analysed soils) correlation coefficients ($\boldsymbol{\rho}_{G,ij}$) between material parameters

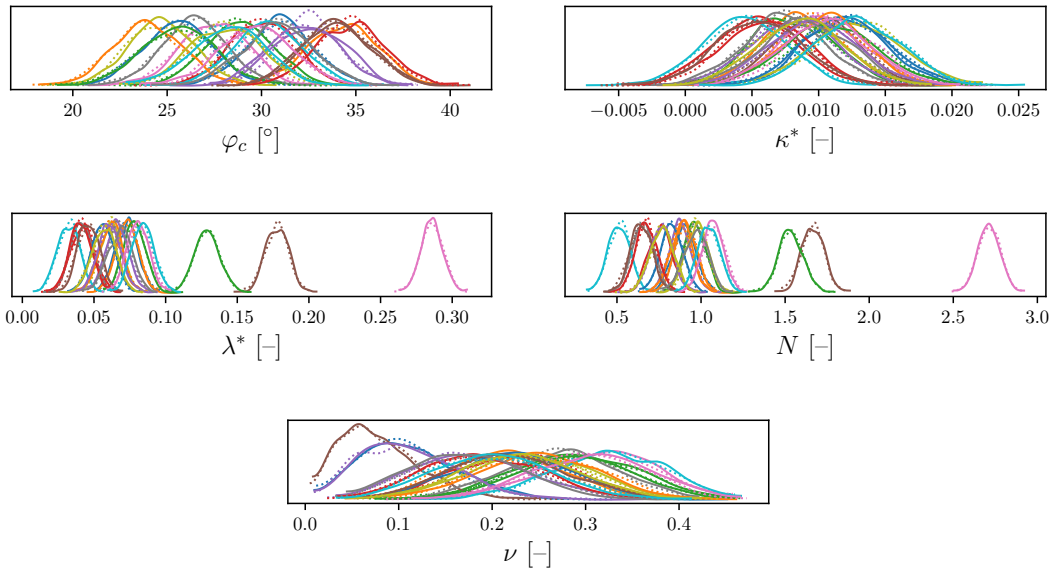

Figure 3.9: Posterior predictive distribution of the unobserved values of the material parameters for each of the soils

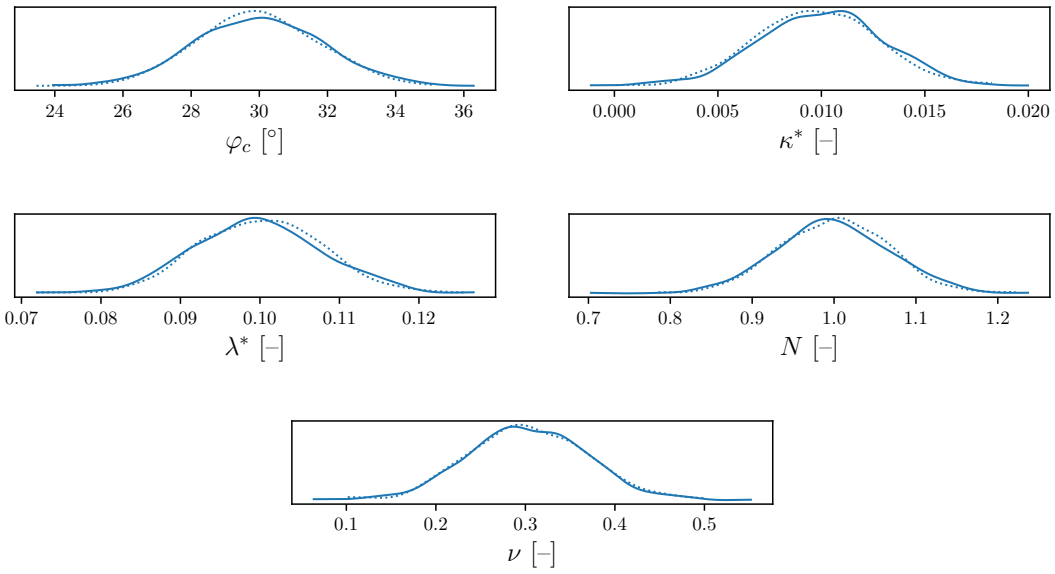

Figure 3.10: Posterior predictive distribution of material parameters of hypothetical soil with fixed mean values $\mu_{\varphi_c} = 30°$, $\mu_{\kappa^*} = 0.01$, $\mu_{\lambda^*} = 0.1$, $\mu_N = 1.0$, $\mu_\nu = 0.3$

calibration returns for different combinations of input data are dispersed around the fixed known mean. Or it can be viewed as the uncertainty of the sought mean values given the material parameters obtained from a single calibration run.

3.4.3 Test for chain convergence

The representatives of the sample chains generated from the posterior distribution was checked by visual inspections and quantified by both the calculation of $\hat{R}$ diagnostics [44] and calculation of effective sample size. The rank-based convergence diagnostics $\hat{R}$ [45] did not exceed 1.01 for any of the variables. The effective sample size was greater than 1000 for all variables.

3.5 Discussion

The distribution of individual means provided in Figure 3.5 shows that not only their locations but also their uncertainty (dispersion) differ for individual soils. This observation is attributed to the different number of material parameter sets, i.e. different number of *trimmed* laboratory protocols, available for each soil, recall last row in Table 3.1. Those soils with more available laboratory tests and therefore with more material parameter sets tend to have narrower posterior distributions of the mean values $\boldsymbol{\mu}_{L,i}$.

One of the two key results of the statistical analysis is the *local* standard deviation displayed in Figure 3.5 on the right. The standard deviations quantify the dispersion of

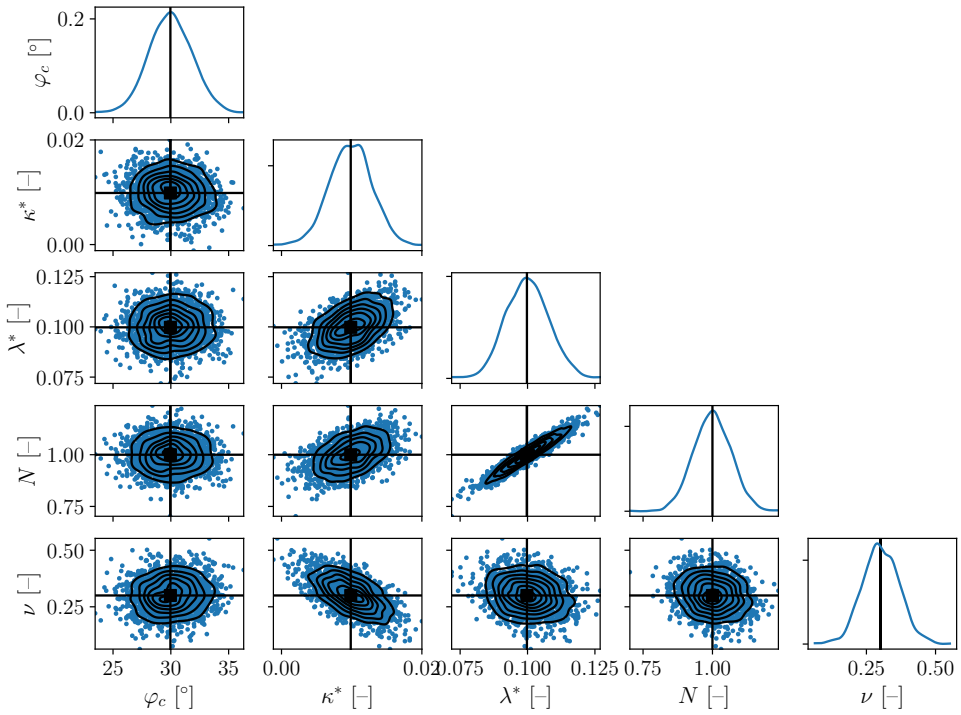

Figure 3.11: Pair plot of posterior predictive distribution of material parameters of hypothetical soil with fixed mean values $\mu_{\varphi_c} = 30°$, $\mu_{\kappa^*} = 0.01$, $\mu_{\lambda^*} = 0.1$, $\mu_N = 1.0$, $\mu_\nu = 0.3$

the data, i.e. the material parameters of the hypoplastic model for clay, obtained for a general soil by the same process of calibration performed on different sets of laboratory tests. The second key result is the local correlation coefficients provided in Figure 3.6 which suggest that some of the material parameters are correlated. In particular, there is a positive correlation close to 1 between the slope of the primary compression line λ^* and the intercept N. Quite expectantly, there is also a positive correlation between the slope of the primary loading line λ^* and the slope of the unloading/reloading line κ^*. This suggests that soils stiffer in primary loading tend to be stiffer upon unloading too. Finally, there is a notable negative correlation between κ^* and the Poisson ratio ν. These correlations should be taken into account when one wants to incorporate the material parameter uncertainty into FEM simulations at the structural level. 3.7.3 provides brief summary of how the results are applicable within the Monte-Carlo method.

Although the posterior distribution of the *global* means $\boldsymbol{\mu}_G$ and *global* standard deviations $\boldsymbol{\sigma}_G$ displayed in Figure 3.7 are not the motivation for the above statistical analysis, they are a convenient byproduct. It shows that the material parameters of a randomly chosen fine-grained soil are expected around $\boldsymbol{\mu}_G$ with the standard deviation of $\boldsymbol{\sigma}_G$. Such information is always helpful in preliminary geotechnical simulations and also for a quick check that a newly obtained parameter set fits into the common ranges. The arguably wide credible intervals of these global parameters are the consequence of the limited number of soils being considered in the study.

A notable result is the distribution of the *global* correlation coefficients and its difference from the distribution of the *local* correlation coefficients. With exception of the correlation between λ^* and N the medians of the correlation coefficients are relatively low. This suggests a good parametrisation of the hypoplastic model for clay, i.e. that different parameters control different properties of the model.

The posterior predictive distribution of the material parameters provided in Figure 3.9 is presented mainly for the illustration purposes. It shows the actual uncertainty in the material parameters that one would obtain when the calibration is performed with yet another combination of the laboratory tests.

Finally, the joint posterior distribution of the material parameters with the fixed mean displayed in Figures 3.10 and 3.11 shows the actual effect of $\boldsymbol{\sigma}_L$ and $\boldsymbol{\rho}_L$ on the uncertainty of the parameters that can be obtained for one typical soil. In particular, the pair plot in Figure 3.11 illustrates how the correlations affect the predicted material parameters. The figure also illustrates what parameters could be used for the traditional Monte-Carlo stochastic simulations at structural level if there was only a point estimate of the material parameters and the uncertainty was adopted from the soils considered in this study.

3.6 Conclusions

The statistical analysis of the material parameters of the hypoplastic model for clay was performed in this study. Several parameter sets were created for each of 20 different fine-grained soils. These different parameter sets were obtained by the same calibration

algorithm run with different combinations of the laboratory test performed for a given soil. This allowed us to analyse the uncertainty attributed to the fact that different oedometer tests and different triaxial shear tests performed on the same soil and used in the same automatic calibration algorithm lead to different material parameters.

The following findings are drawn from the results of the Bayesian inference of the hierarchical stochastic model:

- The standard deviations and mutual correlation coefficient of all five material parameters obtained from different combinations of laboratory tests on one soil are listed in Table 3.2. These values characterise the uncertainty of the material parameters of general fine-grained soil. They can be used to generate random samples around the point estimate of mean, e.g. values obtained from a single calibration run for a different fine-grained soil.

- There is a clear correlation between the material parameters that has to be taken into account when the material parameter uncertainty is used in a subsequent simulation at the structural level.

- The narrow credible intervals of the standard deviations $\boldsymbol{\sigma}_L$ and correlation coefficients $\boldsymbol{\rho}_L$ indicate that they were inferred with a relatively high accuracy. Using their point estimates, i.e. means in Table 3.2, is therefore sufficient for practical applications.

- While not being the primary topic of this study, the hierarchical model also provided the mean values, standard deviations and correlation matrices of the material parameters of the hypoplastic model for clay among different soils. The correlation coefficients between the means are relatively low and with relatively wide confidence intervals. The only exception is the correlation coefficient between the means of slope λ^* and the means of intercept N of the primary compression line.

- Posterior predictive distribution of material parameters of a hypothetical soil with fixed mean parameter values was calculated. It outlines how the random material parameters could be generated for a stochastic analysis on a structural level, e.g. Monte Carlo finite element analysis, when only the point estimate of material parameters are available for the given soil while the uncertainty is inferred from all soil used in this study.

- The hierarchical nature of the statistical model allowed us to separate the calibration uncertainty, quantified by covariance matrix $\boldsymbol{\Sigma}_L$, from the variability of properties of different soils, quantified by the covariance matrix $\boldsymbol{\Sigma}_G$. The model proved well parameterised and the inference was numerically stable. Convergence of the chains was checked with rank-based convergence diagnostic $\hat{R}$ and the effective sample size which was greater than 1000 for all parameters of the statistical model.

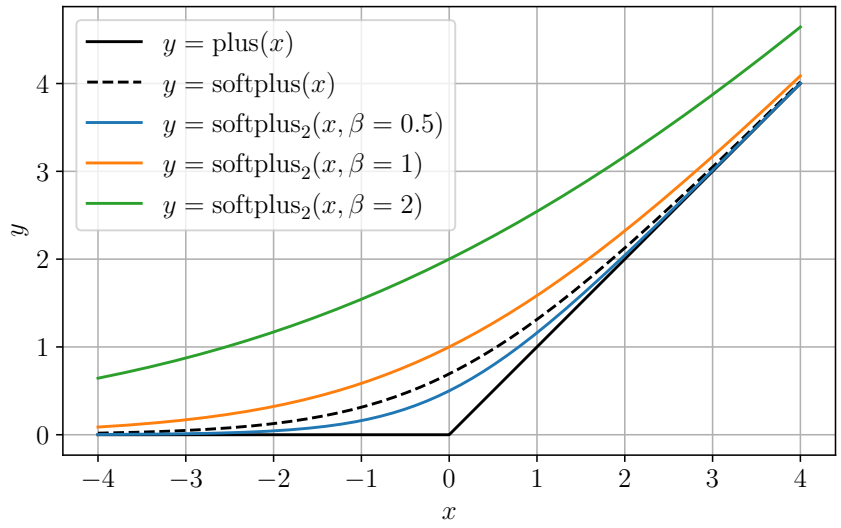

Figure 3.12: Comparison of sofplus_2 function with various values of parameter β

Acknowledgement

The financial support provided by the Czech Grant Agency, project No. 22-12178S is gratefully acknowledged.

3.7 Appendix

3.7.1 Functions softplus() and softclip()

A commonly used smooth analytical approximation of a function returning positive part of a real number, i.e. $x^+ = \max(x, 0)$, is a softplus() function [46]. It is written as

$$\text{softplus}(x) = \ln\left(e^x + 1\right) \tag{3.27}$$

This study uses its parameterised version termed softplus_2. It is written as

$$\text{softplus}_2(x, \beta) = \beta \log_2\left(2^{\frac{x}{\beta}} + 1\right) \tag{3.28}$$

and the parameter β defines its value at $x = 0$. The graph of this function is plotted in Figure 3.12.

The clip function maps real numbers to interval $[0, 1]$. It is defined as

$$\text{clip}(x) = \min(\max(x, 0), 1) \tag{3.29}$$

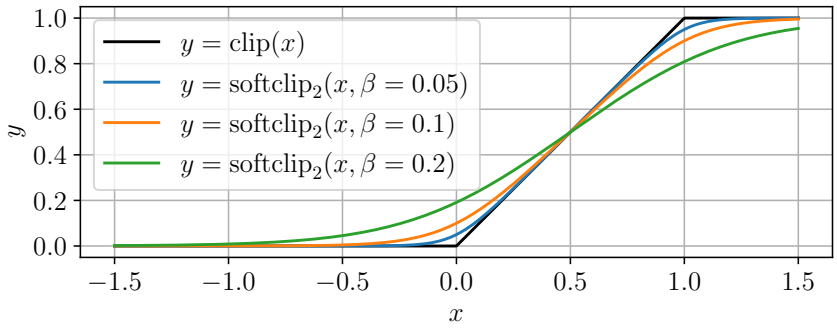

Figure 3.13: Comparison of softclip_2 function with various values of parameter β

Its smooth approximation can be constructed as a difference of two shifted softplus_2 functions as

$$\begin{aligned}\text{softclip}_2(x,\beta) &= \text{softplus}_2(x,\beta) - \text{softplus}_2(x-1,\beta) \\ &= \beta \log_2 \left(\frac{2^{\frac{x}{\beta}}+1}{2^{\frac{x-1}{\beta}}+1} \right)\end{aligned} \tag{3.30}$$

Again, the parameter β controls the function's value such that $\text{softclip}_2(0,\beta) \approx \beta$ and $\text{softclip}_2(1,\beta) \approx 1-\beta$. The function is plotted in Figure 3.13.

3.7.2 Construction of posterior probability density function

Probability density function (PDF) of k-variate normal distribution is

$$f_N(\boldsymbol{x},\boldsymbol{\mu},\boldsymbol{\Sigma}) = (2\pi)^{-\frac{k}{2}} \det(\boldsymbol{\Sigma})^{-\frac{1}{2}} \exp\left((\boldsymbol{x}-\boldsymbol{\mu})^T \Sigma^{-1} (\boldsymbol{x}-\boldsymbol{\mu})\right) \tag{3.31}$$

The PDF of the flat improper distribution is assumed constant

$$f_{\text{Flat}}(x) = c \tag{3.32}$$

The exponential PDF follows

$$f_{\text{Exp}}(x,\lambda) = \lambda \exp(-\lambda x) \tag{3.33}$$

and finally the PDF of the Beta distribution is

$$f_{\mathrm{Beta}}(x,\alpha,\beta) = \frac{1}{\mathrm{B}(\alpha,\beta)} x^{\alpha-1}(1-x)^{\beta-1} \tag{3.34}$$

where $\mathrm{B}(\alpha,\beta) = \int_0^1 t^{\alpha-1}(1-t)^{\beta-1}\,dt$ is the beta function.

Conceptually, the PDF of the multivariate posterior distribution of the probabilistic model parameters f_{post} is then written to be proportional to the expression

$$\begin{aligned} &f_{\mathrm{post}}(\boldsymbol{\mu}_{L,1},\ldots,\boldsymbol{\mu}_{L,n_{soil}},\boldsymbol{\sigma}_L,\boldsymbol{\rho}_L,\boldsymbol{\mu}_G,\boldsymbol{\sigma}_G,\boldsymbol{\rho}_G) \propto \\ &\propto \prod_{i=1}^{n_{soil}} \prod_{j=1}^{n_{set,i}} f_N(\boldsymbol{y}_{obs,ij},\boldsymbol{\mu}_{L,i},\boldsymbol{\Sigma}_L) \times \prod_{i=1}^{n_{soil}} f_N(\boldsymbol{\mu}_{L,i},\boldsymbol{\mu}_G,\boldsymbol{\Sigma}_G) \times \\ &\times \prod_{k=1}^{n_{par}} f_{\mathrm{Flat}}(\mu_{G,k}) \times \prod_{k=1}^{n_{par}} f_{\mathrm{Exp}}(\sigma_{L,k},\lambda) \prod_{\substack{k,l=1 \\ k\neq l}}^{n_{par}} f_{\mathrm{Beta}}(\rho_{L,kl},\alpha,\beta) \times \\ &\times \prod_{k=1}^{n_{par}} f_{\mathrm{Exp}}(\sigma_{G,k},\lambda) \prod_{\substack{k,l=1 \\ k\neq l}}^{n_{par}} f_{\mathrm{Beta}}(\rho_{G,kl},\alpha,\beta) \end{aligned} \tag{3.35}$$

where the data $\boldsymbol{y}_{obs,ij}$, and the hyper parameters λ, α and β are fixed. The covariance matrices $\boldsymbol{\Sigma}_L$ and $\boldsymbol{\Sigma}_G$ depend in deterministic way on the arguments $\boldsymbol{\sigma}_L$, $\boldsymbol{\rho}_L$, $\boldsymbol{\sigma}_G$ and $\boldsymbol{\rho}_G$ according to Eqs. (3.17) and (3.13). Defining the posterior PDF up to multiplication by unknown constant is sufficient in the context of MCMC-based inference because the sampler takes into account only the *ratio* of the f_{post} of two different points. The constant c in Eq.(3.32) is therefore irrelevant. For numerical reasons, the natural logarithm or the above expression termed the log-likelihood is used in the sampler.

The hierarchy of the probabilistic relationships is shown in Figure 3.14. The top level parameters are $\boldsymbol{\mu}_g$ denoted as `mu_g` and the independent components of the Cholesky decomposition of the global and the local covariance matrices denoted as `chol_g` and `chol_l`, respectively. The numbers in the diagram denote the dimensions of the variables, i.e. there are five material parameters and therefore five corresponding global mean values and 15 independent values of each covariance matrix. The prior distribution of $\boldsymbol{\mu}_g$ is flat. The prior distribution of the covariance matrices follows from the LKJ prior construction. The local mean values $\boldsymbol{\mu}_l$ denoted as `mu_l` are not the top-level parameters and therefore are not assigned a prior distribution. Instead, they follow from the multivariate normal distribution. Since there were 20 soils considered in this study, there are 20×5 of these mean values. Finally, the 631×5 observed (grey graph node) parameters follow the multivariate normal distribution. Note that the MCMC chains of the standard deviations $\boldsymbol{\sigma}_l$ resp. $\boldsymbol{\sigma}_g$ and the correlation coefficients $\boldsymbol{\rho}_l$ resp. $\boldsymbol{\rho}_g$ are calculated directly from the chains of the components of the covariance matrices `chol_g` resp. `chol_l`. These nodes are omitted from the graph for clarity.

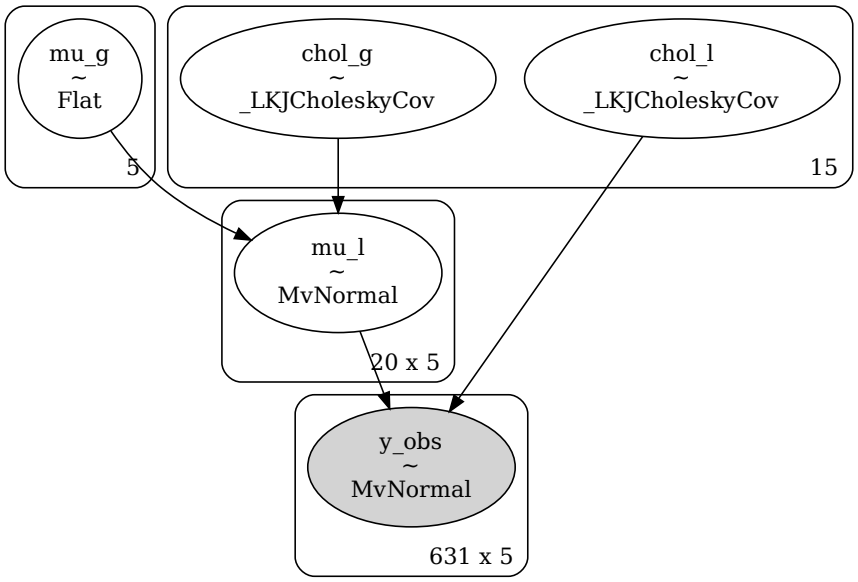

Figure 3.14: Graphical representation of the hierarchical stochastic relations.

Parameter	Mean	SD	HDI 3%	HDI 97%
σ_{L,φ_c}	1.773	0.052	1.684	1.877
σ_{L,κ^*}	0.0031	0.0001	0.003	0.003
σ_{L,λ^*}	0.0078	0.0002	0.007	0.008
$\sigma_{L,N}$	0.065	0.002	0.062	0.069
$\sigma_{L,\nu}$	0.068	0.002	0.065	0.072
$\rho_{L,\varphi_c\kappa^*}$	-0.049	0.041	-0.121	0.034
$\rho_{L,\varphi_c\lambda^*}$	-0.002	0.040	-0.069	0.082
$\rho_{L,\varphi_c N}$	-0.012	0.041	-0.081	0.070
$\rho_{L,\varphi_c\nu}$	0.043	0.040	-0.034	0.116
$\rho_{L,\kappa^*\lambda^*}$	0.451	0.032	0.389	0.511
$\rho_{L,\kappa^* N}$	0.433	0.033	0.369	0.493
$\rho_{L,\kappa^*\nu}$	-0.641	0.024	-0.687	-0.596
$\rho_{L,\lambda^* N}$	0.951	0.004	0.943	0.958
$\rho_{L,\lambda^*\nu}$	-0.214	0.038	-0.288	-0.148
$\rho_{L,N\nu}$	-0.200	0.038	-0.266	-0.123

Table 3.2: Mean values, standard deviations (SD) and bounds of the high density intervals (HDI) of the *local* standard deviations $\boldsymbol{\sigma}_L$ and correlation coefficients $\boldsymbol{\rho}_L$. These parameters characterise the uncertainty of material parameters obtained for one soil.

3.7.3 Summary of the model parameters

The parameters of the hierarchical stochastic model formulated in Section 3.3.9 are inferred in form of the posterior distribution. The results are summarised graphically in Section 3.4. This appendix presents the same results in form of the statistics of the posterior distribution. Table 3.2 shows the mean values, standard deviations (SD) and the boundaries of the highest density intervals (HDI) of the parameters $\boldsymbol{\sigma}_L$ and $\boldsymbol{\rho}_L$. Therefore, it shows the same results as Figures 3.5 and 3.6. These parameters characterise the variability of the material parameters obtained for one fine-grained soil. Since their credible intervals are relatively narrow, the mean values of $\boldsymbol{\sigma}_L$ and $\boldsymbol{\rho}_L$ could be considered without a significant loss of accuracy in subsequent stochastic FEM simulations. For example, having a point estimate $\boldsymbol{\mu}_{pe}$ for the mean value of the material parameters, e.g. from a single run of the calibration procedure, the samples for the Monte-Carlo would be drawn from normal distribution

$$\boldsymbol{y} \sim N(\boldsymbol{\mu}, \boldsymbol{\Sigma}) \tag{3.36}$$

where the covariance matrix is calculated from Eq. (3.17) with the mean values in Table 3.2.

For completeness, Table 3.3 provides analogous statistics for the parameters $\boldsymbol{\mu}_G$, $\boldsymbol{\sigma}_G$ and $\boldsymbol{\rho}_G$ which characterise the variability of material parameters among different fine-grained soils.

Bibliography

[1] J. L. Favre, Errors in geotechnics and their impact on safety, Computers & Structures 67 (1) (1998) 37–45. doi:10.1016/S0045-7949(97)00154-5.

[2] R. Suchomel, D. Mašín, Probabilistic analyses of a strip footing on horizontally stratified sandy deposit using advanced constitutive model, Computers and Geotechnics 38 (3) (2011) 363–374. doi:10.1016/j.compgeo.2010.12.007.

[3] Y. Tao, H. Sun, Y. Cai, Bayesian inference of spatially varying parameters in soil constitutive models by using deformation observation data, International Journal for Numerical and Analytical Methods in Geomechanics 45 (11) (2021) 1647–1663. doi:10.1002/nag.3218.

[4] A. M. Santoso, K.-K. Phoon, S.-T. Quek, Effects of soil spatial variability on rainfall-induced landslides, Computers & Structures 89 (11) (2011) 893–900. doi:10.1016/j.compstruc.2011.02.016.

[5] M. I. Lingwanda, A. Prästings, S. Larsson, D. L. Nyaoro, Comparison of geotechnical uncertainties linked to different soil characterization methods, Geomechanics and Geoengineering 12 (2) (2017) 137–151. doi:10.1080/17486025.2016.1184761.

Parameter	Mean	SD	HDI 3%	HDI 97%
μ_{G,φ_c}	29.630	0.750	28.223	31.016
μ_{G,κ^*}	0.0092	0.0007	0.008	0.010
μ_{G,λ^*}	0.0809	0.0132	0.057	0.107
$\mu_{G,N}$	1.007	0.109	0.806	1.211
$\mu_{G,\nu}$	0.217	0.021	0.177	0.255
σ_{G,φ_c}	3.401	0.512	2.489	4.366
σ_{G,κ^*}	0.0029	0.0005	0.002	0.004
σ_{G,λ^*}	0.0585	0.0095	0.043	0.076
$\sigma_{G,N}$	0.485	0.078	0.346	0.622
$\sigma_{G,\nu}$	0.089	0.016	0.065	0.121
$\rho_{G,\varphi_c\kappa^*}$	-0.377	0.174	-0.699	-0.059
$\rho_{G,\varphi_c\lambda^*}$	-0.025	0.181	-0.366	0.301
$\rho_{G,\varphi_c N}$	-0.106	0.180	-0.417	0.243
$\rho_{G,\varphi_c\nu}$	-0.415	0.171	-0.727	-0.104
$\rho_{G,\kappa^*\lambda^*}$	0.230	0.186	-0.117	0.581
$\rho_{G,\kappa^* N}$	0.281	0.182	-0.054	0.618
$\rho_{G,\kappa^*\nu}$	-0.238	0.197	-0.584	0.130
$\rho_{G,\lambda^* N}$	0.981	0.010	0.964	0.995
$\rho_{G,\lambda^*\nu}$	0.029	0.190	-0.310	0.401
$\rho_{G,N\nu}$	0.090	0.189	-0.247	0.458

Table 3.3: Mean values, standard deviations (SD) and bounds of the high density intervals (HDI) of the *global* means $\boldsymbol{\sigma}_G$, standard deviations $\boldsymbol{\sigma}_G$ and correlation coefficients $\boldsymbol{\rho}_G$. These parameters characterise the distribution of the material parameters among different fine-grained soils.

[6] J. Pieczyńska-Kozłowska, I. Bagińska, M. Kawa, The Identification of the Uncertainty in Soil Strength Parameters Based on CPTu Measurements and Random Fields, Sensors (Basel, Switzerland) 21 (16) (2021) 5393. doi:10.3390/s21165393.

[7] P. Zhang, Y.-F. Jin, Z.-Y. Yin, Machine learning–based uncertainty modelling of mechanical properties of soft clays relating to time-dependent behavior and its application, International Journal for Numerical and Analytical Methods in Geomechanics 45 (11) (2021) 1588–1602. doi:10.1002/nag.3215.

[8] J. Wesseling, J. Kroes, T. Campos Oliveira, F. Damiano, The impact of sensitivity and uncertainty of soil physical parameters on the terms of the water balance: Some case studies with default R packages. Part I: Theory, methods and case descriptions, Computers and Electronics in Agriculture 170 (2020) 105054. doi:10.1016/j.compag.2019.105054.

[9] J. Wesseling, J. Kroes, T. Campos Oliveira, F. Damiano, The impact of sensitivity and uncertainty of soil physical parameters on the terms of the water balance: Some case studies with default R packages. Part II: Results and discussion, Computers and Electronics in Agriculture 170 (2020) 105072. doi:10.1016/j.compag.2019.105072.

[10] M. Lacour, N. A. Abrahamson, Stochastic constitutive modeling of elastic-plastic materials with uncertain properties, Computers and Geotechnics 125 (2020) 103642. doi:10.1016/j.compgeo.2020.103642.

[11] J. Ching, S. Mordechai, Practical Monte Carlo Based Reliability Analysis and Design Methods for Geotechnical Problems, in: Applications of Monte Carlo Method in Science and Engineering, IntechOpen, 2011, pp. 757–780. doi:10.5772/15136.

[12] J. Ching, K.-K. Phoon, Effect of element sizes in random field finite element simulations of soil shear strength, Computers & Structures 126 (2013) 120–134. doi:10.1016/j.compstruc.2012.11.008.

[13] R. Boushehri, R. Motamed, K. Ellison, K. Stanton, Estimating epistemic uncertainty in soil parameters for nonlinear site response analyses: Introducing the Latin Hypercube Sampling technique, Earthquake Spectra 38 (4) (2022) 2422–2450. doi:10.1177/87552930221101413.

[14] M. Oberguggenberger, W. Fellin, Reliability bounds through random sets: Nonparametric methods and geotechnical applications, Computers & Structures 86 (10) (2008) 1093–1101. doi:10.1016/j.compstruc.2007.05.040.

[15] A. Cañavate-Grimal, A. Falcó, P. Calderón, I. Payá-Zaforteza, On the use of stochastic spectral methods in deep excavation inverse problems, Computers & Structures 159 (2015) 41–60. doi:10.1016/j.compstruc.2015.06.009.

[16] A. Prästings, J. Spross, R. Müller, S. Larsson, W. Bjureland, F. Johansson, Implementing the Extended Multivariate Approach in Design with Partial Factors for a Retaining Wall in Clay, ASCE-ASME Journal of Risk and Uncertainty in Engineering Systems, Part A: Civil Engineering 3 (4) (2017) 04017015. doi:10.1061/AJRUA6.0000918.

[17] Q. Pan, X. Qu, L. Liu, D. Dias, A sequential sparse polynomial chaos expansion using Bayesian regression for geotechnical reliability estimations, International Journal for Numerical and Analytical Methods in Geomechanics 44 (6) (2020) 874–889. doi:10.1002/nag.3044.

[18] M. Mohammadi, A. Mosleh, M. Razzaghi, P. Alves Costa, R. Calçada, Stochastic analysis of railway embankment with uncertain soil parameters using polynomial chaos expansion, Structure and Infrastructure Engineering 19 (10) (2022) 1425–1444. doi:10.1080/15732479.2022.2033277.

[19] C. Iodice, R. Di Laora, A. Mandolini, Finite element analyses of energy piles using different constitutive models, E3S Web of Conferences 205 (2020) 05013. doi:10.1051/e3sconf/202020505013.

[20] D. Kolymbas, An outline of hypoplasticity, Archive of Applied Mechanics 61 (3) (1991) 143–151. doi:10.1007/BF00788048.

[21] D. Mašín, A hypoplastic constitutive model for clays, International Journal for Numerical and Analytical Methods in Geomechanics 29 (4) (2005) 311–336. doi:10.1002/nag.416.

[22] D. Mašín, Asymptotic behaviour of granular materials, Granular Matter 14 (6) (2012) 759–774. doi:10.1007/s10035-012-0372-x.

[23] D. Mašín, Clay hypoplasticity with explicitly defined asymptotic states, Acta Geotechnica 8 (5) (2013) 481–496. doi:10.1007/s11440-012-0199-y.

[24] M. Smith, ABAQUS/Standard User's Manual, Version 6.9, Dassault Systèmes Simulia Corp, 2009.

[25] Hypoplastic model with inter-granular strain - PLAXIS UDSM - GeoStudio | PLAXIS Wiki - GeoStudio | PLAXIS - Bentley Communities (Dec. 2019).

[26] Hypoplastic Clay | Nonlinear Models | GEO5 | Online Help, https://www.finesoftware.eu/help/geo5/en/hypoplastic-clay-01/ (2023).

[27] M. Mitew-Czajewska, Evaluation of Hypoplastic Clay Model for Deep Excavation Modelling, Archives of Civil Engineering 62 (4) (Jan. 2016). doi:10.1515/ace-2015-0098.

[28] Z. Galliková, Z. ur Rehman, Appraisal of the hypoplastic model for the numerical prediction of high-rise building settlement in Neogene clay based on real-scale monitoring data, Journal of Building Engineering 50 (Jun. 2022). doi:10.1016/j.jobe.2022.104152.

[29] T. Kadlicek, Applying hypoplastic model for soft soils to the analysis of anchored sheeting wall, Acta Geodynamica et Geomaterialia 13 (2) (2015) 125–136. doi:10.13168/AGG.2015.0050.

[30] M. Mitew-Czajewska, Parametric study of deep excavation in clays, Bulletin of the Polish Academy of Sciences 66 (5) (2018). doi:10.24425/125342.

[31] P. Chattonjai, Hypoplastic model for simulation of compressibility characteristics of cement-admixed Bangkok soft clay at high water content, AIP Conference Proceedings 1738 (1) (2016) 480064. doi:10.1063/1.4952300.

[32] L. Wang, K. Chen, Y. Hong, C. Ng, Effect of consolidation on responses of a single pile subjected to lateral soil movement, Canadian Geotechnical Journal 52 (6) (2015) 769–782. doi:10.1139/cgj-2014-0157.

[33] S. Hernández-Villegas, Determination of the parameters for a hypoplastic constitutive model on clay to be used in the finite element method Tochnog, Tecnología en marcha Journal; 2018: Especial estudiantes Vol. 5 2018; Pág 11-23 (Dec. 2018). doi:10.18845/tm.v31i5.4084.

[34] K. H. Roscoe, J. B. Burland, On the generalised stress-strain behaviour of 'wet' clay, Engineering Plasticity 14 (3) (1968) 535–609. doi:10.1016/0022-4898(70)90160-6.

[35] T. Kadlíček, T. Janda, M. Šejnoha, D. Mašín, J. Najser, S. Beneš, Automated calibration of advanced soil constitutive models. Part I: Hypoplastic sand, Acta Geotechnica 17 (8) (2022) 3421–3438. doi:10.1007/s11440-021-01441-0.

[36] T. Kadlíček, T. Janda, M. Šejnoha, D. Mašín, J. Najser, S. Beneš, Automated calibration of advanced soil constitutive models. Part II: Hypoplastic clay and modified Cam-Clay, Acta Geotechnica 17 (8) (2022) 3439–3462. doi:10.1007/s11440-021-01435-y.

[37] J. P. Bardet, W. Choucair, A linearized integration technique for incremental constitutive equations, International Journal for Numerical and Analytical Methods in Geomechanics 15 (1) (1991) 1–19. doi:10.1002/nag.1610150102.

[38] T. Janda, D. Mašín, General method for simulating laboratory tests with constitutive models for geomechanics, International Journal for Numerical and Analytical Methods in Geomechanics 41 (2) (2017) 304–312. doi:10.1002/nag.2558.

[39] D. Lewandowski, D. Kurowicka, H. Joe, Generating random correlation matrices based on vines and extended onion method, Journal of Multivariate Analysis 100 (9) (2009) 1989–2001. doi:10.1016/j.jmva.2009.04.008.

[40] M. D. Hoffman, A. Gelman, The No-U-Turn Sampler: Adaptively Setting Path Lengths in Hamiltonian Monte Carlo, Journal of Machine Learning Research 15 (2014) 1593–1623. doi:10.48550/arXiv.1111.4246.

[41] M. Betancourt, A Conceptual Introduction to Hamiltonian Monte Carlo (Jul. 2018). arXiv:1701.02434.

[42] M. I. Jordan, Z. Ghahramani, T. S. Jaakkola, L. K. Saul, An Introduction to Variational Methods for Graphical Models, in: M. I. Jordan (Ed.), Learning in Graphical Models, Springer Netherlands, Dordrecht, 1998, pp. 105–161.

[43] J. Salvatier, T. V. Wiecki, C. Fonnesbeck, Probabilistic programming in Python using PyMC3, PeerJ Computer Science 2 (2016) e55. doi:10.7717/peerj-cs.55.

[44] S. P. Brooks, A. Gelman, General Methods for Monitoring Convergence of Iterative Simulations, Journal of Computational and Graphical Statistics (Feb. 2012). doi:10.1080/10618600.1998.10474787.

[45] A. Vehtari, A. Gelman, D. Simpson, B. Carpenter, P.-C. Bürkner, Rank-Normalization, Folding, and Localization: An Improved R^ for Assessing Convergence of MCMC (with Discussion), Bayesian Analysis 16 (2) (2021) 667–718. doi:10.1214/20-BA1221.

[46] C. Dugas, Y. Bengio, F. Bélisle, C. Nadeau, R. Garcia, Incorporating second-order functional knowledge for better option pricing, in: T. Leen, T. Dietterich, V. Tresp (Eds.), Advances in Neural Information Processing Systems, Vol. 13, MIT Press, 2000.

Chapter 4

Applying Bayesian approach to predict deformations during tunnel construction

This chapter presents the preprint version of the journal paper

> Janda, T.; Šejnoha, M.; Šejnoha, J., Applying Bayesian approach to predict deformations during tunnel construction, International Journal for Numerical and Analytical Methods in Geomechanics. 2018, 42(15), 1765-1784. ISSN 0363-9061.

reformatted to align with the style of the thesis.

4.1 Abstract

In this paper a fully probabilistic approach based on the Bayesian statistical method is presented to predict ground settlements in both transverse and longitudinal directions during gradual excavation of a tunnel. To that end, the convergence confinement method is adopted to give estimates of ground deformation numerically. Together with in-situ measurements of the evolution of vertical deflections at selected points along the tunnel line it allows for the construction of a likelihood function and consequently in the framework of Bayesian inference to provide posterior improved knowledge of model parameters entering the numerical analysis. In this regard, the Bayesian updating is first exploited in the material identification step and next used to yield predictions of ground settlement in sections along the tunnel line ahead of the tunnel face. This methodology thus makes it possible to improve original designs by utilizing an increasing number of data (measurements) collected in the course of tunnel construction.

4.2 Introduction

Mathematical modeling of structural systems plays a significant role in the design and assessment of engineering structures. In most fields uncertainty of information entering

a mathematical model is quite low: the structure geometry, material properties and the maximum loading are well known or easy to measure. In such a case the structure reliability is ensured by using reliability approaches provided in the design codes.

However, when uncertainty of input parameters of the underlying mathematical model is high, as in many geotechnical problems, it has to be incorporated into the model. Such stochastic models provide not only the typical output for typical input but also answer the question on how the variability of a particular input parameter influences the variability of the desired output quantity. There are many contributions addressing the variability of soils. These are mostly limited to a random nature of model parameters such as material properties of the selected constitutive model, e.g. cohesion and angle of internal friction in models of the Mohr-Coulomb type [1, 2, 3], hydraulic conductivity when dealing with coupled problems [4], or loading [5]. Application to advanced constitutive models including hypoplasticity can be found in [6]. Not only locally uncertain but also spatially random soils have been investigated [7, 8, 9, 10, 11]. Stochastic finite elements [12], classical stochastic simulations based on the Monte Carlo [13] and Latin Hypercube Sampling methods [14] or simulations exploiting the concept of Neural Networks [15] are often the choice of computational approach.

In the reliability-based design these contributions would be mostly concerned with an aleatory (driven by chance) type of uncertainty [16, 17]. Nevertheless, calibrating constitutive models calls for experiments, which are often sparse and yield another type of uncertainty called epistemic (related to intellectual knowledge). And it is the experimental uncertainty which plays a crucial role in the prediction of structural response grounded on probability analysis [6]. Therein, the Bayesian inference [18, 19] appears a suitable method of attack to reduce the epistemic uncertainties as it accounts for and quantifies uncertainty of the experimentally derived data. The Bayesian interpretation of probability thus allows us to attribute the probability not only to model parameters (unobserved quantities), but also to measured data (observed quantities) including the measurement error. Exploiting their mutual stochastic relationship opens the way, in the framework of Bayesian updating, to reappraise our prior knowledge about the unobserved quantities, i.e. their prior probability densities, and obtain a rationally updated knowledge – their posterior probability density. In geomechanics, this strategy has already been examined in [20, 21] and remained at the forefront of engineering interest up to date [22, 23, 24]. The presented paper falls into this category of cited contributions.

The main advantage of Bayesian updating is its mathematical soundness: if the stochastic relations are properly defined then the posterior belief is the most rational one given the prior belief and the observed data. On the other hand, one must be prepared that the integral statistics of posterior distribution such as the mean value, standard deviation or quantiles can be computed analytically only for a limited category of models. Posterior distribution obtained with models of an arbitrary structure has to be analyzed numerically via Markov chain Monte Carlo methods such as the Metropolis–Hastings algorithm, Gibbs sampling or the Hamiltonian Monte Carlo algorithm. Since these algorithms are implemented in several statistical programs we can concentrate only on the definition of the stochastic model and the prior distribution of its parameters. This strat-

egy has successfully been applied to the analysis of glued laminated timber beams [25] and later in the prediction of settlements during tunnel excavation [26] using a simple excavation model originating from a rather complex quasi three-dimensional soil structure interaction analysis [27]. The knowledge gained through the solution of these two projects is elaborated here to address the design of gradually excavated tunnels supported by ongoing monitoring in the light of stochastic modeling [28]. In this spirit, the proposed approach is consistent with that of the observational (design) method by Terzaghi and Peck, see [29]. The original process of initial design and its progressive modification was further elaborated by other authors, see e.g. [30, 31]. Since Peck's approach is based on the most probable initial ground conditions it is deemed (i) best suited for designs governed by serviceability states and (ii) less suited, but still applicable, to the failure limit states with ductile, rather than brittle, failure. All thinks considered, it well covers the cases, similar to the present approach, with epistemic uncertainties tending to decrease as more observational data become available [32]. Hence, the proposed probabilistic approach may be considered as a supporting tool to at least some of the eight ingredients identified by Peck as attributes of the observational method based design.

The paper is organized as follows. The basic principles and computational steps linked to Bayesian updating are briefly reviewed in Section 4.3. The search for improved posterior knowledge on input parameters of a theoretical model is described in Section 4.4. The procedure utilizes measurements of vertical displacements and predicts gradual evolution of ground deformation as a function of the working face advancement. To that end, the Convergence Confinement method, popular among design engineers, is adopted in the formulation of the deterministic model. Given the posterior knowledge of the selected model parameters, Section 4.5 attempts to provide improved predictions of ground deformation in sections not affected by excavation to its full extent. While Section 4.4 is more or less concerned with parameters identification, in Section 4.5 we may fully appreciate the principal idea of Bayesian updating in reducing the epistemic uncertainties as the pool of measured data is continuously being filled with new information. The most important conclusions are finally summarized in Section 4.6.

4.3 Bayesian model in context of engineering applications

This section briefly describes the theoretical background and the approaches later applied to the problem of parameter inference and prediction of settlements induced during tunnel excavation.

The notion of probability in the Bayesian context differs from the frequentist one. While frequentists derive the probability from the relative frequency of observed data, the Bayesians use probability to express the degree of believe in particular values of a random quantity. Technically, the probabilities are represented equally in both frameworks - a continuous quantity is described by the probability density function and a discrete quantity is defined by the probability mass function. The difference is that the Bayesian probability can be assigned to unobservable variables for which the frequency of occurrence makes no sense. Parameters of stochastic model, e.g. the standard deviation

of measurement error, are a typical example of this type of unobservable variables.

Bayesian parameters inference is a method for deducing the probability distribution of model parameters driven by the observed data. It is expressed by the Bayes theorem written as

$$p(\boldsymbol{\theta}|\boldsymbol{y}) = \frac{p(\boldsymbol{y}|\boldsymbol{\theta})p(\boldsymbol{\theta})}{p(\boldsymbol{y})}, \tag{4.1}$$

where $p(\boldsymbol{y})$ and $p(\boldsymbol{\theta})$ represent the probability density functions of $\boldsymbol{\theta}$ and $\boldsymbol{y}$, respectively. The bold letters denote vector quantities. Notation, e.g. $p(\boldsymbol{y}|\boldsymbol{\theta})$ means conditional probability, i.e. the probability of $\boldsymbol{y}$ given fixed values of $\boldsymbol{\theta}$. The vector $\boldsymbol{y}$ represents the observed data. The vector $\boldsymbol{\theta}$ represents the model parameters. The Bayesian theorem thus defines the posterior distribution[1] of the model parameters $\boldsymbol{\theta}$ given the observed data $\boldsymbol{y}$. Since the observed data $\boldsymbol{y}$ are fixed, the right hand side is treated as a function of $\boldsymbol{\theta}$ only. The denominator $p(\boldsymbol{y})$ is therefore just a constant and the posterior distribution is proportional to the product of the likelihood function, $p(\boldsymbol{y}|\boldsymbol{\theta})$, and the prior distribution of parameters, $p(\boldsymbol{\theta})$. Note that the likelihood function is in fact the probability of the data given the parameters. The term likelihood is used to emphasize the fact that the expression is viewed as a function of $\boldsymbol{\theta}$.

4.3.1 Forward stochastic model

The first of the two ingredients of the Bayes theorem is the likelihood function. It is constructed as the stochastic model of the observed data given fixed values of the parameters. This model is sometimes called the forward model and its formulation draws on our understanding of the underlying physical process. Such a process is described by a suitable deterministic model suggesting how the measured data would be generated when no uncertainty in the input parameters and no modeling or measurement errors were present. In practical applications the deterministic model involves numerical simulations using for example the Finite Element Method (FEM) or its approximation as discussed in the next section. In a typical scenario of an engineering application the measured data are randomly distributed around some theoretical value. This theoretical value is a result of a deterministic simulation with the (fixed) model parameters. All parameters entering the simulation and controlling the randomness of the measured values are either known/fixed or uncertain and stored in vector $\boldsymbol{\theta}$.

4.3.2 Surrogate model

Computing the moments of the posterior distribution such as the mean value or variance requires evaluating the integrals of the related probability density function. This can be done in closed form only for very simple forward models with conjugate prior

[1] The posterior distribution manifests, how our original prior knowledge of model parameters, expressed in terms of their prior probability distributions, is enriched as both the number and credibility of observed data increases. It is also worth mentioning that no improvement of a given model parameter might be achieved if there is no or a weak link between this parameter and the observed data.

distributions. For more complex models the closed form may not exist and the integrals are approximated by statistics of samples generated from the posterior distribution. In this scenario the samples are drawn from the posterior distribution using one of the Markov chain Monte Carlo techniques. Utilizing this technique requires expressing the likelihood function and thus running the simulation many times often exceeding several thousands. To maintain the sampling computationally feasible the deterministic model (the simulation) is often substituted with a computationally cheaper approximation.[2] This approximation is termed the surrogate model. Other terms as the response surface model [16, 17, 33] or metamodel [34] are also used.

The problem of construction and verification of the efficient surrogate model is a wide and separate topic. With reference to Bayesian inference and parameter identification we refer the interested reader, e.g. to [35, 36, 37]. Here we limit our attention to very simple approximation of the original model using linear regression. Let's abstract the deterministic simulation with given input parameters $\boldsymbol{x} = \langle x_1, \ldots, x_i, \ldots, x_m \rangle$ as an evaluation of function f producing the simulation results $z = f(\boldsymbol{x})$. We can construct the surrogate model $\tilde{f}$ in the form

$$\tilde{f}(\boldsymbol{x}) \quad = \quad \sum_{j=1}^{n} \beta_j g_j(\boldsymbol{x}) \tag{4.2}$$

where β_j are scalar coefficients and $g_j(\boldsymbol{x})$ is a collection of arbitrary functions. The choice of functions g_j might be inspired by the role of the particular parameter x_i in the true model.

Linear regression is used to find the optimal values of the coefficients β_j for a limited set of the original model simulations. Suppose that the model has been evaluated n_k-times and denote the result of the model evaluated at k-th point $z_k = f(\boldsymbol{x}_k)$. The optimal values of $\boldsymbol{\beta}$ are expressed as $\boldsymbol{\beta} = (\boldsymbol{X}^T\boldsymbol{X})^{-1}\boldsymbol{X}^T\boldsymbol{z}$, where $\boldsymbol{z} = \langle z_1, \ldots, z_k, \ldots, z_{n_k} \rangle$ are the results of simulations and the elements of matrix $X_{kj} = g_j(\boldsymbol{x}_k)$ are the functions g_j evaluated for each point $\boldsymbol{x}_k$. The coefficients obtained using linear regression minimize the sum of squares of the error in the surrogate model at the points $\boldsymbol{x}_k$.

4.4 Predicting settlements during tunnel excavation via Bayesian model

As already stated in the introductory part the present contribution deals with the application of Bayesian updating in the field of geotechnical engineering. As an example we consider the prediction of ground settlement as well as underground deformation caused by tunnel excavation. This choice is driven by a high variability of material properties and limitations of the most common computational approach highly dependent on the designer experience on the one hand and ongoing monitoring providing instantaneous

[2] This will prove useful in our particular case where the FEM simulation may take several minutes thus making the Bayesian updating unfeasible.

information about global response of the structure on the other hand. Both issues promote exploitation of Bayesian updating to provide improved knowledge about uncertain parameters and consequently improved prediction of the deformation field to yet occur.

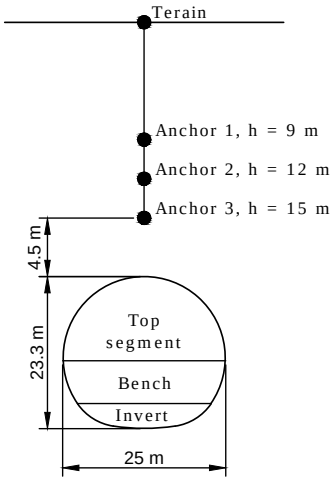

Figure 4.1: Typical cross-section of the Blanka tunnel with horizontal sequencing and position of the points at which the vertical displacement was monitored

Fig. 4.1 shows a typical cross-section of the road tunnel Blanka in Prague. An initial site investigation revealed reasonable geological conditions which in turn allowed for a horizontal sequencing of the tunnel face. The New Austrian Tunneling Method (NATM) was applied to perform excavation. When applied to horizontal sequencing the excavation proceeds such that the top segment is excavated first to a certain distance ahead of the original tunnel face and then stabilized with sprayed concrete creating the initial lining. A similar procedure is applied subsequently to the bench and eventually to the invert. The present study concentrates on the first two excavation steps for which the monitoring data, the evolution of vertical displacements at selected points seen in Fig. 4.1, were available.

As evident, each monitored cross-section was equipped with three extensometers located above the tunnel crown. This instrumentation together with the geodetic measurements of the settlement yield the time evolution of vertical displacements of the terrain and at a depth of 9 m, 12 m and 15 m, respectively. For illustration, we present such measurements, pertinent to one particular cross-section, in Fig. 4.2(a). Henceforth, this section is labeled as J022. The common excavation process of NATM is obvious from Fig. 4.2(a) showing advancement of excavation steps starting with top segment and followed subsequently by excavation of bench. This is manifested by a sudden increase in the rate of displacement evident in Fig. 4.2(a). For the sake of Bayesian updating it appears useful to re-plot the results from Fig. 4.2(a) as a function of the position of the tunnel face with respect to the location of the monitored section. Such results appear separately for the excavation of top segment in Fig. 4.2(c) and for the excavation of bench in Fig. 4.2(d).

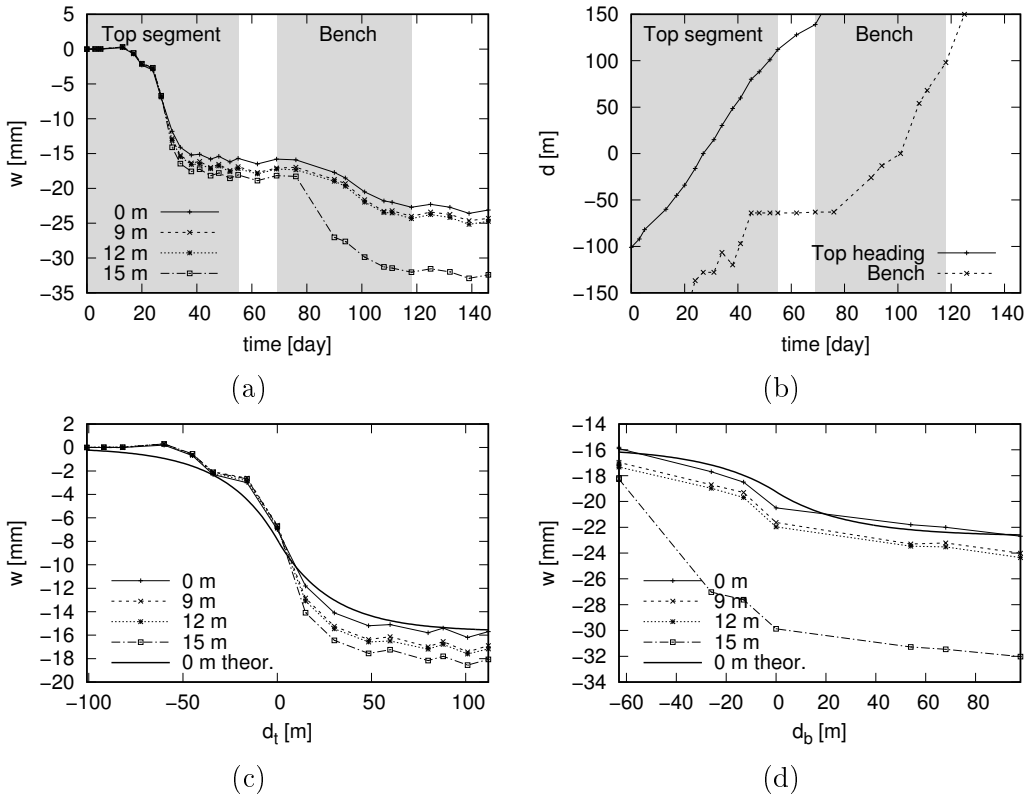

Figure 4.2: Monitored section J022: a) time evolution of vertical displacement at selected points, b) time evolution of tunnel face position with respect to monitored section, c)-d) evolution of vertical displacement at selected points as a function of tunnel face location - c) excavation of top segment, d) excavation of bench

Based on our prior research effort in describing the soil-structure interaction during tunnel excavation efficiently [27], we promote the following set of exponential functions $b(d)$ to represent the shape of the curves in Figs. 4.2(c,d) as

$$b(d) = \begin{cases} \frac{1}{2}\exp(\alpha d), & \text{if } d < 0, \\ 1 - \frac{1}{2}\exp(-\alpha d), & \text{otherwise,} \end{cases} \tag{4.3}$$

where d stands for either d_t or d_b and denote the distance of the tunnel face from the monitored cross-section. The symbols d_t and d_b in Figs. 4.2(c,d) are introduced to make distinction between the tunnel faces associated with the excavation of top segment and bench, respectively, recall Fig. 4.2(b).

Clearly, the negative values of d represent the situation when the tunnel face has not reached the monitored cross-section yet. In a limiting case $d \to -\infty$ we get $b(-\infty) = 0$. In parallel, the positive value of d identifies the case when the tunnel face has already passed the monitored section. Large values of $d \to \infty$ then render the value of function

b equal to 1. Eq. (4.3) therefore serves as a longitudinal shape function of vertical displacement whose shape is controlled by a single fitting parameter α to be identified.

Given this function the gradual evolution of the vertical displacement $w(d)$ at any point of the domain can be written in terms of the ultimate displacement w^{fin} as

$$w(d) = b(d)w^{fin}. \tag{4.4}$$

Because in numerical simulations described in the next section we consider the top segment and bench be excavated separately[3], we rewrite the general Eq. (4.4) for the two tunnel sections separately as

$$w_h(d_t) = b(d_t)w_{t,h}^{fin}, \tag{4.5}$$

$$2w_h(d_b) = (1 - b(d_b))w_{t,h}^{fin} + b(d_b)w_{b,h}^{fin}, \tag{4.6}$$

where subscript $h = 0, 9, 12, 15$ m identifies a particular curve in Fig. 4.2. Similarly, $w_{t,h}^{fin}, w_{b,h}^{fin}$ represent the final settlement after completing the excavation of top segment and bench, respectively.

4.4.1 Numerical prediction of ultimate displacement w^{fin}

While tunnel excavation is clearly a three-dimensional process, a vast majority of design engineers usually rely on two-dimensional modeling. When simulating this process within the framework of NATM the Convergence Confinement Method (CCM) [38, 39] is often employed. This method is briefly discussed in Section 4.4.1.1. In most practical applications, this method is introduced in the framework of Finite element [40, 41, 42] or Finite difference [17] method. This in turn may prove computationally unfeasible in conjunction with Bayesian updating. Formulation of a surrogate model is therefore needed. A specific format adopted in the present study is described in Section 4.4.1.2.

4.4.1.1 Finite element analysis using Convergence Confinement Method

The Convergence Confinement Method attempts to predict the actual volume loss as the excavation proceeds by prescribing a certain proportion of unloading before the lining construction is installed. The procedure is outlined in Fig. 4.3.

In particular, Fig. 4.3(a) shows an evolution of differential displacements of the crown and invert of a tunnel as the excavation process proceeds. A longitudinal view of a tunnel segment near the tunnel face is plotted in Fig. 4.3(b) identifying the lack of support in the proximity of the face. It is the goal of CCM to reproduce such three-dimensional effects through a simplified solution of a two-dimensional plane strain analysis of a typical section. A gradual evolution of the differential displacements at this section as a result

[3]This assumption is supported by Figs. 4.2(a,b) showing that the settlement linked to the excavation of top segment arrived at its final value well before the excavation of bench had any substantial effect on the change of settlement in the monitored cross-section, see the white area in between the two gray regions.

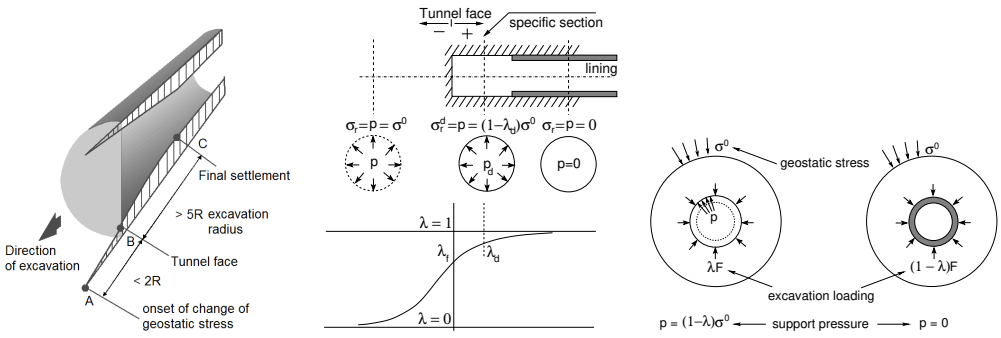

Figure 4.3: Principles of of Convergence Confinement Method: a) evolution of differential settlement along the tunnel axis, b) evolution of parameter λ as a function of support pressure p, c) representation of excavation forces

of the tunneling process can be simulated by a continuous reduction in the radial stress σ_r acting on the tunnel perimeter from its initial value σ^0 to zero. The remainder of the initial stress σ^0 then represents a support pressure p to simulate the stiffening effect of the actual three-dimensional system of rock mass and lining near the working face as schematically shown in Fig. 4.3(c). In finite element simulations, the vector of equivalent nodal forces $\boldsymbol{F}_0$ corresponding to the excavation being proportional to the initial stress vector $\boldsymbol{\sigma}^0$ is split into two parts. The fraction of this vector, $\lambda\boldsymbol{F}_0$, is applied first to the unsupported tunnel boundary to simulate the stiffness reduction at a given section due to continuous excavation, see Fig. 4.3(c). The corresponding support pressure then equals to $p = (1-\lambda)\sigma^0$. At this instant the lining is installed and the remainder of the equivalent nodal forces $(1-\lambda)\boldsymbol{F}_0$ is applied to create the lining stress.

Table 4.1: Selected results for four different mesh refinements

Model number	Edge length Min/Max [m]	Number of Nodes	Number of Elements	N [kN] | λ [%]			E_d^{pl} [%] | λ [%]		
				20	40	60	20	40	60
1	2/8	934	366	1057	887	710	1.46	1.64	1.94
2	1/6	1927	819	1072	907	738	2.13	2.12	2.95
3	0.5/4	4849	2187	1063	910	748	3.47	3.46	3.57
4	0.25/2	17934	8507	1035	890	744	6.12	5.37	5.30

To show the influence of parameter λ on the evolution of displacement field we performed a convergence study for three different values of $\lambda = 20, 40, 60\%$ and four mesh refinements. The model dimensions appear in Fig. 4.4(a), whereas the tunnel dimensions are evident from Fig. 4.1. The assumed mesh refinement is available in Table 4.1 showing in the 2nd column the assigned maximum and minimum element edge length resulting in the corresponding number of nodes and elements stored in the 3rd and 4th column, respectively. Figure 4.4(d) plots the evolution of vertical displacements measured on terrain, tunnel crown and bottom of the bench as a function of number of elements.

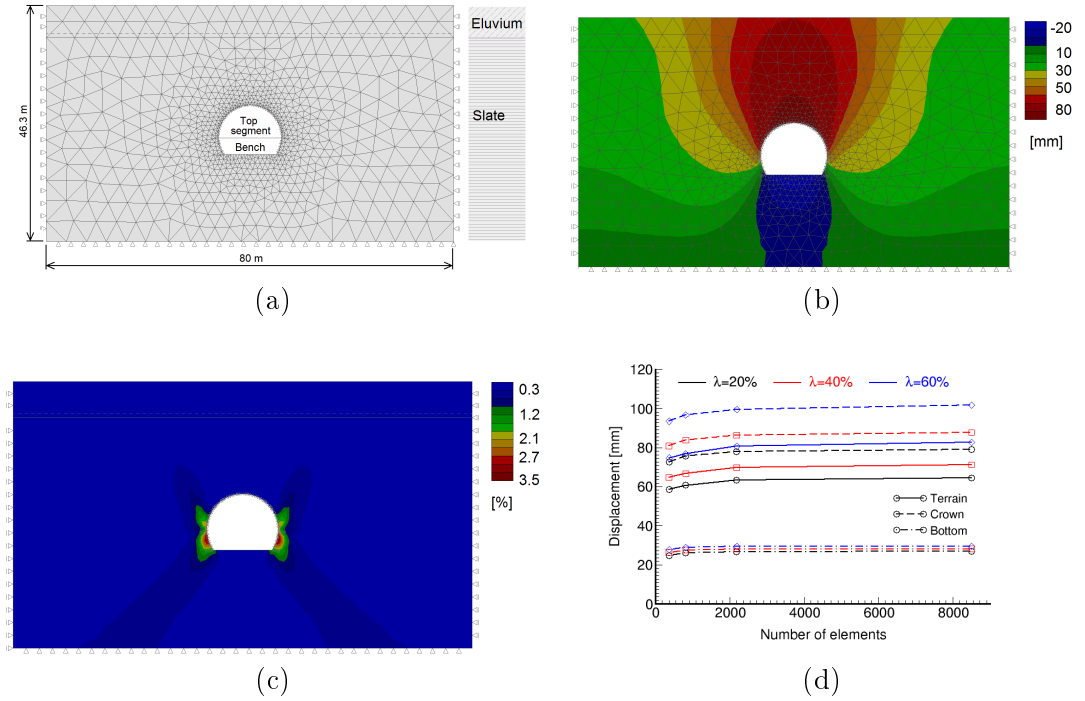

Figure 4.4: Finite element simulation using CCM. Model No. 3, $\lambda = 40\%$: a) soil layers and FEM mesh, b) final vertical displacement w^{fin}, c) final equivalent deviatoric plastic strain, d) convergence study - evolution of final vertical displacements for various mesh refinement and 3 different values of λ, see Table 4.1

Inspecting this figure promotes the model No. 3 as sufficient to tune the previously mentioned surrogate model, both in terms of accuracy and computational efficiency. This is supported by the distribution of ultimate vertical displacement w_b^{fin} and equivalent deviatoric plastic strain E_d^{pl} found at the end of the excavation sequence and plotted in Figs. 4.4(b) and (c) for illustration.

Table 4.2: Material parameters of subsoil layers

Soil layer	E [MPa]	ν [-]	c [kPa]	φ [°]	ψ [°]	γ [kN/m^3]
Eluvium (F3)	12	0.4	15	23	0	19
Slate (R3)	120	0.2	55	25	0	25

These results were derived with the help of the Mohr-Coulomb constitutive model. The model parameters are provided in Table 4.2, where $E, \nu, c, \varphi, \gamma$ are the Young modulus, Poisson ratio, cohesion, angle of internal friction and bulk weight of individual soils. The two soil layers were classified as Eluvium (F3) and Slate (R3) based on the geological survey carried out by the SG Geotechnika a.s., the results of which are available from the BARAB information system (www.barab.eu), see e.g. [43], together with the convergence measurements presented already in Fig. 4.2. Since no laboratory measurements

were available for the actual soils the required values were taken from a private database of Pudis a.s. listing ranges of stiffness and strength parameters of soils and rocks located in the Prague region. These ranges were then adopted in the formulation of prior distributions of the selected parameters, see Table 4.3. In the present convergence study the lower bound of these data summarized in Table 4.2 was used. A non-associated flow rule with the dilation angle $\psi = 0$ was assumed for both soils.

In accordance with Fig. 4.2 and the concept of CCM the simulation was split into five calculation stages. The first stage served to calculate the initial geostatic stress. This was followed by excavation of the top segment performed within calculation stages two and three. It is therefore assumed that at the end of calculation stage three the settlement associated with the excavation of top segment reached its final value. The analysis was then completed by excavating bench in calculation stages four and five. Remember the results of actual excavation sequence in the form of settlement curves in Fig. 4.2 to support this numerical splitting. For both sections, the parameter λ was assumed the same.

While standard six-node triangular plane strain elements were used to discretize the soil displacements, three-node Mindlin beam elements served to represent the concrete lining. The GEO5 Tunnel software [44][4] was exploited to run the numerical analysis. Point out that excavation of invert has not been simulated as no measured data were available with this construction step. To prevent a non-realistic settlement of the lining opened along the invert a special type of beam element, representing the so called elephant foot, was adopted, see [44] for further details.

Apart from the results displayed in Fig. 4.4, some additional data derived from the application of all computational models can be found in Table 4.1. As expected, the smaller the value of parameter λ the larger percentage of load must be accommodated by the soil-lining system. This is evident from both the values of the generated normal force and the values of vertical displacements in Fig. 4.4(d). Undoubtedly, the choice of λ may quite significantly affect the results of numerical simulations for a given soil stiffness.

4.4.1.2 Surrogate model formulation

As suggested in Section 4.3.2, the finite element computations were approximated by a surrogate model in the form of Eq. (4.2). In the light of FEM analysis we need to specify the vector of input parameters $\boldsymbol{x}$, the vector of output values $\boldsymbol{y}$ and the sequence of functions $g_j(\boldsymbol{x})$. The vector of input parameters $\boldsymbol{x} = \{E, \varphi, c, \lambda\}$ represents all variables entering the finite element analysis, i.e. the material parameters and the parameter λ related to the convergence confinement method. Other parameters entering the FEM analysis, such as geometry or material properties of the surface layer (Eluvium) together with the specific weight of soil γ and the dilation angle ψ, were assumed constant. This is because γ serves to generate the initial stress state in the calculation stage one only and $\psi = 0$ is a typical choice to simulate critical state conditions with the Mohr-Coulomb

[4]The authors of this paper are also the authors of the source code of the GEO5 Tunnel software.

model.

To build the surrogate model, three rational functions were considered for each parameter. To allow more precise fit two the model two cross terms, $E\lambda$ and φc in particular, were added as these pairs of variables are expect to show some degree of correlation. This resulted into the following specific form of Eq. (4.2)

$$\begin{aligned} \tilde{f}_h(\boldsymbol{x}) &= \beta_h^1 + \beta_h^2 \frac{1}{E} + \beta_h^3 \frac{1}{\varphi} + \beta_h^4 \frac{1}{c} + \beta_h^5 \frac{1}{\lambda} + \beta_h^6 E + \beta_h^7 \varphi + \beta_h^8 c + \beta_h^9 \lambda + \\ &+ \beta_h^{10} E^2 + \beta_h^{11} \varphi^2 + \beta_{12} c_h^2 + \beta_h^{13} \lambda^2 + \beta_h^{14} E\lambda + \beta_h^{15} \varphi c, \end{aligned} \tag{4.7}$$

where the subscript h identifies, similar to Eq. (4.5), a particular measurement point. Clearly, a unique surrogate model was constructed for each of the measurement points at depths $h = 0, 9, 12, 15$ m and each profile segment, i.e. top segment and bench, making in total 120 unknown β parameters to be calculated. To that end, a series of 40 FEM simulations was carried out for various combinations of model parameters sampled from the entire parameter space considered to build the uniform prior distributions, see ahead Section 4.4.2 and Table 4.3 in particular. The results from the FEM simulations were then used to calculate the coefficients β_h^i in Eq. (4.2).

The approximation was validated by running additional FEM simulations at points randomly chosen from the prior distribution and comparing the results to the output of the surrogate model. The relative error in the computed vertical displacement was found below 5% for all points, which is within a reasonable accuracy for an engineering application. To support this we compare in Fig. 4.5 the results provided by FEM and the assumed surrogate model. These were generated, for the sake of illustration, for fixed values of parameters $\lambda = 40\%$ and strength parameters of the Slate layer $c = 70$ kPa and $\varphi = 33°$ while changing the values of Young's modulus E only. The material parameters of the Eluvium layer were taken from Table 4.2.

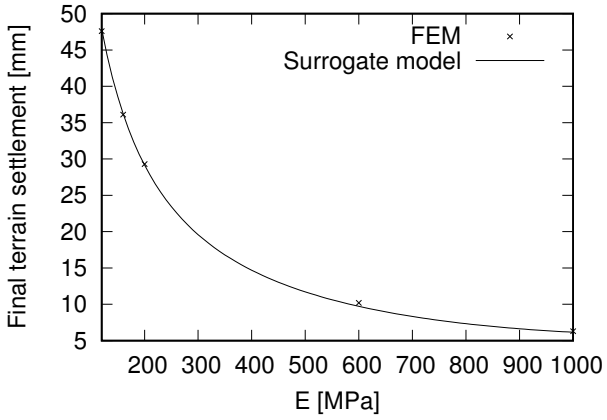

Figure 4.5: Comparing the prediction of the final terrain settlement at the end of calculation stage five provided by both FEM and the surrogate model

If desired, the accuracy of the surrogate model can be improved by extending the series of functions g_j. Other more general surrogate models of the FEM analysis, which is seen as a black box, can be found in [45]. These include for example the thin plate spline technique or kriging. The first approach is multidimensional analogy of physical two-dimensional thin plate with deflection $f(x_i, y_i)$ prescribed at points $[x_i, y_i]$. The optimal shape of surface connecting these points is governed by minimization of the stored elastic energy of the deformed plate. In kriging, the approximated values are seen as a stochastic process which parameters are estimated based on the known output values for given input parameters. An example construction of kriging-based surrogate model for FEM analysis is published in [46].

4.4.2 Forward stochastic model and posterior distribution

The previous paragraphs identified both the observed (measured) data and unobservable variables affecting their theoretical prediction from simulations. Accepting a random nature of both sets of quantities allows us to construct a forward stochastic model offering the notion about the probability distribution of the measured data being represented by the likelihood function.

The measured values of vertical displacements $w_{ij}(d_{s,i})$[5]. were already introduced at the beginning of this section. In what follows the subscript i is linked to the position of the tunnel face $d_{s,i}$ relative to the position of the monitored section and the subscript j is associated with the measured depth h[6], recall Figs. 4.1 and 4.2. The parameters of the stochastic model appear in Eqs. (4.3) and (4.4), and naturally in the FEM model to give the ultimate settlement w_{ij}^{fin}. In this regard we take no notice to the influence of the model geometry, boundary conditions and finite element mesh and concentrate on the stiffness and strength parameters of the constitutive model of the soil being excavated through the λ-method. These parameters are collected in the vector $\boldsymbol{\theta} = \langle \alpha, \lambda, E, c, \varphi, \sigma_w \rangle$ where E, c, φ and σ_w are the Young modulus, cohesion, angle of internal friction of the excavated soil (Slate) only, and the displacement error, respectively.

The stochastic model then assumes the following form

[5]Subscript s in subsequent expressions should be replaced either by t or b depending on the excavated section being considered, recall Eqs. (4.5) - (4.6)

[6]Subscript h in Eqs. (4.5), (4.6) and (4.7) is replaced by subscript j in Eqs. (4.9) and (4.11) to be more consistent with a typical notation used for summation indexes.

$$
\begin{aligned}
w_{ij} &\sim \mathcal{N}(\overline{w}_{ij}, \sigma_w), && (4.8)\\
\overline{w}_{ij} &= b_i \overline{w}_j^{fin}, && (4.9)\\
b_i &= \begin{cases} \frac{1}{2}\exp(\alpha d_{s,i}), & \text{if } d_{s,i} < 0, \\ 1 - \frac{1}{2}\exp(-\alpha d_{s,i}), & \text{otherwise,} \end{cases} && (4.10)\\
\overline{w}_j^{fin} &= \tilde{f}_j(E, \varphi, c, \lambda) && (4.11)\\
E &\sim \mathcal{U}(E_{min}, E_{max}), && (4.12)\\
\varphi &\sim \mathcal{U}(\varphi_{min}, \varphi_{max}), && (4.13)\\
c &\sim \mathcal{U}(c_{min}, c_{max}), && (4.14)\\
\lambda &\sim \mathcal{U}(\lambda_{min}, \lambda_{max}), && (4.15)\\
\alpha &\sim \mathcal{U}(\alpha_{min}, \alpha_{max}), && (4.16)\\
\sigma_w &\sim \mathcal{U}(\sigma_{w,min}, \sigma_{w,max}). && (4.17)
\end{aligned}
$$

Relation (4.8) implies that the measured displacements w_{ij} are normally distributed around the theoretical mean value $\overline{w}_{ij}$ with a standard deviation σ_w. This way the measurement error and the modeling uncertainty are jointly covered by a simple stochastic relation. The theoretical mean values $\overline{w}_{ij}$ follow from (4.4) and the theoretical ultimate displacement $\overline{w}_j^{fin}$ is provided by the surrogate model, Eq. (4.7).

Stochastic relations (4.12)–(4.17) represent the uniform prior distributions of the parameters of the theoretical model between certain fixed ranges.

Having the model formulated we may now move one step further and rephrase the Bayesian statistical method to get the posterior (improved) joint probability distribution function of model parameters. We first denote the normal and uniform probability distribution functions with mean μ and standard deviation σ

$$
\begin{aligned}
f_N(x; \mu, \sigma) &= \frac{1}{\sigma\sqrt{2\pi}}\, e^{-\dfrac{(x-\mu)^2}{2\sigma^2}}, && (4.18)\\
f_U(x; l_b, u_b) &= \begin{cases} \dfrac{1}{u_b - l_b} & \text{for } x \in [l_b, u_b] \\ 0 & \text{otherwise} \end{cases}. && (4.19)
\end{aligned}
$$

In the light of Bayesian theorem (4.1) the posterior probability distribution function of model parameters then becomes

$$
\begin{aligned}
\pi(\alpha, \lambda, E, c, \varphi, \sigma_w | \langle w_{ij} \rangle) \propto \prod_{i=1}^{N_{s,face}} \prod_{j=1}^{N_{depth}} f_N(\langle w_{ij} \rangle; \langle \overline{w}_{ij} \rangle, \sigma_w) \times \\
f_U(\alpha; \alpha_{min}, \alpha_{max}) \times f_U(\lambda; \lambda_{min}, \lambda_{max}) \times f_U(E; E_{min}, E_{max}) \times \\
f_U(c; c_{min}, c_{max}) \times f_U(\varphi; \varphi_{min}, \varphi_{max}) \times f_U(\sigma_w; \sigma_{w,min}, \sigma_{w,max}), \qquad (4.20)
\end{aligned}
$$

where $\langle w_{ij} \rangle$ is a vector collecting all measured points, i.e. in total the number of face locations with respect to the monitored section $N_{s,face}\times$ the number of monitored points along the cross-section depth N_{depth}.

The first term on the right hand side of Eq. (4.20) is the likelihood function (the probability distribution of the measured data). Clearly, the model parameters are initially assumed to be statistically independent. However, their statistical dependency naturally arises through the definition of the posterior joint probability distribution function on the left hand side of Eq. (4.20). This will be demonstrated later in Section 4.4.3.2. The operator "$\propto$" means proportional to (that is, the two sides are equal except for the normalizing constant C, the denominator in Eq. (4.1)).

4.4.3 Bayesian inference based on data measured in section J022

Suppose that data (convergence measurements) collected at one particular cross-section are already available. This allows us, with the help of the stochastic model outlined in the previous section, to obtain improved (posterior) knowledge about the model parameters, which in turn can be used to get an improved prediction of the impact of tunneling process in sections at which the tunnel face has not arrived yet. The first step, striving for improved knowledge of model parameters, is described next. The second step, aiming at improved predictions, is discussed in Section 4.5.

Table 4.3: Assumed ranges of prior distribution of model parameters in section J022

Parameter	Units	Minimum (l_b)	Maximum (u_b)
E	MPa	120	1000
φ	deg.	25	40
c	kPa	55	100
λ	%	20	60
α	–	0.01	0.5
σ_w	mm	0.1	5.0

As mentioned already in Section 4.4.1.1 the ranges of the uniform prior distributions of material parameters listed in Table 4.3 were adopted from the private material database supplied by Pudis a.s. Ranges for the remaining parameters follow from the authors' experience. For parameters λ and α, in particular, we refer the interested reader to [27]. In any case, these ranges are wide enough to support the robustness of the updating procedure based on the Bayesian inference. The observed data were collected at one particular cross section for several positions of tunnel faces identified by symbols on individual curves in Fig. 4.2. In this particular case, $N_{t,face} = 16, N_{b,face} = 8$ and $N_{depth} = 4$ were adopted in Eq. (4.20).

4.4.3.1 Sampling method

For the sake of efficiency, the surrogate model presented in Section 4.4.1.2 was implemented, together with the hierarchical model formulated in Section 4.4.2, into the JAGS program [47] adopting the dialect of the BUGS language [48]. Note that this program allows for the implementation of relatively simple functions to evaluate the observed variables numerically. The use of FEM, regardless of the computational time, is therefore precluded so making the application of the surrogate model necessary.

The program uses Gibbs sampling to generate the samples of the model parameters according to the joint posterior distribution. The burn-in period of 2000 samples, which were discarded, was followed by generating two chains of 10000 samples. For illustration, the Markov chains for all searched parameters are displayed in Fig. 4.6. The computational time to generate these chains was in the order of minutes on a standard personal computer.

All chains show a sufficient mixing of the generated samples indicating proper settings of the Gibbs sampling algorithm. Therefore, the generated histograms should converge to the theoretical continuous distributions. It can be also noted that the samples in the first four chains in Figs. 4.6(a-d) concentrate within a narrow band with respect to their assumed prior ranges, recall Table 4.3. This may suggest more preferred values in posterior distributions of these parameters. On the other hand, the samples in chains in Figs. 4.6(e,f) are drawn nearly from the entire prior range, so higher variability in the posterior distributions of these parameters can be expected. All this is confirmed by examining the histograms of marginal posterior distributions discussed next.

4.4.3.2 Marginal posterior distributions of model parameters

The posterior marginal distributions of model parameters extracted from Markov chains generated according to the posterior joint probability function in Eq. (4.20) are presented in Fig. 4.7 in the form of histograms and compared to the originally assumed prior distributions. Their difference suggests, how the prior, relatively vague, knowledge about the parameter value changed after the measured data have been observed.

The following partial conclusions can be drawn. Clearly, the standard deviation of displacement error σ_w was identified relatively well suggesting a sufficient number of measured data used in the updating procedure. This may also support the resulting distribution of parameter α promoting this variable to be considered as almost deterministic. We should remind that this parameter, controlling the shape of the settlement line, is primarily linked to shear stiffness of the soil [26, 27] much similar to the well known Winkler-Pasternak subsoil model. The fact that it is well approximated by exponential functions $b(d)$ in Eq. (4.3) is illustrated in Figs. 4.2(c,d) showing approximations of the terrain settlement associated in turn with the excavation of top segment (the theoretically derived solid line in Fig. 4.2(c)) and bench (the solid line in Fig. 4.2(d)). These plots were obtained with the help of Eqs. (4.5) and (4.6) by adopting for α the value of the maximum a posteriori probability (MAP) estimate from Fig. 4.7(a) and for $w_{s,0}^{fin}$ the measured values of terrain settlement found at the right edge of the two gray areas cor-

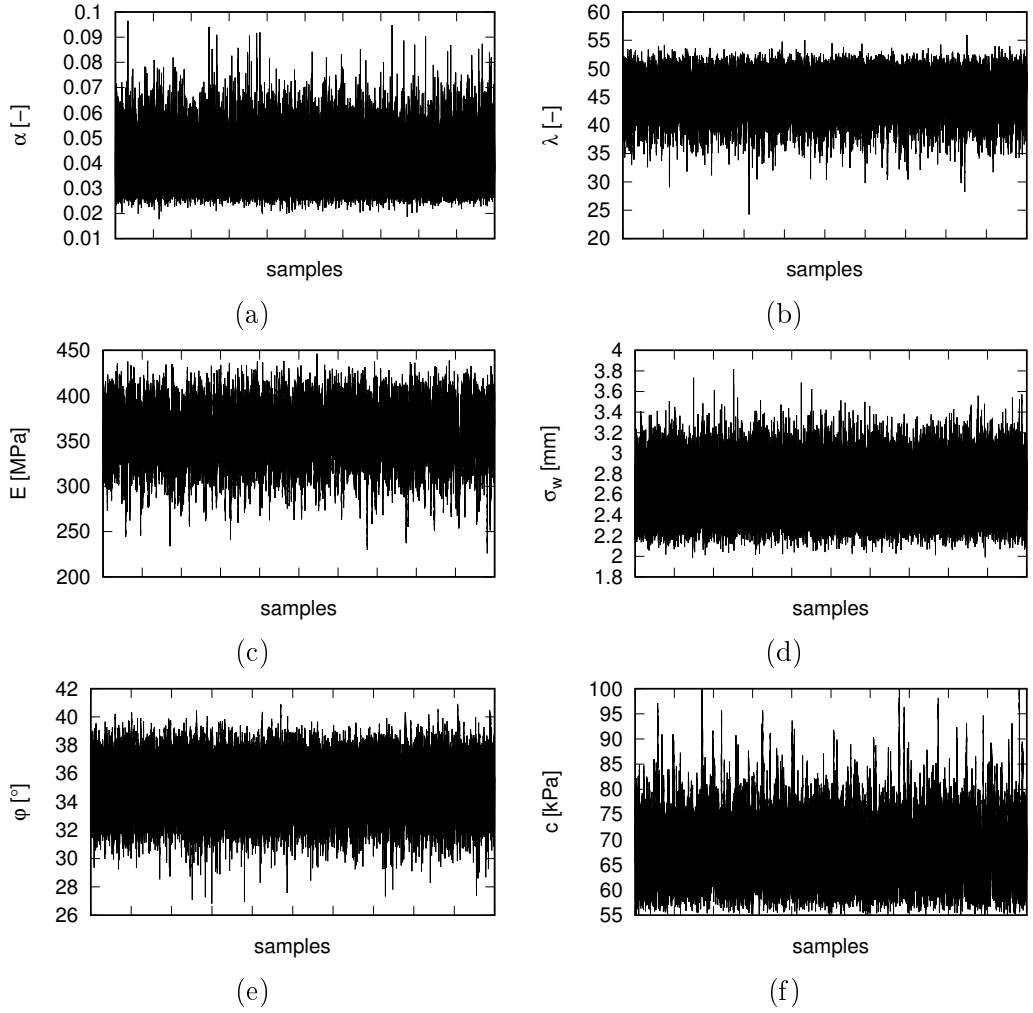

Figure 4.6: Markov chains of generated samples of: a) parameter α, b) parameter λ, c) Young's modulus E, d) standard deviation of displacement error σ_w, e) angle of internal friction φ, f) cohesion c,

responding to 58 (top segment) and 118 (bench) days from the onset of measurements.[7] However, in the updating procedure they are predicted by the surrogate model, recall Eq. (4.11).

Although not as unambiguous as the previous two parameters, the the Young modulus E and the parameter λ are still predicted relatively well. This is not surprising as the first parameter controls the material stiffness and thus the value of settlement. However, unlike parameter α, these two model parameters compete for the same type of data being the in situ measured final settlement. Improvements in parameter identification could be expected if in situ measurements were accompanied by laboratory data obtained for

[7] These values substitute the theoretical values of $w_{s,0}^{fin}$ at time $\to \infty$.

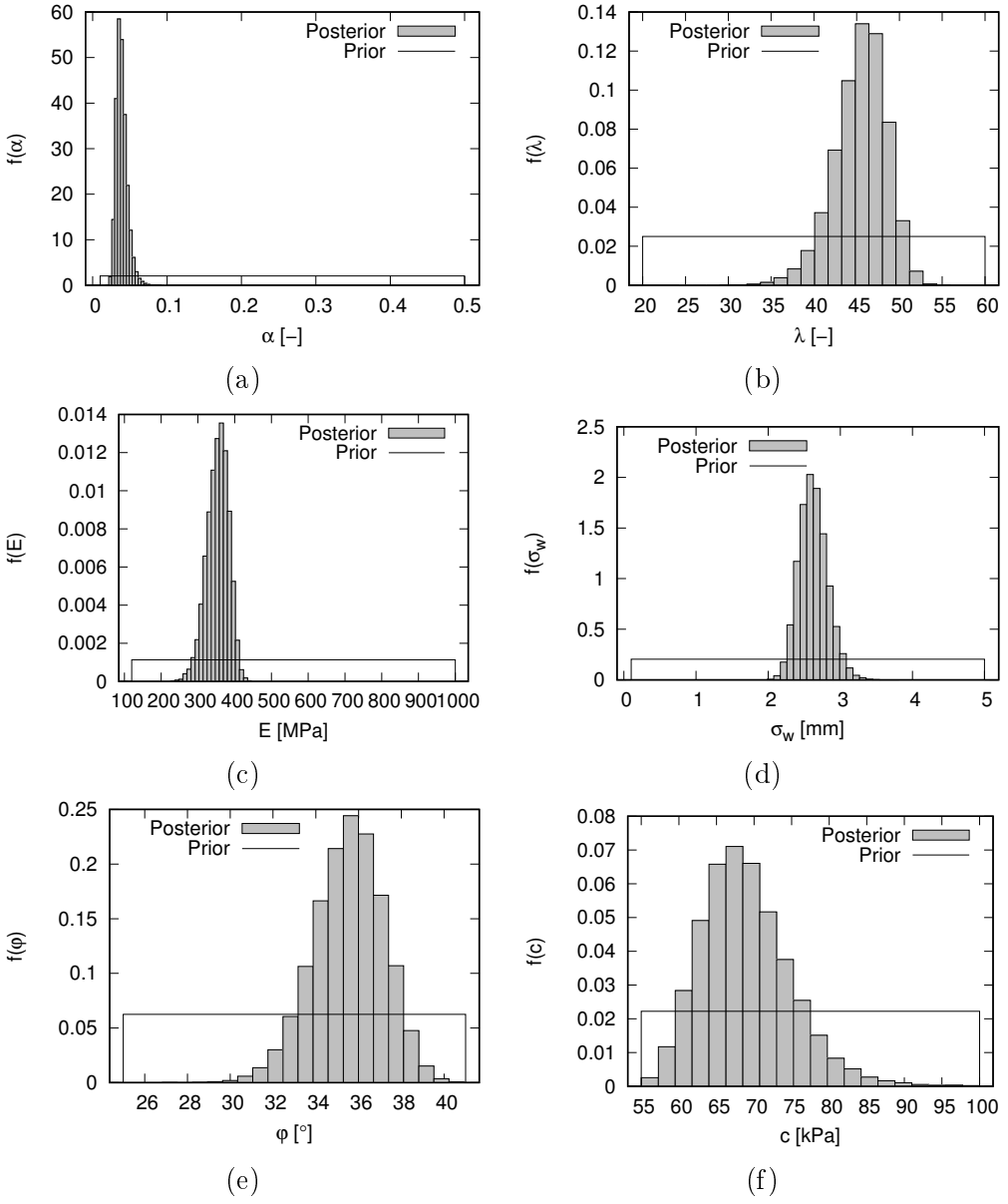

Figure 4.7: Prior and posterior marginal distributions of: a) parameter α, b) parameter λ, c) Young's modulus E, d) standard deviation of displacement error σ_w, e) angle of internal friction φ, f) cohesion c

example from oedometer or triaxial tests. This is perfectly in accord with the Bayesian inference, which allows for combing variety of data to give more freedom to the identification of seemingly unrelated model parameters. Such an approach was successfully employed, e.g. in [49, 50].

It is also evident from Figs. 4.7(e,f) that the initial guess of the soil shear strength

parameters has not been refined as sufficiently. However, realizing the localization of plastic strains seen in Fig. 4.4(c) it can be suggested that other data such as relative horizontal convergence of tunnel lining, not adopted in the present study, would possibly improve the prediction of these two parameters.

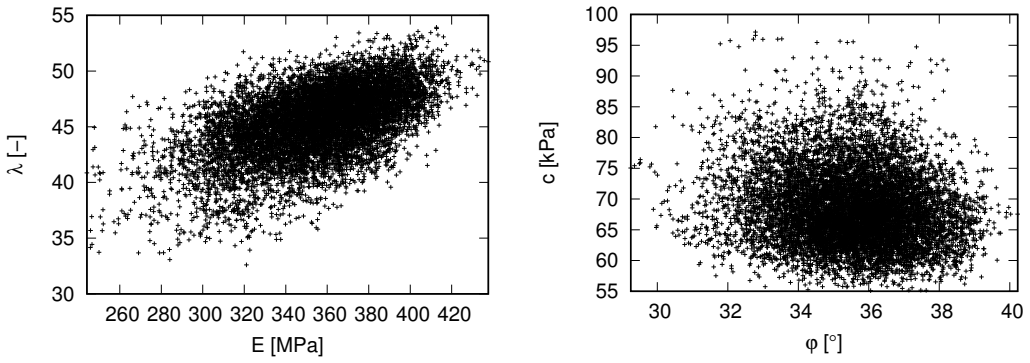

(a) (b)

Figure 4.8: Scatter diagrams: a) $E-\lambda$, b) $\varphi - c$

Nevertheless, the Bayesian updating can still prove useful if the statistical dependence of the model parameters is of interest[8]. While the prior distributions on the right hand side of Eq. (4.20) are assumed statistically independent, the posterior joint probability distribution function (PDF) on the left hand side of Eq. (4.20) allows us to address the mutual correlation of individual model parameters.[9] For illustration we provide in Figs. 4.8 the scatter diagrams of $E-\lambda$ and $\varphi-c$ pairs. Individual points were taken from the posterior Markov chains. Mathematically, the degree of correlation can be judged based on, e.g., the Pearson coefficient of correlation equal to 0.54 and -0.13 for $E-\lambda$ and $\varphi - c$ pairs, respectively.

4.5 Exploiting improved posterior distributions in predicting settlements in other sections to be yet excavated

The general property of the Bayesian updating is to improve the current knowledge of model parameters as the set of measured data is gradually increasing. This idea is examined hereinafter while taking the results generated in the previous section into account.

In particular, the previous analysis resulted in posterior distributions of material parameters E, φ and c found in the cross-section J022 together with the model parameters α, λ and σ_w. Our objective now is to predict the evolution of settlement in a different

[8]Spacial correlation of individual model parameters is not considered as no correlation length enters the stochastic model.

[9]Recall that the joint PDF is represented here in discrete format by Markov chains generated through the updating procedure.

cross-section denoted here as J024. Based on initial geological survey, the principal difference between the two sections is expected in the change of material properties of rock to be excavated.

Table 4.4: Ranges of prior uniform distribution of material parameters used in cross-section J024

Parameter	Units	Minimum	Maximum
E	MPa	40	2000
φ	deg.	22	36
c	kPa	10	50

In this case, the rock is classified as R4 according to the BARAB system, thus less stiff. Since lacking more specific information about this material we start again from a relatively wide range of potential values of the stiffness and strength properties E, c, φ listed in Table 4.4. It would perhaps be reasonable to assume a less severe variability in rock properties between the two sections J022 and J024 than suggested by the design codes and adopt also the posterior distributions of material parameters in Fig. 4.7 as the source of prior knowledge for the settlement prediction. Nevertheless, choosing a simple uniform distribution of these parameters allows us to illustrate more clearly how the Bayesian inference reduces the epistemic uncertainties with increasing amount of observed data.

The other three model parameters $\alpha, \lambda, \sigma_w$ affect the prediction of the soil settlement during tunnel excavation more globally. In this sense it appears reasonable to accept their posterior distributions derived from the original identification step in cross section J022 as the prior distributions in the subsequent analysis[10]. This for example suggests that although larger settlements can be anticipated, based solely on the adopted soil classification, the shape of the settlement curve controlled by the parameter α can be assumed unaffected. We shall comment on this assumption later in this section.

Thus accepting that the shape parameter α, the model parameter λ and the standard deviation of displacement error σ_w have identical distributions in both cross-sections we formulate the following stochastic model for identification/prediction procedure in cross-

[10]Remind that not only the material parameters E, c, φ, but also the remaining model parameters $\alpha, \lambda, \sigma_w$ will still be updated.

section J024[11]

$$
\begin{aligned}
w_{ij} &\sim \mathcal{N}(\overline{w}_{ij}, \sigma_w) \qquad \text{for } i = 1 \dots N_{t,face}, j = 1 \dots N_{depth}, && (4.21)\\
\overline{w}_{ij} &= b_i \overline{w}_j^{fin}, && (4.22)\\
b_i &= \begin{cases} \frac{1}{2}\exp(\alpha d_{s,i}), & \text{if } d_{t,i} < 0, \\ 1 - \frac{1}{2}\exp(-\alpha d_{t,i}), & \text{otherwise,} \end{cases} && (4.23)\\
\overline{w}_j^{fin} &= \tilde{f}_{FEM,j}(E, \varphi, c, \lambda) && (4.24)\\
E &\sim \mathcal{U}(E_{min}, E_{max}), && (4.25)\\
\varphi &\sim \mathcal{U}(\varphi_{min}, \varphi_{max}), && (4.26)\\
c &\sim \mathcal{U}(c_{min}, c_{max}), && (4.27)
\end{aligned}
$$

where the data w_{ij} represent again the i-th measurement of a vertical displacement at the j-th monitoring point now in the cross-section J024. Thus all measured data are exploited albeit only the ultimate settlement needs to be predicted since the shape parameter α is assumed to be well represented by the posterior distribution in Fig. 4.7(a). In this case, the analysis takes into account the data associated with the excavation of top segment only, so that $s = t$ and $N_{t,face} = 1, 2 \dots, 14$ in Eq. (4.21).

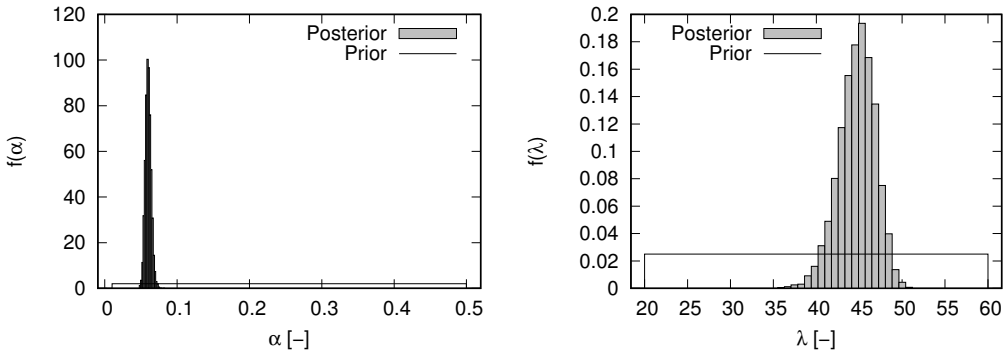

(a) (b)

Figure 4.9: Posterior marginal distributions of: a) parameter α, b) parameter λ employing all measurements collected in section J024

Note first on the state when all data ($N_{t,face} = 14$) collected in section J024 were employed to see in Fig. 4.9 that the distribution of parameter λ remained essentially the same and the parameter α was modified only slightly thus supporting our original assumption. This is because the actual settlement reached, more or less, one-half of its final value when the excavation face arrived at the monitoring section, $d_t = 0$ in Fig. 4.10. This is exactly what is predicted by the present simple format of Eq. (4.3). Clearly, in many real situations this assumption might not be met and more complex representation of the shape of the settlement curve would be required.

[11] Although keeping the same notation as used in the previous sections, all the variables now refer to cross-section J024.

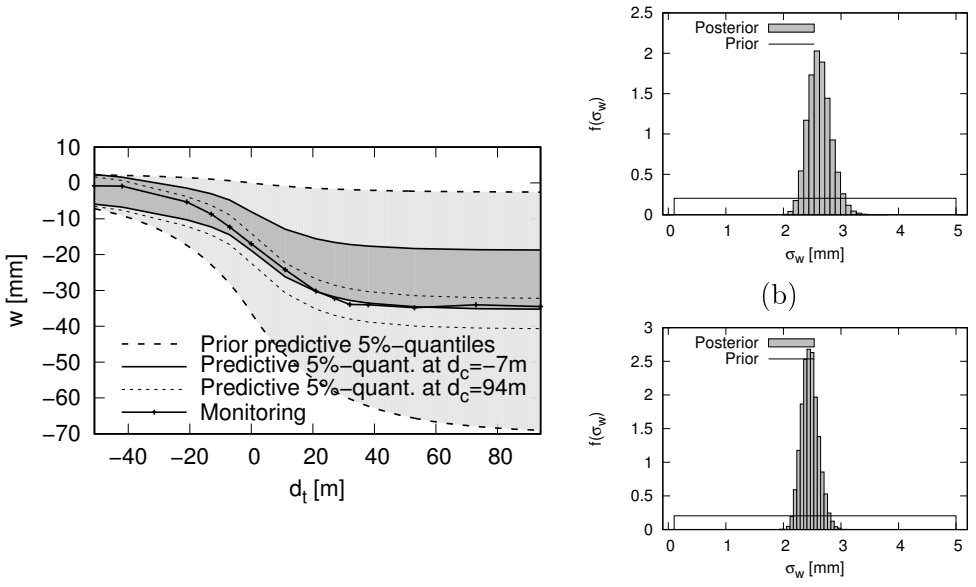

Figure 4.10: a) Evolution of vertical displacement at selected points as a function of tunnel face location, b) standard deviation of displacement error σ_w for $N_{t,face} = 1$, c) standard deviation of displacement error σ_w for $N_{t,face} = 14$

Concentrating next on Fig. 4.10(a) brings us back to our original goal attempting to predict the settlement based on the identification step carried out in section J022. The dashed lines show 5% quantiles of the terrain settlement when no data in section J024 have been collected yet. Similar plots for $d_t = -7$ m and $d_t = 94$ m give the idea, how the knowledge about the model behavior can be improved as more data become available. While for $d_t = -7$ m ($N_{t,face} = 5$) we may still talk about prediction, exploiting all measured data with $N_{t,face} = 14$ for $d_t = 94$ m corresponds essentially to the identification step. It is perhaps worth noting that these plots were obtained such that the theoretically generated values of the settlement given by Eq. (4.22) were adjusted by adding a settlement error randomly generated from normal distribution with zero mean and standard deviation σ_w corresponding to the same sample in the chain. For illustration the distribution of the settlement error σ_w for $N_{t,face} = 1$ (prior distribution) and $N_{t,face} = 14$ (posterior distribution) extracted from 10000 samples in the chain is shown in Figs. 4.10(b,c) to see, how the standard deviation of displacement error changed.

We should still keep in mind the original prior range of material parameters to be narrowed down with the help of the stochastic model, relations (4.22)-(4.27). Apart from identification of the distribution of Young's modulus E our interest is now directed also to the distribution of the theoretical ultimate displacements $\overline{w}_{t,h}^{fin}$. These marginal distributions can be again approximated by the histograms plotted for the samples generated from the joint posterior distribution function $\pi(E, c, \varphi|\langle w_{ij}\rangle)$, recall (4.1). This process can be repeated as the measured data series w_{ij} unfolds and $N_{t,face}$ increases with the

tunnel face advancement. The results are plotted in Figs. 4.11 and 4.12.[12]

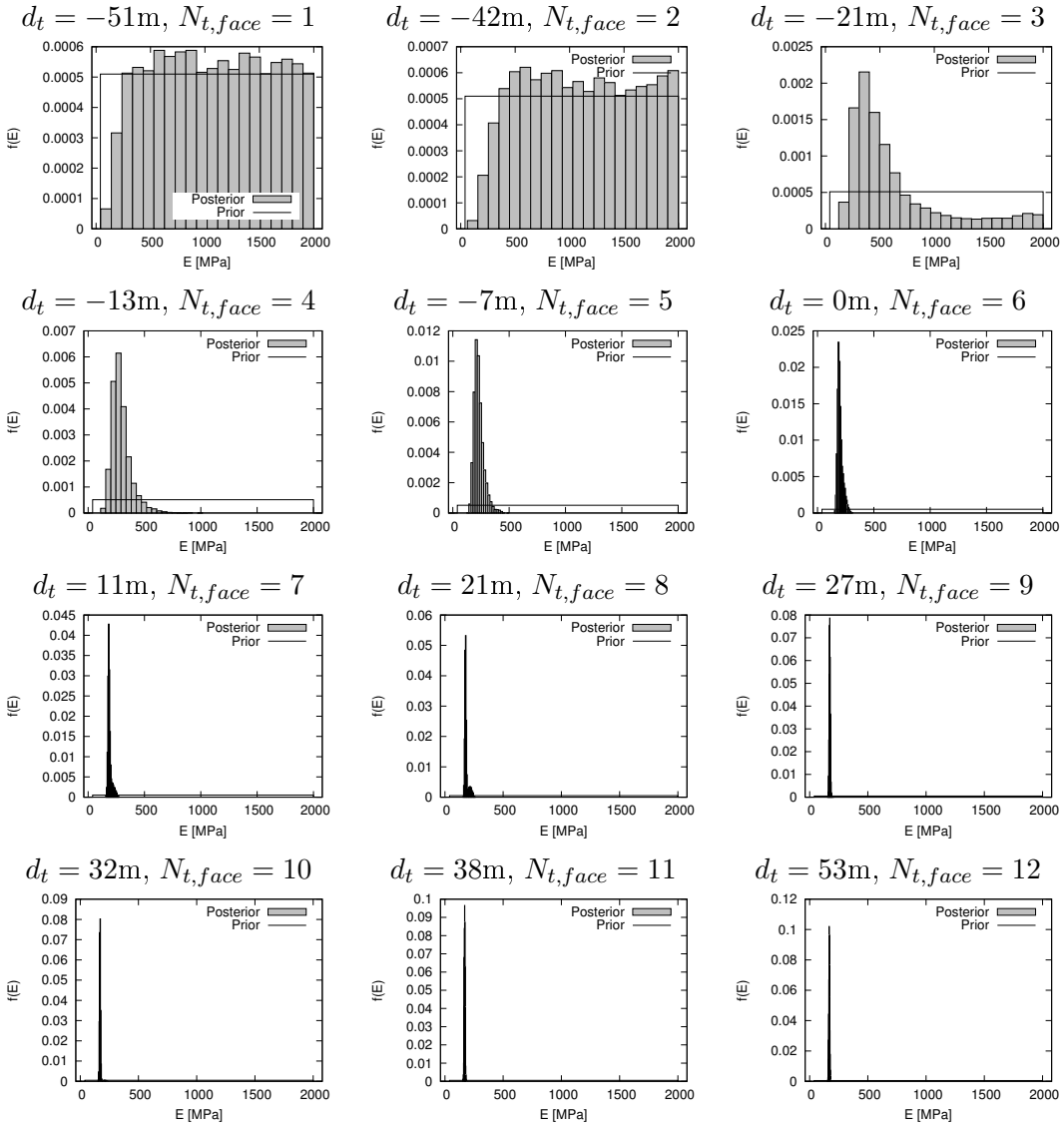

Figure 4.11: Posterior distribution of Young's modulus E in cross-section J024. The sequence of the plots show how the distribution of E evolves as the tunnel face progresses and more data is collected. Individual figures refer to number of sections ($N_{t,face}$) taken into account in the updating process with the location of excavated face (d_t) with respect to the monitored section

Fig. 4.11 shows how our belief in possible values of E evolves from the prior, quite broad, uniform distribution to a relatively narrow posterior distribution, as more mea-

[12]The results for last two sections ($N_{t,face} = 13, 14$) are not shown.

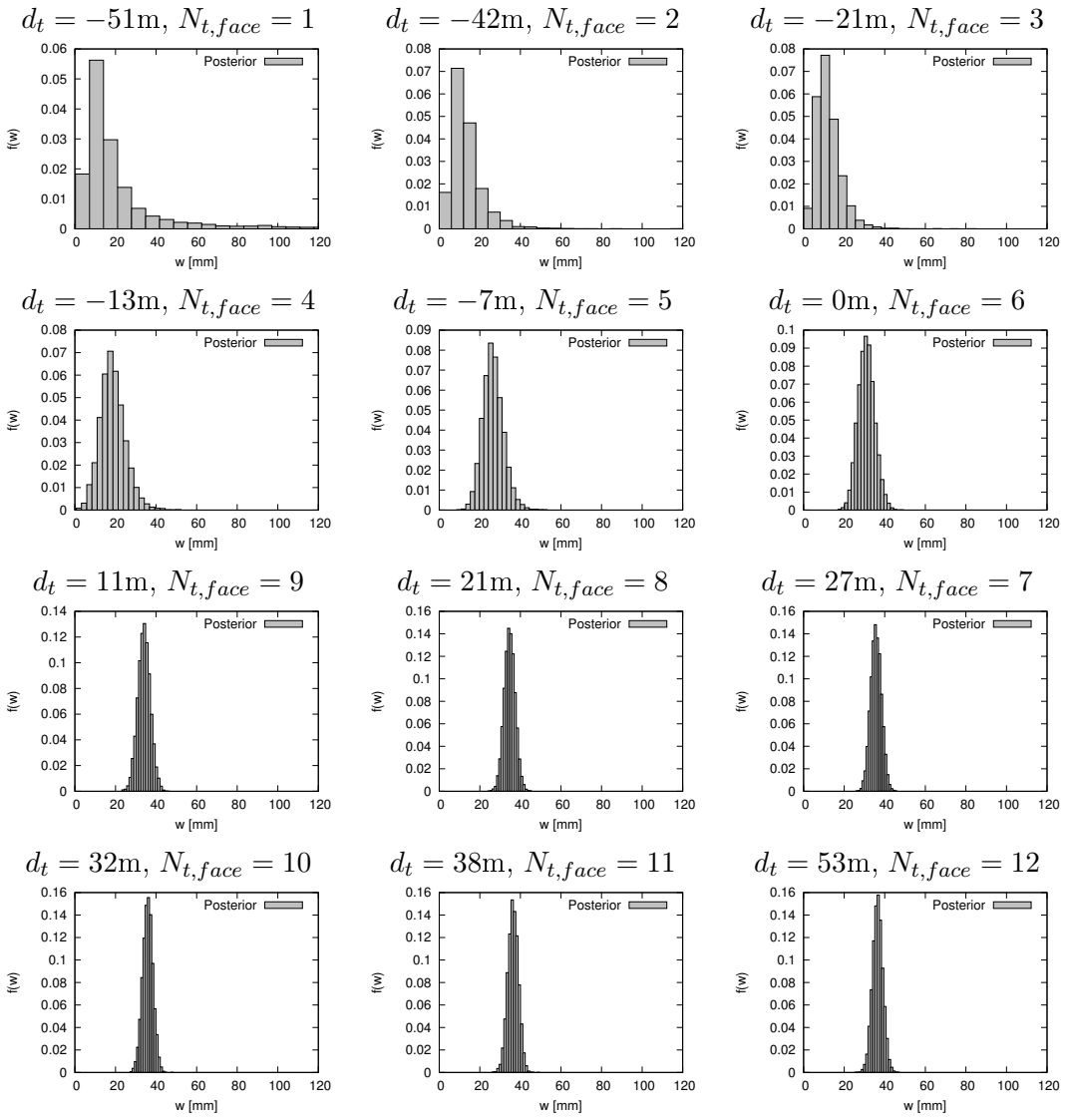

Figure 4.12: Posterior predictive distribution of ultimate terrain settlement $w_{t,0}^{fin}$ in cross-section J024. The sequence of plots show how the distribution evolves as the tunnel face progresses and more data is collected. Individual figures refer to number of sections ($N_{t,face}$) taken into account in the updating process with the location of excavated face (d_t) with respect to the monitored section

surements become available with the tunnel face advancement. In particular, skipping the first two steps ($N_{t,face} = 1, 2$) the MAP estimate of E was reduced quite quickly from 366 MPa for $N_{t,face} = 3$ to 210 MPa for $N_{t,face} = 5$ being already close to its final value of 169 MPa. Similarly, it can be seen from Fig. 4.12 that even a small number of measurements ($N_{t,face} = 3, 4, 5$) can already provide some notion about the predictive final settlement $w_{t,0}^{fin}$, particularly its upper bound found close to 40 mm in the present case. Again, these predictive distributions of ultimate terrain settlement $w_{t,0}^{fin}$ for various locations of the excavation face were constructed from the sampled theoretical values $\overline{w}_{t,0}^{fin}$ adjusted by the standard deviation of displacement error.

Although it is not generally the case, we may take advantage of the available measurements to validate our numerical predictions. It is seen in Fig. 4.10(a) that the measured ultimate settlement taken for $d_t = 94$ m falls within the 5% quantiles even for predictions based on a limited number of measurements collected for $N_{t,face} = 5$. This band is further narrowed down with more data available. Interestingly, when all measurements are reflected in the updating process ($N_{t,face} = 14$), we arrive at the MAP estimate of the predictive ultimate terrain settlement $w_{t,0}^{fin} = 36$ mm that is basically identical to its measured counterpart. Thus if the standard deviation of displacement error, reflecting also the predictive model inaccuracies, is properly accounted for, the present model shows a reasonable predictive capability at least from the engineering point of view.

4.6 Conclusion

In this paper a practical application of the Bayesian statistics to the prediction of settlements evolving during the tunnel excavation was presented.

In particular, two aspects of Bayesian inference were explored. First, this methodology was adopted to refine a prior, rather blurred, knowledge of parameters of the selected computational model. This was achieved by utilizing the already known measurements from the early stages of tunnel excavation, recall Section 4.4. This improved knowledge itself should allow us to improve our predictions of the structure response in sections, which are to be yet excavated. This second stage of analysis fully exploits the principal strength of Bayesian inference, which is the reduction of epistemic uncertainties as more data are collected. The results presented in Section 4.5 strongly support this statement. Remember Figs. 4.11 and 4.12 to point out that not only the knowledge of model parameters, which may change along the tunnel line, but also the numerical prediction of, e.g. the settlements, is improved when the set of measured data in the investigated cross-section grows with each advancement of the tunnel face. In our particular case the amount of data increased from 4 ($N_{t,face} = 1$) measured vertical displacements above the expected tunnel crown up to 56 ($N_{t,face} = 14$) corresponding to situation, when the tunnel face passed the investigated cross-section sufficiently far so no further differential settlements are observed. What, however, is more important is the fact that already a few measurements were sufficient to provide an impression about the structure response, with the tunnel face not reaching the investigated cross-section yet, e.g. $N_{t,face} = 3, 4, 5$.

This in turn may provide sufficient time to propose changes to the original design, and thus reduce the risk and prevent potential failures, providing a sign of this occurs because of the lack of initial knowledge of material data due to, e.g. an insufficient site investigation.

Obviously, similar to all probabilistic analyses, the method has limitations. It has been seen through the results presented in Fig. 4.7 that while due to the model structure some of the parameters are refined substantially (Young's modulus E , shape parameter α, standard deviation of displacement error σ_w), other parameters may be identified less accurately or their prior distribution may remain practically unchanged as was observed for the angle of internal friction φ and cohesion c when analyzing section J024. This is natural because some of the parameters do not influence the type of the observed data and thus the knowledge of the data does not refine their prior distribution. Nevertheless, recall the discussion in Section 4.4.3.2, the predictions obtained by the stochastic model outlined in this paper could have been further improved, if additional data such as the measurements of displacements sideways to the tunnel tube or even data from standard laboratory tests were available. Although several rather strong assumptions were made in the deterministic description of the excavation process, e.g. the longitudinal shape of the settlement trough controlled by a single parameter α only, or the limited number of ad-hoc chosen functions in the surrogate model, the stochastic model still preserve its predictive capability. The impact of the adopted simplifications on the accuracy of predictions is quantified by the model parameter σ_w, which covers not only the measurement error but also the modeling errors. In case of oversimplified deterministic model, the theoretical predicted values of settlement would be substantially different from the observed values rendering the high value of parameter σ_w. The quantification of how the theoretical model comply with observations and taking that into account when making predictions is yet another favorable property of Bayesian inference.

Acknowledgement

The financial support of the project no. TE01020168 provided by TA ČR is gratefully acknowledged. The authors would also like to thank the company SG Geotechnika a.s. for providing us with the monitoring data and the company Pudis a.s. for the empirical prior ranges of the material parameters employed in this study.

Bibliography

[1] D. V. Griffiths, Stability analysis of highly variable soils by elasto-plastic finite element, International Journal for Numerical Methods in Engineering 50 (2001) 2667–2682.

[2] G. A. Fenton, D. V. Griffiths, Probabilistic foundation settlement on spatially random soils, ASCE Journal of Geotechnical and Geoenvironmental Engineering 128 (5) (2002) 381–390.

[3] G. A. Fenton, D. V. Griffiths, A. Urquhart, A slope stability model for spatially random soils, in: Proceedings of the 9th International Conference on Applications of Statistics and Probability in Civil Engineering - ICASP 9, San Francisco, USA, Rotterdam:Millpress, 2003.

[4] S. Gui, R. Zhang, J. P. Turner, X. Xue, Probability slope stability analysis with stochastic soil hydraulic conductivity, Journal of Geotechnical Engineering ASCE 126 (2000) 1–9.

[5] S. D. Koputa, Pore pressure development: Probability analysis, in: P. Spanos (Ed.), Probabilistic Methods in Civil Engineering, ASCE Publication, New York, 2002, pp. 57–60.

[6] D. Mašín, The influence of experimental and sampling uncertainties on the probability of unsatisfactory performance in geotechnical applications, Géotechnique 65 (11) (2015) 897–910.

[7] R. Popescu, G. Deodatis, A. Nobahar, Effects of random heterogeneity of soil properties on bearing capacity, Probabilistic Engineering Mechanics 20 (2005) 324–341.

[8] S. Wang, H. Hao, Effects of random variations of soil properties on site amplification of seismic ground motions, Soil Dynamics and Earthquake Engineering 22 (2002) 551–564.

[9] G. A. Fenton, D. V. Griffiths, Bearing capacity prediction of spatially random c-φ soils, Canadian Geotechnical Journal 40 (1) (2003) 54–65.

[10] R. Suchomel, D. Mašín, Comparison of different probabilistic methods for predicting stability of a slope in spatially variable c-phi soil, Computers and Geotechnics 37 (1-2) (2010) 132–140.

[11] G. Mollon, K. K. Phoon, D. Dias, A.-H. Soubra, Validation of a new 2D failure mechanism for the stability analysis of a pressurized tunnel face in a spatially varying sand, Journal of Engineering Mechanics 137 (1) (2011) 8–21.

[12] R. Mellah, G. Auvinet, F. Masrouri, Stochastic finite element method applied to non-linear analysis of embankments, Probabilistic Engineering Mechanics 15 (3) (2000) 251–259. doi:10.1016/S0266-8920(99)00024-7.

[13] V. R. Greco, Efficiet Monte-Carlo technique for locating critical slip surface, Journal of Geotechnical Engineering ASCE 122 (1996) 517–525.

[14] M. Šejnoha, J. Šejnoha, M. Kalousková, J. Zeman, Stochastic analysis of failure of earth structures, Probabilistic Engineering Mechanics 29 (2) (2007) 206–218.

[15] J. Pruška, Neural networks in back analysis of tunnels, in: V. P. A. Kravcov, E.B. Cherepetskaya (Ed.), Durability of Critical Infrastructure, Monitoring and Testing, Proceedings of the ICDCF 2016, Springer Singapore, 2017, pp. 27–34.

[16] G. Mollon, D. Dias, A.-H. Soubra, Probabilistic analysis of circular tunnels in homogeneous soil using response surface methodology, Journal of Geotechnical and Geoenvironmental Engineering 135 (9) (2009) 1314–1325.

[17] A. Hamrouni, D. Dias, B. Sbartai, Reliability analysis of shallow tunnels using the response surface methodology, Underground space 2 (4) (2017) 246–258.

[18] N. Siu, D. Kelly, Bayesian parameter estimation in probabilistic risk assessment, Reliability Engineering and System Safety 62 (1998) 89–116.

[19] D. Kelly, C. Smith, Bayesian inference in probabilistic risk assessment - The current state of the art, Reliability Engineering and System Safety 94 (2009) 628–643.

[20] A. Cividini, G. Maier, A. Nappi, Parameter estimation of a static geotechnical model using a Bayes' approach, International Journal of Rock Mechanics and Mining Sciences & Geomechanics 20 (5) (1983) 215–226.

[21] H. Wu, R. Gilbert, W. Tang, G. Fenton, Probabilistic Methods in Geotechnical Engineering, in: G. Fenton (Ed.), ASCE GeoLogan'97 Conference, Logan, Utah, 1997.

[22] K. Garbulevski, S. Jabanovski, S. Rabarijoely, Advantage of Bayesian approach to geotechnical designing, Land Reclamation 41 (2) (2009) 83–93.

[23] Y. Wang, Z. Cao, D. Li, Bayesian perspective on geotechnical variability and site characterization, Engineering Geology 203 (25) (2016) 117–125.

[24] Y. Wang, T. Zhao, Bayesian assessment of site-specific performance of geotechnical design charts with unknown model uncertainty, International Journal for Numerical and Analytical Methods in Geomechanics 41 (5) (2017) 781–800.

[25] M. Šejnoha, T. Janda, L. Melzerová, V. Nežerka, J. Šejnoha, Modeling glulams in linear range with parameters updated using Bayesian inference, Engineering Structures 138 (2017) 293–307.

[26] T. Janda, J. Šejnoha, M. Šejnoha, Hierarchical stochastic model of terrain subsidence during tunnel excavation, IOP Conference Series: Materials Science and Engineering 236 (2017).

[27] M. Šejnoha, T. Janda, J. Šejnoha, Tunnel 2D3D: FEM program for modeling tunnel-structure interaction, in: M. Hilar, A. Butovič, I. Škopková, J. Zlámal (Eds.), 13th International Conference on Undeground Construction Prague 2016, JMP Praha, 2016.

[28] K.-H. Cho, M.-K. Choi, S.-W. Nam, I.-M. Lee, Geotechnical parameter estimation in tunnelling using relative convergence measurement, International Journal for Numerical and Analytical Methods in Geomechanics 30 (2) (2006) 137–155.

[29] R. Peck, Advantages and limitations of the observational method in applied soil mechanics, Géotechnique 9 (2) (1969) 171–187.

[30] A. Powderham, The observational method - application through progressive modification, Civil Engineering Practice: Journal of the Boston Society of Civil Engineers Section/ASCE 13 (2) (1998) 87–100.

[31] A. Muir Wood, Tunneling: Management by Design, F& FN Spon, London, 2000.

[32] A. Nossan, Observations on the observational method.

[33] G. Mollon, D. Dias, A.-H. Soubra, Range of the safe retaining pressures of a pressurized tunnel face by a probabilistic approach, Journal of Geotechnical and Geoenvironmental Engineering 139 (11) (2013) 1954–1967.

[34] Q. Pan, D. Dias, Sliced inverse regression-based sparse polynomial chaos expansions for reliability analysis in high dimensions, Reliability Engineering and System Safety 167 (2017) 484–493.

[35] Y. Marzouk, H. Najm, Dimensionality reduction and polynomial chaos acceleration of Bayesian inference in inverse problems, Journal of Computational Physics 228 (6) (2009) 1862–1902.

[36] A. Kučerová, J. Sýkora, B. Rosić, H. Matthies, Acceleration of uncertainty updating in the description of transport processes in heterogeneous materials, Journal of Computational and Applied Mathematics 236 (18) (2012) 4862–4872.

[37] B. Rosić, A. Kučerová, J. Sýkora, O. Pajonk, A. Litvinenko, H. Matthies, Parameter identification in a probabilistic setting, Engineering Structures 50 (2013) 179–196.

[38] M. Panet, A. Guenot, Analysis of convergence behind the face of a tunnel, in: Proc. Tunnelling 82, London, The Institute of Mining & Metallurgy, 1982, pp. 197–204.

[39] S. Kielbassa, H. Duddeck, Strain fields at the tunnelling face - Three-dimensional analysis for two-dimensional technical approach, Rock Mechanics and Rock Engineering 24 (1991) 115–132.

[40] T. Svoboda, D. Mašín, Comparison of displacement field predicted by 2D and 3D finite element modelling of shallow NATM tunnels in clays, Geotechnik 34 (2009) 115–126.

[41] T. Janda, M. Šejnoha, J. Šejnoha, Application of converegence measurements in 2D analysis of tunnel excavation in comparison with Convergence Confinement Method, Tunel 19 (4) (2010) 52–57.

[42] T. Janda, M. Šejnoha, J. Šejnoha, Modeling successive excavation within two dimensional finite element mesh, Acta Geodynamica et Geomaterialia 8 (1) (2011) 69–78.

[43] R. Bernard, T. Mikolášek, A. Rozsypal, Application of the BARAB information system to the monitoring of the Slivenec tunnel excavation, Tunel 16 (4) (2007) 44–50.

[44] Fine-Ltd., Geo5 FEM, Geo5 Tunnel, http://www.fine.cz/, 2017.

[45] T. W. Simpson, J. D. Peplinski, P. N. Koch, J. K. Allen, On the use of statistics in design and the implications for deterministic computer experiments, Tech. rep., in Design Theory and Methodology - DTM'C97 (1997).

[46] X. Yang, X. Guo, H. Ouyang, D. Li, A Kriging Model Based Finite Element Model Updating Method for Damage Detection, Applied Sciences 7 (10) (2017) 1039. doi:10.3390/app7101039.

[47] M. Plummer, JAGS: A Program for Analysis of Bayesian Graphical Models Using Gibbs Sampling (2003).

[48] D. Lunn, D. Spiegelhalter, A. Thomas, N. Best, The BUGS project: Evolution, critique and future directions, Statistics in Medicine 28 (25) (2009) 3049–3067. doi:10.1002/sim.3680.

[49] M. Šejnoha, T. Janda, L. Kucíková, P. Padevět, Combining homogenization, indentation and Bayesian inference in estimating the microfibril angle of spruce, Procedia Engineering 190 (2017) 310–317.

[50] M. Šejnoha, L. Kucíková, J. Vorel, V. Hrbek, J. Němeček, Comparing nano and macroindentation in search for microfibril angle in spruce, Internationl Journal of Computational Methods and Experimental Measurements 5 (2) (2017) 135–143.

Chapter 5

Experimental and numerical investigation of the response of GLT beams exposed to fire

This chapter presents the preprint version of the journal paper

> Kucíková, L.; Janda, T.; Sýkora, J.; Šejnoha, M.; Marseglia, G., Experimental and numerical investigation of the response of GLT beams exposed to fire, Construction and Building Materials. 2021, 299 1-18. ISSN 1879-0526.

reformatted to align with the style of the thesis.

5.1 Abstract

This paper presents a combined experimental and numerical investigation of the behavior of glued laminated timber beams when exposed to fire. The influence on the time variation of charring rates based on the evolution of temperature profiles is examined for different fire scenarios and durations as well as different beam's cross-section sizes. Predictions of charring depths provided by numerical simulations of heat transfer and simplified charring rate models are compared. In the absence of a mass transport representation, a Bayesian inference is introduced to identify the temperature-dependent material parameters for the conventional heat transfer model. A similar approach is adopted when adjusting the selected parameters of the charring rate models to account for variations in actual fire scenarios, which potentially depart from standard fire exposure. When compared to experimental results, both approaches confirmed their predictive capabilities, particularly in the stage of initial design. Since presented in the framework of Bayesian statistics, they open the door to fully stochastic analysis with an emphasis on the load bearing capacity of the studied beams.

5.2 Introduction

Timber in general and glued laminated timber (GLT) beams, in particular, enjoy ever-growing popularity among the designers of building structures. However, since these materials are combustible, it is of engineering interest to examine not only the behavior of timber during fire but also the load-bearing capacity of residual structural elements. While load-bearing capacity is typically addressed with the help of simplified charring rate models, the simulation of the various physical processes taking place in wood during fire is a complex analysis task.

In solid wood, modeling the development of fire under external heat flux is a multi-disciplinary problem which must account for heat transfer by conduction, mass transport through evaporation, phase changes and associated volume and porosity changes, production of volatiles, the influence of internal gas pressure, and the variation of basic material parameters evolving with temperature. Several constitutive models attempting to describe the most relevant pyrolysis processes have been proposed, see e.g. [1, 2, 3, to cite a few]. For an extensive review of the available material models, the interested reader is also referred to [4].

Such complex models are typically adopted when addressing biomass pyrolysis. The major drawback preventing their broader applicability in structural engineering for describing the degradation of solid wood during fire is the relatively large number of input parameters. The second issue, perhaps more relevant, is the fact that structural engineers are mostly concerned with the dimensions of the residual cross-section together with the evolution of temperature therein to predict or estimate the residual strength and stiffness of the remaining solid wood. This is also the main objective of this study, with an emphasis placed on the prediction of the evolution of charring depth. We examine two routes most often for the design of timber structures and to assess their stability and reliability if exposed to a fire on a construction site.

Limiting our attention to GLT beams, we set up the extensive experimental program described in Section 5.3 to provide data for the determination of charring depth:

1. Indirectly from the temperature isotherm representing the char front. Focusing on engineering practice, conventional heat transport models have proven promising for predicting the evolution of temperature in wood exposed to fire. König showed that calibration of temperature-dependent material parameters depends strongly on the loading temperature curve which may prevent the material parameters derived for standard fire exposure [5] from a direct application to natural fires [6]. This was also the case of our study, although we attempted to deliver a unique set of parameters for several loading curves all resembling standard rather than parametric fires. Tuning the model parameters of their non-smooth functional dependence usually calls for computational approaches based on soft computing, often employing a combination of genetic algorithms, simulated annealing, and differential schemes [7, 8, 9, to cite a few]. Bayesian inference is another promising approach gaining popularity in real engineering applications [10, 11, 12]. In the present context, it was employed to calibrate the heat transport model in [13] to model the behavior of

fire insulation panels exposed to fire. The application of both methods is outlined in Section 5.4.

2. From simplified linear charring rate models. This is the most common approach adopted by designers and probably because of this, it has received considerable attention even in the scientific literature. A comprehensive review of these models addressing their predictive capability when applied to both solid wood and GLT structural elements is available in [14, see also the literature cited therein]. The two basic linear models proposed in [15] and [16] for standard fire exposure are revisited here. Apart from testing their performance in light of the presented experimental program, we also offer, with the help of Bayesian inference, a stochastic version in order to illustrate the potential range of some of the parameters of the model for including natural wood variability in structural designs. The theoretical background and a comprehensive statistical evaluation of the selected models are presented in Section 5.5.

The above two approaches are finally compared, and the most essential results are summarized in Section 5.6.

5.3 Experimental program

An extensive experimental program was designed to address the performance of GLT beams exposed to fire. Unlike other experimental investigations, see [17, 18], we limited our attention to fire loading (standard fire exposure) with no mechanical loads beyond for the self-weight of a beam.

Tests were designed to examine the influence of the intensity and duration of a fire together with the size of the structural element on the evolution of temperature profiles and charring depths within beam cross-sections. These measurements allowed us to calibrate the adopted conventional heat transfer model, test the validity of simple charring rate models, and propose potential improvements to the models. While beyond the scope of this paper, the influence of elevated temperature on mechanical properties such as strength and stiffness while exploiting the fire test measurements was also investigated.

All fire tests were conducted at the AdMaS Experimental Centre, Faculty of Civil Engineering, Brno University of Technology, Brno, Czech Republic. A medium-sized furnace with $1.8\times1\times1$ m, inner dimensions, primarily designed to test structural elements made of concrete, was used. Because control over various input parameters, including air ventilation and oxygen content, was not possible using this furnace, we could not guarantee the same temperature curves measured in the furnace as dictated by various standards. The actual evolution of furnace temperature was also influenced by the sequence of individual tests which not always started from a cold furnace state. Note, however, that for the purpose of this study, aimed at formulating and calibrating a simplified heat transport model and modifying common charring rate models, these conditions did not cause any obstacle. All results presented here, whether measured or computationally derived, refer to actually measured temperatures.

Given the dimensions of the furnace, sixteen spruce wood GLT beams with dimensions (Group 1: Samples 1-8) 0.1×0.32×2.38 m and (Group 2: Samples 9-16) 0.16×0.32×2.40 m were tested. Each beam contained eight rows of lamellae connected vertically with melamine-urea-formaldehyde glue and horizontally by finger joints. Each lamella was cut from the part of the stem near the center of a tree and, in some cases, contained pith. Careful inspection of all beams revealed a certain number of knots, cracks (mainly radial), and other discontinuities (e.g. resin pockets). This proved important when preparing the samples for mechanical testing. In light of the residual load-bearing capacity assessment, the positions of individual lamellae within the whole beam were also recorded.

5.3.1 Moisture content and density

All beams were stored in the testing hall sufficiently long enough to reach the ambient relative humidity (i.e. air-dry state).

The moisture content (MC) was examined in-situ before and after the fire test using an Ahlborn Almemo FHA 696 MF capacitive hygrometer with an accuracy of 0.1%, see Table 5.1. This type of hygrometer measures the average moisture content of a surface only up to a depth of 3 cm. The values before the fire test were measured on selected beams (Samples 5-8) in a grid with a total of 26 points. Measurement after the fire test was performed on extinguished beams, cleaned from charcoal, and left to dry at the ambient temperature. The number of points after the test varied from 54 to 75. The relevant results (averages over all measurements within a given sample) appear in Table 5.1.

Table 5.1: Mean MC of beams from surface measurements before and after fire test.

Sample	MC (before) [%]	MC (after) [%]
3-4	-	5.44
5	10.54	-
6	11.05	9.22
7	11.17	9.61
8	10.70	8.81

Samples not subjected to fire exposure were considered to check the measurements. Three groups of spruce prisms (66 in total) with dimensions of 30×30×40 mm were weighed using a Kern ABS analytical balance with an accuracy of ±0.3 mg, their precise dimensions were measured with a caliper, and they were observed as "air-dry". All samples were then dried in a Memmert UFE 400 universal oven at 103°C for 27 hours. The samples were weighed periodically in groups of 5 until the difference between two subsequent measurements became less than 0.02 g in a 2 hour interval, i.e., dry state [19, 20], and the dimensions of each sample were measured again.

Table 5.2: Gravimetric moisture content and density of control samples.

Sample	$\rho_{air-dry}$ [kgm^{-3}]			ρ_{dry} [kgm^{-3}]			MC [%]		
	Mean	StdDev	N	Mean	StdDev	N	Mean	StdDev	N
CT1	416.42	54.67	42	384.39	48.19	20	9.42	0.17	20
CT2	421.67	48.87	20	401.41	36.13	10	9.30	0.09	10
CT3	406.05	28.78	56	389.66	29.02	36	9.34	0.15	36

The gravimetric moisture content was computed as [19]

$$\mathrm{MC} = \frac{m_{wet} - m_{dry}}{m_{dry}} \times 100[\%], \tag{5.1}$$

where m_{wet} [g] and m_{dry} [g] are weights before and after the desiccation, respectively. The results are summarized in Table 5.2 together with the computed air-dry and oven-dry densities.

Comparing the moisture content measurements in Tables 5.1 and 5.2 supports the capacitive hygrometer for estimating the initial moisture content of the tested beams.

5.3.2 Fire test setup

The experiment was arranged to simulate ceiling joists. In each test, two beams were inserted into a box with one open side made of oriented strand boards (OSBs). The boards were protected by an 80 mm thick layer of Isover UNI stone wool insulation. Two layers were used along short edges to protect beam heads at the support section, see Figs. 5.1 and 5.2.

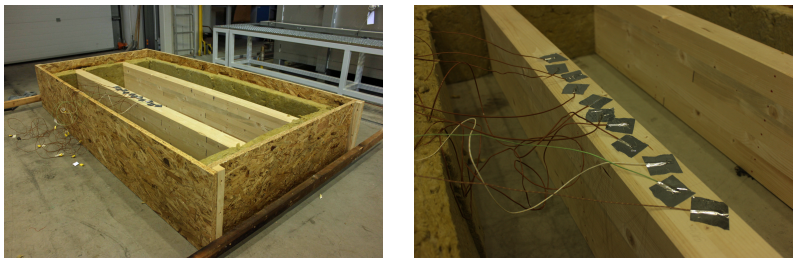

(a) (b)

Figure 5.1: a) Experimental set-up for fire test, b) thermocouples with drilled holes covered by aluminum foil.

In each setup, one beam (even-numbered) was equipped with eleven thermocouples placed in drilled holes located in the mid-span of each beam. Thermocouple locations varied both in depth and position within each beam's cross-section, see Fig. 5.1(b) and Fig. 5.6(b). The openings located on the top of the beams were initially covered with loosely laid stone wool that enabled the beams to burn on all four sides. Unfortunately, the hot air flowing into the holes equipped with thermocouples quite significantly affected

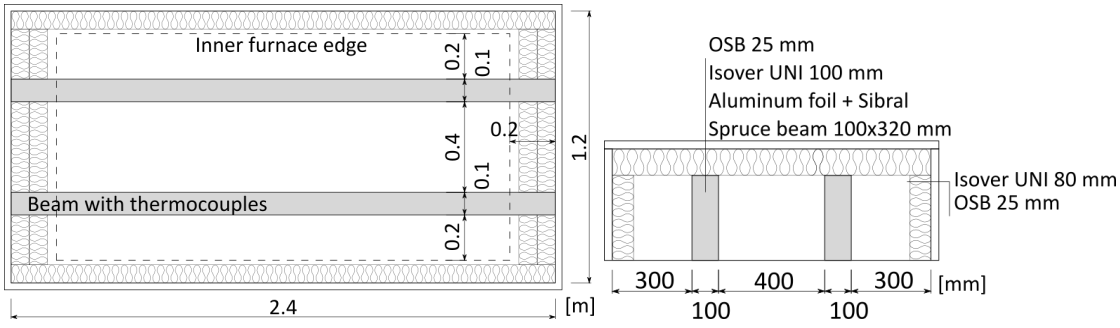

a) Scheme for samples 1-8

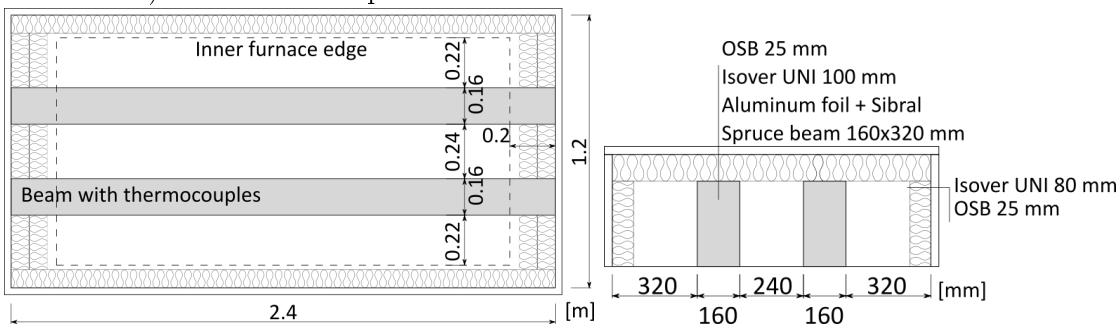

b) Scheme for samples 9-16

Figure 5.2: Experimental set-up for fire test (Th. = thermocouple).

the reliability of the measurements observed as fluctuations in the temperature curves. Therefore, an extra layer of Sibral ceramic blanket was placed directly on top of the openings and secured with nails and aluminum tape to prevent thermocouples from malfunctioning. The whole setup was then centered on the top of the horizontal furnace with the open side down and closed at the top with another layer of insulation wool and an OSB board to prevent the heat from escaping.

5.3.3 Testing procedure

Heat was supplied by two gas burners located at the bottom of the furnace according to the *Set temperature curves*. While the first loading curve was set to follow the temperature curve specified by ČSN EN 1363-1 (Samples 1-4 and 9-16), the second temperature curve assumed the same initial stage but was set constant when reaching 600°C (Samples 5-8). The set temperature curves are plotted as black solid lines in Fig. 5.3. The gas burners were controlled via a thermocouple placed near the bottom of the furnace, at approximately the same level as burners. Henceforth, the corresponding temperatures are referred to as *Furnace temperature curves*.

It is evident from Fig. 5.3 that none of the measured furnace temperature curves copy the set temperature curves entirely. In all cases, the furnace temperature curves exceed the set temperature curves already at an early stage. Considering a constant 600°C curve, Fig. 5.3(b), both furnace temperature curves were ever increasing functions

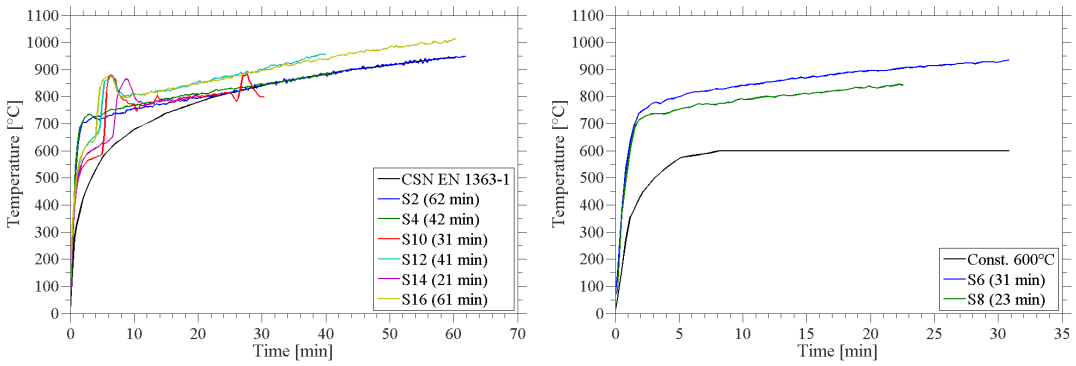

(a) (b)

Figure 5.3: Set and furnace temperature curves: a) ČSN EN 1363-1 temperature curve, b) temperature curve set constant at 600°C.

running significantly above the set temperature curve. These curves even exceeded the furnace temperature curves associated with the ČSN EN 1363-1 setting. As already suggested, this can be attributed to the heat already accumulated in the furnace since the second test was carried out a short time after terminating the first test, and not from a cold furnace state.

Considering the ČSN EN 1363-1 curve, all furnace temperature curves experienced a steeper initial stage when compared to the set temperature curve. While those starting from the cold state (curves 2, 4, 10, and 14) approached the set temperature curve after some time, the two curves corresponding to the hot initial state (curves 12 and 16) continued to run above the set temperature curve although not as significantly as observed for the 600°C curve. Also, the furnace temperature curves from Group 2 (Samples 10-16) showed slightly different shapes than those in Group 1 (Samples 2 and 4) with pronounced peaks occurring at about 5 min.

Only temperature and time were measured during the experiments. Air from outdoors was supplied through vents at the bottom of the furnace, resulting in changing over-pressure and under-pressure in the chamber. Quantities such as oxygen content, air supply, the pressure inside the furnace chamber, heat, and so on, which can affect the charring rate [21, 22, 23], could neither be measured nor controlled with this experimental set-up.

To address the evolution of charring depth in the early stage of a fire, a standard 60 min fire duration was accompanied by three other tests for both groups terminating at 40 min, 30 min, and 20 min, respectively. When the test ended, the entire box with the samples was removed from the furnace and the beams were extinguished with water, see Fig. 5.4. This process took about 5 to 10 minutes. Next, fully extinguished beams were taken out of the OSB box, the charcoal layer was cleaned away mechanically, and each beam was left to dry at the ambient temperature.

Most of the beams, as seen in Table 5.4, were cut lengthwise into ten (Group 1) and eleven (Group 2) pieces, respectively. The letter R in Fig. 5.5 (red for Group 1 and blue

(a) (b)

Figure 5.4: Fire test termination: a) removing samples, b) extinguishing samples.

for Group 2) marks each cut considered for image analysis used to estimate the evolution of charring rate. Each section was documented using a Canon EOS 600D DSLR camera held by hand. Effort was made to eliminate image distortion as much as possible. These images were then edited and scaled, see Fig. 5.9.

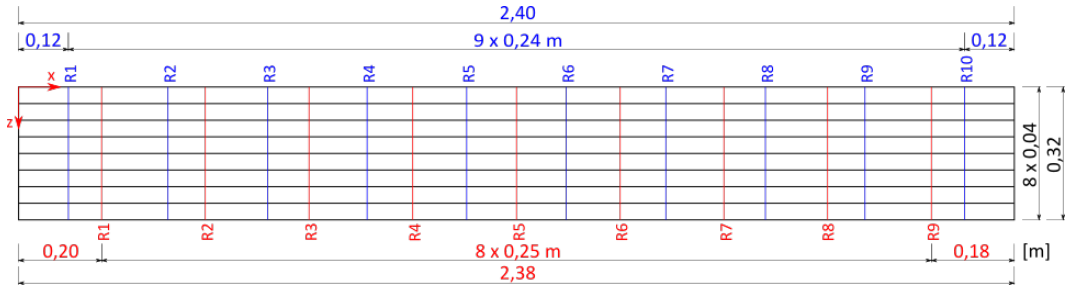

Figure 5.5: Scheme of cuts (R) for image analysis (red = Group 1, blue = Group 2).

Results are presented in the next two subsections starting with the measured temperature curves, which allowed us to indirectly track the evolution of charring depth. Direct measurements of charring depths at the end of the test are presented next. Both types of measurements were further employed when examining the selected charring depth numerically.

5.3.4 Measured temperature curves

The main output of the fire tests were temperature curves describing the evolution of temperature over time in all measured points. Temperature fluctuations, indicating damage to the thermocouples or other inaccuracies, were excluded. Therefore, some curves are shorter than others, as seen in the temperature curves for Samples 2 and 4 (Group 1) not protected by the ceramic blanket, and Samples 12 and 14 (Group 2), where the ceramic blanket failed to protect the thermocouples.

Plateaus at about 100°C indicating water evaporation [21] were observed in all cases, see Fig. 5.6 for illustration. This reflects the amount of energy required for evaporation,

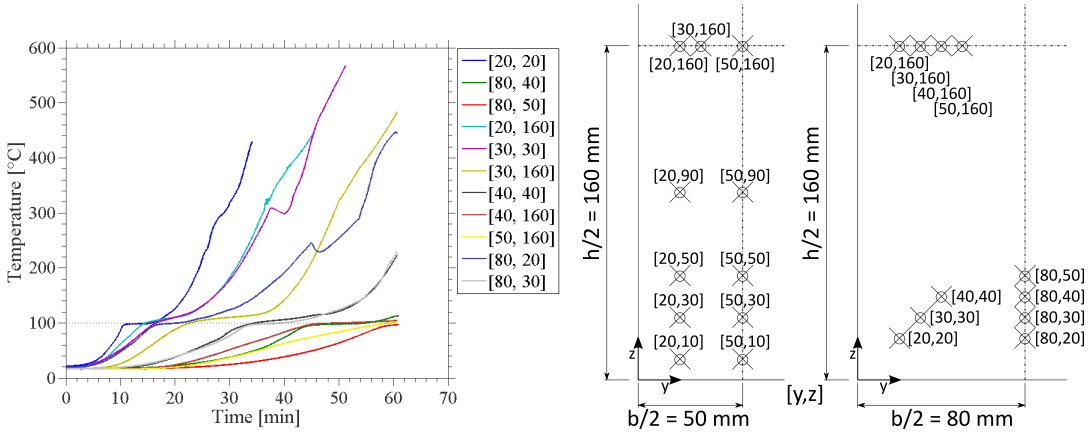

(a) (b)

Figure 5.6: a) Temperature curves recorded for Sample 16 (duration 60 min, cross section 0.16×0.32 m), b) positions of thermocouples within both cross sections (Groups 1 and 2).

with less energy available for heating of the material and pyrolysis, and also implying that as moisture content increases, the charring rate decreases [21, 22]. The plateaus correlated well with the distance from the surface with shorter plateaus corresponding to thermocouples near the surface. This was also observed by Schaffer [24], who described the proportionality of plateaus ('dwell time'), occurring at 93-138°C, with equilibrium moisture content and exposure temperature. At positions near the center of the beam, the evaporation temperature was not even reached, especially for shorter tests. Temperature exceeding 100°C in the whole cross-section was observed only in samples subjected to the test lasting one hour.

As evident from Fig. 5.7(a), plotting all temperature curves for the same point within a cross-section provides a very similar course with no pronounced deviations. Figure 5.7(b) compares curves for the two groups (Group 1: cross-section of 0.1×0.32 m; Group 2: cross-section of 0.16×0.32 m) measured at a point located horizontally in the middle but at the same height z=30 mm. Point out that the slopes for Group 1 are notably steeper when compared to Group 2, which indicates two-dimensional heat flow.

5.3.5 Measured charring depth

Charring depth d_{char} is a parameter entering most of simple charring rate models. It can be determined either indirectly from the evolving temperature profile or directly from images of residual cross-sections. These two approaches are discussed and compared below.

The base of char layer (i.e. char-line) is mostly assumed to be at 300°C [15] or 288°C (550°F) [16, 25] isotherm, respectively. In some studies, this is defined differently. Mikkola [26], for example, defined the char front at 360°C or Lange et al. [18] at 270°C.

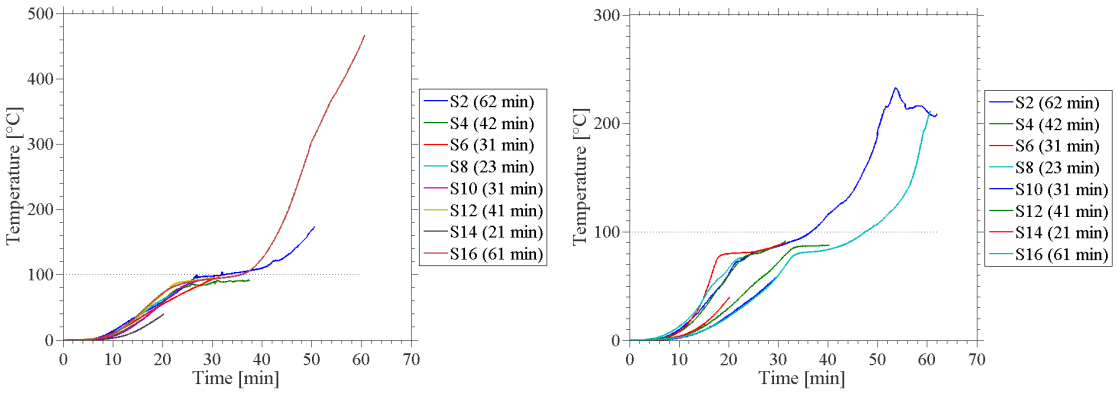

Figure 5.7: Comparison of temperature curves for one point in cross-section: a) position y=30 mm, z=160 mm, b) position y=middle (Group 1: y=50 mm, Samples 2, 4, 6, 8; Group 2: y=80 mm, Samples 10, 12, 14, 16), z=30 mm.

In [27] the authors identified the charring depth with the mass loss of samples as

$$d_{char} = 1.36 \times (\text{mass loss}) + 3.242. \tag{5.2}$$

In this study, we considered two char-line temperatures for the sake of comparison, namely 280°C and 300°C isotherms. The time needed for the selected two temperature isotherms to arrive at a given location with the smaller coordinate representing the charring depth is presented in Table 5.3 for every temperature curve having a known distance from the initial surface.

According to Eurocode 5 [15] these two parameters are sufficient for defining the most simple charring rate model in the form

$$d_{char} = \beta t, \tag{5.3}$$

where β is the charring rate (the basic characteristic of wood burning) and t is the time of exposure to fire. We bring this formula to the reader's attention just for the sake of illustration.

Variability of β, both in terms of thermocouple location (coordinates [y, z]) and time, provided by Eq. (5.3) is evident from the values listed in Table 5.3 and graphical representation in Fig. 5.8. Therein, the values lower than 0.4 mm/min, mainly at a depth of 10 mm from the surface, correspond to a vertical charring rate. An initial low charring rate can be attributed to a slowing down of the heat flow due to evaporation. Values larger than 0.8 mm/min were obtained for thermocouples located in the corner, which is reasonable, because in these locations heat flowed from both sides.

Direct measurement of the charring depth typically involves images of the residual cross-section shown in Fig. 5.9 for selected samples from Group 1. These images were edited, scaled and inserted into a rectangle representing the original cross-section. The

Table 5.3: Charring rate determined indirectly for 280°C and 300°C isotherms.

Sample	[y, z] [mm]	$t_{280°C}$ [min]	$t_{300°C}$ [min]	d_{char} [mm]	$\beta_{280°C}$ [mm/min]	$\beta_{300°C}$ [mm/min]
2	[20, 90]	34.08	35.84	20	0.59	0.56
2	[20, 30]	30.24	31.04	20	0.66	0.64
2	[20, 10]	22.81	24.87	10	0.44	0.40
2	[50, 10]	32.08	34.08	10	0.31	0.29
4	[20, 10]	34.01	35.93	10	0.29	0.28
4	[50, 10]	34.08	35.12	10	0.29	0.28
4	[20, 30]	25.53	26.47	20	0.78	0.76
6	[20, 30]	29.04	29.99	20	0.69	0.67
8	[20, 10]	21.32	-	10	0.47	-
12	[20, 20]	20.35	20.93	20	0.98	0.96
16	[20, 20]	27.37	29.02	20	0.73	0.69
16	[20, 160]	35.25	36.13	20	0.57	0.55
16	[30, 30]	36.22	37.10	30	0.83	0.81
16	[30, 160]	48.27	49.13	30	0.62	0.61
16	[80, 20]	52.77	54.07	20	0.38	0.37

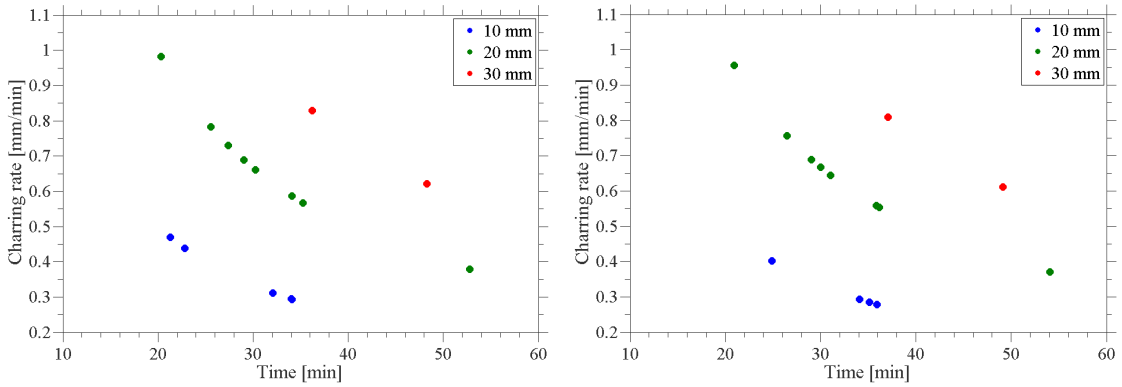

Figure 5.8: Charring rates determined indirectly for 280°C and 300°C isotherms at various depths (all samples together): a) char-line at T = 280°C , b) char-line at T = 300°C.

lines corresponding to the edges of individual lamellae, also evident in Fig. 5.9, helped in centering the images more accurately.

Images in Fig. 5.9 show rounding of corners, a generally accepted phenomenon, also implemented in Eurocode 5 [15]. To avoid these rounded parts, only the four innermost lamellae were considered when measuring charring depth as the distance from the edge of the original cross-section (black rectangle) to the first black pixel. For each image, recall Fig. 5.5, we collected 66 measurements starting 80 mm from the top and bottom of

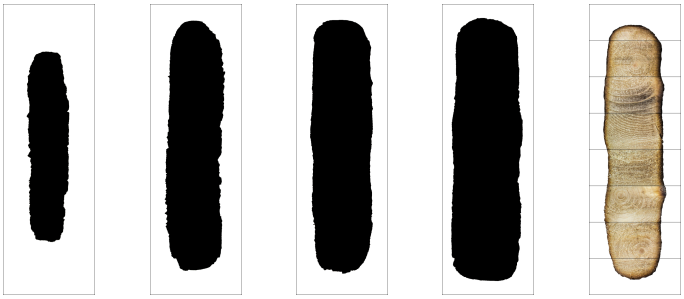

(a) (b) (c) (d) (e)

Figure 5.9: Images of residual cross-sections taken from center of a beam after fire tests lasting: a) 62 min (S2), b) 42 min (S4), c,e) 31 min (S5), d) 23 min (S7).

Table 5.4: Charring rates determined directly using image analysis

Sample	t [min]	d_{char} [mm]	β [mm/min]
1	62.32	30.95	0.50
2	62.32	28.98	0.46
3	42.15	20.90	0.50
4	42.15	20.05	0.48
5	31.40	17.86	0.57
6	31.40	17.93	0.57
7	22.90	13.76	0.60
8	22.90	13.58	0.59
10	30.82	15.79	0.51
12	40.70	21.82	0.54
14	20.55	8.42	0.41
16	60.95	33.70	0.55

the original cross-section. The mean values of charring depth for individual samples are listed in Table 5.4 together with fire duration times. The associated charring rates were obtained again from Eq. (5.3). Figure 5.10 combines all the results presented in Fig. 5.8 and Table 5.4.

On average, the values of β obtained from direct measurement of d_{char} did not exceed the value of $\beta_0 = 0.65$ mm/min for one-dimensional charring recommended by EN 1995-1-2 [15]-Table 3.1. On the other hand, the values resulting from the application of temperature isotherms show a quite significant dependence on a number of factors such as the high initial heat flux; one- vs. two-dimensional heat flow given by the location of thermocouples and the duration of a fire where, especially at the onset of burning, mass transport plays a major role. Nevertheless, the values of β, firmly corresponding to one-dimensional heat flow, fall below the standard value as seen in Tables 5.3 and 5.4.

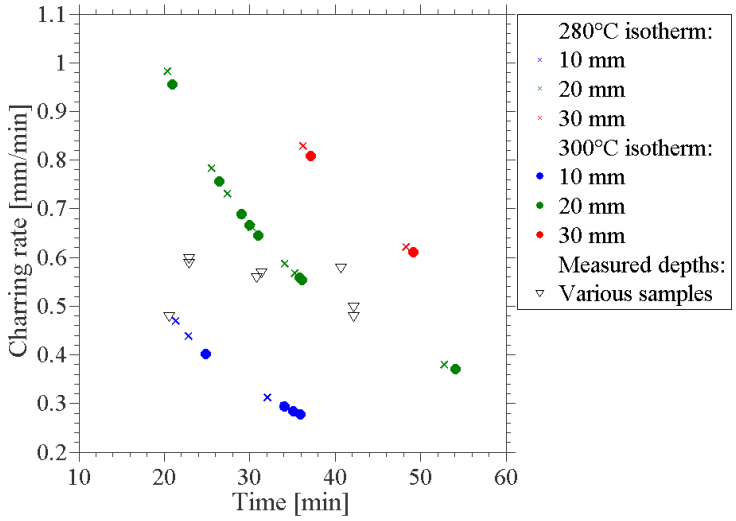

Figure 5.10: Comparison of charring rates determined indirectly for 280°C and 300°C isotherms and those determined directly from measured char depth.

Inspired by mechanical tests and in support of the presented measurements we mention one additional indirect method for estimating the charring depth. Because we take into account an entire residual cross-section, the results associate with 2D charring rate models and can be used to deliver directly the notional charring rate β_n [mm/min]. In this context, an irregular cross-section in Fig. 5.9 is first replaced by an equivalent rectangle $b_{fi} \times h_{fi}$ with a reduced width b_{fi} [mm] and height h_{fi} [mm] such that

$$b_{fi} = b - 2d_{char}, \qquad h_{fi} = h - 2d_{char}, \tag{5.4}$$

where b, h are their original counterparts. Following the idea promoted in [18], charring depth d_{char} can be now calculated by comparing, e.g. the second moment of area for an equivalent rectangle

$$I_{fi} = \frac{b_{fi} h_{fi}^3}{12}, \tag{5.5}$$

and one corresponding to the actual residual cross-section obtained using a suitable graphical software.

To directly account for the zero-strength layer d_0 [mm] and to avoid choosing a particular value, e.g., $d_0 = 7$ mm as recommended in EN 1995-1-2 [15], the results of a three point bending test (3PB) [28, 29] may be employed to estimate an effective charring depth d_{eff}. To illustrate this, Fig. 5.11(a) plots the load-displacement curves for the Group 1 beams.

Assuming an elastic response, the maximum deflection w_{max} measured at the mid span of a beam relates to the beam span $L = 2200$ [mm], the Young modulus E [GPa],

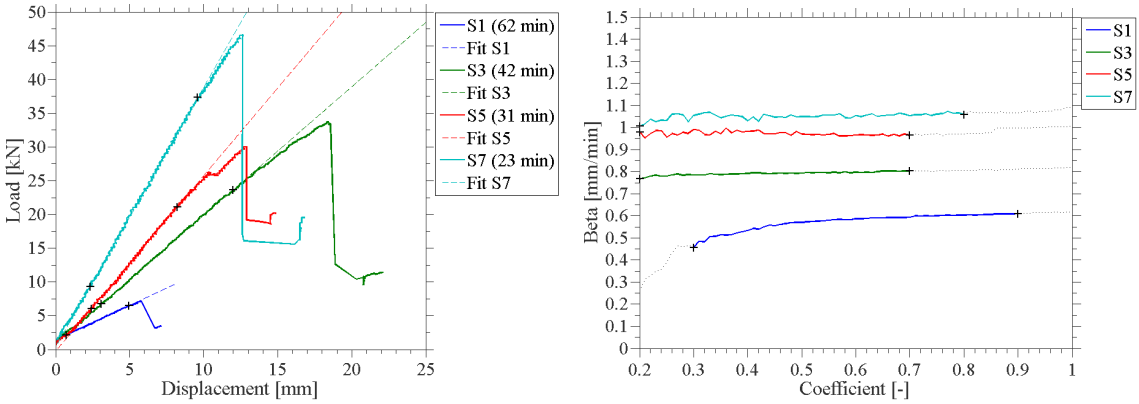

(a) (b)

Figure 5.11: a) Load–displacement curves from 3PB test (Group 1 beams subjected to fire prior to mechanical testing), b) effective charring rates given by Eq. (5.3) with $d_{char} = d_{eff}$.

the applied force F [kN], and the reduced second moment of area I_{fi} [mm^4] as

$$w_{max} = \frac{FL^3}{48EI_{fi}} = \frac{1}{(b - d_{eff})(h - d_{eff})^3} \frac{FL^3}{4E}. \tag{5.6}$$

The Young modulus was determined from a series of tensile tests performed on dog bone specimens extracted from burned samples. Only non-brown specimens free of any defects were considered to get the mean value of E equal to 10.18 GPa [30].

To obtain the effective charring depth d_{eff} from Eq. (5.6), several pairs of (F^i, w^i_{max}) were taken from the interval of $0.2F_{max}$ to $(0.7\text{-}0.9)F_{max}$ depending on the linear range of the load displacement-curve (crosses in Fig. 5.11(a)). The value of d^i_{eff} was then introduced in Eq. (5.3) assuming $d^i_{char} = d_{eff}$ to get the corresponding effective charring rate β^i_{eff}. The results are plotted in Fig. 5.11(b) with abscissa representing the ratio of F_{max}.

Although not fully compatible, we list in Table 5.5 the values of d_0 to give the value of $d_{eff} = d_{im} + d_0$ identical to that obtained from Eq. (5.6). Recall that d_{im} corresponds to the 1D image analysis summarized in the 3rd column of Table 5.4. The values of d_{eff} in Table 5.5 were calculated for the maximum force fraction considered in Fig. 5.11(b).

Note that a more rigorous application of d_0 in 2D charring rate models would require deriving the notional charring depth, e.g., from 2D image analysis as in [18]. In any case, it is interesting to see that for the fire lasting one hour the value of β^{7mm}_{im} is quite close to β_{eff} provided by 3PB, thus supporting the value of $d_0 = 7$ mm [15], while for shorter fires the value of $d_0 = 7$ mm appears nonconservative, which supports observations in [31]. Nevertheless, the higher values of d_0 stored in Table 5.5 are still within the range of values reported in the literature [18, 28]. This final comparison thus promotes measurements from 1D image analysis to be further used in Section 5.5.

Table 5.5: Effective charring rate from bending test.

Sample	t_{fi} [min]	d_{im} [mm]	d_{eff} [mm]	d_0 [mm]	β_{im} [mm/min]	β_{im}^{7mm} [mm/min]	β_{eff} [mm/min]
1	62.32	30.95	38.14	7.20	0.50	0.61	0.58
3	42.15	20.90	34.05	13.15	0.50	0.66	0.80
5	31.40	17.86	30.53	12.67	0.57	0.79	0.98
7	22.90	13.76	24.57	10.81	0.60	0.91	1.07

$d_{im} \equiv d_{char}$ from 1D image analysis; $d_0 = d_{eff} - d_{im}$, β_{im}^{7mm} for $d_{eff} = d_{im} + 7$ mm

5.4 Charring depth from numerical simulation of heat transport

As suggested in Section 5.3.5, one of the options for determining the charring depth is associating it with a specific isotherm representing the char front. This, in turn, calls for a reliable forward model predicting the evolution of temperature in the domain of interest. If this is the only objective a detailed description of wood pyrolysis becomes impractical because the conventional heat transfer model with temperature adjusted parameters has proven sufficiently accurate [5, 6, 13]. Such a model, in general, grounds on the heat balance equation written as

$$\rho(\theta)c(\theta)\frac{\partial\theta}{\partial t}(\mathbf{x},t) = \nabla(\lambda(\theta)\nabla\theta(\mathbf{x},t)) = 0, \quad \mathbf{x},t \in D \times (0,t_s)\,, \tag{5.7}$$

where $\theta\,[°\mathrm{C}]$ is the temperature inside the open bounded domain $D \subseteq \mathbb{R}^3$, $\rho\,[\mathrm{kgm}^{-3}]$ is the volumetric mass density, $c\,[\mathrm{JKg}^{-1}\mathrm{K}^{-1}]$ is the specific heat capacity, $\lambda\,[\mathrm{Wm}^{-1}\mathrm{K}^{-1}]$ is the thermal conductivity, and $t_s\,[\mathrm{s}]$ is the final time of the simulation. The strong formulation requires supplementing the balance equation with boundary conditions. In general, the Dirichlet, Neumann and Robin boundary conditions specified along the boundary $\partial D = \partial D_\theta \cup \partial D_q \cup \partial D_r$ read

$$\theta(\mathbf{x},t) = \theta_0(t), \quad \mathbf{x} \in \partial D_\theta, \tag{5.8}$$

$$\lambda\frac{\partial\theta}{\partial n}(\mathbf{x},t) = q_n(\mathbf{x},t), \quad \mathbf{x} \in \partial D_q, \tag{5.9}$$

$$\lambda\frac{\partial\theta}{\partial n}(\mathbf{x},t) = \alpha(\theta(\mathbf{x},t) - \theta_\infty(\mathbf{x},t)) + e\sigma(\theta^4(\mathbf{x},t) - \theta_\infty^4(\mathbf{x},t)),\ \mathbf{x} \in \partial D_r, \tag{5.10}$$

where θ_0 is the temperature prescribed on D_θ, $q_n\,[\mathrm{Wm}^{-2}]$ is the prescribed heat flux in the direction n normal to D_q, and θ_∞ is the ambient temperature. The radiation condition (5.10) specified on ∂D_r introduces three environmental parameters α, e, σ, where $\alpha\ [\mathrm{Wm}^{-2}\mathrm{K}^{-1}]$ is the heat transfer coefficient, $e\,[-]$ is the emissivity of the surface, and $\sigma\,[\mathrm{Wm}^{-2}\mathrm{K}^{-4}]$ is the Stefan-Boltzmann constant.

The finite element method (FEM) limited for simplicity to the one-dimensional (1D) analysis was used to solve Eq. (5.7) employing the radiation condition (5.10) on both ends of the 1D domain specified by the width of the cross-section of the beams tested.

To this end, Eq. (5.7) was first discretized in time using the midpoint integration rule and then introduced in the weak form, which upon discretization in space provided the final system of nonlinear algebraic equations solved incrementally with the help of the Newton-Raphson iterative procedure.

Both one-dimensional and two-dimensional (2D) versions of Eq. (5.7) were implemented into our in-house Matlab finite element code. While the 2D version was expected to describe the evolution of the char front within an entire cross-section, the 1D variant was adopted in the time-consuming calibration procedure presented next in Sections 5.4.1 and 5.4.2. To compare and verify both implementations, 2D analysis assumed the domain discretization into a narrow band of 3-node triangular elements with element edges equal on average to 0.8 mm. This resulted in 258 and 412 degrees of freedom for cross-sections 100 mm and 160 mm wide, respectively. Simple 2-node rod elements were considered next with the element size of 2 mm to yield 51 and 81 degrees of freedom for the two cross-sections. The time increment was set to 1 s for all temperature curves. This degree of complexity was found optimal from both the computational time and accuracy points of view, providing essentially the same response for both implementations.

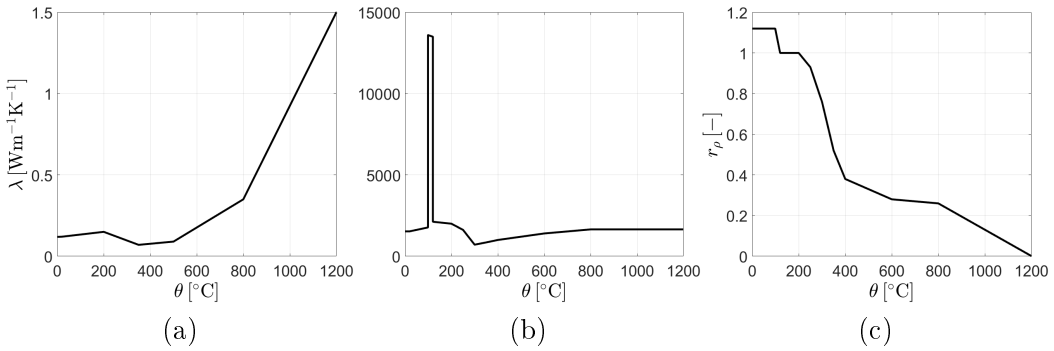

Figure 5.12: Eurocode EN 1995–1–2: Temperature dependent (a) thermal conductivity, (b) specific heat capacity, (c) density ratio.

For Equations (5.7)-(5.10) to simulate the process of pyrolysis, the literature offers several relations stating the functional dependence of model parameters on temperature, see e.g. [4] for a comprehensive list. Here, we built upon the relations presented in Eurocode EN 1995–1–2 [15]. The actual curves describing the evolution of thermal transport coefficients under fire conditions are shown in Fig. 5.12. Since computational results obtained with these specific representations did not satisfactorily match our experimental data, we decided to parametrize them following [13].

To that end, 13 variables in total were introduced to parametrize the temperature-dependent relations of parameters in the model, see Table 5.6. The specific heat capacity and mass density were considered to be a multiplication of a constant value and a dimensionless function defining the functional dependency on temperature as

$$\rho(\theta) = \rho_{\text{in}} r_\rho(\theta), \qquad c(\theta) = c_{\text{in}} r_c(\theta), \tag{5.11}$$

Table 5.6: Definition of ξ-parameters introduced into temperature-dependent relations of thermal properties.

Symbol	Description	Range	Unit
ξ_1		$[100, 300]$	$[°C]$
ξ_2		$[301, 500]$	$[°C]$
ξ_3		$[501, 700]$	$[°C]$
ξ_4	$[\lambda(0), \lambda(\xi_1)]$	$[0.01, 0.4]$	$[\mathrm{Wm^{-1}K^{-1}}]$
ξ_5	$[\lambda(\xi_2), \lambda(\xi_3)]$	$[0.01, 0.4]$	$[\mathrm{Wm^{-1}K^{-1}}]$
ξ_6	$\lambda(1200°C)$	$[0.1, 1.5]$	$[\mathrm{Wm^{-1}K^{-1}}]$
ξ_7	$r_c(\xi_1)$	$[1, 100]$	$[-]$
ξ_8	$r_c(\xi_1 - \xi_8) = 1$	$[10, 90]$	$[°C]$
ξ_9	$r_c(\xi_1 + \xi_9) = 1$	$[10, 90]$	$[°C]$
ξ_{10}	$r_\rho(\xi_2) = 1 - \xi_{10}$	$[0.01, 0.25]$	$[-]$
ξ_{11}	$r_\rho(\xi_3) = 1 - \xi_{10} - \xi_{11}$	$[0.01, 0.25]$	$[-]$
ξ_{12}	$r_\rho(1200°C) = 1 - \xi_{10} - \xi_{11} - \xi_{12}$	$[0.01, 0.49]$	$[-]$
ξ_{13}	c_{in}	$[700, 1300]$	$[\mathrm{Jkg^{-1}K^{-1}}]$

where $r_\rho\,[-]$ and $r_c\,[-]$ are the dimensionless density and specific heat capacity ratios, respectively, both nonlinearly dependent on temperature, and ρ_{in} is the constant value of the mass density set to $\rho_{air-dry} = 410\ \mathrm{kgm^{-3}}$, the mean value from all control samples in Table 5.2. For illustration, the parametrized thermal properties as a function of temperature and ξ-parameters are plotted in Fig. 5.13.

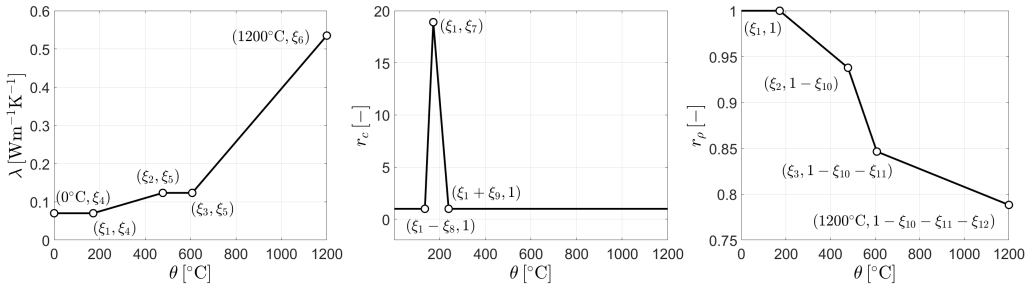

(a) (b) (c)

Figure 5.13: Parametrized thermal properties as a function of temperature and ξ-parameters: (a) thermal conductivity, (b) specific heat capacity ratio, (c) density ratio.

Two approaches, described next, were employed to find the set of optimal parameters given in Table 5.6 exploiting the measured temperature curves acquired from the fire tests. For the sake of completeness, we replotted the adopted furnace temperature curves in Fig. 5.14, recall Section 5.3 and Fig. 5.3 for the set temperatures (black curves) pertinent to individual samples.

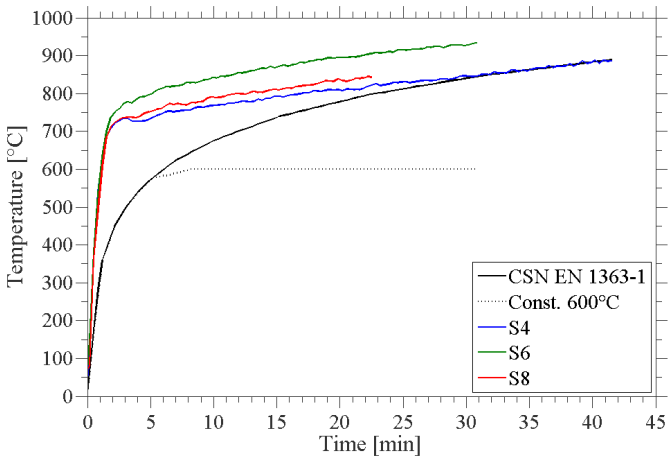

Figure 5.14: Furnace temperature curves used in calibration.

5.4.1 Deterministic calibration

A variety of deterministic identification procedures can be used to find an optimal solution to the identification problem, each having its advantages and drawbacks. Mentioning all of them goes beyond the scope of this paper and we limit the reader's attention here to our in-house algorithm GRADE [9]. GRADE is a real-coded stochastic[1] optimization algorithm combining the principles of genetic algorithms and differential evolution.

In this setup, all 13 ξ-parameters were calibrated according to the ranges summarized in Table 5.6. Moreover, for each of the laboratory tests, one additional parameter was introduced to properly capture a slightly different loading fire regime in the testing chamber, see the definition of boundary condition (5.10). The variables $\xi_{14}, \xi_{15}, \xi_{16}$ stand for the heat transfer coefficient α tuned specifically for the examined experiments No. 2 (Sample 4), 3 (Sample 6), and 4 (Sample 8), respectively.[2] However, the calibration procedure was performed for all parameters simultaneously employing the three experiments all at once.

The resulting set of optimally fitted material parameters $\xi_1 - \xi_{13}$ and boundary terms $\xi_{14}, \xi_{15}, \xi_{16}$ is available in Table 5.7. A graphical representation of optimal functional variations of model parameters λ, c, r_ρ is evident in Fig. 5.15.

The numerically predicted evolutions of temperature, based on the distributions in Fig. 5.15, appear in Fig. 5.16. Recall that a unique set of parameters $\xi_1 - \xi_{13}$ is adopted regardless of the type of loading curve, while the tuned transfer coefficient α relates to a given fire test. Although an initial plateau was difficult to reproduce, note similar predictions presented in [6], the overall trend, especially in light of the temperature predicted in the residual cross-section, appears satisfactory. However, we should keep in mind that this good match required an independent determination of the transfer

[1] The solution is obtained in the form of deterministic ξ-parameter set, but the initial/starting point is chosen randomly.

[2] Emissivity e is assumed constant in the calibration process.

Table 5.7: Optimal values of ξ-parameters derived from deterministic and stochastic minimization processes.

Symbol	Deterministic	Stochastic				Unit
		Mean	StdDev	Min	Max	
$\xi_1/\boldsymbol{\xi}_1$	190.8	149.4	29.4	100.0	172.9	[°C]
$\xi_2/\boldsymbol{\xi}_2$	314.3	474.7	5.35	450.6	480.4	[°C]
$\xi_3/\boldsymbol{\xi}_3$	501.8	611.1	5.71	603.2	623.4	[°C]
$\xi_4/\boldsymbol{\xi}_4$	0.11	0.10	0.06	0.07	0.34	[$\mathrm{Wm^{-1}K^{-1}}$]
$\xi_5/\boldsymbol{\xi}_5$	0.15	0.10	0.04	0.02	0.16	[$\mathrm{Wm^{-1}K^{-1}}$]
$\xi_6/\boldsymbol{\xi}_6$	1.49	0.54	0.03	0.49	0.65	[$\mathrm{Wm^{-1}K^{-1}}$]
$\xi_7/\boldsymbol{\xi}_7$	14.5	15.0	10.9	1.65	63.1	[–]
$\xi_8/\boldsymbol{\xi}_8$	55.8	43.9	6.30	28.1	56.0	[°C]
$\xi_9/\boldsymbol{\xi}_9$	89.2	68.9	1.18	66.8	72.2	[°C]
$\xi_{10}/\boldsymbol{\xi}_{10}$	0.03	0.05	0.01	0.04	0.07	[–]
$\xi_{11}/\boldsymbol{\xi}_{11}$	0.06	0.08	0.01	0.04	0.09	[–]
$\xi_{12}/\boldsymbol{\xi}_{12}$	0.43	0.07	0.02	0.04	0.11	[–]
$\xi_{13}/\boldsymbol{\xi}_{13}$	1355.0	978.6	53.0	790.3	1061.4	[$\mathrm{Jkg^{-1}K^{-1}}$]
$\xi_{14}/\boldsymbol{\xi}_{14}$	10.1	22.0	1.32	17.8	25.8	[$\mathrm{Wm^{-2}K^{-1}}$]
ξ_{15}	7.32					[$\mathrm{Wm^{-2}K^{-1}}$]
ξ_{16}	49.3					[$\mathrm{Wm^{-2}K^{-1}}$]

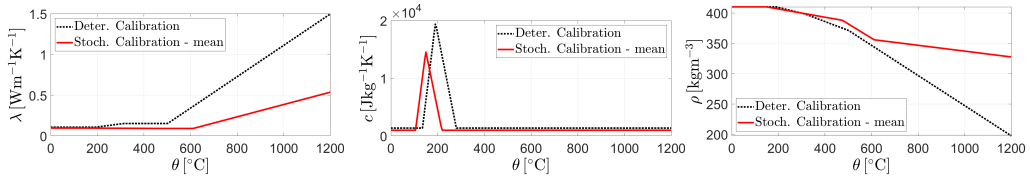

(a) (b) (c)

Figure 5.15: Comparison of thermal properties computed for the best fitted deterministic parameter set with averaged values obtained from the Bayesian calibration: (a) thermal conductivity, (b) specific heat capacity, (c) density.

parameter α for each loading fire curve, and this is unacceptable. An attempt to resolve this issue is discussed below.

5.4.2 Stochastic calibration

Unlike the deterministic approach, the stochastic approach yields the identified parameters in terms of distributions. Similar to [13] we grounded this approach on Bayesian inference, which allowed us to rigorously represent the natural variability in material parameters as well as in experimental measurements. In this framework, the uncertainty in experimental measurements was estimated along with the desired material parameters. As described in Section 5.4.3, we began with an expert prior knowledge about material

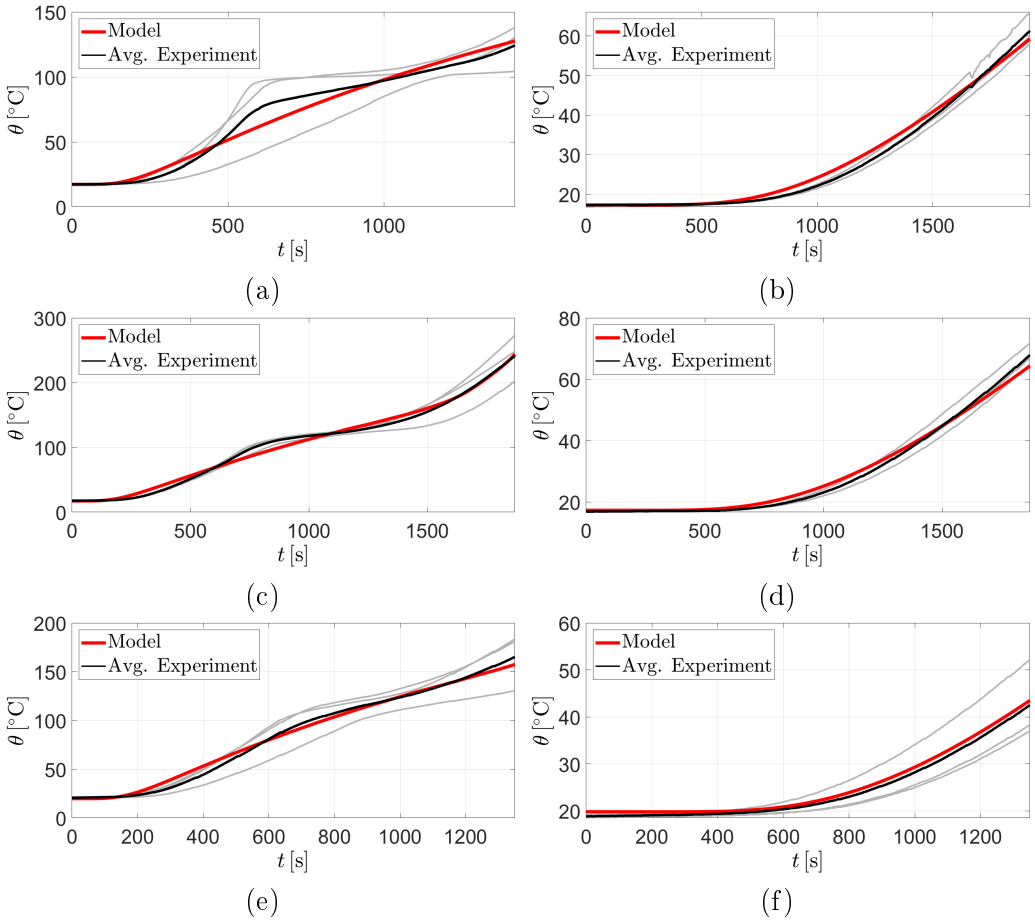

Figure 5.16: Comparison of experimental data and numerical response computed for the best fitted deterministic parameter set: (a) Sample 4, depth 20 mm, $\alpha = 10.1$, (b) Sample 4, depth 50 mm, $\alpha = 10.1$, (c) Sample 6, depth 20 mm, $\alpha = 7.3$, (d) Sample 6, depth 50 mm, $\alpha = 7.3$, (e) Sample 8, depth 20 mm, $\alpha = 49.3$, (f) Sample 8, depth 50 mm, $\alpha = 49.3$; α is given in [$\mathrm{Wm^{-2}K^{-1}}$].

values. By exploiting the Bayesian theorem, we searched for improved posterior probabilistic distributions of calibrated parameters [32]. For simplicity, the prior knowledge of calibrated parameters $\boldsymbol{\xi}_i$ was assumed in the form of uniform distributions with ranges given again in Table 5.6. As in the case of deterministic minimization, an additional uniformly distributed parameter $\boldsymbol{\xi}_{14}$, corresponding to the heat transfer coefficient α, was introduced, but in this case, it was considered unique regardless of the type of fire. Further details and other similar applications can be found in [33] and [32].

The basic statistics of calibrated parameters appear in Table 5.7. These were derived from 30,000 realizations generated by the application of the Markov chain Monte Carlo method in the updating process, see Section 5.5 for further details. The results obtained indicate, how the initial, a relatively vague, knowledge about the material parameters was

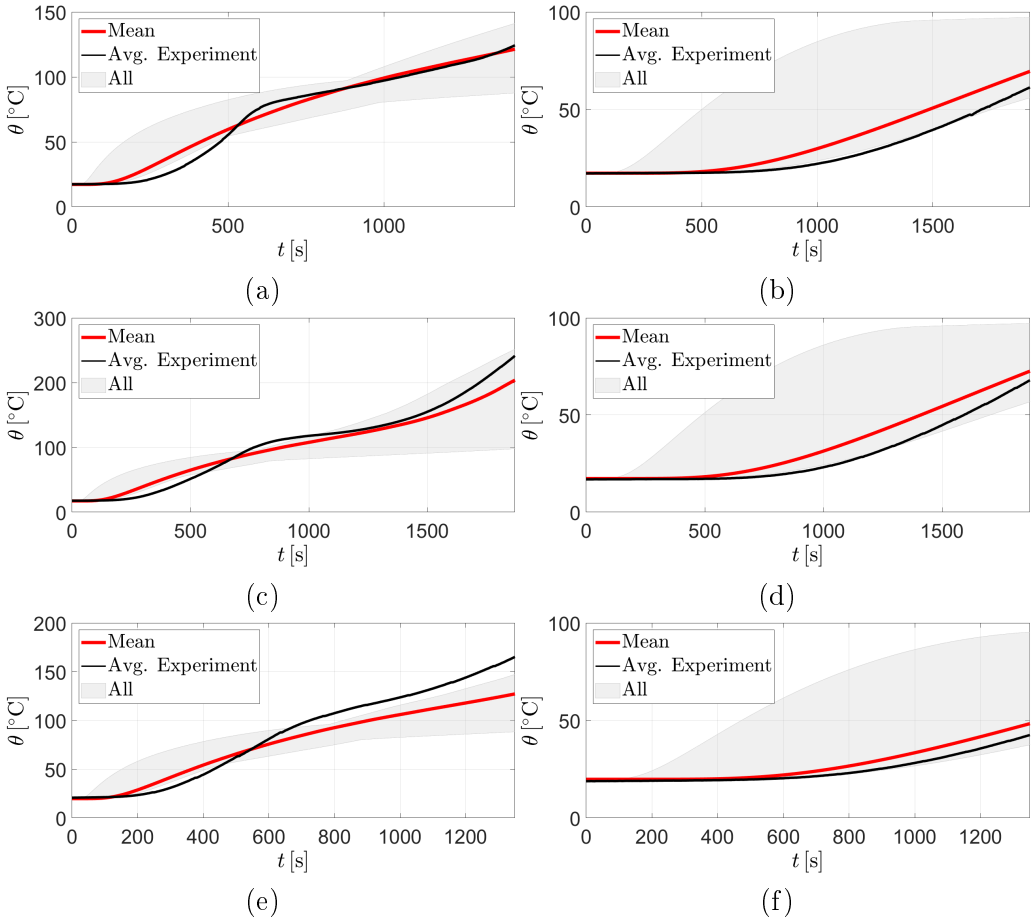

Figure 5.17: Comparison of experimental data and numerical response computed using thermal parameters calibrated using the Bayesian framework: (a) Sample 4, depth 20 mm, (b) Sample 4, depth 50 mm, (c) Sample 6, depth 20 mm, (d) Sample 6, depth 50 mm, (e) Sample 8, depth 20 mm, (f) Sample 8, depth 50 mm.

improved based on the available measurements. The associated numerical predictions are compared to experimental measurements in Fig. 5.17. The red lines were constructed by employing the mean values of ξ-parameters. The gray surface contains all numerical responses computed for the posterior ξ-sets. When compared to results in Fig. 5.16 the stochastic approach may seem less accurate. Remind, however, that the calibrated transfer parameter α was assumed unique for all fire scenarios. It is also worth mentioning that the stochastic approach has one important added value: it accounts for the natural variability in wood and opens the door to a probabilistic assessment of structural designs.

5.4.3 Predicted charring depth from computationally determined char front

This section focuses on the numerical prediction of charring depth by simulating the evolution of char front represented by a certain temperature isotherm. We assumed that wood chars instantaneously once reaching this temperature limit. To comply with Section 5.3.5, 280°C and 300°C isotherms were examined.

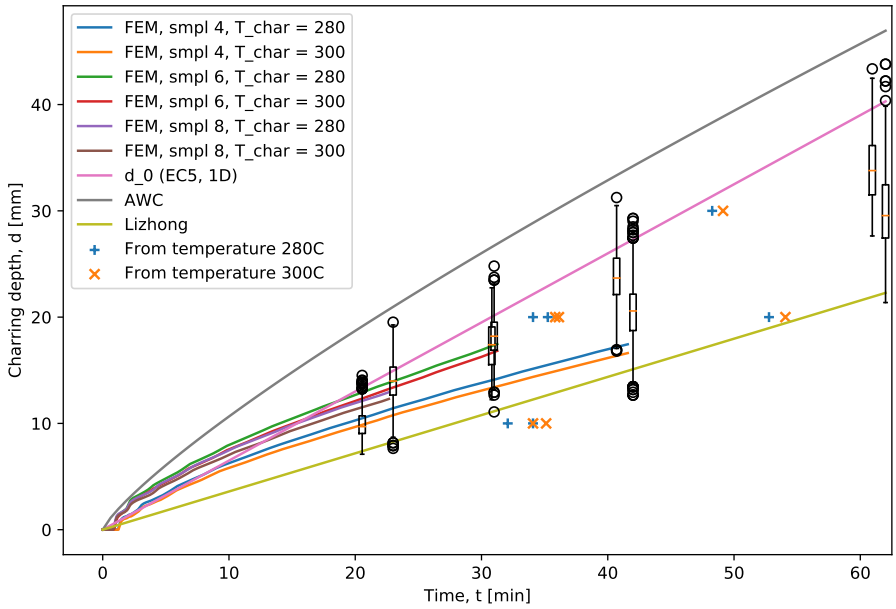

Figure 5.18: Evolution of charring depth. Charring depths measured for eight fire experiments are displayed in the form of a box plot, i.e., showing their interquartile intervals, range, and outliers.

Figure 5.18 presents our results and introduces four types of data. The measured charring depths obtained from eight fire tests as described in Section 5.3.5 are displayed in the form of a box plot. The box extends from the lower to upper quartile values of measured data with the line marking the median. The whiskers extending from the box show the range of data and the points mark individual outliers. The second type of data is plotted in the form of curves labeled "FEM". These show the evolution of charring depth deduced as the position of the 280°C or 300°C isotherm predicted by the FEM heat model.

Following the discussion in the last paragraph of Section 5.4.2 we adopted in numerical simulations the temperature variation of model parameters in Fig. 5.15 derived from the application of stochastic calibration approach. The remaining curves present three chosen empirical relations for charring depth. The EC5 curve represents charring depth evolution for one-dimensional charring as recommended in EN 1995-1-2[15] with $\beta_0 = 0.65$ mm/min, the AWC curve is the 1D variant of the curve suggested by the

American Wood Council [16], see Eq. (5.25) in Section 5.5.3, and the Lizhong curve corresponds to the empirical model presented in [34]. Individual dots mark times at which the temperature measured for a given distance from the surface of a beam reached 280°C or 300°C assuming 1D charring.

It is seen that numerically predicted charring depths, essentially bounded by the selected simplified charring rate models, follow the experimentally obtained data fairly well. The reason why the simulations corresponding to Samples 4 and 6 arrived at approximately the same charring depth of about 17 mm for different durations of a fire is explained in Fig. 5.14, which suggests that Sample 6 (green curve) was exposed to a fire of higher intensity than Sample 4 (blue line). This example illustrates the principle advantage of using simulations to predict the evolution of charring depth as oppose to adopting simple charring rate models discussed in the next section: the former approach essentially reflects the type of fire load whereas the latter only assumes standard fire exposure, as to be discussed in Section 5.5.5.

5.5 Charring depth from simple charring rate models

Perhaps the most common approach for predicting the evolution of charring depth is the application of a charring rate model. The literature offers several models with varying levels of complexity, see [14, and the cited references], which provide a critical overview of the performance of individual models depending on the kind of fire scenario, type of wood, and structural elements.

In this paper, we revisit some of these models in an attempt to improve their predictive power based on available experimental measurements. For this reason, we limited our attention to the two most simple models adopted by the European [15] and American [16] design codes. While the former model assumes a constant value for the charring rate β in Eq. (5.3), the latter formula, originally proposed by White [25] for one-dimensional charring allows the charring rate to vary over time. Because of the natural variability of wood and also in light of the stochastic calibration described in Section 5.4.2 we approached these models in the statistical framework.

With reference to Eq. (5.3), all models express the expected value of charring depth $\overline{d}_{char}$ as a product of the potentially time-dependent charring rate β and fire duration t

$$\overline{d}_{char}(t) = \beta(t)t. \tag{5.12}$$

The measured value, herein the values collected from the analysis of images in Fig. 5.9 with their mean values stored in Table 5.4, is assumed normally distributed around the expected value with a standard deviation σ_d

$$d_{char}(t) \sim \mathcal{N}(\overline{d}_{char}(t), \sigma_d). \tag{5.13}$$

For all models, the distribution of the parameters was deduced from the measured charring depths via Bayesian inference. In the following text, the fire experiments with different durations are indexed with $i = 1, \ldots, N$, $N = 8$, while index $j = 1, \ldots, M_i$

denotes the j-th charring depth measurement for a given sample. Thus d_{ij} represents the j-th charring depth measured on all specimens subjected to fire duration t_i, recall the segments in Fig. 5.5 subjected to image analysis. Equation (5.13) will be now examined in the formulation of the following three stochastic models.

5.5.1 Model 1 (M1): fixed charring rate β

In the simplest model, we assume the charring rate to be independent of time with a fixed, known value $\beta(t) = \beta_0$, where $\beta_0 = 0.65$ mm/min is the one-dimensional design charring rate suggested in Eurocode 5 [15]. The model's probabilistic and deterministic relations then read[3]

$$d_{ij} \sim \mathcal{N}(\overline{d}_i, \sigma_d) \quad \text{for} \quad i = 1 \dots N,\, j = 1 \dots M_i \tag{5.14}$$

$$\overline{d}_i = \beta_0 t_i \quad \text{for} \quad i = 1 \dots N \tag{5.15}$$

$$\sigma_d \sim \mathcal{U}(\sigma_{d,min}, \sigma_{d,max}) \tag{5.16}$$

where the last relation indicates uniform distribution with limits $\sigma_{d,min}$ and $\sigma_{d,max}$ being the prior distribution for σ_d; notice the similarity with the assumed initial, rather vague, knowledge about the random model parameters also accepted in Section 5.4.2. Thus in this model, the measurement error, given by the distribution of σ_d, is the only parameter to be identified.

5.5.2 Model 2 (M2): constant but unknown charring rate β_0

In a direct extension of the above model, we add β_0 to the list of model parameters and infer its distribution from measured data instead of relying upon a specified fixed value. The relations of this model are given by

$$d_{ij} \sim \mathcal{N}(\overline{d}_i, \sigma_d) \quad \text{for} \quad i = 1 \dots N,\, j = 1 \dots M_i \tag{5.17}$$

$$\overline{d}_i = \beta_0 t_i \quad \text{for} \quad i = 1 \dots N \tag{5.18}$$

$$\sigma_d \sim \mathcal{U}(\sigma_{d,min}, \sigma_{d,max}) \tag{5.19}$$

$$\beta_0 \sim \mathcal{U}(\beta_{min}, \beta_{max}) \tag{5.20}$$

where Eq. (5.20) indicates the prior distribution of β_0, again being uniform.

5.5.3 Model 3 (M3): time-dependent charring rate β

In this model, we acknowledge the nonlinear evolution of charring depth described and approximated by White [25]

$$t = m\overline{d}^{\alpha}, \tag{5.21}$$

[3] Henceforth, we drop the subscript *char* for the sake of simplicity.

where the value $\alpha = 1.23$ proposed by White is based on the measurement of various wood slabs exposed to fire. Rewriting Eq. (5.21) into the form of Eq. (5.12) we get

$$\overline{d}(t) = \beta(t)t = \frac{a\beta_0}{t^b}t, \tag{5.22}$$

where $b = 1 - 1/\alpha$, β_0 is the nominal one-dimensional charring rate for a 60-minute fire and $a = 60^b$ guarantees $\overline{d}(60 \text{ min}) = 60\beta_0$. With reference to Eq. (5.22) and assuming b and β_0 as unknown parameters, we formulate the corresponding statistical model as follows

$$d_{ij} \sim \mathcal{N}(\overline{d}_i, \sigma_d) \quad \text{for} \quad i = 1 \dots N,\ j = 1 \dots M_i \tag{5.23}$$

$$\overline{d}_i = \beta_i t_i \quad \text{for} \quad i = 1 \dots N \tag{5.24}$$

$$\beta_i = \frac{a\beta_0}{t_i^b} \quad \text{for} \quad i = 1 \dots N \tag{5.25}$$

$$a = 60^b \tag{5.26}$$

$$\sigma_d \sim \mathcal{U}(\sigma_{d,min}, \sigma_{d,max}) \tag{5.27}$$

$$\beta_0 \sim \mathcal{U}(\beta_{min}, \beta_{max}) \tag{5.28}$$

$$b \sim \mathcal{U}(b_{min}, b_{max}) \tag{5.29}$$

where Eq. (5.29) indicates a uniform prior distribution of b.

The assumed ranges of uniform prior distributions for the above model parameters σ_d, β_0, b are listed in Table 5.8.

Table 5.8: Ranges of prior uniform distributions for model parameters.

Parameter	Unit	Lower limit	Upper limit
σ_d	[mm]	0.1	10.0
β_0	[mm/min]	0.01	10.0
b	[-]	0.01	1.0

Grounding on the Bayesian theorem [10, 11, 35, 36, to cite a few], the posterior joint probability density functions (PDFs) of the parameters of the three models then become

$$\pi(\sigma_d|\langle d_{ij}\rangle) \propto \prod_{i=1}^{N}\prod_{j=1}^{M_i} f_N(d_{ij}, \overline{d}_i, \sigma_d) \times f_U(\sigma_d, \sigma_{d,min}, \sigma_{d,max}), \tag{5.30}$$

$$\pi(\sigma_d, \beta_0|\langle d_{ij}\rangle) \propto \prod_{i=1}^{N}\prod_{j=1}^{M_i} f_N(d_{ij}, \overline{d}_i, \sigma_d) \times$$
$$f_U(\sigma_d, \sigma_{d,min}, \sigma_{d,max}) \times f_U(\beta_0, \beta_{min}, \beta_{max}), \tag{5.31}$$

$$\pi(\sigma_d, \beta_0, b|\langle d_{ij}\rangle) \propto \prod_{i=1}^{N}\prod_{j=1}^{M_i} f_N(d_{ij}, \overline{d}_i, \sigma_d) \times$$
$$f_U(\sigma_d, \sigma_{d,min}, \sigma_{d,max}) \times f_U(\beta_0, \beta_{min}, \beta_{max}) \times f_U(b, b_{min}, b_{max}), \tag{5.32}$$

where

$$f_N(x,\mu,\sigma) = \frac{1}{\sigma\sqrt{2\pi}} e^{-\frac{1}{2}\left(\frac{x-\mu}{\sigma}\right)^2} \tag{5.33}$$

and

$$f_U(x,a,b) = \begin{cases} \frac{1}{b-a} & \text{for } a \le x \le b, \\ 0 & \text{for } x < a \text{ or } x > b \end{cases} \tag{5.34}$$

represent the PDFs of normal and uniform distributions, respectively, and $\langle d_{ij} \rangle$ is a vector collecting all measured depths. The function f_N stands for the likelihood function, which in fact is the probability distribution of the measured depths.

5.5.4 Inference of model parameters

The standard approach for inspecting a nontrivial Bayesian model consists of drawing samples from the posterior distribution of parameters and calculating their statistics such as the mean, higher moments, quantiles, and correlation coefficients. In this study, the NUTS sampler [37] from the PyMC3 [38] Python package for Bayesian statistical modeling was employed to generate two independent Markov chains with 2000 samples for each model. The posterior distribution of the model parameters, given a) the measured values of charring depth $\{d_{ij}\}$ and b) the boundaries of the prior uniform distributions listed in Table 5.8, are presented in the form of kernel densities (KDEs) in Figs. 5.19 - 5.21 together with the chains of sampled values[4].

To compare the inferred distribution of parameters for the M1, M2, and M3 models, we first looked at the marginal distributions of σ_d. Since the M1 model has a fixed value of charring rate $\beta_0 = 0.65\,\text{mm/min}$, all discrepancies of the observed charring depth d_{ij} are explained by the standard deviation σ_d only, which thus centers around a relatively high value of $\sigma_d = 6.23$ mm/min. On the other hand, the M2 and M3 models, which infer the value of β_0 from the data although starting from a broad prior distribution, yielded a significantly lower value of σ_d centered around 3.2 mm/min and 3.025 mm/min, respectively. The nominal charring rate β_0 is centered around 0.522 mm/min for the M2 model and around 0.504 mm/min for the M3 model. The fact that the parameter b of the M3 model is centered around a positive value 0.145 indicates that the instantaneous charring rate $\beta(t)$ decreases slightly with time and that the function $d(t)$ is concave. This finding agrees with that of White [25].

All parameters in the model were identified fairly well, despite relatively vague initial knowledge about them, as seen in Table 5.8. This is strongly supported by narrow posterior distributions observed in Figs. 5.19 - 5.21.

[4]Displaying both chains and their corresponding KDEs in a single image provides a quick visual check of whether the generated chains converged to the expected probability distribution.

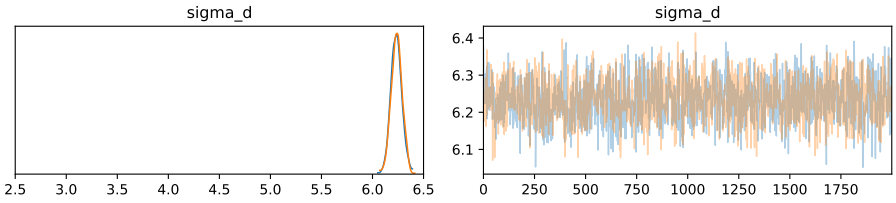

Figure 5.19: Posterior distributions and traces σ_d in the M1 statistical model of charring depth, i.e. with constant $\beta(t) = \beta_0 = 0.65$.

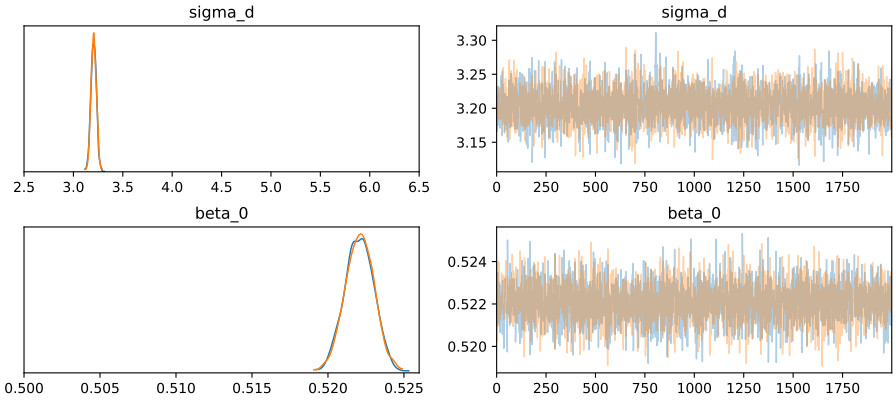

Figure 5.20: Posterior distributions and traces of σ_d and β_0 in the M2 statistical model of charring depth, i.e. with time-independent but unknown $\beta(t) = \beta_0$.

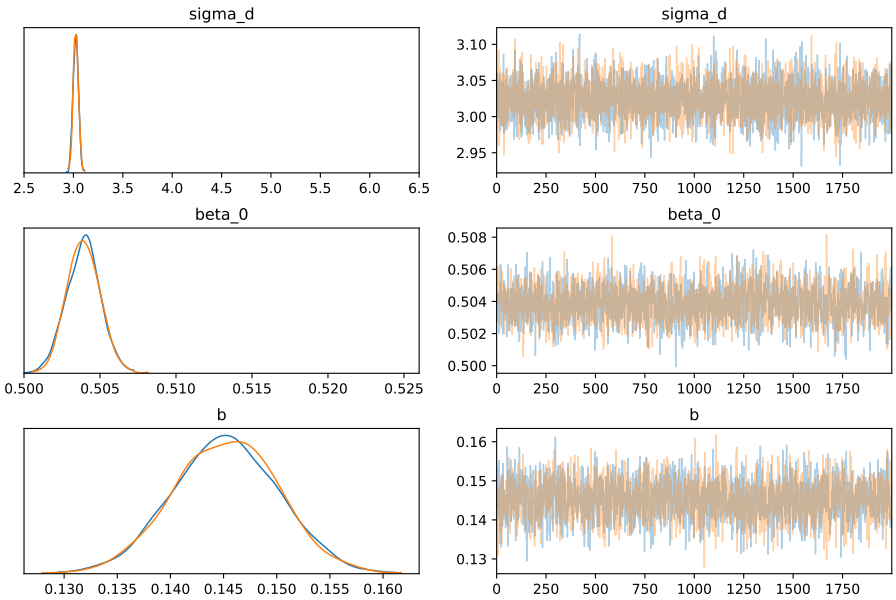

Figure 5.21: Posterior distributions and traces of σ_d, β_0 and b in the M3 statistical model of charring depth, i.e. with time-dependent $\beta(t, \beta_0, b)$.

5.5.5 Posterior predictions

A crucial feature of statistical models is their ability to predict the quantity of interest. For the models described above it is the charring depth at a given exposure time. The predicted quantity is again not a single value but rather a random variable with a posterior predictive distribution. The mean and the credible 95% interval of the predicted charring depth as a function of time are displayed for each model in Figs. 5.22-5.24.

Apart from the median line surrounded by a 95% confidence band, the figures show the directly measured charring depths and the charring depths calculated from the temperature measurements listed in Table 5.3. The similarity of both the median line and width of the credible band, apparent when comparing Figs. 5.23 and 5.24, suggests that the nonlinearity introduced in the M3 model is quite marginal. From the engineering point of view, the error one makes using the M2 model with a constant charring rate is therefore negligible compared to the inherent uncertainty attributed to charring depth in general.

To bring the predictions provided by the FEM heat model developed in Section 5.4 and the simplified charring rate models to the same footing we introduced in Figs. 5.22-5.23 also the results derived for standard fire exposure using FEM. Remember that the parameters of the model were identified from three fire scenarios slightly differing from standard fire. In this regard, the FEM results (blue curve) match the mean predictions obtained from the three adopted models (red curve) remarkably well. On the one hand, this indicates that convectional heat transfer models are reliable for estimating the evolution of charring depth. On the other hand, it confirms the applicability of basic charring rate models when limiting attention to standard fire exposure. But keep in mind that the FEM approach is more general and can be used for any type of fire, although more complex parametric fires may call for another set of parameters to represent the cooling branch [6] better.

Table 5.9: Credible intervals for charring depth [mm] predicted by the statistical model with the time-dependent charring rate compared to ranges of measured data and charring depth predicted by the FEM model.

Time [min]	Posterior predictions (M3)	Measured	FEM model
23	7.52 – 19.16	10.29 – 17.41	12.30 (S8)
31	11.10 – 23.02	13.98 – 21.90	16.82 (S6)
42	16.30 – 28.38	15.04 – 25.80	16.62 (S4)
62	25.00 – 36.92	23.22 – 37.20	–

The 95% confidence interval bounds provided by the M3 model for different times are summarized in Table 5.9 together with the measured minimum and maximum charring depths and the values obtained from the FEM heat model for individual fire scenarios. The reason for arriving at almost the same charring depth for two different fire durations (Samples 6 and 4) has already been explained in the last paragraph in Section 5.4.3.

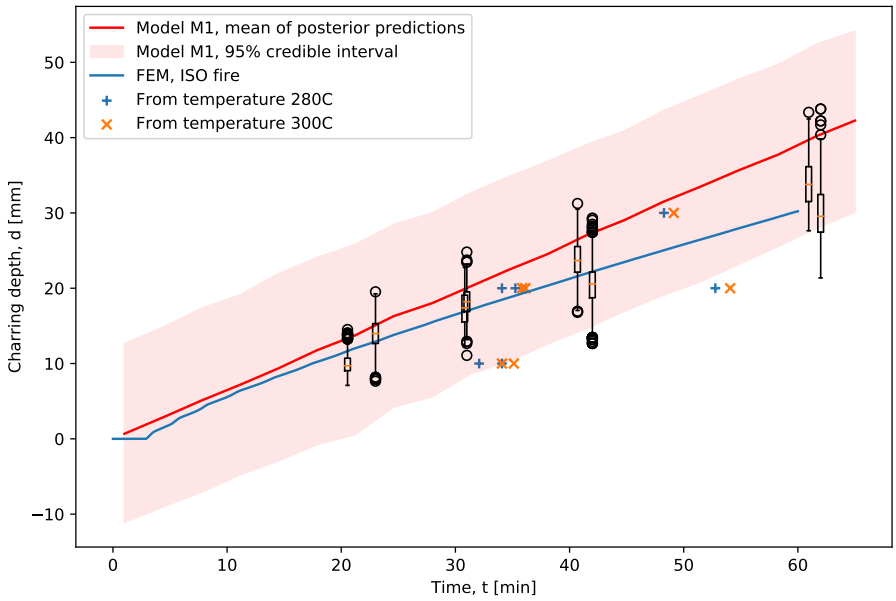

Figure 5.22: Posterior distribution of charring depth predicted by the model with fixed charring rate $\beta = 0.65$.

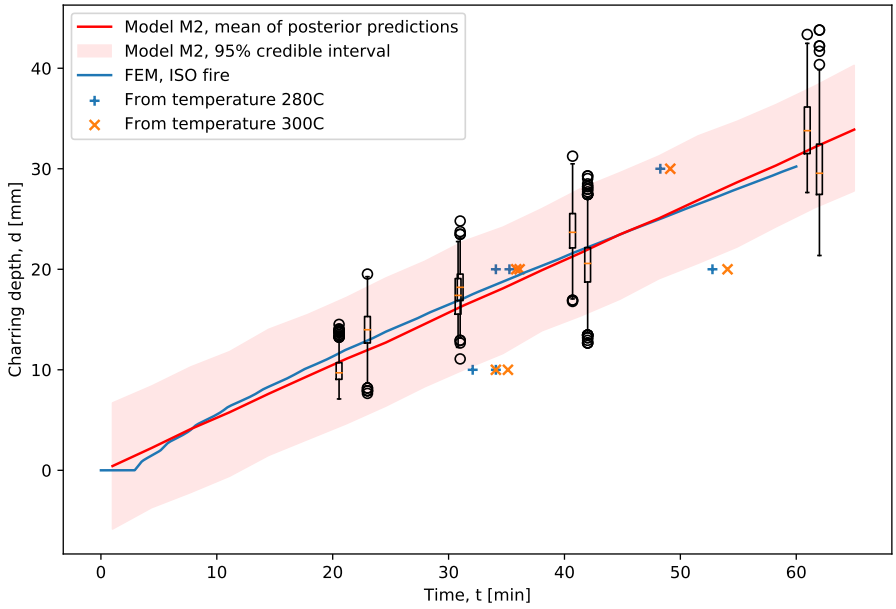

Figure 5.23: Posterior distribution of charring depth predicted by the model with time-independent charring rate β.

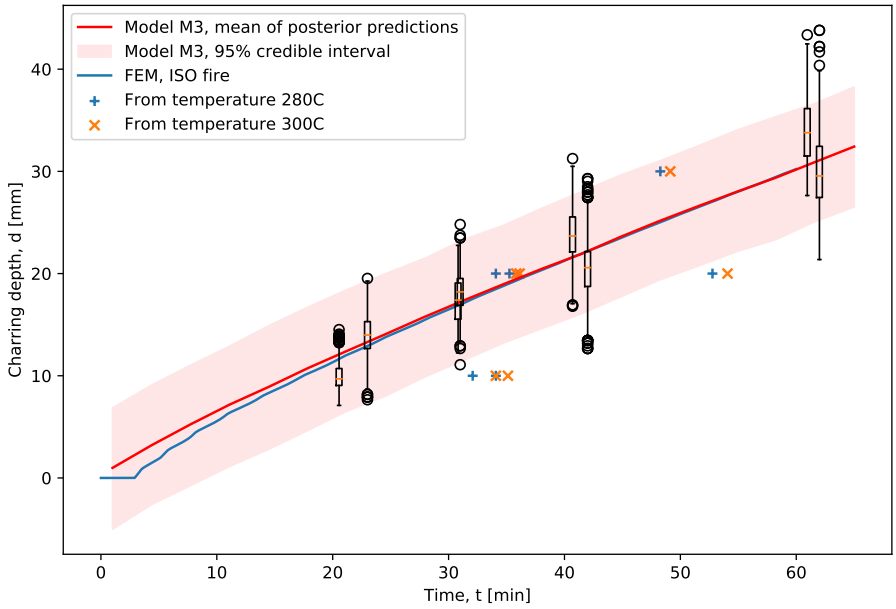

Figure 5.24: Posterior distribution of charring depth predicted by the model with time-dependent charring rate β.

5.6 Conclusions

This paper described the methods for the probabilistic analysis of the evolution of charring depth in GLT beams made of spruce wood when exposed to fire. The results of an extensive experimental program were presented first to provide the basic data needed in the theoretical part of this paper. To that end, several *furnace temperature curves* were recorded for two load scenarios, the ČSN EN 1363-1 and CONST 600° curves displayed in Fig. 5.3. Apart from that, variable initial conditions of the furnace led to variations in actual furnace temperature curves and therefore also to variations in the distribution of temperatures recorded at several points within beam's cross-section. This first set of experimental data was supplemented by directly measuring the charring depth with the help of image analysis and by employing an indirect approach based on the 300° C (280° C) isotherm and the knowledge of the deflection of residual beams subjected to a 3PB test. As expected, the acquired values of the charring depth confirmed a nonlinear dependence on the duration of a fire and the influence of actual loading conditions.

Combining the uncertainty in the actual fire scenario and natural variability in wood properties promotes an application of the tools of mathematical statistics when predicting the evolution of charring depth computationally. In this regard, two commonly used theoretical approaches were examined and compared.

The first approach allows for reflecting the actual fire test and builds upon the application of the conventional heat transfer model. From the engineering point of view, this was shown to be sufficient as the interest is primarily in the prediction of temperature

within beam's cross-section and not in the detailed description of complex physical processes taken place in the burning section during pyrolysis. This is particularly seen in Fig. 5.18 showing good agreement of theoretically predicted charring depth based on the 300° C isotherm with the experimentally measured one especially if taking into account the actual fire scenario. Recall that the calibration procedure for this model took advantage of Bayesian inference yielding the basic material parameters of the heat transport model in terms of distributions. This opens the way to stochastic analysis to examine the influence of elevated temperature the wood is exposed to during fire on the material parameters such as strength and stiffness.

The second approach is rather standard and grounds on the application of simple linear charring rate models. The Bayesian statistical approach was adopted again to address the variability of the parameters of the selected models when departing from standard fire assumed by these models. Limiting attention to a one-dimensional fire and two basic models included in the design codes we observed no added value for use of the nonlinear M3 model [16, 25] when compared to the linear M2 model [15]. For fires examined here, which did not deviate much from standard fire exposure, the mean values of β_0 were 0.522 mm/min for the M2 model and 0.504 mm/min for the M3 model, respectively, rather close to the 0.65 mm/min value used by Eurocode 5 [15]. Bear in mind, however, that the parameters of the model were again provided in terms of distributions and thereby reflected the variability of charring depth predictions caused by fluctuations in the fire load. Recall that the experimental charring depths obtained from all fire tests of Group 1, both directly and indirectly, were adopted in the identification process.

To compare both approaches, FEM simulations were carried out for standard fire exposure resulting in an almost perfect match with predictions provided by the most simple charring rate models, notably the M2 and M3 models. A similar comparative study could have been performed for other simplified models such as the Lizhong model [34], where the numerically predicted heat flux rate, hardly constant, could be employed. However, the corresponding stochastic model would grow in complexity as the error of numerical analysis would have to be included, and this was beyond the scope of this investigation.

In support of the simplified, yet sufficiently accurate, approaches presented here, the necessity of a rapid decision-making process after a real fire harnessing the power of such models is perhaps more useful, from an engineering point view, than employing complex constitutive models with a large number of parameters and unknown levels of accuracy.

Acknowledgment

We are thankful for financial support provided by the Czech Grant Agency, project No. 18-05791S.

Bibliography

[1] M. L. Janssens, Modeling of the thermal degradation of structural wood members exposed to fire, Fire and Materials 28 (2-4) (2004) 199–207.

[2] C. Lautenberger, C. Fernandez-Pello, Generalized pyrolysis model for combustible solids, Fire Safety Journal 44 (6) (2009) 819–839.

[3] B. Moghtaderi, The state-of-the-art in pyrolysis modelling of lignocellulosic solid fuels, Fire and Materials 30 (1) (2006) 1–34.

[4] L. Shi, M. Y. L. Chew, A review of fire processes modeling of combustible materials under external heat flux, Fuel 106 (2013) 30–50.

[5] J. König, L. Walleij, One-dimensional charring of timber exposed to standard and parametric fires in initially protected and non-protected fire situation, Tech. rep., Trätake: Swedisch Institute for Wood Technology Research, Stockholm (1999).

[6] J. König, Effective thermal action and thermal properties of timber members in natural fire, Fire and Materials 30 (2006) 51–63.

[7] K. Matouš, M. Lepš, J. Zeman, M. Šejnoha, Applying genetic algorithms to selected topics commonly encountered in engineering practice, Computer Methods in Applied Mechanics and Engineering 190 (13–14) (2000) 1629–1650.

[8] J. Zeman, M. Šejnoha, Numerical evaluation of effective properties of graphite fiber tow impregnated by polymer matrix, Journal of the Mechanics and Physics of Solids 49 (1) (2001) 69–90.

[9] A. Kučerová, Identification of nonlinear mechanical model parameters based on soft computing methods, Ph.D. thesis, Ecole Normale Supérieure de Cachan, Laboratoire de Mécanique et Technologie (2007).

[10] T. Janda, M. Šejnoha, J. Šejnoha, Applying Bayesian approach to predict deformations during tunnel construction, International Journal for Numerical and Analytical Methods in Geomechanics 42 (2018) 1765–1784.

[11] T. Janda, J. Šejnoha, M. Šejnoha, Hierarchical stochastic model of terrain subsidence during tunnel excavation, IOP Conference Series: Materials Science and Engineering 236 (2017).

[12] M. Šejnoha, T. Janda, J. Vorel, L. Kucíková, P. Padevět, V. Hrbek, Bayesian inference as a tool for improving estimates of effective elastic parameters of wood, Computers & Structures 218 (2019) 94–107. doi:10.1016/j.compstruc.2019.03.006.

[13] P. R. Wagner, R. Fahrni, M. Klippel, A. Frangi, B. Sudret, Bayesian calibration and sensitivity analysis of heat transfer models for fire insulation panels, Engineering Structures 205 (2020).

[14] K. L. Friquin, A review of models for charrig rate of solid wood, nail- and glue-laminated structural members, Journal of Structural Fire Engineering 1 (1) (2010) 61–72.

[15] Eurocode 5: Design of Timber Structures - Part 1-2: General - Structural Fire Design, European Committee for Standardization, Brussels, 2004.

[16] American Wood Council: Calculating the fire resistance of wood members and assemblies, Technical report no. 10, Tech. rep., American and Forest Association (2003).

[17] R. White, Fire resistance of exposed wood fire, in: Wood and Fire Safety, 5th International Scientific Conference, Štrbské Pleso, Slovak Republik, 2004, pp. 337–344.

[18] D. Lange, L. Boström, J. Schmid, A. J, The influence of parametric fire scenarios on structural timber performance and reliability, Tech. rep., SP Technical Research Institute of Sweden (2014).

[19] European Committee for Standardization, EN 13183-1: Moisture content of a piece of sawn timber — Part 1: Determination by oven dry method (2002).

[20] European Committee for Standardization, EN 844: Round and sawn timber - Terminology (2019).

[21] K. L. Friquin, Material properties and external factors influencing the charring rate of solid wood and glue-laminated timber, Fire and Materials 35 (5) (2011) 303–327. doi:10.1002/fam.1055.

[22] A. I. Bartlett, R. M. Hadden, L. A. Bisby, A review of factors affecting the burning behaviour of wood for application to tall timber construction, Fire Technology 55 (2019) 1–49. doi:10.1007/s10694-018-0787-y.

[23] M. Dietenberger, L. Hasburgh, Wood Products Thermal Degradation and Fire, Reference Module in Materials Science and Materials Engineering (2016) 1–8.

[24] E. L. Schaffer, Charring rate of selected woods–transverse to grain., Tech. rep., Forest Products Laboratory Madison Wisconsin (1967).

[25] R. H. White, E. V. Nordheim, Charring Rate of Wood for ASTM E 119 Exposure, Fire Technology 28 (1) (1992) 5–30.

[26] E. Mikkola, Charring Of Wood Based Materials, Fire Safety Science 3 (1991) 547–556.

[27] J. Martinka, P. Rantuch, M. Liner, Calculation of charring rate and char depth of spruce and pine wood from mass loss, Journal of Thermal Analysis and Calorimetry 132 (2018) 1105–1113. doi:10.1007/s10973-018-7039-8.

[28] J. Schmid, A. Just, M. Klippel, M. Fragiacomo, The Reduced Cross-Section Method for Evaluation of the Fire Resistance of Timber Members: Discussion and Determination of the Zero-Strength Layer, Fire Technology 51 (2015) 1285–1309. doi:10.1007/s10694-014-0421-6.

[29] L. Kucíková, T. Janda, M. Šejnoha, J. Sỳkora, Experimental investigation of fire resistance of GLT beams, International Journal of Computational Methods and Experimental Measurements 8 (2) (2020) 99–110.

[30] L. Kucíková, M. Šejnoha, T. Janda, P. Padevět, G. Marseglia, Evaluation of impact of elevated temperatures on Young's modulus of GLT beams, in: P. Padevět (Ed.), NMM 2020 - Nano & Macro Mechanics 2020, Acta Polytechnica CTU Proceedings, 2020, pp. 0–0.

[31] J. Schmid, J. König, A. and Just, The Reduced Cross-Section Method for the Design of Timber Structures Exposed to Fire-Background, Limitations and New Developments, Structural Engineering International 22 (4) (2012) 514–522. doi:10.2749/101686612X13363929517578.

[32] J. Havelka, A. Kučerová, J. Sýkora, Dimensionality reduction in thermal tomography, Computers & Mathematics with Applications 78 (9) (2019) 3077–3089.

[33] A. Kučerová, J. Sýkora, Uncertainty updating in the description of coupled heat and moisture transport in heterogeneous materials, Applied Mathematics and Computation 219 (13) (2013) 7252–7261.

[34] Y. Lizhong, Z. Yupeng, W. Yafei, G. Zaifu, Predicting charring rate of woods exposed to time-increasing and constant heat fluxes, Journal of Analytical and Applied Pyrolysis 81 (1) (2008) 1–6. doi:10.1016/j.jaap.2007.06.006.

[35] D. Kelly, C. Smith, Bayesian inference in probabilistic risk assessment - The current state of the art, Reliability Engineering and System Safety 94 (2009) 628–643.

[36] A. Gelman, J. Carlin, H. Stern, D. Dunson, A. Vehtari, D. Rubin, Bayesian Data Analysis, Third Edition, Chapman & Hall/CRC Texts in Statistical Science, Taylor & Francis, 2013.

[37] M. D. Hoffman, A. Gelman, The No-U-Turn Sampler: Adaptively Setting Path Lengths in Hamiltonian Monte Carlo, Journal of Machine Learning Research 15 (2014) 1593–1623. doi:10.48550/arXiv.1111.4246.

[38] J. Salvatier, T. V. Wiecki, C. Fonnesbeck, Probabilistic programming in Python using PyMC3, PeerJ Computer Science 2 (2016) e55. doi:10.7717/peerj-cs.55.

Chapter 6

Modeling glulams in linear range with parameters updated using Bayesian inference

This chapter presents the preprint version of the journal paper

> Šejnoha, M.; Janda, T.; Melzerová, L.; Nežerka, V.; Šejnoha, J., Modeling glulams in linear range with parameters updated using Bayesian inference, Engineering Structures. 2017, 138 293-307. ISSN 0141-0296.

reformatted to align with the style of the thesis.

6.1 Abstract

A stochastic hierarchical model of a glued laminated timber beam loaded in bending is formulated in this paper. Being attributed to the limited number of observed data the model captures both the inherent variability of the elastic properties of individual timber boards making up the laminated beam and the uncertainty of the parameters controlling their probability distributions. Apart from the deflection measurements obtained from the full scale displacement-controlled, four point bending tests the model also incorporates the data from numerous nondestructive macroindentation measurements. The forward deterministic model of laminated beam is based on the Mindlin beam theory combined with the finite element method to simulate the laboratory measurements numerically. The inference of the model parameters is performed in the framework of Bayesian statistics. Apart from improved posterior distributions of material data, we also offer an improved formula for estimating the longitudinal elastic modulus from indentation measurements.

6.2 Introduction

Current building designs focus primarily on energy efficiency, minimal environmental impact, and healthy and safe conditions. To fulfill the mentioned criteria, timber structures

are a promising alternative to traditional concrete/masonry construction approaches. Among other applications the glued laminated timber (GLT) beams receive a particular interest owing to both their strength and aesthetic performance. On the other hand, since being manufactured from natural wood they may experience a significant variability in their local material properties. At the structural level this variability may further increase by producing unbalanced beams having boards of a higher quality on the tension side in comparison to those placed on the compression side.

The manufacturing process, where individual timber boards of variable lengths are bonded with adhesives, may result in cases where two neighboring boards differ more than twice in terms of their stiffness. This finding follows from the results of an extensive experimental program, which involved five laminated timber beams made of spruce. The beams were subjected to 3600 macroscopic indentation measurements carried out on both sides of individual boards in a predefined grid of points spread 10 cm apart [1, 2]. Point out that only clear wood was indented. Thus if the selected point was found in a knot, the indentation was shifted sufficiently far from the knot (at least 3× the average indentation depth amounting to about 3 cm). The measured indentation depth was then transformed into a local value of the modulus of elasticity along the fiber direction using an empirical expression

$$E = A + Bd, \tag{6.1}$$

where E is the longitudinal Young modulus in GPa, d is the indentation depth in [mm] and A, B are the fitting parameters. Generally, Eq. (6.1) is used to provide estimates of the Young modulus of clear wood free of weak sections such as knots or knot clusters. Despite an unavoidable inaccuracy in the mapping equation, a significant genuine variability in material properties of GLT beams is indisputable.

Introduction of wood variability into structural design has been at the forefront of engineering interest for last few decades. Attention has mostly been devoted to mechanical properties such as stiffness or strength being influenced in general by the presence of knots and knot clusters and consequently by variation of grain angle along the longitudinal path. This promotes a stiffness/strength profile in each board be regarded as a one-dimensional stochastic process either discrete or continuous [3]. The mid-point method is a typical representative of the former model whereas, for example Karhunen-Loeve (KL) method (see e.g. [4] for applications in other engineering areas) or the spectral density method proposed in [5] belong to the latter category.

This classification reflects both computational and experimental approaches needed for obtaining stochastic model parameters. The first category covers the discrete parameter space models (DPS). It is based on splitting each board into cells of equal size being assigned a constant value of stiffness/strength. The second category represents the continuous parameter space models (CPS), where no fixed grid or coordinates are imposed on the parameter space variable x. It can be further classified into two sub/categories: (i) weak zone models (WZ) characterized by randomly distributed WZs, each having a given length and constant material parameters and (ii) a truly continuous model allowing for differentiable stiffness profiles. Each model group makes it possible to construct a set of process realizations from which the process characteristics can be obtained. On

micro-scale, the stiffness mean and the auto-covariance function express random material properties stemming from irregularities within each board due to knot clusters. On mesoscale, the cross-covariance functions reflect the dependence of these properties between adjacent boards.

The WZ models, associated with the hierarchical (micro/meso) models [6], became very popular in the 1990s and were originally intended to predict strength. In [7] also stiffness as an exception is addressed. Building up on an extensive laboratory measurements carried out in [8] the total knot area ratio tKAR and the dynamic stiffness E_{dyn} were observed as the most useful indicators for the prediction of stiffness and strength of both the clear wood (CWS) and knot sections (WS). In this model, tKAR is expressed as an exponential function of three variables - the deterministic logarithmic mean tKAR of all WS within a sample of boards, next the microscopic normally distributed fluctuations of the logarithmic tKAR_{ij} of the WS_j within the board i, and finally, the mesoscopic normally distributed difference between the logarithmic mean tKAR of individual boards and a sample of all boards. In truly continuous models the micromechanical models, see Section 6.4.3, are recommended in conjunction with grain angle information obtained by laser scanning [3]. In view of prospective numerical analysis the stochastic process is prevailingly expressed as a linear combination of deterministic functions with random coefficients such as, e.g. in the KL expansion. It is argued in [9] that the WZ models, in analogy to the DPS models, are not expected, in contradiction to the CPS models, to correctly consider the fiber deviations before knot and after knot clusters. Probabilistic models either discrete or continuous if focused just on variations within one board may underestimate, particularly in GLT beams, the mitigating impact of clear wood in adjacent boards (above and below) on the vicinity of the WZ in the middle board. To analyze this problem consistently, the cross-covariance functions of material properties need to be at hand. The difference of the logarithmic tKARs between the boards as proposed in [7], however promising, could capture the spatial variability only on average.[1]

It is clear that on this structural level the macroscopic properties of boards are highly dependent on the way they are processed from original wood although they are cut merely along the grain. Apart from that, the wood microstructure should not be completely omitted when referring to its macroscopic properties. To that end, a considerable differences in the porosity of early and latewood, volume fractions of individual material phases building the cell wall, and the microfibril orientation angle (MFA), in particular, play a significant role in estimating the effective properties, e.g. from homogenization [11, 12, 13, 14]. Although the random nature of volume fraction of lumens and MFA will not be directly addressed in this paper, some elements of homogenization will be adopted to provide initial estimates of shear moduli also needed in the adopted numerical analysis, see Section 6.4.

In all above cases the initial estimates of material properties entering the predictive numerical analyses often show a considerable scatter and call for improvement. Here,

[1] A similar mitigating effect is well known from aerodynamics. As was recognized in the early 1990s, the average pressure of turbulent air flow on a surface decreases with the area of the surface. This phenomenon is described, e.g. by means of the coherence function, see [10].

a suitable method of attack is the Bayesian statistical method [15, 16] or the Bayesian inference if referring directly to the process of updating our prior state of knowledge about the adopted parameters based on what we know now, see also [17] for a particular application to wood. The Bayesian inference finds its application in many fields when one wants to update the prior belief about distribution of possible values of unobservable model parameters such as material properties or fitting parameters based on various types of measured data, e.g. displacements. This is commonly the case in engineering, since there are numerous ways the parameters can influence the measurable properties of the system in question. With reference to GLT beams a general methodology has been suggested in [18] concentrating, however, on the longitudinal modulus of wood only. In this paper, we revisit this task in much broader sense addressing other sources of uncertainties in the material model and accounting for the geometrical assumptions when designing a macroscopic model of the beam as a whole.

The Bayesian notion of probability is taken more generally as we commonly do. The distribution of values, typically given by the probability density function (PDF) is attributed not only to the observed data but also to the unobserved model parameters. The Bayes theorem serves us to reappraise our prior belief (distribution) of the model parameters based on the data that the model produced. The result is an updated (posterior) distribution of the model parameters. The main advantage of this approach is that the extent to which our prior belief gets refined inherently reflects the number and credibility of the observed data. On the other hand, the method does not provide any feedback about the model correctness and prior parameter distribution suitability. If these are wrong, we get the wrong posterior distribution without warning.

Although formulation of the posterior distribution is quite straightforward, the process of obtaining the statistics of this distribution, e.g. expected values and standard deviations, can be challenging especially when the joint posterior distribution is of a high dimension. Then the posterior distribution has to be analyzed numerically from simulations, which is typically a variant of the Markov chain Monte Carlo method (MCMC) such as the Metropolis–Hasting algorithm, Hamiltonian Monte Carlo algorithm or Gibbs sampling. For details on these algorithms we refer the interested reader to [19]. Note that in many cases there is no need to program own code as for example the last method is implemented in open source program JAGS (Just Another Gibbs Sampler, [20]), which allows the user to specify the stochastic model declaratively in a dialect of BUGS (Bayesian inference Using Gibbs Sampling, [21]) language and generate the samples of unobserved model parameters distributed according to their posterior joint distribution. This program is also exploited in the present study.

While not of our primary interest the joint probability density function provided by MCMC can be used to extract marginal distributions of model parameters of interest to be further utilized in other types of stochastic simulations adopting typically the finite element method (FEM) to solve the underlying structural problem, e.g. the GLT beam. As typical of many branches of engineering, the following three technologies are advocated for a fully probabilistic reliability analysis of timber structures, e.g. [9]: (i) Stochastic FEM in conjunction with Monte Carlo or Latin Hypercube Sampling simulations, (ii)

the perturbation method, (iii) the spectral stochastic FEM. The perturbation method involves linearization at the mean and as such is limited to small values of coefficients of variation (COV should be less then 0.1), see e.g. [22]. As was corroborated by data presented in [9], this requirement is mostly (as a rule) met. The opposite is rather an exception though it cannot be ruled out with a certainty. This piece of knowledge will be exploited in Section 6.5.2 when linearizing the proposed finite element model of GLT beam.

This short exposure to various approaches to the analysis of wood and timber structures proves a considerable interest in stochastic and probabilistic modeling. However, to bring this issue to points of practical applications seems far from satisfactory. To reach out to practical engineers while still reflecting the random nature of wood properties in structural design we propose a simple tool allowing for a reliable prediction of the linear response of glued laminated timber beams, thus concentrating on stiffness or serviceability. The present approach can be regarded as an alternative to standard discrete as well as continuous models. From the practical applicability point of view it falls into the category of models exploiting nondestructive measuring techniques such as laser scanning [9, 23] or application of more appealing descriptors such as knot indicator K_m or the dynamic modulus of elasticity E_m [7] which can be all adopted with or linked to the machine grading process.

To proceed one step further towards the evaluation of already existing beams in cases where no control on layup of commercially produced beams is being enforced, we consider the material parameters be obtained from standard macroscopic indentations measurements using the Pilodyn device together with Eq. (6.1). This requires:

- Formulating an efficient and sufficiently accurate FEM model of a glued laminated timber beam. If limiting our attention to elasticity the standard beam elements developed on the bases of Mindlin's beam theory prove sufficient.

- Improving estimates of the longitudinal elastic modulus E provided by the Pilodyn device through the modified parameters A, B, recall Eq. (6.1). In such a case this equation is approached in a broader sense to give values of a certain model parameter representing a smeared longitudinal elastic stiffness of wood that combines both the clear wood and weak sections.

- Estimating the longitudinal shear modulus G or the G/E ratio that appears in the formulation of the material model and the derivation of the through thickness homogenized properties of GLT beams.

This methodology would thus allows for combining the developed computational model and the indentation measurements employing the improved parameters A,B in predicting the response of other GLT beam to be used on the construction side, which can be possibly compared with the original design.

Achieving this goal is outlined in the remainder of the paper. To introduce the subject we begin in Section 6.3 with the description of the stochastic model where individual stochastic parameters are identified. Determination of the experimentally measured data

is provided in Section 6.4. Therein, we also show how our initial guesses about stochastic parameters, which enter the Bayesian theorem, are obtained. We then proceed to Section 6.5 by formulating the corresponding finite element model for the evaluation of some of the measured data numerically. Finally Sections 6.6 and 6.7 provide discussions and comments on the results and validation of the proposed methodology.

6.3 Hierarchical stochastic model

Hierarchical stochastic model is a system of parameters and data linked by either stochastic or deterministic relations. The stochastic relation $x \sim \mathcal{A}(a,b)$ means that the quantity x is distributed according to distribution $\mathcal{A}$ with parameters a and b. The deterministic relation $x \leftarrow A(a,b)$ states that the quantity x takes the value of expression A involving parameters a and b. Following the BUGS language inspired notation the present model reads

$$
\begin{aligned}
w_{ij} &\sim \mathcal{N}(\tilde{w}_{ij}, \sigma_w), && (6.2)\\
\tilde{w}_{ij} &\leftarrow f_{ij}(\boldsymbol{E}, \boldsymbol{G}), && (6.3)\\
\gamma_j &\sim \mathcal{N}(\tilde{\gamma}_j, \sigma_\gamma), && (6.4)\\
\tilde{\gamma}_j &\leftarrow g_j(\boldsymbol{E}, \boldsymbol{G}), && (6.5)\\
d_{kl} &\sim \mathcal{N}(\tilde{d}_k, \sigma_d), && (6.6)\\
\tilde{d}_k &\leftarrow (E_k - A)/B, && (6.7)\\
G_k &\leftarrow r_{GE} E_k, && (6.8)\\
E_k &\sim \mathcal{N}(\mu_E, \sigma_E), && (6.9)\\
\mu_E &\sim \mathcal{U}(\mu_{E,min}, \mu_{E,max}), && (6.10)\\
\sigma_E &\sim \mathcal{U}(\sigma_{E,min}, \sigma_{E,max}), && (6.11)\\
\sigma_w &\sim \mathcal{U}(\sigma_{w,min}, \sigma_{w,max}), && (6.12)\\
\sigma_\gamma &\sim \mathcal{U}(\sigma_{\gamma,min}, \sigma_{\gamma,max}), && (6.13)\\
\sigma_d &\sim \mathcal{U}(\sigma_{d,min}, \sigma_{d,max}), && (6.14)\\
A &\sim \mathcal{U}(A_{min}, A_{max}), && (6.15)\\
B &\sim \mathcal{U}(B_{min}, B_{max}), && (6.16)\\
r_{GE} &\sim \mathcal{U}(r_{GE,min}, r_{GE,max}). && (6.17)
\end{aligned}
$$

The stochastic model describes how the measured data are actually generated. Since concentrating on serviceability of GLT beams we choose deflections w_{ij} as the most easily measurable macroscopic indicator of bending stiffness expected also to suffer from much smaller measurement error in comparison for example to longitudinal strains. The average shear strain γ_j is then selected to address the variability of shear stiffness entering, apart from the longitudinal stiffness, the computational model discussed in detail in Section 6.5. The variability of the longitudinal stiffness within each board is finally linked to the indentation depth d_{kl} as the most easily measurable indicator of local

stiffness. While the first two quantities follow from the four point bending test, the last quantity is obtained from the application of the Pilodyn 6J indentation device [1, 14], see also Section 6.4 for some details on the present experimental program. Nevertheless, some brief explanation is needed already here to understand the adopted notation. In particular, we expect that the vertical deflection w_{ij} is measured at selected points ($i = 1, \dots, N_w$) on the bottom face of the beam and recorded for each of the applied loading steps. Although the behavior is essentially elastic, choosing a relatively large number of loading steps ($j = 1, \dots, N_F$) gives us a sufficient amount of data for properly identifying the measurement error. The average shear strain γ_j was determined indirectly by means of digital image correlation (DIC) again for all loading steps. The indentation depth d_{kl} identifies the lth indentation ($l = 1 \dots N_{ind,k}$) measured in the kth board ($k = 1 \dots N_b$), where N_b and $N_{ind,k}$ represent the total number of boards making up the beam and the corresponding number of indentations within a given board, respectively.

Equation (6.2) expresses our assumption that the measured values of the vertical displacement w_{ij} are normally distributed around their theoretical values $\tilde{w}_{ij}$ with standard deviation σ_w. This assumption is equivalent to the measured values being influenced by a random error, i.e. $w_{ij} = \tilde{w}_{ij} + \epsilon$, where $\epsilon \sim N(0, \sigma_w)$ is a normally distributed measurement error with zero mean and standard deviation σ_w. The theoretical value of the displacement $\tilde{w}_{ij}$ follows from the FEM simulation for given values of the longitudinal elastic and shear moduli. The FEM simulation is formally denoted in Eq (6.3) as $f_{ij}(\boldsymbol{E}, \boldsymbol{G})$, where $\boldsymbol{E}, \boldsymbol{G}$ represent the vectors of particular outcomes, E_k, G_k, of moduli in each board k. In analogy, Eqs. (6.4) and (6.5) state that the average shear strain γ_j is normally distributed around the theoretical value $\tilde{\gamma}_j$ with a different standard deviation σ_γ. Its theoretical value is again obtained by FEM computations denoted as $g_j(\boldsymbol{E}, \boldsymbol{G})$. Similarly, the measured values of indentation depths d_{kl} are normally distributed around their theoretical value $\tilde{d}_k$ with standard deviation σ_d. Although we assume in the computational part a homogeneous material in each board, the stochastic relation (6.6) captures both the experimental error and the natural variability of the wood properties. The theoretical mean value of the penetration depth $\tilde{d}_k$ is assumed unique for each board k and depends linearly on the theoretical value of the Young modulus E_k according to relation (6.7). It is clear from Eq. (6.8) that the board shear modulus G_k is not taken as an independent quantity subject to identification but is rather tied to a corresponding Young modulus E_k through the r_{GE} ratio, which in turn is considered stochastic and shared by all boards.

Equations (6.9)–(6.17) provide a list of unobservable parameters considered random in the present model and expresses our prior belief about their values. The values of the Young modulus E_k are again assumed normally distributed with the mean μ_E and the standard deviation σ_E, both common to all timber boards. This stems from the fact that the entire beam is composed of one type of wood only. In particular, the analyzed beam was produced commercially out of spruce timber of average density $\rho = 499$ kg/m^3 resulting in the glulam strength class GL28h as specified by the supplier.

Stochastic relation (6.9) then reflects the natural variability of the wood quality among different boards. The hierarchy of the model now becomes clear once choosing

the parameters μ_E and σ_E as random and statistically independent. These parameters, together with the measurement error measures $\sigma_w, \sigma_\gamma, \sigma_d$ and the G/E ratio r_{GE}, are termed the top level parameters in this hierarchical model. To complete our exposure to the model parameters we mention the last two top level parameters A and B in Eq. (6.7). This parametric equation is in general used in its inverse version to allow for mapping the indentation depth to the longitudinal elastic modulus, recall Eq. (6.1). However, unlike treating them as deterministic, which is a common engineering approach, these parameters are considered random thus allowable for updating.

For simplicity, all the top level model parameters are assigned uniform prior distributions $\mathcal{U}(x_{min}, x_{max})$. By this choice we express our believe that the value of a particular parameter is within certain limits (x_{min}, x_{max}), but no value within these limits is assumed to be more probable than any other. For particular values, see Section 6.4. Choosing w_{ij}, γ_j, d_{kl} and E_k to follow normal distribution is also driven purely by simplicity. While adopting log-normal distribution appears more appropriate to avoid sampling negative values, the use of normal distribution proved sufficient as no such difficulties have been observed in our study. This is attributed to a moderate variability of wood seen for example in the distributions of board elastic moduli E_k in Fig. 6.12 found from the original Pilodyn equation (6.22). Comparison of the measurements of elastic modulus of Norway Spruce fitted to various types of distributions can be found, e.g. in [24] for a broad range of grain orientation and load direction showing no particular difference between normal and log-normal distribution thus further supporting the present choice.

Before proceeding with the mathematical formulation of the Bayesian theorem pertinent to the present model we would like to mention several assumptions adopted when building the model. These include ergodicity of the experimental errors σ_w and σ_d and their independence of the actual value of the measured deflection or indentation depth. Further, we assume that the same experimental error applies to all three locations where the deflection is monitored. We further assume that the geometry of the beam, i.e. the board length and thickness, the distance of the supports, the position of the loading forces and deflection sensors are known exactly. We also do not concede any error in the value of the loading force F_j.

The following paragraphs outline the specific format of the Bayesian theorem in the light of the present model. An inexperienced reader may also consult a brief exposition to a general theory of Bayes' theory and Bayesian updating given in the appendix.

Suppose that vector $\boldsymbol{a} = \langle a_i \rangle$ represents the sequence

$$\langle a_i \rangle_{1 \le i \le n} = (a_1, a_2, \ldots, a_n)$$

and $\langle a_{ij} \rangle$ stands for

$$\langle a_{ij} \rangle_{1 \le i \le m, 1 \le j \le n_i} = (a_{11}, a_{12}, \ldots, a_{1n_1}, a_{21}, a_{22}, \ldots, a_{2n_2}, \ldots, a_{m1}, a_{m2}, \ldots, a_{mn_m}).$$

The normal distribution and uniform distribution PDFs are denoted as

$$f_N(x;\mu,\sigma) = \frac{1}{\sigma\sqrt{2\pi}}\, e^{-\frac{(x-\mu)^2}{2\sigma^2}}, \tag{6.18}$$

$$f_U(x;a,b) = \begin{cases} \dfrac{1}{b-a} & \text{for } x \in [a,b] \\ 0 & \text{otherwise} \end{cases}. \tag{6.19}$$

Having the model formulated and taking into account the above notation we may now proceed to rephrase the Bayesian statistical method to express the posterior (improved) joint PDF of model parameters as

$$\begin{aligned} &\pi(\langle E_k\rangle, \mu_E, \sigma_E, \sigma_w, \sigma_\gamma, \sigma_d, A, B, r_{GE} | \langle w_{ij}\rangle, \langle\gamma_j\rangle, \langle d_{kl}\rangle) \propto \\ &\prod_{i=1}^{N_w}\prod_{j=1}^{N_F} f_N(w_{ij};\tilde{w}_{ij},\sigma_w) \times \prod_{j=1}^{N_F} f_N(\gamma_j;\tilde{\gamma}_j,\sigma_\gamma) \times \prod_{k=1}^{N_b}\prod_{l=1}^{N_{ind,k}} f_N(d_{kl};\tilde{d}_k,\sigma_d) \times \\ &\prod_{k=1}^{N_b} f_N(E_k;\mu_E,\sigma_E) \times f_U(\mu_E;\mu_{E,min},\mu_{E,max}) \times f_U(\sigma_E;\sigma_{E,min},\sigma_{E,max}) \times \\ &f_U(\sigma_w;\sigma_{w,min},\sigma_{w,max}) \times f_U(\sigma_\gamma;\sigma_{\gamma,min},\sigma_{\gamma,max}) \times f_U(\sigma_d;\sigma_{d,min},\sigma_{d,max}) \times \\ &f_U(A;A_{min},A_{max}) \times f_U(B;B_{min},B_{max}) \times f_U(r_{GE};r_{GE,min},r_{GE,max}), \end{aligned} \tag{6.20}$$

where the operator "$\propto$" means proportional to (that is, the two sides are equal except for the normalizing constant C). The quantities $\langle\tilde{w}_{ij}\rangle$, $\langle\tilde{\gamma}_j\rangle$, $\langle\tilde{d}_k\rangle$, entering the likelihood function (the first three terms on the right hand side of Eq. (6.20)), and the shear moduli $\langle G_k\rangle$ are computed according to the deterministic relations (6.3), (6.5), (6.7) and (6.8), respectively. The prior distributions of the top level parameters (the terms following the likelihood functions) are assumed statistically independent. This, however, is no longer true when referring to the posterior joint PDF on the left hand side of Eq. (6.20), because the statistical dependence manifests itself through the data entering this equation.

The expression on the right hand side is thus not exactly a PDF in the statistical sense as its (N_b+8)-dimensional integral over the entire stochastic domain would not equal to one but to the aforementioned constant C. Fortunately, the family of MCMC algorithms allows us to generate samples of parameters distributed according to the posterior distribution in such a proportional form. Once we have a sufficiently large number of samples of the updated model parameters (the Markov chain is sufficiently long to produce stationary distributions - in the present the length of chain amounted to 5000 samples with the burn-in period equal to 1000 samples), we compute their statistics from marginal distributions, compare them to the prior distributions and thus learn how the observed data changed our prior estimates of the model parameters. To support credibility of the obtained results, two such chains were generated and compared.

But before arriving at these distributions presented in Section 6.6 there are still a few steps to take as discussed next.

6.4 Laboratory testing of laminated timber beam and prior distributions

An extensive laboratory program has been established to acquire the necessary information needed in Eq. (6.20). The observable measured data, i.e. w_{ij}, γ_j, d_{kl} entering the definition of the likelihood function were determined by combining the macroscopic four-point bending and Pilodyn 6J indentation tests. These were accompanied by small scale nanoindentation tests combined with homogenization in the solution of a certain inverse problem to obtain a rough notion about the bounds appearing in the prior distributions, namely Eq. (6.17). This, however, goes beyond the present scope and the interested reader is referred to [25]. For convenience, some elementary steps concerning the homogenization of wood will be outlined later in this section. In addition, Eq. (6.7) given in its original form with the values of parameters A, B typically used in engineering practice will be employed to feed Eqs. (6.9)–(6.11).

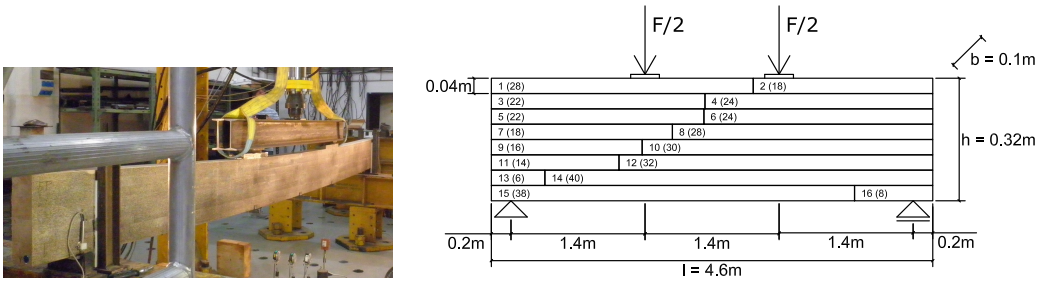

(a) (b)

Figure 6.1: Four point bending test: (a) experimental setup, (b) geometry, loading conditions, board number, number of indents in parenthesis for the GLT-2 beam, see Section 6.4.1

6.4.1 Four-point bending test and digital image correlation

The standard four-point bending test enhanced by Digital Image Correlation (DIC) has been chosen to measure the beam vertical displacements, and through-thickness strain averages.

Three simply supported GLT beams, further referred to as GLT-1, GLT-2, GLT-3, were tested after several weeks of being stored in the lab which resulted in the average moisture content $u \approx 12\%$. All experiments were performed in a displacement control regime with a gradual increase of the prescribed vertical displacements at two different loading rates ($r_1 = 1.2\,\mathrm{mm/min}, r_2 = 0.3\,\mathrm{mm/min}$) until failure as shown in Fig. 6.2(a). The locations of the two loading points is seen in Fig. 6.1 together with the beam geometry (length $L = 4600$ mm, width $b = 100$ mm, height $h = 320$ mm), layup, and the actual board number. Three vertical displacements were measured at the bottom surface of the beam below the two loading points (w_1, w_3) and at the beam center (w_2). Thus $i = 1, 2, 3$ in Eq. (6.2).

While the results pertinent to the GLT-2 beam were exploited in the derivation of the posterior PDF and the associated marginal distributions including the Pilodyn equation parameters A, B, the results of the other two beams were used to check, at least partially, the applicability of the proposed strategy mentioned in the introductory part.

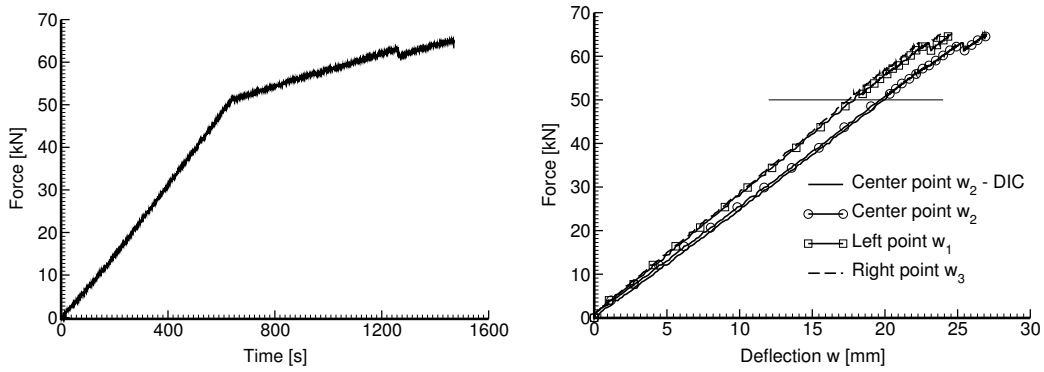

(a) (b)

Figure 6.2: Results of the four point bending test for GLT-2: (a) variation of the resulting force as a function of time, (b) variation of vertical displacements at selected points w_1, w_2, w_3 as a function of the applied load

In particular, variation of the measured vertical displacements as a function of the applied load is plotted in Fig. 6.2(b).[2] The horizontal line indicates the maximum load level of $F = 50$ kN adopted in the Bayesian updating. This value is found well bellow the ultimate load $F_u = 65.6$ kN, thus ensuring the assumption of the linear behavior of the system.

Recall that even the theoretical values of vertical displacements $\tilde{w}_{ij}$ depend on the value of shear modulus G linked in the Mindlin beam theory to the cross-section shear strain $\tilde{\gamma}_j$. If we wish to introduce this quantity in the Bayesian inference a corresponding measured value is needed. Unlike a vertical displacement, a direct measurement of this quantity is not an easy task. Herein, DIC method was used to provide local strain profiles, see also [23].

It allows for tracking the motion and distortion of the speckled color pattern applied on the surface of a specimen. It should be noted that the pattern quality has a dominant influence on the resolution and accuracy of the DIC results. Beside the high-contrast requirement, the pattern must be random and isotropic [26, 27, 28].

The main idea of DIC is to match a subset of gray-scale pixels in the reference image (representing the initial state) to a similar subset in the target image of a deformed surface. The output of DIC is provided in the form of a grid containing information about displacements and strains with respect to the reference configuration. For details on DIC algorithms, we refer the interested reader to [29, 30]. For illustration, some of the results derived from the four-point bending test are presented for the left part of the

[2]For the sake of brevity and if not otherwise stated the plotted results were found for the GLT-2 beam.

beam in Fig. 6.3.[3] Therein, the results found directly from the reference-deformed image mapping were further interpolated to get the plotted continuous fields.

The results in Figs. 6.3(c,e) support the theoretically expected zero shear strain and no dependence of through-thickness variation of axial strain on x in the mid section of the beam between the two loading points. They were derived with the open-source code Ncorr-Post-CSTool [31, 32], applied successfully to more advanced issues such as cracking of cementitious composites [33], as an extension of DIC code Ncorr v1.2 [34].

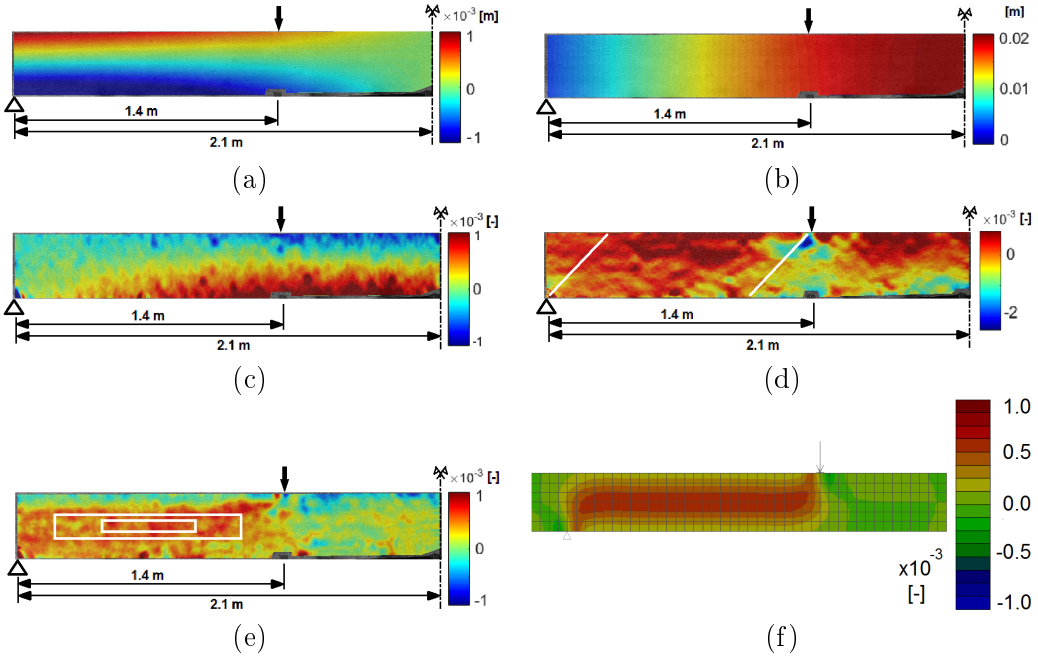

Figure 6.3: Selected results from DIC measurements for GLT-2 pertinent to load step No. 25: (a) horizontal displacement [m], (b) vertical displacement [m], (c) axial strain [–], (d) vertical strain [–], (e) shear strain [–], (f) shear strain from FEM [–]

The fact that in the Mindlin beam theory the shear strain is assumed constant over the beam height promotes two options how to introduce this quantity into the Bayesian inference. One can either calculate the average shear strain at a given location, say $x = \bar{x}$, adopting the Mindlin beam theory as

$$\gamma_{xz}(\bar{x}) = \underbrace{\varphi_y(\bar{x})}_{\frac{\Delta u(\bar{x})}{h}} + \frac{\mathrm{d}w}{\mathrm{d}x}(\bar{x}), \tag{6.21}$$

where h is the beam height, or by averaging the shear strain derived directly from DIC, recall Fig. 6.3(e). This latter option has been adopted in the present study. Unfortunately,

[3] Note that due to laboratory space limitations only one side of the beam was subjected to DIC measurements. Also, the end sections to the left and right from the beam supports were not examined due to presence of stabilization elements, see Fig. 6.1(a).

for specimens of this size the resulting strains show a considerable noise when plotted point-wise at specific locations. Some sort of averaging is therefore needed to arrive at meaningful results. Here, the variation of the "maximum" shear strain as a function of the applied load within the section of a theoretically constant shear force was found by averaging the local strains over a certain region. In particular, two such regions on both halves of the beam having dimensions 500 $\times$ 50 mm and 1000 $\times$ 100 mm, respectively, were analyzed, see Fig. 6.3(e). It is evident from Fig, 6.3(e) that both averaging regions fall out of the reach of local effects as schematically depicted in Fig. 6.3(d) and further corroborated by numerical results in Fig. 6.3(f). Note that the FEM analysis was carried out assuming a homogeneous beam with an equivalent Young's modulus derived from Eq. (6.38).

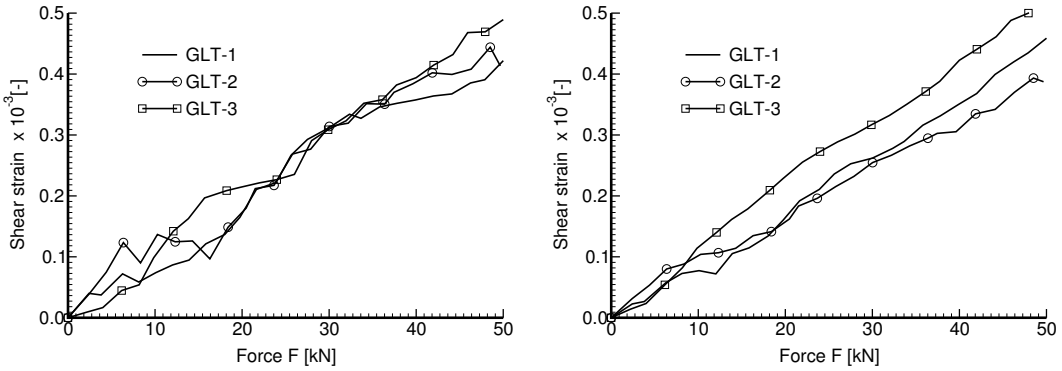

(a) (b)

Figure 6.4: Variation of the average shear strain γ as a function of the applied load derived by scaling the "maximum" shear strain averaged over a) 500 $\times$ 50mm and b) 1000 $\times$ 100mm sections

Assuming that the actual shear strain follows parabolic distribution over the beam height these values were further scaled by the factor of 2/3 to get the required strain averages. The associated variation of the shear strain is plotted in Figs. 6.4(a,b)[4]. A simple 2D FEM plane stress analysis was performed for the homogeneous beam with some equivalent properties listed in the last row of Table 6.2 to check the credibility of this approach. To give reasons for the finding that the GLT-3 beam exhibits a slightly less stiff response, seen e.g. in Fig. 6.4(b), we store in Table 6.1 the equivalent bending stiffnesses for individual beams derived from the four point bending test together with basic statistics of the axial Young modulus found from all indentation measurements using the original (PO) as well as updated (PU) parameters A, B in the Pilodyn equation (6.1). Derivation of these quantities is provided in detail in Section 6.6.

[4]Note that the parabolic shear strain averaged over a certain mid section s of the beam height h equals to $\langle\gamma\rangle_s = \gamma_{max}\,(1 - \frac{1}{3}(\frac{s}{h})^2)$. Thus in our two cases (s_1=100mm and s_2=50mm) we get $\langle\gamma\rangle_{100} = 0.97\gamma_{max}$ and $\langle\gamma\rangle_{50} = 0.99\gamma_{max}$, respectively.

Table 6.1: Equivalent bending modulus derived from the four point bending test and averages and standard deviations of the axial Young modulus calculated from indentation measurements. All values are in [GPa]

Beam	E_{eq} (bending test)	μ_E^{PO}	σ_E^{PO}	μ_E^{PU}	σ_E^{PU}
GLT-1	11.66	13.62	1.048	12.35	1.424
GLT-2	12.15	13.59	0.836	12.31	1.136
GLT-3	10.09	12.82	1.477	11.26	2.008

6.4.2 Macroscale indentation with Pilodyn 6J testing device

Modulus of elasticity of wood can be measured by various methods. When considering wood segments already built into an existing structure it is necessary to adopt non-destructive testing methods, which cause either no or negligible damage to the tested material. Owing to a considerable heterogeneity of laminated timber structures a large number of local measurements is needed. At present, only one such experimental method, which builds upon driving an indenter with the help of Pilodyn 6J device in Fig. 6.5 into the wood, is available.

Figure 6.5: Pilodyn 6J indentation device

In particular, a spike of 2.5 mm in diameter is shot into the wood with the enforced energy of 6 J. While driving the indenter more or less in the transverse direction, the empirical equations (6.1) or (6.7) provide the local elastic modulus in the fiber direction [1, 14]. For spruce the following values of parameters A, B have been found optimal

$$E = A + Bd = 19.367 - 0.5641d. \tag{6.22}$$

The Pilodyn 6J device allows for reading d with the accuracy of 0.5 mm, which yields the corresponding error of the computed elastic modulus equal to 0.28 GPa. Additional error follows from the material heterogeneity and uneven inclination of tangents to annual rings at the point of indentation with respect to the vertical surface of the structural element. In the presented Bayesian inference all these errors are reflected by a single parameter σ_d in Eq. (6.6).

Basic statistical evaluation summarized in the last four columns of Table 6.1 was performed on the basis of 368 indentations for GLT-1, 368 indentations for GLT-2, and 328 indentations for GLT-3, respectively. The measurements of indentation depth were carried out on both sides of all beams on a regular grid of points spread 20 cm apart. These measurements provided also bounds on parameters μ_E, σ_E in Eq. (6.9). The number of indents is much smaller in comparison to 3600 indents examined in [1] and used in [18] to determine statistical moments pertinent to each board and subsequently to specify the prior distributions for each board directly in the form of normal distribution. Also note that the number of indents in some of the boards indicated in Fig. 6.1(b) is not sufficient to arrive at reliable mean values, which further promotes our present hierarchical model.

6.4.3 Homogenization of wood

Unfortunately, there is no such simple experiment to measure the shear properties of wood. Therefore, if the influence of shear stiffness is to be investigated independently from tensile/compression effects, we should seek for an alternative such as homogenization. Because only a rough estimate of the longitudinal shear modulus is needed, we adopt here the Mori-Tanaka [35] analytical scheme, thus omitting some of the microstructural details [36]. Moreover, we follow closely the footprints of a hierarchical homogenization laid down in [11] combined here with nano [13, 37, 38] or macroindentation [14] to address the influence of MFA, which considerably influences the effective shear stiffness.

Performing a two-step homogenization procedure at the level of cell wall as proposed in [11] yields the estimates of effective properties of the cell wall. This comprehensive paper provides all the necessary information regarding the tissue independent properties of individual material phases including their volume fractions to enter the Mori-Tanaka predictions of the homogenized stiffness $\mathbf{L}^{\mathsf{hom}}$ and compliance $\mathbf{M}^{\mathsf{hom}}$ matrices written as

$$\mathbf{L}^{\mathsf{hom}} = \left[\sum_{r=1}^{N} c_r \mathbf{L}_r \mathbf{T}_r\right] \left[\sum_{r=1}^{N} c_r \mathbf{T}_r\right]^{-1}, \quad \mathbf{M}^{\mathsf{hom}} = \left[\sum_{r=1}^{N} c_r \mathbf{M}_r \mathbf{W}_r\right] \left[\sum_{r=1}^{N} c_r \mathbf{W}_r\right]^{-1}, \quad (6.23)$$

where c_r is the volume fraction of the phase r, $\mathbf{L}_r$ and $\mathbf{M}_r$ store the corresponding stiffnesses and compliances and N is the number of phases. $\mathbf{T}_r$ and $\mathbf{W}_r$ are the partial strain and stress concentration factors depending on the shape and orientation of the inclusion and the properties of the matrix phase and follow from the solution of the Eshelby transformation inclusion problem. For further details we refer the interested reader to [13, 35].

The resulting elastic properties for the crystalline cellulose being aligned with the direction of lumens are stored in the 1st row of Table 6.2, where subscripts A, T refer to axial and transverse directions, respectively. To arrive at these results, we neglected for simplicity water and other wood extractives and considered only the cylindrical fiber-like aggregates of crystalline cellulose and of amorphous cellulose embedded into an isotropic polymer matrix of hemicellulose and lignin, see [13] for details. This simplification is in

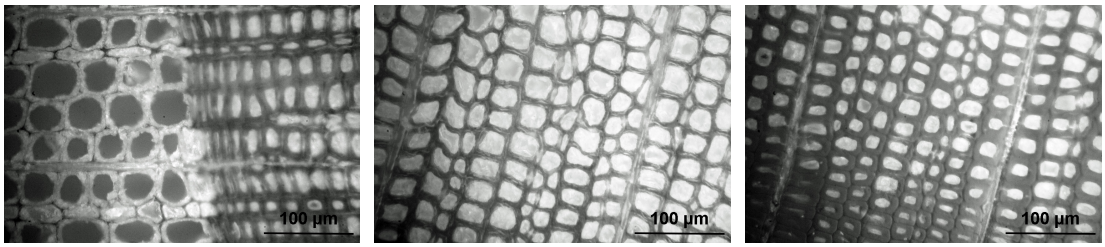

(a) (b) (c)

Figure 6.6: Transverse cross-section of spruce provided by optical microscope: a) microstructure of early and latewood transition, b) detailed representation of earlywood, c) detailed representation of latewood

accordance with the fact that only a rough estimate of $r_{G/E}$ ratio is needed to formulate the prior distribution of this quantity to run the Bayesian updating.

Obtaining the effective properties of wood requires two additional homogenization steps as evident from Fig. 6.6. At the level of early and latewood the next homogenization step still exploits Eq. (6.23) but in this case we consider a composite having the properties of the homogeneous cell wall and being weakened by aligned cylindrical voids (lumens). In the present study the volume fraction of lumens for both early ($c_{LE} = 0.54$) and latewood ($c_{LL} = 0.28$) were found simply from binary counterparts of color images in Figs. 6.6(b,c). The last homogenization step exploits the laminated structure of annual rings seen in Fig. 6.6(a). Using standard rule of mixture the Voigt and Reuss bounds on the effective stiffness and compliance matrices follow from

$$\mathbf{L}^{\text{voigt}} = c_{EW}\mathbf{L}^{\text{EW}} + c_{LW}\mathbf{L}^{\text{LW}}, \quad \mathbf{M}^{\text{reuss}} = c_{EW}\mathbf{M}^{\text{EW}} + c_{LW}\mathbf{M}^{\text{LW}}, \tag{6.24}$$

where $c_{EW} = 0.69, c_{EM} = 0.31$ stand for the volume fractions of the earlywood and latewood, respectively.

Table 6.2: Effective elastic properties from four-step homogenization

Level	E_A [GPa]	G_A [GPa]	ν_A [–]	E_T [GPa]	G_T [GPa]	ν_T [–]	G_A/E_A [–]
Cell wall (MFA=0°)	42.34	2.91	0.25	9.23	2.74	0.42	0.07
Cell wall (MFA=30°)	22.72	6.45	0.45	8.73	3.27	0.34	0.28
Wood (MFA=0°)	22.56	1.09	0.25	2.22	0.82	0.36	0.05
Wood (MFA=30°)	12.07	2.30	0.45	2.49	0.88	0.31	0.19

But before proceeding with this machinery we return back to the level of cell wall. The literature offers a number of evidences suggesting a non-zero MFA. The results provided by nanoindentation is just one particular source [37, 38]. In conjunction with this

approach one may run a solution of a certain inverse problem to estimate the distribution of MFA from a large pool of nanoindentation measurements to be compared with the outcomes of homogenization. A rigorous approach based on the theory of anisotropic nanoindentation has been offered in [39]. We revisited this approach in [40] where detailed comparison between the MFA estimates provided by both the isotropic and anisotropic theory of nanoindentation and Pilodyn type of macroindentation is given. When limiting our attention to anisotropic theory of nanoindentation we receive the value of MFA= 30° calculated as an average from 50 nanoindentations. The corresponding values of elastic stiffnesses are stored in the 2nd row of Table 6.2.

Given the particular value of MFA it is now possible to project the local properties, calculated in the direction of crystalline cellulose, along the direction of lumens, say x_3. Further suppose, that MFA is defined as the angle between the x_3-axis and a line x_{MFA} contained by a plane being perpendicular to the x_1x_2 plane, i.e. the plane normal to the x_3-axis. If no preferential direction of this plane is assumed than orientation averaging is employed to account for all possible orientations of the x_3x_{MFA} plane. In case of discrete averaging the moduli in the 2nd and 3rd rows of Table 6.2 were extracted from

$$\left\langle\left\langle \mathbf{L}^{\mathsf{CW}} \right\rangle\right\rangle = \frac{1}{N}\sum_{i=1}^{N} \mathbf{L}^{\mathsf{CW}}(\alpha_i, \mathrm{MFA}, 0), \tag{6.25}$$

were $N \to \infty$ and $\mathbf{L}^{\mathsf{CW}}$ is the stiffness matrix of the homogenized material surrounding the lumens, thus the properties of the cell wall. This results in a transversely isotropic material. These properties then enter the subsequent homogenization steps at the level of earlywood, latewood and laminate to get the searched value of the effective $r_{G/E}$ ratio.

To conclude this part of the study point out that the averaging based on Eq. (6.25) corresponds to the Voigt type of bound. It is worth mentioning that an analogous approach having attributes of the Reuss averaging, i.e. the stiffness matrix $\mathbf{L}$ is replaced with the compliance matrix $\mathbf{M}$ in Eq. (6.25), predicts for the same searched indentation modulus a different, typically much smaller, value of MFA so that $\langle\langle \mathbf{L}^{\mathsf{CW}} \rangle\rangle^{-1} \neq \langle\langle \mathbf{M}^{\mathsf{CW}} \rangle\rangle$, although $E_A^{\mathsf{Reuss}} \approx E_A^{\mathsf{Voigt}}$. This is not the case when orientation averaging is performed directly within the Mori-Tanaka method, see e.g. [13, 41, 42], rendering a unique value of MFA being almost identical to the Voigt bound further supporting the present choice of Eq. (6.25). Some improvements can be expected if adopting the lamination theory outlined in [43].

The effective properties of the clear wood are listed in the last two rows of Table 6.2 together with the r_{GE} ratio. Clearly, neglecting the non-zero value of MFA largely overestimates the actual wood stiffness.

6.4.4 Selected parameters of prior distributions

Based on the previous experimental-numerical studies the following limits on top level prior distributions listed in Table 6.3 were chosen in this study. Clearly, some of them are unnecessarily wide. But this is done on purpose to show the robustness of Bayesian

inference in conjunction with the MCMC method and support the choice of observable parameters to drive the updating process.

Table 6.3: Minimum and maximum values of the top level parameters set in the uniform prior distributions

Parameter	Unit	lower limit	upper limit
μ_E	GPa	4	30
σ_E	GPa	0.05	4
σ_w	mm	0.1	2
σ_γ	–	0.00001	0.0002
σ_d	mm	0.1	4
A	GPa	$19.367 - 5.0$	$19.367 + 5.0$
B	GPa/mm	-2	0
r_{GE}	–	0.05	0.5

6.5 Finite element model of laminated timber beam

To provide the theoretical values of the vertical displacement $\tilde{w}_{ij}$ and the average shear strain $\tilde{\gamma}_j$ from deterministic relations (6.3) and (6.5) the four point bending test was simulated by means of the Finite Element Method (FEM) assuming one-dimensional beam elements to discretize the laminated beam at hand. The element formulation is based on the Mindlin beam theory taking both the curvature and shear strain into account as outlined next in Section 6.5.1. Although quite simple and efficient the resulting finite element model will appear still to complex for a direct use with the JAGS software. Therefore, a further simplification, discussed in Section 6.5.2, is needed.

6.5.1 Element stiffness matrix and discretization

To formulate the bending and shear stiffnesses of the beam we first express the effective properties of a rectangular cross-section which consists of eight layers, recall Fig. 6.1(b), with different values of E and G, see Figure 6.7(a).

In what follows, E_m denotes the value of Young's modulus, G_m is the shear modulus and z_m is the distance between the mth segment center and the center of the entire cross-section. The homogenized bending stiffness of the cross-section then becomes

$$D_b = bd^3 \frac{1}{12} \sum_{m=1}^{8} E_m + db \sum_{m=1}^{8} E_m (z_m - z_T)^2, \tag{6.26}$$

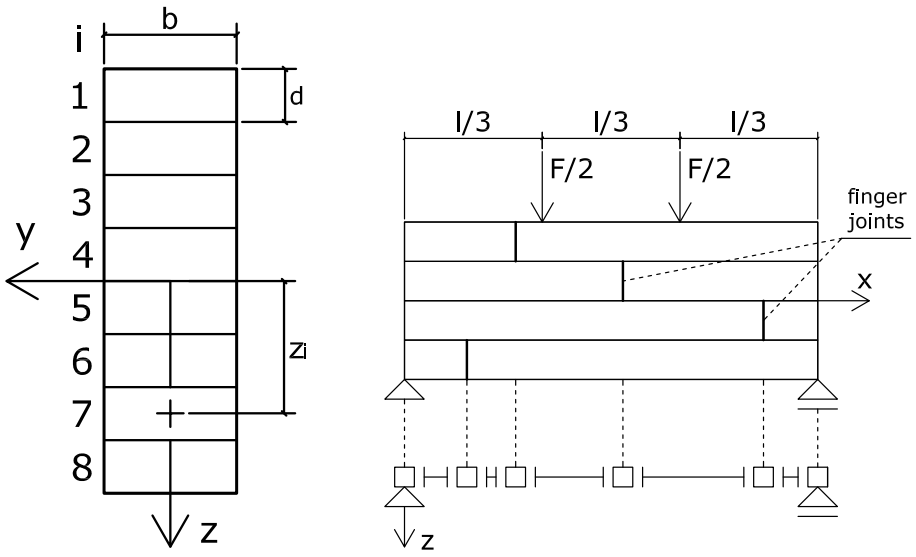

Figure 6.7: a) Geometry of the laminated timber beam cross-section, b) Model of laminated timber beam (note that rectangles denote nodes and the connecting lines denote elements)

where d and b are the board width and thickness, respectively, and z_T represents the position of the centroid of the homogenized cross-section written as

$$z_T = \frac{\sum_{m=1}^{8} E_m z_m}{\sum_{m=1}^{8} E_m}. \tag{6.27}$$

The homogenized shear stiffness of the cross-section reads

$$kGA = \frac{D_b^2 b^2}{bd \sum_{m=1}^{8} \frac{(ES)_m^2}{G_m}}, \tag{6.28}$$

where

$$(ES)_m = bd \sum_{n=m}^{8} E_n (z_n - z_T). \tag{6.29}$$

Conventionally, the vector of nodal forces of the finite element is expressed as a product of the element stiffness matrix and the vector of nodal displacements

$$\boldsymbol{R}^e = \mathbf{K}^e \boldsymbol{r}^e. \tag{6.30}$$

Omitting the axial forces, which are zero during a pure bending, we express the vectors of nodal forces and displacements as

$$\boldsymbol{R}^e = \{Z_1, M_1, Z_2, M_2\}^{\mathrm{T}}, \tag{6.31}$$

$$\boldsymbol{r}^e = \{w_1, \varphi_1, w_2, \varphi_2\}^{\mathrm{T}}. \tag{6.32}$$

The associated stiffness matrix of the beam element with the length L simplifies to

$$\mathbf{K}^e = \frac{2Db}{(1+2\kappa)L} \begin{bmatrix} \frac{6}{L^2} & -\frac{3}{L} & -\frac{6}{L^2} & -\frac{3}{L} \\ -\frac{3}{L} & 2+\kappa & \frac{3}{L} & 1-\kappa \\ -\frac{6}{L^2} & \frac{3}{L} & \frac{6}{L^2} & \frac{3}{L} \\ -\frac{3}{L} & 1-\kappa & \frac{3}{L} & 2+\kappa \end{bmatrix}, \tag{6.33}$$

$$\kappa = \frac{6D_b}{kGAL^2}. \tag{6.34}$$

Apart from the material properties of participating boards E_m, G_m the element stiffness matrix depends on the element length L^e. This length is chosen such as to span the distance between the two closest finger joints in the entire beam as schematically illustrated in Fig. 6.7(b). With reference to Fig. 6.1(b) we arrive in this particular case at a finite element model having 8 elements of a different length, recall Fig. 6.1(b). Obviously, the element stiffness matrix remains constant within each element but may change from element to element depending on the actual values of E_k, G_k in a given board $k = 1, \ldots, N_b$ generated when constructing a Markov chain during the Bayesian inference.

Upon assembly we obtain a system of liner equations to provide unknown nodal displacements and rotations for a given value of the applied load. Using the standard shape functions for beam elements we express the displacements at the three monitored points, i.e. $w_1 = w(x = l/3)$, $w_2 = w(x = l/2)$ and $w_3 = w(x = 2l/3)$, and the average shear strain $\gamma = \gamma(x = 0)$ above the left support.

For the use within the hierarchical stochastic model it is convenient to think of the FEM computations as a simple function mapping an arbitrary set of values E_k, G_k and the load force F_j to the displacements $\tilde{w}_{ij}$ and shear strain $\tilde{\gamma}_j$ at measured points as, recall Eqs. (6.3) and (6.5),

$$\tilde{w}_{ij} = f_i(\boldsymbol{E}, \boldsymbol{G})F_j, \qquad \tilde{\gamma}_j = f_\gamma(\boldsymbol{E}, \boldsymbol{G})F_j. \tag{6.35}$$

Although the MCMC programs are capable of calling a user defined function from an external module, this approach can be limiting for two reasons. First, the function (the finite element model) has to be implemented exclusively in C++, compiled only with recommended compiler and wrapped up in module class implementing specific interfaces. Even though the process of creation custom module is documented to a certain level it can

be quite demanding to wire things together correctly. The second potential reason is the performance limit. The custom function is evaluated every time the MCMC algorithm generates one of typically thousands of samples (outcomes). Therefore, an alternative approach to overcome these drawbacks is proposed in the next section.

6.5.2 Approximation of FEM model

The objective here is to replace the previously formulated FEM model with its suitable approximation, which can be directly implemented in the stochastic model definition and is also faster to evaluate. In the present context, it follows from the linearization of function f_i in Eq. $(6.35)_1$ in the form

$$\overline{f}_i(\boldsymbol{E},\boldsymbol{G}) = f_i(\boldsymbol{E}_0,\boldsymbol{G}_0) + (\nabla f_i)_{\boldsymbol{E}_0,\boldsymbol{G}_0} \cdot (\boldsymbol{E}-\boldsymbol{E}_0,\boldsymbol{G}-\boldsymbol{G}_0). \tag{6.36}$$

The derivatives of f_i with respect to the components of $\boldsymbol{E}$ are precomputed numerically as

$$\frac{\partial f_i}{\partial E_j}\Big|_{\boldsymbol{E},\boldsymbol{G}} \approx \frac{f_i(\langle E_k+\delta_{jk}h\rangle,\langle G_k\rangle) - f_i(\langle E_k+\delta_{jk}h\rangle,\langle G_k\rangle)}{2h}, \tag{6.37}$$

where h represents a small change in the particular value of E_k. The partial derivatives of f_i with respect to the components of $\boldsymbol{G}$ are computed analogically. Similar actions are taken to get an approximation to function f_γ in Eq. $(6.35)_2$. The applicability of Eq. (6.36) has been tested in [18] by comparing predictions provided by this simplified approach with a detailed two-dimensional finite element simulations for given values of material parameters. The components of vectors $\boldsymbol{E}_0,\boldsymbol{G}_0$ were chosen based on homogenization.

Having the precomputed function values and derivatives at hand the evaluation of the approximated function (6.36) involves only matrix operations which are trivial to express in the dialect of modeling language provided by JAGS.

6.6 Resulting estimates of posterior distributions

Running the model in the JAGS program produces a Markov chain (a sequence of samples of random parameters) whose stationary distribution is the searched posterior joint probability distribution $\pi(\langle E_k\rangle,\mu_E,\sigma_E,\sigma_w,\sigma_\gamma,\sigma_d,A,B,r_{GE}|\langle w_{ij}\rangle,\langle\gamma_j\rangle,\langle d_{kl}\rangle)$ in Eq. (6.20) conditional on the measured data $\langle w_{ij}\rangle,\gamma_j,\langle d_{kl}\rangle$. Picking only the components of the chain pertinent to a given parameter allows us to estimate the corresponding marginal distribution. These are plotted in terms of histograms together with the original uniform prior distributions in Figs. 6.8–6.11. The basic statistics of individual distributions are summarized in Table 6.4.[5]

It is obvious that our original, relatively vague, knowledge of these parameters has been considerably improved. In particular, given a relatively large number of measurements, even though assuming an elastic response throughout the loading process, provided a very clear indication of the measurement errors. Second, almost a deterministic

[5]Recall that measurements from the GLT-2 beam were exploited in the Bayesian updating.

Table 6.4: Resulting statistics of the top level parameters extracted from the resulting Markov chain

Parameter	Unit	expected value	standard deviation
μ_E	GPa	12.30	0.191
σ_E	GPa	0.655	0.222
σ_w	mm	0.269	0.023
σ_γ	–	1.21×10^{-5}	1.83×10^{-6}
σ_d	mm	1.30	0.049
A	GPa	20.15	0.109
B	GPa/mm	-0.766	0.187
r_{GE}	–	0.16	0.0017
μ_E^{PO}	GPa	13.59	0.83
μ_E^{PU}	GPa	12.31	1.13

value of the identified mean of the Young modulus of wood indicates that the four point bending test is a "correct" experiment to update this parameter. This is supported by the results in Fig. 6.10(b). Take note that the average of the r_{GE} ratio amounts to 0.16 which is rather close to the ratio predicted by homogenization, recall the last row in Table 6.2. Finally, the results in Fig. 6.11 confirm a truly empirical format of Eq. (6.22) suggesting that a considerable scatter of Young's moduli can be expected if using solely this equation for their estimation.

In [18] the prior distributions were estimated directly from statistics of Young's moduli derived for individual boards purely from indentation. It might therefore be interesting to compare these distributions with those provided by the present model. This can be done as the MCMC produces samples of E_k for each board, recall Eq. (6.9). We plot the resulting histograms for the selected boards in Fig. 6.12. It is perhaps fair to mention that in some cases, recall Fig. 6.1(b), the construction of PDF from Eq. (6.22) relies, as mentioned before in Section 6.4.2, on a limited number of indents. Nevertheless, the message is clear. In particular, improvements to our initial assumption in the distribution of E_k can be expected in boards which may considerably affect the measured vertical displacements as is the case of, e.g. boards No. 14, 15, presented in Figs. 6.12(a,b). On the contrary, boards No. 11, 13, 16 have smaller effect on the vertical deflection which causes a wider spread around the mean value, see also Table 6.5. Both these, rather intuitive, findings are consistent with the Bayesian inference which strongly depends on the construction of a suitable likelihood function.

A final note to this subject addresses the updated parameters A, B. Undoubtedly, if these are introduced in the Pilodyn equation (6.22), a better prediction of the Young modulus, measured by the expected value, is achieved, both in terms of the mean value and standard deviation.

This is also supported by the statistics found from all measurements for individual beams when compared to the associated equivalent bending modulus in Table 6.1

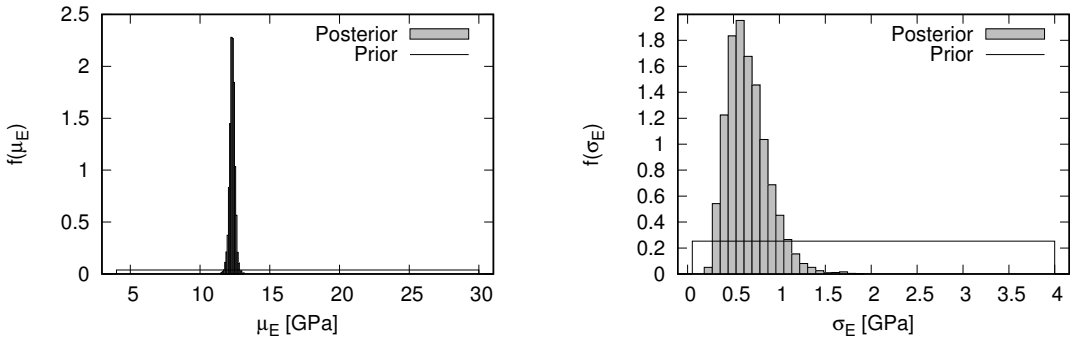

(a) (b)

Figure 6.8: Prior and posterior distribution of Young's modulus of wood: (a) μ_E (b) σ_E

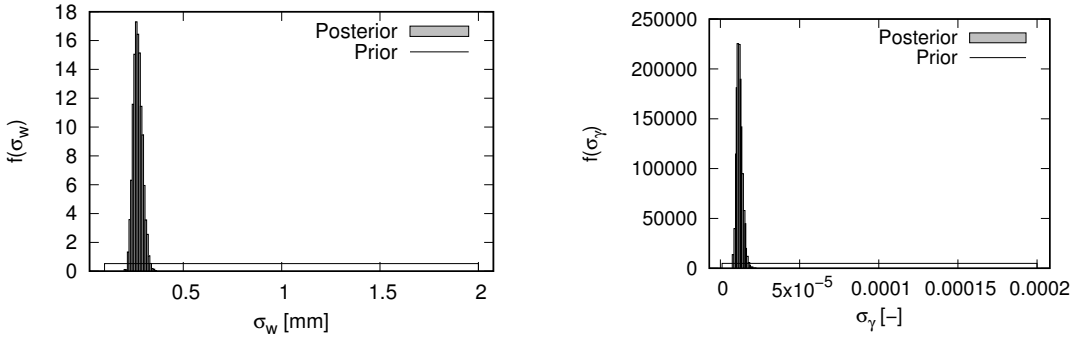

(a) (b)

Figure 6.9: Prior and posterior distribution of measuring errors: (a) σ_w, (b) σ_γ

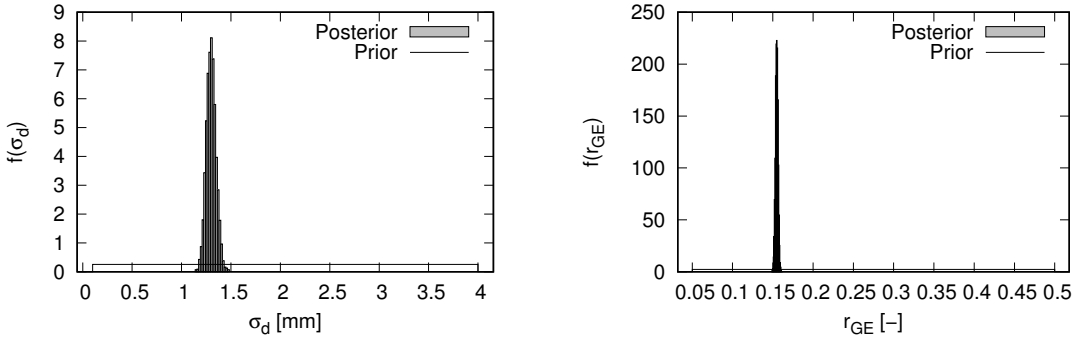

(a) (b)

Figure 6.10: (a) Prior and posterior distribution of (a) measuring error σ_d and (b) ratio r_{GE}

provided by familiar formula, see e.g. [7],

$$E_{eq} = \frac{3aL^2 - 4a^3}{2bh^3\left(2\dfrac{w_2 - w_1}{F_2 - F_1} - \dfrac{6a}{5Gbh}\right)}, \tag{6.38}$$

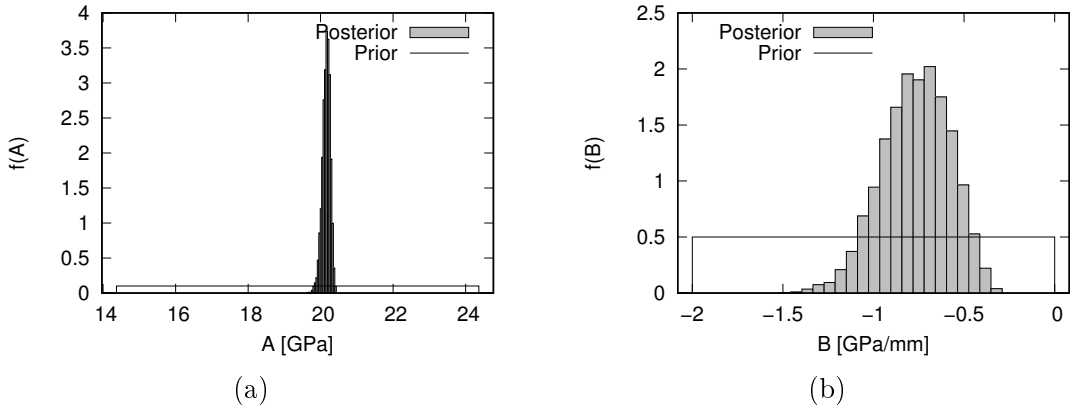

Figure 6.11: Prior and posterior distribution of parameters of Pilodyn equation (6.22): (a) A, (b) B

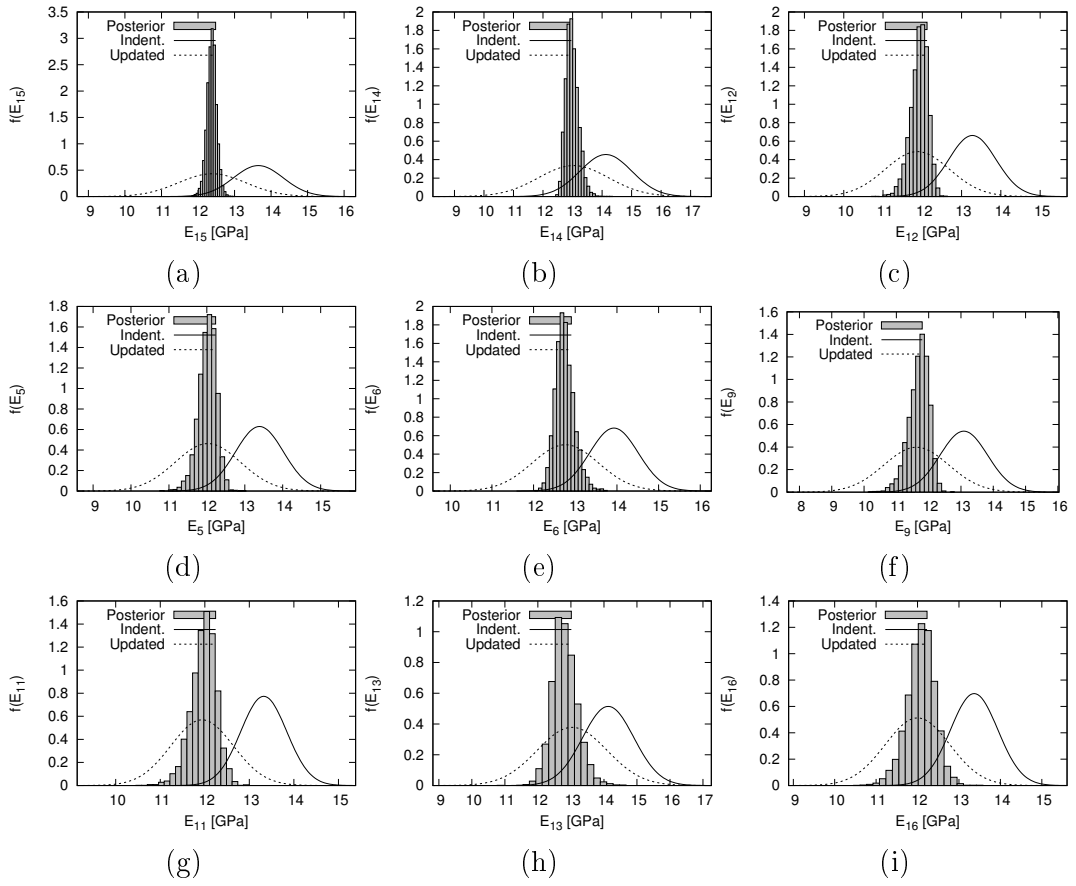

Figure 6.12: Posterior distribution of Young's modulus E_k in selected boards compared to the standard PDF corresponding to the mean and standard deviation of E obtained from indentation depths using Pilodyn equation (6.22) with the original and updated values of coefficients A and B

Table 6.5: Statistics of Young's moduli in each lamina provided by the Pilodyn equation (6.1) using original (PO) and updated (PU) parameters A,B and extracted directly from posterior (pos) marginal distribution; l_i is the board length, N_{ind} is the number of indentations in a board

i	l_i	N_{ind}	μ_E^{PO}	σ_E^{PO}	μ_E^{PU}	σ_E^{PU}	μ_E^{pos}	σ_E^{pos}
	[m]		[GPa]					
1	2.53	28	13.87	0.85	12.69	1.16	12.56	0.16
2	1.67	18	14.45	0.62	13.48	0.84	13.45	0.36
3	2.026	22	13.08	0.76	11.61	1.04	11.60	0.30
4	2.174	24	12.69	0.85	11.08	1.16	11.28	0.32
5	2.015	22	13.38	0.63	12.02	0.86	12.01	0.23
6	2.185	24	13.92	0.58	12.76	0.79	12.74	0.22
7	1.686	18	13.86	0.76	12.67	1.04	12.61	0.24
8	2.514	28	13.68	0.72	12.43	0.98	12.44	0.20
9	1.37	16	13.08	0.73	11.61	1.00	11.69	0.31
10	2.83	30	13.47	0.75	12.14	1.02	12.17	0.20
11	1.128	14	13.32	0.51	11.93	0.70	11.97	0.28
12	3.072	32	13.27	0.60	11.87	0.81	11.92	0.22
13	0.354	6	14.13	0.77	13.03	1.05	12.81	0.38
14	3.846	40	14.12	0.87	13.03	1.19	12.98	0.21
15	3.588	38	13.65	0.67	12.38	0.92	12.37	0.13
16	0.612	8	13.36	0.57	11.99	0.77	12.08	0.33

where a is the distance between the point of load application and the support, L, b, h are the length, width and height of the beam, respectively, $F_2 - F_1$ is the rate of loading within the load interval between $0.1F_u$ and $0.4F_u$, w_1, w_2 are the associated deflections and G is the shear modulus, which is often neglected. For illustration, this quantity is compared for the GLT-2 beam with the statistics of the moduli found for individual elements E_{eq}^e from Eq. (6.26) when dividing the homogenized bending stiffness D_b by the beam moment of inertia $I = bh^3/12$. The marginal distributions of E_k pertinent to individual boards ($k = 1, \ldots, 16$) were adopted. In particular, the actual values from Markov chain E_k^I ($I = 1, \ldots, 5000$) were associated with E_m for a given board in a given element in Eq. (6.26). The results are listed in Table 6.6. The equivalent bending modulus in the last row of this table, recall also Table 6.1, was calculated from Eq. (6.38) setting both $G = 0$ and $G = 2.3$ GPa (the value of longitudinal shear modulus found from homogenization), but the difference was negligible.

This finally brings us to the point of checking, whether the improved parameters A, B of the Pilodyn equation allow for better predictions when adopted in the analysis of a different beam, which falls at least into the same strength class. To that end, the GLT-1 and GLT-3 beams were evaluated numerically and compared with laboratory measurements. This comparison in terms of vertical deflection and average shear strain appears in Table 6.7. Note that when computing the homogenized bending and shear stiffnesses

Table 6.6: Statistics of the equivalent element bending moduli derived from through thickness homogenization for GLT-2 beam

Element No.	$\mu_{E^e_{eq}}$ [GPa]	$\sigma_{E^e_{eq}}$ [GPa]
1	12.34	0.082
2	12.36	0.056
3	12.36	0.054
4	12.36	0.054
5	12.36	0.054
6	12.35	0.052
7	12.61	0.094
8	12.53	0.131
Average	12.41	
Experiment Eq. (6.38)	12.15	

Table 6.7: Comparison of the measured and predicted vertical deflections w and the average shear strain γ for the associated load $F = 50$ kN for individual beams

Beam	Method	w_1	w_2	w_3	γ
		[mm]			[-]
GLT-1	Measured	18.5	20.8	18.4	0.00046
	FEM-PO	15.6	17.9	15.6	0.00037
	FEM-PU	17.0	19.6	17.1	0.00041
GLT-2	Measured	17.2	19.7	17.9	0.00039
	FEM-PO	15.8	18.2	15.9	0.00035
	FEM-PU	17.4	20.1	17.5	0.00040
GLT-3	Measured	21.7	23.9	21.2	0.00051
	FEM-PO	17.2	19.7	17.1	0.00038
	FEM-PU	19.6	22.6	19.6	0.00044

of individual elements, only the averages of Young's moduli for individual boards, found adopting either the original (FEM-PO) or the updated (FEM-PU) parameters A, B, were used.

Obviously, almost perfect match is found for the GLT-2 beam when comparing the measurements and the results from FEM-PU. For other two beams it is not as good, but the improvement in the prediction of the beam response with FEM-PU in comparison to FEM-PO is clear.

It remains to verify that the proposed linearization is adequate in view of the actual FEM analysis. To that end, individual samples generated in the Markov chain were again exploited. In particular, 5000 pairs of E_k, G_k within each board were adopted to

calculate mid-span deflections of the GLT-2 beam for the load level of 50 kN using both the linearized (w_{LIN}) and FEM (w_{FEM}) models. The results summarized in Table 6.8 in terms of means and standard deviations from 5000 realizations indicate that linearization introduces an error of about 0.15%, which is negligible.

Table 6.8: Comparing mid-span deflection of GLT-2 beam for the load level of 50 kN provided by linearized and FEM models

Method	μ_w [mm]	σ_w [mm]
Linearization (w_{LIN})	20.05	0.057
FEM (w_{FEM})	20.09	0.054
Difference ($\Delta w = \lvert w_{FEM} - w_{LIN} \rvert$)	0.03	0.006

6.7 Conclusions

A stochastic hierarchical model developed on the basis of a four-point bending test of a glued laminated timber beam was presented. Treating the material as characterized by random variables the Bayesian statistical theory was exploited to improve our initial (prior) information about their variability. The presented results offer the following conclusions:

- Grounding the formulation of the likelihood function on vertical displacements for updating the expected value of the longitudinal Young modulus μ_E appears reasonable, recall Fig. 6.8(a).
- The Bayesian inference enhanced by the MCMC method allowed us to quantify a natural variability of the elastic properties for different pieces of spruce appearing in the beam, recall Fig. 6.12.
- Although not directly related to the stochastic model, the present study verified the simple FEM model of a beam with the homogenized layered cross-section.
- One may notice a certain difference in the posterior mean value of the longitudinal Young modulus μ_E in comparison to the predictions provided by homogenization. In particular, a slight increase in the Young modulus and a slight decrease in the shear modulus provided by the Bayesian inference is observed. While these parameters are controlled solely by the macroscopic data, i.e. deflection and shear strain of the beam and its computational simplification in FEM analysis, the homogenized properties depend primarily on the local elastic properties and microstructural details. We would like to point out that in homogenization only the MFA was taken as a random parameter whereas other parameters such as volume fractions of lumens of early and latewood were assumed deterministic and derived from a single

sample only. Much effort is now being invested into this issue and the results are to be published shortly.

However, explaining this difference is perhaps much simpler. First, no account has been made to the effect of glue in deriving the homogenized cross-sectional stiffness parameters of a beam element, recall Eqs. (6.26)–(6.29). Next, the differences in moduli can also be attributed to the Mindlin assumptions reducing the number of degrees of freedom of the cross-section in warping.

Thus to avoid further confrontation of the two vastly different approaches we may associate the posterior estimates of material parameters not directly with wood but rather with the glued laminated beam made of spruce representing the adopted simplified FEM model. Such parameters might be recommended to use when predicting the response of similar beams in other practical applications. This can be supported by the results obtained for GLT-1 and GLT-3 beams when using the updated Pilodyn equation parameters A,B to estimate the longitudinal elastic stiffness of individual boars making up those beams. Recall that these updates were found from the application of experimental data associated with other GLT-2 beam.

While still to be confirmed by a large experimental program we wish to conclude that with these updated information we should be able to predict, hopefully more accurately, the values of the vertical deflection in case of another laminated beam. If the new beam is tested by the Pilodyn device we may estimate the values of Young's moduli in each board by conditioning the distribution of $E \sim \mathcal{N}(\mu_E, \sigma_E)$ on the measured data. These values would then enter the FEM model. One option would be to get the most probable value of the deflection using the highest likelihood estimates of the model parameters. The second option would require sampling parameters from the posterior distribution to obtain the corresponding samples of deflections and subsequently to compute the confidence intervals for deflections.

Acknowledgments

The financial support provided by the GAČR grant No. 15-10354S is gratefully acknowledged.

Appendix

Bayes' theorem is the only way in which a coherent analyst can update his/her state of knowledge [15]. One of the most useful formulas in the theory of applied probability, Bayes' theorem, can be derived by using the concept of conditional probability in this form

$$P(A|B) = \frac{P(B|A)P(A)}{P(B)} \propto P(B|A)P(A). \tag{6.39}$$

Let A represent a proposition of interest and B some new information. Bayes' theorem states that the analyst's probability A, given new evidence B, is proportional to the product of the probability for the truth of A prior to the collection of new evidence, i.e. $P(A)$, and the probability that evidence B would be observed if A is indeed true, i.e. $P(A|B)$. The proportionality (normalizing) constant is provided by $P(B)$.

Let now A be a continuous model parameter Θ, e.g. the shear modulus. Then the probability that $\vartheta \leq \Theta \leq \vartheta + \mathrm{d}\vartheta$ (before collecting new evidence $B = E$) is

$$P(\vartheta \leq \Theta \leq \vartheta + \mathrm{d}\vartheta) = f_\Theta(\vartheta)\,\mathrm{d}\vartheta, \tag{6.40}$$

and Eq. (6.39) assumes this form

$$\pi(\vartheta|E) \propto L(E\vartheta) f_\Theta(\vartheta), \tag{6.41}$$

where $L(E|\vartheta)$, the analog to $P(B|A)$ is called the likelihood function. It either the conditional probability of observing E (e.g. the beam's deflection), given ϑ, or proportional to that probability; $f_\Theta(\vartheta)$ is the prior probability density function. In this paper it is expressed hierarchically, recall Section 6.3. The posterior probability density function $\pi(\vartheta|E)$ is to be obtained, e.g. using the JAGS computer code.

Bibliography

[1] L. Melzerová, M. Šejnoha, Interpretation of results of penetration tests performed on timber structures in bending, Applied Mechanics and Materials 486 (2014) 347–352.

[2] L. Melzerová, M. Šejnoha, Results of penetration tests performed on timber GLT beams, 2014.

[3] G. Kandler, J. Füssl, E. Serrano, J. Eberhardsteiner, Effective stiffness prediction of GLT beams based on stiffness distributions of individual lamellas, Wood Science and Technology 49 (2015) 1101–1121.

[4] M. Lombardo, J. Zeman, M. Šejnoha, G. Falsone, Stochastic modeling of chaotic masonry via mesostructural characterization, International Journal for Multiscale Computational Engineering 7 (2) (2009) 171–185.

[5] M. Shinozuka, G. Dedatis, Simulation of stochastic processes by by spectral representation, Applied Mechanics Reviews 44 (4) (1991) 191–204.

[6] B. Källsner, O. Ditlevsen, Lengthwise bending strength variation of structural timber, Tech. rep., IUFRO S 5.02 Timber Engineering, Sydney (1994).

[7] G. Fink, Influence of varying material properties on the load-bearing capacity of glued laminated timber, Ph.D. thesis, Istitute für Baustatik und Konstruktion, ETH Zürich (Nov. 2014).

[8] G. Fink, J. Kohler, A. Frangi, Bending tests on glued laminated timber beams with well-known material properties, Tech. rep., Istitute für Baustatik und Konstruktion, ETH Zürich (Jul. 2013).

[9] G. Kandler, J. Füssl, J. Eberhardsteiner, Stochastic finite element approaches for wood-based products: Theoretical framework and review of methods, Wood Science and Technology 49 (2015) 1055–1097.

[10] A. Davenport, The application of statistical concept to the wind loading of structures, Proceedings of the Institution of Civil Engineers 19 (1961).

[11] K. Hofstetter, Ch. Hellmich, J. Eberhardsteiner, Development and experimental validation of a continuum micromechanics model for the elasticity of wood, European Journal of Mechanics - A/Solids 24 (6) (2005) 1030–1053.

[12] K. Hofstetter, Ch. Hellmich, J. Eberhardsteiner, Continuum micromechanics estimation of wood strength 6 (2006) 75–78.

[13] M. Šejnoha, J. Zeman, Micromechanics in Practice, WIT Press, Southampton, Boston, 2013.

[14] L. Melzerová, L. Kucíková, T. Janda, M. Šejnoha, Estimation of orthotropic mechanical properties of wood based on non-destructive testing, Wood Research 61 (6) (2016) 861–870.

[15] N. Siu, D. Kelly, Bayesian parameter estimation in probabilistic risk assessment, Reliability Engineering and System Safety 62 (1998) 89–116.

[16] D. Kelly, C. Smith, Bayesian inference in probabilistic risk assessment - The current state of the art, Reliability Engineering and System Safety 94 (2009) 628–643.

[17] J. Köhler, J. D. Sorensen, M. H. Faber, Probabilistic modeling of timber structures, Structural Safety 29 (2007) 255–267.

[18] L. Melzerová, T. Janda, M. Šejnoha, J. Šejnoha, FEM Models of glued laminated timber beams enhanced by Bayesian Updating of Elastic Moduli, 2015.

[19] Ch. P. Robert, G. Casella, Monte Carlo Statistical Methods, 2nd Edition, III, Springer-Verlag, 2004.

[20] M. Plummer, JAGS: A Program for Analysis of Bayesian Graphical Models Using Gibbs Sampling (2003).

[21] MRC-Biostatistics-Unit, The BUGS Project.

[22] W. K. Liu, T. Belytschko, A. Mani, Random field finite elements, International Journal for Numerical Methods in Engineering 23 (1986) 1831–1845.

[23] M. Hu, M. Johansson, A. Olsson, J. Oscarsson, B. Enquist, Local variation of modulus of elasticity in timber determined on the basis of non-contact deformation measurement and scanned fibre orientation, European Journal of Wood and Wood Products 73 (1) (2014) 17–27.

[24] Ch. Jenkel, C. Gebhardt, M. Kaliske, Modelling of Structural and Material Inhomogenites in Wood, in: Proceedings of World Congress on Timber Engineering 2016, 2016.

[25] M. Šejnoha, L. Kucíková, V. Králík, J. Šejnoha, Combining homogenization, nanoindentation and Bayeasian updating in search for MFA, in: B. Topping (Ed.), Proceedings of the the Fifteenth International Conference on Civil, Structural and Environmental Engineering Computing, Prague, Czech Republic, Civil-Comp Press, 2015.

[26] D. Lecompte, A. Smits, S. Bossuyt, H. Sol, J. Vantomme, D. Hemelrijck, A. Habraken, Quality assessment of speckle patterns for digital image correlation, Optics and Lasers in Engineering 44 (2006) 1132–1145.

[27] G. Stoilov, V. Kavardzhikov, D. Pashkouleva, A comparative study of random patterns for digital image correlation, Journal of Theoretical and Applied Mechanics 42 (2012) 55–66.

[28] B. Pan, D. Yu, L. Wu, L. Tang, Systematic errors in two-dimensional digital image correlation due to lens distortion, Optics and Lasers in Engineering 51 (2013) 140–147.

[29] H. Lu, P. Cary, Deformation measurements by digital image correlation: Implementation of a second-order displacement gradient, Experimental Mechanics 40 (2000) 393–400.

[30] B. Pan, Z. Lu, H. Xie, Mean intensity gradient: An effective global parameter for quality assessment of the speckle patterns used in digital image correlation, Optics and Lasers in Engineering 48 (2010) 469–477.

[31] V. Nežerka, Ncorr-post: DIC Post-Processing Tool, Tech. rep., http://mech.fsv.cvut.cz/ nezerka/dic/index.htm (2014).

[32] V. Nežerka, Ncorr-post-CSTool: ...DIC Post-Processing Tool to Display Strains along Cross-Section, Tech. rep., http://mech.fsv.cvut.cz/ nezerka/dic/index.htm (2015).

[33] V. Nežerka, J. Antoš, T. Sajdlová, P. Tesárek, Open source DIC tools for analysis of multiple cracking in fiber-reinforced concrete, Applied Mechanics and Materials 827 (2016) 336–339.

[34] J. Blaber, Ncorr: Digital Image Correlation Software, Tech. rep., http://www.ncorr.com/ / Georgia Institute of Technology, U.S. (2014).

[35] Y. Benveniste, A new approach to the application of Mori-Tanaka theory in composite materials, Mechanics of Materials 6 (1987) 147–157.

[36] J. Vorel, J. Sýkora, S. Urbanová, M. Šejnoha, From CT scans of wood to finite element meshes, in: B. Topping (Ed.), Proceedings of the the Fifteenth International Conference on Civil, Structural and Environmental Engineering Computing, Prague, Czech Republic, Civil-Comp Press, 2015.

[37] W. Gindl, T. Schöberl, The significance of the elastic modulus of wood cell walls obtained from nanoindentation measurements, Composites Part A: Applied Science and Manufacturing 35 (11) (2004) 1345–1349.

[38] A. Jäger, Th. Bader, K. Hofstetter, J. Eberhardsteiner, The relation between indentation modulus, microfibril angle, and elastic properties of wood cell walls, Composites Part A: Applied Science and Manufacturing 42 (6) (2011) 677–685.

[39] E. K. Gamstedt, T. K. Bader, K. de Borst, Mixed numerical–experimental methods in wood micromechanics, Wood Science and Technology 47 (2013) 183–202.

[40] M. Šejnoha, L. Kucíková, J. Vorel, V. Hrbek, J. Němeček, Comparing nano and macroindentation in search for microfibril angle in spruce, Internationl Journal of Computational Methods and Experimental Measurements 5 (2) (2017) 135–143.

[41] J. Skoček, J. Zeman, M. Šejnoha, Effective properties of Carbon-Carbon textile composites: Application of the Mori-Tanaka method, Modelling and Simulation in Materials Science and Engineering 16 (8) (2008) paper No. 085002.

[42] J. Vorel, M. Šejnoha, Evaluation of homogenized thermal conductivities of imperfect carbon-carbon textile composites using the Mori-Tanaka method, Structural Engineering and Mechanics 33 (4) (2009) 429–446. arXiv:0809.5162.

[43] G. W. Milton, The Theory of Composites, Cambridge Monographs on Applied and Computational Mathematics, Cambridge University Press, 2002.

Chapter 7

Bayesian inference as a tool for improving predictions of effective elastic properties of wood

This chapter presents the preprint version of the journal paper

> Šejnoha, M.; Janda, T.; Vorel, J.; Kucíková, L.; Padevět, P.; Hrbek, V., Bayesian inference as a tool for improving estimates of effective elastic parameters of wood, Computers and Structures. 2019, 218 94-107. ISSN 0045-7949.

reformatted to align with the style of the thesis.

7.1 Abstract

A simple approach to the identification of geometrical and material uncertainties of wood is presented. This stochastic mechanics problem combines classical micromechanics, computational homogenization and experimental measurements with Bayesian inference to estimate potential errors in the prediction of macroscopic elastic properties of wood caused by randomness of microstructural details on the one hand and experimental error on the other hand. The former source of uncertainty includes, for example, variability in microfibril angle and growth ring density. Even such limiting consideration of random input illustrates the need for combined computational and experimental approach in a reliable prediction of the desired material properties. Tying the two approaches in the framework of Bayesian statistical method proves useful when addressing their limitations and as such giving better notion on the credibility of the prediction. This is demonstrated here on one particular example of spruce wood.

7.2 Introduction

In recent years, the Bayesian inference has been successfully exploited in many fields of engineering particularly in cases where the material, model or even computational

uncertainty is relatively high [1, 2, 3]. In case of wood the concept of Bayesian statistics has been adopted, e.g. in [4, 5, and references therein] to narrow down uncertainty of the computed as well as locally measured elastic moduli of individual plies of a glued laminated timber (GLT) beam.

While elastic response of such structures may not draw particular attention, the issue of uncertainty quantification gains importance once exceeding the strength limits. A reliable description of fracture is then driven by the overall material anisotropy. Even if limiting attention to macroscopically orthotropic systems, the determination of all material constants purely experimentally is a challenging task introducing, apart from aleatory, also the epistemic uncertainties associated with the measurements.

Other method of attack offers homogenization [6, 7]. Such an analysis requires knowledge of material properties of various material components on very low scale and detailed description of wood microstructure. This approach is certainly appealing from the engineering point of view as it provides the full stiffness matrix at a macroscopic material point while accounting for the overall material anisotropy specified by the material symmetry of local phases and microstructural details of wood. A single value (deterministic) prediction may, however, be rather erroneous given large scatter in local properties and microstructure complexity of natural materials.

It is therefore logic to combine both experimental and numerical approaches in order to identify/limit errors, which may arise, if applying them independently. This brings us back to Bayesian inference as a method, which provides their natural link. Such a way of thinking makes it possible to formulate the principal objectives of this contribution:

- Derive macroscopically homogeneous stiffness matrix of spruce wood by incorporating homogenization, nanoindentation at cell wall level, and macroscopic tensile tests into the framework of Bayesian inference.

- Alongside this, focus on properly addressing an experimental uncertainty with emphases on identifying a measurement error as it plays a crucial role in successfully completing the above task.

In case of input variables we admit variability in microfibril angle orientation and dry wood density of earlywood, i.e. volume fraction of earlywood within an annual ring, only. Therefore, the elastic properties of individual constituents building the cell wall together with their volume fraction and the volume fraction of lumens within the earlywood and latewood are considered constant. An initiative work on this subject can be found in [8]. To arrive at the desired results we organize the remainder of the paper as follows.

In Section 7.3 we provide a brief theoretical background of analytical and computational micromechanics to formulate the forward deterministic model for the prediction of effective properties on individual scales. This step relies on the definition of relevant volume fractions. Measurements on a series of wood specimens presented in [9] suggest constant values of volume fractions of lumens in both earlywood and latewood. On the contrary, a notable variability of dry wood density from specimen to specimen and thus also the associated variability of volume fraction of earlywood within growth rings has been observed. It would thus appear reasonable to treat this parameter as random in

stochastic simulations. Within the present concept of Bayesian updating this would, however, required knowing the variation of earlywood volume fraction from ring to ring in a given specimen. Because this detailed information is not available at present and the variability measure is provided only in terms of the bulk value, the average volume fraction of earlywood pertinent to the whole specimen, we considered this variable also constant in Bayesian inference but variable from specimen to specimen in the homogenization step.

An extensive experimental program to provide measured data of observed variables needed in Bayesian inference is summarized in Section 7.4. In Section 7.4.2 we begin with measurements of indentation moduli at cell wall level. Following in footsteps of [10, 11] by employing the theory of anisotropic indentation described in details in [12, 13] allows us to introduce a link between the only currently assumed random variable, the microfibril angle (*MFA*), and the theoretically calculated indentation modulus. This step calls for homogenization, because expressing the indentation modulus requires the knowledge of cell wall stiffness. While a direct comparison of theoretically derived and measured indentation moduli appear sufficient in estimating *MFA*, we proceed further in Section 7.4.1 with macroscopic tensile tests on elastic longitudinal modulus and Poisson ratio, considered also random, to support/decline the credibility of the measured nanoindentation moduli.

The principal part of this contribution, the Bayesian inference, is finally described in Section 7.5. An engineering friendly introduction to this subject is provided in [14, 15]. Similarly to [1, 2, 5], the proposed formulation introduces a hierarchical stochastic model that allows us, through the application of Bayes theorem, to improve our prior knowledge on input random parameters given the measured data. Mathematically, such improved/updated notion about random variables is represented by their posterior joint probability distribution function. Because the measurement error of the observed (measured) variables is also considered random with some prior distribution, the Bayesian updating naturally reveals the epistemic uncertainties of the adopted experimental data. The posterior distribution function is typically constructed numerically from simulations employing the Markov chain Monte Carlo (MCMC) algorithm [16]. The theoretical formulation of the present stochastic model is given in Sections 7.5.2 and 7.5.3, while specifics on numerical implementation together with obtained results are described next in Section 7.5.4.

The list of essential conclusions and some potential future perspectives are provided in Section 7.6.

7.3 Effective elastic properties from homogenization

Since the early work of Eshelby [17] and Hill [18] analytical micromechanics based models, although ignoring the inhomogeneity of local deformation and stress fields, have proved useful in many areas of engineering. Among them, the Mori-Tanaka [19] method has enjoyed a particular interest. In some applications, detailed distribution of local fields is important, which calls for numerical simulations performed on microstructure based

computational models, unit cells [20]. A comprehensive overview of both analytical and numerical homogenization schemes is available in [21, 22]. In many applications that require hierarchical homogenization, the two approaches are often combined.

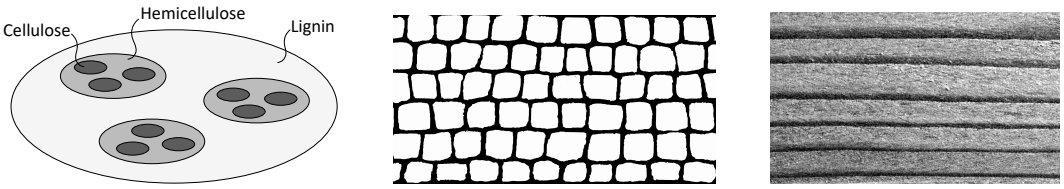

(a) (b) (c)

Figure 7.1: a) Cell wall level (schematic representation of microfibrils [6] embedded in the matrix of lignin), b) Level of lumens (binary image of earlywood), c) Level of annual rings (gray scale image suggesting laminate like structure of earlywood and late wood)

To introduce this subject, we draw the reader's attention to Fig. 7.1 identifying three scales we consider here in the derivation of effective elastic properties of spruce wood. To be consistent with [9] we build our homogenization model at the cell wall level on the data adopted from [6]. Therein, a multilayered structure of cell wall is simplified to three layers: M layer (middle lamella, primary wall and outer layer of secondary wall S_1), S_2 layer (middle layer of secondary wall), and S_3 layer (inner layer of secondary wall). Each layer is further decomposed into three basic phases: lignin, hemicellulose, cellulose (crystalline and amorphous). Their elastic properties are listed in Table 7.1. Because of limited information, these parameters are assumed constant (deterministic). The same assumption is accepted for the phase volume fractions in individual layers. Other cell wall constituents such as extractives and water were neglected.

Table 7.1: Phase properties at cell wall level and their volume fractions in M, S_2 and S_3 layers [6].

Local	E_{11}	$E_{22,33}$	$G_{12,13}$	$\nu_{21,31}$	ν_{23}	Volume fractions [-]		
constituents	[GPa]	[GPa]	[GPa]	[-]	[-]	M	S_2	S_3
Cellulose	150.00	17.50	4.50	0.01	0.50	0.20	0.49	0.49
Hemicellulose	16.00	3.50	1.50	0.10	0.40	0.15	0.27	0.27
Lignin	2.75	2.75	1.03	0.33	0.33	0.15	0.27	0.27

Considering a statistically homogeneous and ergodic distribution of the basic constituents building the cell wall opens the way to the application of the Mori-Tanaka method to establish effective properties on this smallest scale. Referring to Fig. 7.1(a) these are found in two steps imagining first an elliptic cylinder like cellulose in the matrix of hemicellulose. This new homogeneous inclusion (microfibril) of a similar shape is then introduced in the matrix of lignin. The ratio of major to minor semi-axes of the elliptical cross-section is taken from [6] being equal to 3 and 2.5 for S_2 and S_3 layers and 5 and 3.5 for M layer for the two homogenization steps, respectively. In each step, a two-phase composite is therefore considered which results in the estimate of the effective stiffness

matrix in the form

$$\mathbf{L}_{\mathrm{cw}}^{\mathrm{hom}} = \mathbf{L}_0 + f_1(\mathbf{L}_1 - \mathbf{L}_0)\mathbf{A}_1^{\mathrm{dill}} \left(f_0\mathbf{I} + f_1\mathbf{A}_1^{\mathrm{dill}} \right)^{-1}, \tag{7.1}$$

where $\mathbf{L}_0$ and $\mathbf{L}_1$ are the stiffness matrices of the matrix and inclusion, $\mathbf{I}$ is the second order identity tensor, f_0 and f_1 are the volume fractions of corresponding phases, and $\mathbf{A}_1^{\mathrm{dill}}$ is the partial strain concentration factor of the inclusion given by

$$\mathbf{A}_1^{\mathrm{dill}} = \left(\mathbf{I} + \mathbf{S}_1\mathbf{L}_0^{-1}(\mathbf{L}_1 - \mathbf{L}_0) \right)^{-1}, \tag{7.2}$$

where $\mathbf{S}_1$ is the Eshelby tensor depending on the inclusion shape.

At the level of lumens, Fig. 7.1(b), the microstructure images allow us to construct a realistic computational model, a unit cell (UC). A reasonable point of departure in constructing the UC model would be to treat the cell wall thickness and shape and area of lumens as random and derive, by matching material statistics of real microstructure and UC, the so called statistically equivalent periodic unit cell (SEPUC) [20, 22]. However, this step goes beyond the present scope and we settle for a simple model based on an hexagonal arrangement of lumens of both earlywood and latewood, respectively, and constant cell wall thickness.

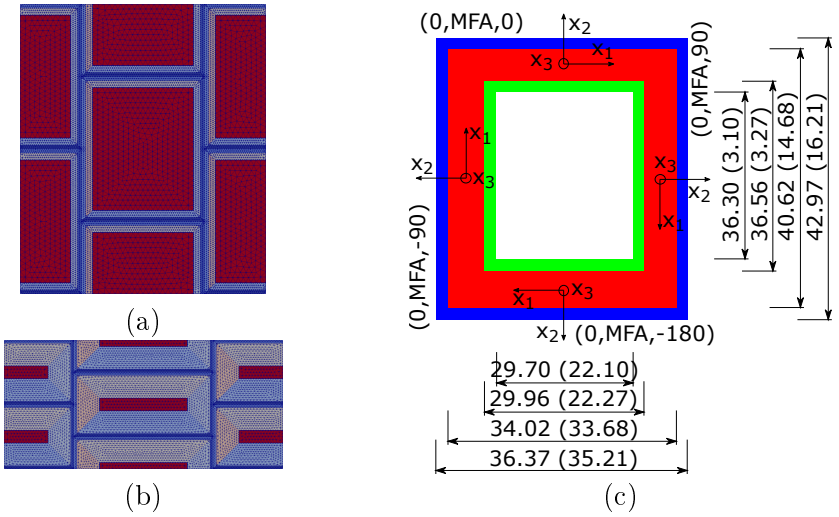

Figure 7.2: Geometry and plane view of discretized PUCs: a) earlywood, b) latewood; c) Dimensions of M (green), S_2 (red) and S_3 (blue) layers

The corresponding periodic unit cells (PUC) are displayed in Fig. 7.2(a,b). Both models involve all three layers of the cell wall. This is evident from Fig. 7.2(c) schematically showing the PUCs dimensions[1]. These dimensions were obtained by first associating the inner dimensions of lumens with the major and minor semi-axes of the ellipse approximating their real shape. An experimental study performed on the analyzed specimens of

[1] Dimensions pertinent to latewood are given in parentheses.

spruce, see [9, 23] and Fig. 7.3, further revealed more or less constant volume fractions of both earlywood (EW) and latewood (LW) set equal to $f_{\mathrm{lum,EW}} = 0.69$ and $f_{\mathrm{lum,LW}} = 0.12$ in the present study. The estimated cell wall thickness together with volume fractions of individual layers taken again from [6], see Table. 7.2, then rendered the final geometry of both PUCs.

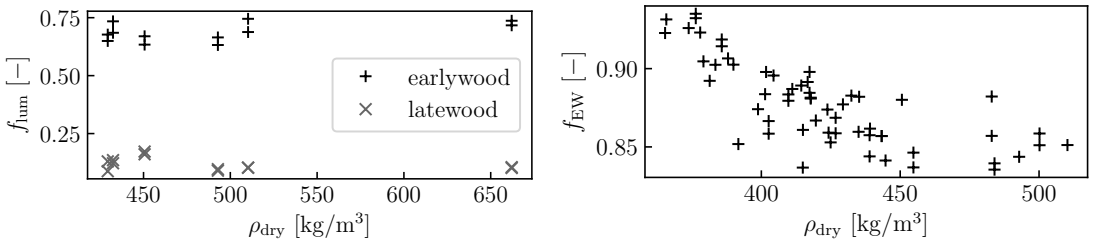

Figure 7.3: Volume fraction of a) lumens in earlywood and late wood, b) earlywood of tested specimens with a given dry wood density

It is well known that microfibrils wound helically within the cell wall and are not perfectly aligned with the longitudinal (lumen) direction. Instead, they deviate by a certain angle called the microfibril angle. This is schematically shown, together with the assumed local coordinate system[2], in Fig. 7.2(c). The corresponding Euler angles following $z-y'-z''$ convention then serve to transform the homogenized stiffness matrix provided by Eq. (7.1) into the global coordinate system of the unit cell.

Table 7.2: Volume fraction and *MFA* of individual cell wall layers [6].

Layer	M	S_2	S_3
$f_{\mathrm{M,S_2,S_3}}$(EW)	0.352	0.609	0.039
$f_{\mathrm{M,S_2,S_3}}$(LW)	0.117	0.870	0.013
MFA [°]	± 45	± *MFA*	± 75

The fact that S_2 layer is the principal carrier of the wood stiffness promotes its *MFA* be considered random, while the remaining two layers adopt constant values specified in Table 7.2.

The computational homogenization then follows the lines outlined in [24]. To that end, suppose that the composite is loaded on its external boundary by displacements compatible with the macroscopic strain $\boldsymbol{E}$. The local displacements and strains then split into homogeneous and fluctuating parts as

$$\boldsymbol{u} = \boldsymbol{E} \cdot \boldsymbol{x} + \boldsymbol{u}^*, \qquad \boldsymbol{\varepsilon} = \boldsymbol{E} + \boldsymbol{\varepsilon}^*. \tag{7.3}$$

For the prescribed displacement boundary conditions the Hill lemma reads

$$\frac{1}{\Omega} \int_{\Omega} \delta\boldsymbol{\varepsilon}^{\mathsf{T}} \boldsymbol{\sigma} \, \mathrm{d}\Omega = 0, \tag{7.4}$$

[2]Axis 1 is reserved for the microfibril direction assuming *MFA*=0°.

where Ω is the volume of the unit cell. Substituting Eq. $(7.3)_2$ into Eq. (7.4) yields

$$\int_\Omega \delta\boldsymbol{\varepsilon}^{*\mathsf{T}}\mathbf{L}\boldsymbol{\varepsilon}^*\,\mathrm{d}\Omega = -\int_\Omega \delta\boldsymbol{\varepsilon}^{*\mathsf{T}}\mathbf{L}\boldsymbol{E}\,\mathrm{d}\Omega, \tag{7.5}$$

where $\mathbf{L}$ is the local stiffness matrix. Eq. (7.5) is typically solved using the finite element method. The periodic boundary conditions are generally adopted to enforce the volume average of the fluctuation part of strain field $\boldsymbol{\varepsilon}^*$ disappear, see e.g. [22]. In deriving the homogeneous stiffness matrix at the level of lumens $\mathbf{L}^{\mathrm{hom}}_{\mathrm{lum}}$ we load the unit cell in turn by each component of $\boldsymbol{E}$, while the other components vanish. The corresponding volume stress averages normalized with respect to $\boldsymbol{E}$ then furnish individual columns of $\mathbf{L}^{\mathrm{hom}}_{\mathrm{lum}}$.

The last homogenization step is concerned with the level of annual rings where the parallel arrangement of the earlywood and latewood, recall Fig. 7.1(c), suggests application of lamination theory [25]. This step, which involves the volume fractions of earlywood and latewood within annual rings, renders the searched homogeneous stiffness matrix of wood $\mathbf{L}^{\mathrm{hom}}_{\mathrm{w}}$.

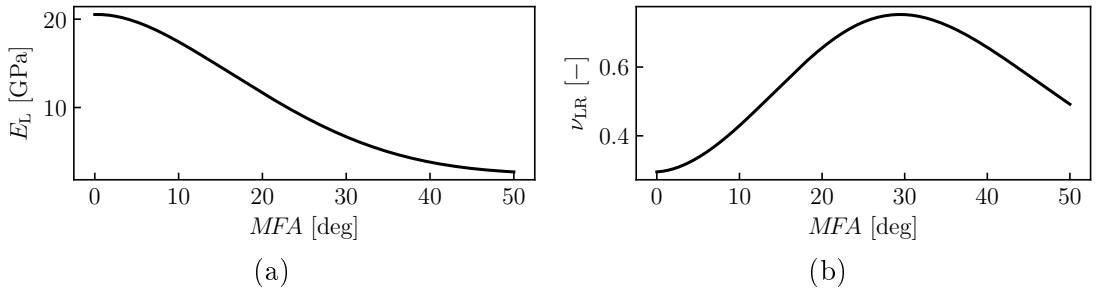

Figure 7.4: Variation of a) elastic modulus E_{L}, b) Poisson ratio ν_{LR} as a function of *MFA* assuming dry wood density $\rho_{\mathrm{dry}} = 410$ kgm^{-3}

For illustration, in Fig. 7.4 we plot the distribution of the macroscopic elastic modulus E_{L} and Poisson ratio ν_{LR} to be determined also experimentally.

7.4 Experiment

Formulation of the stochastic model presented in Section 7.5 relies on two types of experiments. While nanoindentation may provide an insight into the response of wood at the lowest considered scale, the macroscopic tensile tests may serve to validate the whole homogenization process. The two experiments are now briefly discussed.

7.4.1 Macroscopic tensile tests combined with digital image correlation

The macroscopic tensile tests aimed at determining the longitudinal elastic modulus E_{L} and Poisson ratio ν_{LR} of wood. This notation is consistent with a schematic representation of specimen orientation and loading conditions in Fig. 7.5(a) so that

$$\varepsilon_{\mathrm{L}} = \frac{\sigma_{\mathrm{L}}}{E_{\mathrm{L}}}, \qquad \varepsilon_{\mathrm{R}} = -\frac{\nu_{\mathrm{LR}}\sigma_{\mathrm{L}}}{E_{\mathrm{L}}}, \qquad \nu_{\mathrm{LR}} = -\frac{\varepsilon_{\mathrm{R}}}{\varepsilon_{\mathrm{L}}}. \tag{7.6}$$

Fig. 7.5(b) clearly indicates a deviation of grains in real specimens which in turn is the source of potential mismatch of measured and theoretically derived Poisson's ratio in particular. An experimental setup is illustrated in Fig. 7.5(c).

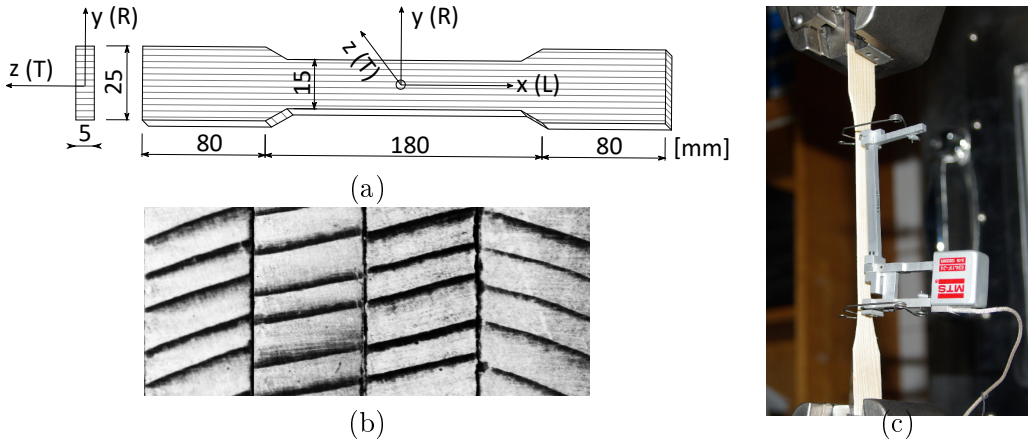

Figure 7.5: a) Specimen geometry and assumed orientation of grains, b) Real orientation of grains in plane normal to loading direction, c) Example of tensile test setup

The tensile test measurements were carried out on 28 specimens in the displacement control regime using an electromechanic MTS Alliance RT30kN loading machine. A standard extensometer with the measurement length of 100 mm, the measurement range from +5 to -2.5 mm and sensitivity of 0.1% was adopted first to measure extension of 20 specimens, see Fig. 7.5(c). To allow for the determination of Poisson's ratio, the results from 8 specimens were evaluated using digital image correlation (DIC). This approach has proved useful in many engineering applications where all strain components in the measured plane are needed [9]. To that end, the examined specimens were airbrushed with a random pattern of black dots. Tracking the motion and distortion of the speckled pattern makes possible to evaluate the local strain profiles. Details on DIC algorithms are available, e.g. in [26, 27, 28]. Note that our interest here is in the bulk response only. The local strains are then conveniently provided as volume averages derived from the evolution of displacements along a certain boundary line Γ as

$$\varepsilon_{ij} = \frac{1}{2A} \int_{\Gamma} (u_i n_j + u_j n_i) \, \mathrm{d}\Gamma, \tag{7.7}$$

where u_i, n_i represent, respectively, the components of the displacement field and unit outward normal to the boundary line. They were derived with the open-source code Ncorr-Post-CSTool [29, 30].

Three regions displayed in Fig. 7.6 were examined in numerical evaluation of Eq. (7.7). A potential influence of the selected region on the measured strains, a clear example of an epistemic error, is indicated by averages of elastic modulus and Poisson's ratio calculated over the range of tensile stress $\sigma_{\mathrm{L}} \in < 20, 60 >$ MPa, see Table 7.3.

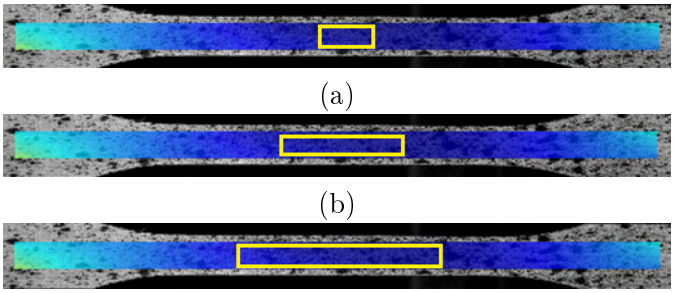

(a) (b) (c)

Figure 7.6: Regions to perform calculation of macroscopic strains: a) region 1, a) region 2, a) region 3

Table 7.3: Elastic modulus E_{L} and Poisson's ratio ν_{LR} determined from DIC measurements using Eqns. (7.7) and (7.6)

Specimen	Elastic modulus E_{L} [GPa]			Poisson ratio ν_{LR} [-]		
No.	Region 1	Region 2	Region 3	Region 1	Region 2	Region 3
1	13.539	13.783	14.009	0.588	0.535	0.409
2	16.918	16.612	16.502	0.558	0.520	0.427
3	14.727	14.828	14.966	0.484	0.485	0.403
4	15.676	16.048	16.017	0.394	0.408	0.382
5	14.867	14.539	14.162	0.760	0.822	0.739
6	12.231	12.337	12.617	0.265	0.243	0.218
7	12.788	12.822	12.843	0.147	0.095	0.067
8	17.472	16.608	16.316	0.706	0.733	0.743
9	14.043	13.739	13.845	0.449	0.488	0.459
10	11.304	11.405	11.496	0.162	0.177	0.181

7.4.2 Nanoindentation measurements at cell wall level

Nanoindentation tests became a common mean of assessing material properties at the level of microns. Also in timber engineering, applications of this experimental technique are growing [10, 11, 22, 31, 32, 33]. In the context of this contribution the most relevant work is that of Jäger et al. [11], where micromechanical homogenization was combined with indentation into S_2 layer to determine *MFA*. The same strategy is employed henceforth focusing also on the prediction of measurement error.

Indentation measurements were conducted on 6 specimens extracted from 6 specimens tested previously in tension. An attempt was made to identify indents not falling into S_2 layer, which would be excluded from further analysis. Examples of such a visual inspection appear in Fig. 7.7(a,b). Red and green circles indicate indents potentially made into M and S_3 layers, respectively. Orange circles indicate indents, which are considered suspicious. A similar attention as to applicability of the collected data was given to indentation curves in Fig. 7.7(c). All measurements resulting in curves similar

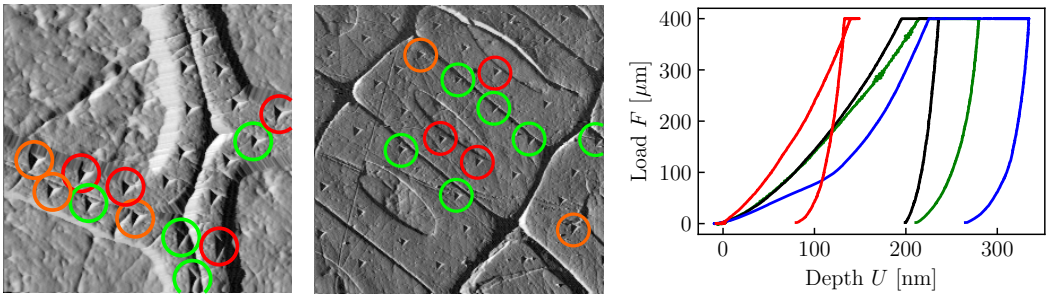

(a) (b) (c)

Figure 7.7: Indentation into: a) earlywood, b) latewood; c) Indentation curves

to the green curve showing oscillations due to local vibrations, the blue curve indicating an excessive creep, and the red curve associated with a sudden drop in air pressure were excluded. Thus only measurements associated with curves of a similar shape as the black one were taken into account. After eliminating all unacceptable measurements we remained with 507 indents to enter the process of *MFA* estimation.

In a typical indentation test, an indenter is driven into the material of interest at a constant loading or displacement rate until a certain load or depth is reached. After a short hold period, the load is gradually removed from the indenter. During this process, both load and displacement are recorded continuously. The recovery during the unloading process, i.e. the initial slope of unloading curve, is then calculated based on the theory of elasticity as presented, e.g., in [34]

$$S = \frac{\mathrm{d}F}{\mathrm{d}U} = \frac{2}{\sqrt{\pi}} M^{\mathrm{exp}} \sqrt{A_c}, \tag{7.8}$$

where F is the applied load, U stands for the penetration depth and A_c is the projected area of contact under the indenter and M^{exp} is the indentation modulus.

Because of material anisotropy of S_2 layer an anisotropic nanoindentation theory is needed to relate the measured and theoretically calculated indentation moduli. At this point, we wish to remain as brief as possible and refer the interested reader to [11, 12, 13] for details on theoretical formulation. For simplicity, we consider the same arrangement of indentation test as presented in [11]. In particular, we consider a conical indenter being driven into a generally anisotropic half space, see Fig. 7.8(a). Therein, x_i axes represent the material local coordinate system with the x_1 axis aligned with the microfibril direction. The x_3 axis, independent of *MFA*, is located in the loaded area. The loading direction is assumed to be aligned with the direction of lumens and perpendicular to the loaded area of a cell wall material.

An approximate solution to this problem departs from Barber's theorem [35] suggesting that the contact area A_c in Eq. (7.8) is the one that maximizes the indentation force F. Assuming an elliptical shape of contact area and applying this theorem Vlassak et al. [13] provides a theoretical derivation of indentation modulus M^{num} starting from a

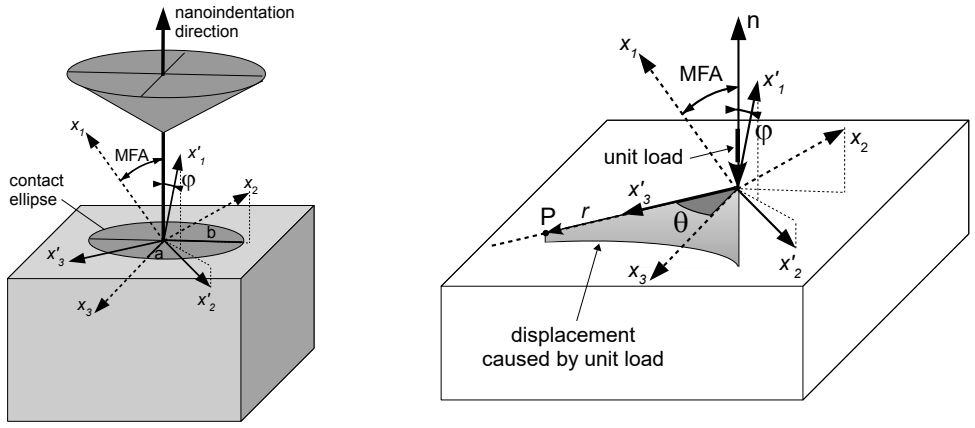

Figure 7.8: a) Conical indentation in S_2 layer: orientation of the material axis (x_1, x_2, x_3), indentation direction, and elliptical projected contact area with semi-axis a, b, b) Coordinate system (x'_1, x'_2, x'_3) to define Green's function

displacement $w(r, \theta)$ caused by a concentrated force

$$w(r, \theta) = \frac{h(\theta)}{r}, \tag{7.9}$$

where $h(\theta)$ is the angle dependent part of surface Green's function [12] and r, θ are polar coordinates[3]. A graphical representation, adopted from [11], is plotted in Fig. 7.8(b). Given this function Vlassak et al. [13] derived, for a flat punch and conical indenter, the relation between indentation force F and penetration U as[4]

$$F(e) = \frac{U^2}{\cot\gamma\alpha(e)E(e)}, \qquad \alpha(e) = \int_0^\pi \frac{h(\theta)}{\sqrt{1 - e^2\cos^2\theta}}\,\mathrm{d}\theta, \tag{7.10}$$

where $E(e)$ is the complete elliptic integral of the second kind, $e = \sqrt{1 - b^2/a^2}$ is the eccentricity of contact ellipse in Fig. 7.8(a), a, b are the major and minor semi-axes, and γ is the cone angle[5]. According to Barber's theorem the solution of conical contact, Eq. $(7.9)_1$, is obtained by choosing the eccentricity e that minimizes the product $\alpha(e)E(e)$. Introducing this equation into Eq. (7.8) then gives the equivalent, theoretically calculated, indentation modulus in the form

$$M^{\mathrm{num}} = \frac{1}{\alpha(e)(1 - e^2)^{1/4}}. \tag{7.11}$$

[3]Angle φ in Fig. 7.8 also enters definition of $h(\theta)$, see [12, 13] for details.

[4]It is assumed that x_3 axis in Fig. 7.8 is taken as the reference direction for definition of function $h(\theta)$.

[5]Note that the Berkovitch indenter with $\gamma = 70.32°$ was used in actual measurements. It has been suggested in [12] that cone representation of the Berkovitch tip is sufficiently accurate.

Because definition of Green's function requires knowing the whole stiffness matrix of S_2 layer, which in turn depends on microfibril angle, it is now possible by matching the measured and theoretically calculated indentation moduli to get for each indent the corresponding *MFA*.

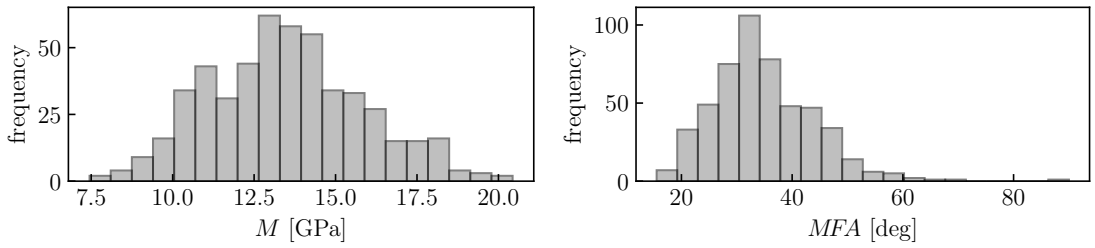

Figure 7.9: Histograms of: a) measured indentation modulus M^{exp}, b) microfibril angle *MFA*

Figure 7.9 illustrates the distributions of measured indentation moduli and the corresponding distribution of calculated microfibril angles. A high variability of the measured indentation modulus is evident. One also observes a relatively low value of this quantity on average resulting in a high value of *MFA*. Inspection of Fig. 7.4(a) then suggests unrealistically low value of the longitudinal modulus. These issues will be elaborated next in Section 7.5.

7.5 Bayesian inference

This section follows the usual steps of Bayesian inference to derive the posterior distribution of the unobservable model parameters. The main advantage of this approach over single point estimation such as maximum likelihood estimation is that the result contains information not only about the most probable (optimal) values of the model parameters but also the information about its possible ranges, e.g. the confidence intervals.

The distribution of the measured data is specified by a hierarchical system of stochastic and deterministic relations. This system is sometimes called a forward model as it describes our belief on how the observed random data are generated given certain fixed values of model parameters and explanatory variables. The forward model thus completely defines the multivariate probability density function (PDF) of data y. Viewing PDF as a function of model parameters θ, while data y are fixed at their measured values, defines the likelihood $p(y|\theta)$. The posterior PDF of the parameters is then given by the Bayes theorem in the form

$$p(\theta|y) \propto p(y|\theta)p(\theta), \tag{7.12}$$

where $p(\theta)$ is the prior distribution and symbol $\propto$ means that the left hand side is proportional to the right hand side up to a constant independent of θ.

The posterior distribution defined in this manner is typically intractable analytically but it is possible to sample from it using a variety of Markov chain Monte Carlo methods.

7.5.1 Observed data

As outlined in Section 7.4, the data from three types of experiments are assumed in this analysis. Henceforth, the tensile test with axial strains recorded using the contact extensometer, recall Fig. 7.5(c), will be termed the standard tensile test. The 2nd, 6th and 10th columns in Table 7.4 identify the number of strain measurements collected at various stress levels for particular specimens. The number of measurements of axial and radial strains provided by DIC as described in Section 7.4.1 are available in the 3rd, 7th and 11th column of Table 7.4. One particular example of such data is plotted in Fig. 7.10 for illustration. The last set of data corresponding to indentation moduli extracted from nanoindentation measurements described in Section 7.4.2 are available in the 4th, 8th and 12th column of Table 7.4.

Table 7.4: Overview of specimens: i is the specimen's number, N_i is the number of stress-strain pairs from the tensile test with extensometer, N_i^{ic} is the number of records from the tensile test with DIC measurement and N_i^{ni} is the number of indents at i-th specimen.

i	N_i	N_i^{ic}	N_i^{ni}	i	N_i	N_i^{ic}	N_i^{ni}	i	N_i	N_i^{ic}	N_i^{ni}
1	50	–	77	11	–	205	–	21	31	–	52
2	58	–	–	12	–	190	–	22	52	–	–
3	63	–	–	13	42	–	–	23	50	–	–
4	64	–	70	14	90	–	–	24	39	–	–
5	–	225	–	15	76	–	–	25	60	–	–
6	86	–	–	16	–	132	–	26	21	–	134
7	–	96	–	17	52	–	–	27	51	–	–
8	31	–	77	18	–	113	–	28	60	–	–
9	33	–	–	19	–	150	–				
10	17	–	97	20	–	84	–				

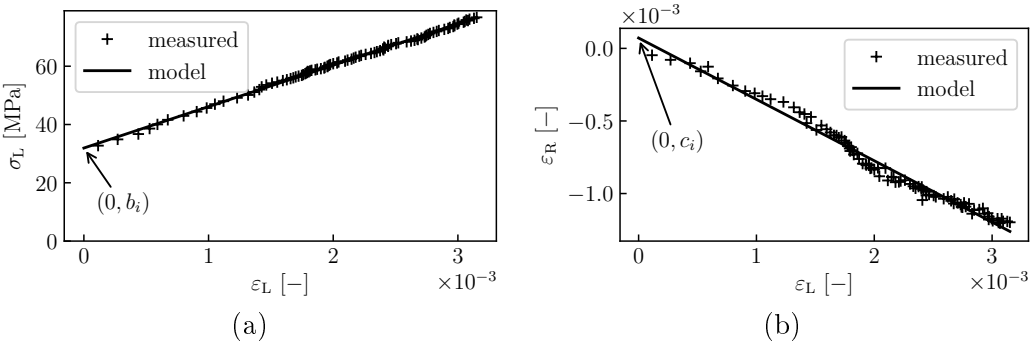

Figure 7.10: Example of experimental data recorded during tensile test with DIC measurements on specimen No. 5

7.5.2 Hierarchical model

The forward hierarchical model describes how the measured random data are generated given fixed values of parameters and explanatory avriables[6]. To specify the model, we begin by providing notation and a theoretical representation of the available experimental data. A standard tensile test performed on the i-th specimen provides a sequence of measured longitudinal strains $\varepsilon_{\mathrm{L},ij}$ and a corresponding sequence of measured stresses[7] $\sigma_{\mathrm{L},ij}$. Therefore, $i \in A$ and $j \in \{1 \dots N_i\}$, where, with reference to Table 7.4, A represents a set of specimen numbers that underwent the tensile test and N_i is the number of data points measured on the i-th specimen. The measured stresses are assumed normally distributed around a theoretical mean value $\overline{\sigma}_{ij}$ with standard deviation $s_{\sigma,i}$. This relation is written as

$$\sigma_{\mathrm{L},ij} \quad \sim \quad \mathrm{Normal}(\overline{\sigma}_{\mathrm{L},ij}, s_{\sigma,i}), \tag{7.13}$$

where $s_{\sigma,i}$ is a top-level parameter[8] attributed to each i-th specimen. The prior distributions of all top-level parameters are specified in Section 7.5.3. The theoretical mean value of the measured stress is given by the one-dimensional Hooke's law in the form

$$\overline{\sigma}_{\mathrm{L},ij} \quad = \quad E_{\mathrm{L},i}\varepsilon_{\mathrm{L},ij} + a_i, \tag{7.14}$$

where $E_{\mathrm{L},i}$ is the longitudinal elastic modulus and a_i is the intercept of the stress-strain diagram on a vertical axis for the i-th specimen. It plays a similar role as the intercept b_i associated with DIC measurements, which is schematically shown in Fig. 7.10(a). Each intercept a_i is a top-level parameter.

As mentioned in Section 7.3, elastic modulus depends (deterministically) on *MFA* and the volume fraction of earlywood f_{EW}. Homogenization of wood properties, recall Section 7.3, can be regarded as a function $g_E(MFA, f_{\mathrm{EW}})$, resp. $g_\nu(MFA, f_{\mathrm{EW}})$, that maps the microfibril angle and the volume fraction of earlywood to the longitudinal elastic modulus E_{L} and the Poisson ratio ν_{LR}, respectively. Since these functions have to be evaluated many times during the MCMC sampling, it is convenient to construct their faster approximation. In particular, the assumed polynomial representation of the $4th$ order is a perfect match to the results derived from homogenization, see Fig. 7.11. Isolines of these approximations are plotted in Fig. 7.12.

[6] We distinguish between three types of quantities: The *explanatory variables* are known and fixed (or more specifically "we do not need to bother to model them as random"[36]). The *explained variables* are observable and modeled as random but stochastically related to explanatory variables. In Bayesian approach the observed explanatory variables are called *data*. Finally, *parameters* are the unobservable quantities that we want to infer from observed data. Since in Bayesian approach all unknown quantities are considered random, there is no clear distinction between parameters and latent (unobservable) variables.

[7] The measured stresses are essentially derived from the reaction force corresponding to the prescribed displacement as a force divided by the area of specimen cross-section. The term "measured" is used for convenience to identify them with experiments.

[8] The top-level parameters are random model parameters with the specified prior distribution, see Table 7.5.

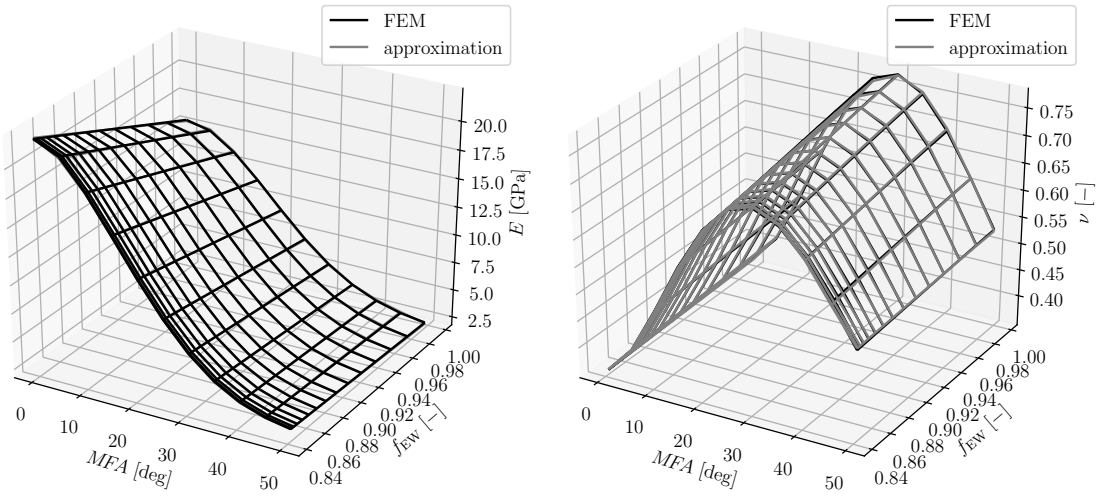

Figure 7.11: Comparison of values of a) E_{L} and b) ν_{LR} obtained from FEM homogenization with the polynomial approximation

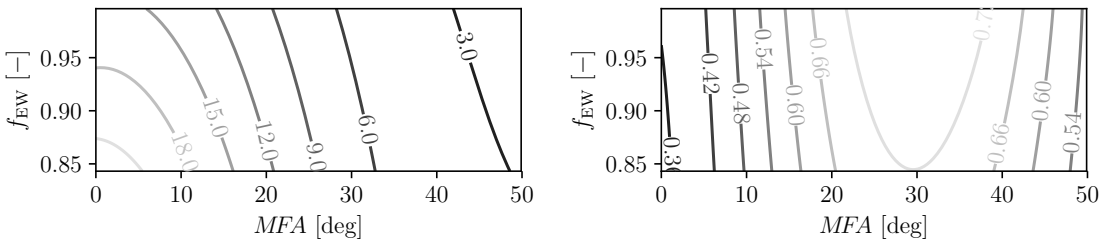

Figure 7.12: Isolines of functions a) $g_E(MFA, f_{\mathrm{EW}})$ and b) $g_\nu(MFA, f_{\mathrm{EW}})$

Therefore, the longitudinal elastic modulus of the i-the specimen can formally be expressed as

$$E_{\mathrm{L},i} \quad = \quad g_E(MFA_i, f_{\mathrm{EW},i}). \tag{7.15}$$

As already mentioned in the introductory part, see also Fig. 7.3 in Section 7.3(b), the volume fraction of earlywood varies from specimen to specimen but for a given specimen is considered known and fixed explanatory variable in the Bayesian updating.

The sought distribution of the microfibril angle within each specimen is assumed to be bounded in the interval $(0, MFA_{\max} = 50°)$[9]. To define its bounded distribution, we map MFA to its normalized value m_i by

$$MFA_i \quad = \quad m_i MFA_{\max}, \tag{7.16}$$

[9]The values of MFA in Fig. 7.9, which fall out of this interval, are assigned to M and S_3 layers not previously eliminated by visual inspection, recall Section 7.4.2.

where m_i ranges from 0 to 1. At this interval, m_i is assumed to follow the beta distribution

$$m_i \sim \text{Beta}(\alpha_m, \beta_m), \tag{7.17}$$

with parameters α_m and β_m being the top-level parameters common to all specimens. This relation expresses the idea that the values of MFA_i are not mutually independent but rather share the above distribution and its parameters which are intrinsic properties of the tested spruce wood.

Analogically, for specimens that underwent tensile tests with DIC measurements we work with a series of measured longitudinal strains $\varepsilon^{\text{ic}}_{\text{L},ij}$, radial strains $\varepsilon^{\text{ic}}_{\text{R},ij}$ and longitudinal stresses $\sigma^{\text{ic}}_{\text{L},ij}$ with $i \in A_{\text{ic}}$, $j \in \{1 \dots N^{\text{ic}}_i\}$ where A_{ic} is a set of numbers of specimens in question and N^{ic}_i is the number of records in Table 7.4 obtained for the i-th specimen. Similarly to Eq. (7.13) the measured stress is normally distributed around its theoretical value with standard deviation of the measurement error

$$\sigma^{\text{ic}}_{\text{L},ij} \sim \text{Normal}(\overline{\sigma}^{\text{ic}}_{\text{L},ij}, s^{\text{ic}}_{\sigma}), \tag{7.18}$$

where standard deviation s^{ic}_{σ} is the top-level parameter[10] whereas the mean value of stress is given by

$$\overline{\sigma}^{\text{ic}}_{ij} = E_{\text{L},i}\varepsilon^{\text{ic}}_{\text{L},ij} + b_i, \tag{7.19}$$

where b_i is again the intercept of the stress-strain diagram depicted for clarity in Fig. 7.10(a). Therein, this intercept arises because the reference image used in DIC does not correspond to the zero level of the applied load. The measured radial strain $\varepsilon^{\text{ic}}_{\text{R},ij}$ is also assumed to be subjected to a measurement error with an unknown standard deviation $s^{\text{ic}}_{\varepsilon}$ and therefore normally distributed

$$\varepsilon^{\text{ic}}_{\text{R},ij} \sim \text{Normal}(\overline{\varepsilon}^{\text{ic}}_{\text{R},ij}, s^{\text{ic}}_{\varepsilon}). \tag{7.20}$$

The mean value is calculated from the Poisson ratio and longitudinal strain as

$$\overline{\varepsilon}^{\text{ic}}_{\text{R},ij} = -\nu_{\text{LR},i}\varepsilon^{\text{ic}}_{\text{L},ij} + c_i, \tag{7.21}$$

where c_i is possibly a nonzero intercept of this linear relationship observed in Fig. 7.10(b) for illustration. Similarly to $E_{\text{L},i}$, the Poisson ratio $\nu_{\text{LR},i}$ is therefore a parameter attributed to the i-th specimen and is deterministically related to the microfibril angle and the volume fraction of earlywood. Here, however, we do not proceed directly in footsteps of Eq. (7.15). Instead, we admit a certain uncertainty associated with the DIC measurements of radial strains. The corresponding uncertainty in experimentally determined Poisson ratio can be foreseen from the variability of ν_{LR} in Table 7.3 potentially attributed to the actual orientation of grains in Fig. 7.5(b) not reflected in Eq. (7.21). To incorporate this issue in the model formulation we consider the "measured" Poisson ratio,

[10] The standard deviation of the DIC measurement error is the same for all specimens.

i.e. the slope of the line approximating the data in Fig. 7.10(b), be normally distributed around its theoretical value $\overline{\nu}_{\mathrm{LR},i}$, i.e.

$$\nu_{\mathrm{LR},i} \quad \sim \quad \mathrm{Normal}(\overline{\nu}_{\mathrm{LR},i}, s_\nu). \tag{7.22}$$

The standard deviation s_ν is a top-level parameter and the theoretical value of Poisson ratio $\overline{\nu}_{\mathrm{LR},i}$ is deterministically defined by *MFA* and f_{EW} as

$$\overline{\nu}_{\mathrm{LR},i} \quad = \quad g_\nu(MFA_i, f_{\mathrm{EW},i}). \tag{7.23}$$

Thus the difference between the two types of errors, one with standard deviations $s_\varepsilon^{\mathrm{ic}}$ and the other with standard deviation s_ν is that the former describes the noise of the measured data points around the theoretical line while the latter characterizes the uncertainty of the experimentally obtained slope of this linear relationship.

Finally, nanoindentation provides a series of indentation moduli M_{ij} for $i \in A_{\mathrm{ni}}$, $j \in \{1 \dots N_i^{\mathrm{ni}}\}$, where A_{ni} is the set of specimen numbers involved in nanoindentation tests and N_i^{ni} is the number of indents in the i-th specimen specified again in Table 7.4. The measured values of indentation modulus M_{ij} are normally distributed around a mean value $\overline{M}_{ij} + \Delta\overline{M}$ with standard deviation s_M

$$M_{ij} \quad \sim \quad \mathrm{Normal}(\overline{M}_i + \Delta\overline{M}, s_M), \tag{7.24}$$

where $\overline{M}_i$ is a theoretical value of the indentation modulus in the i-th specimen, $\Delta\overline{M}$ is the correction of a systematic error of nanoindentation tests and s_M is standard deviation of the measured values. The parameters $\Delta\overline{M}$ and s_M are the top-level parameters, while $\overline{M}_i$ depends deterministically on the microfibril angle according to

$$\overline{M}_i \quad = \quad g_M(MFA_i), \tag{7.25}$$

where g_M is a polynomial approximation of the relationship between *MFA* and M provided by the theory of anisotropic indentation, recall Section 7.4.2. This function is plotted in Fig. 7.13, analogously to E_{L} and ν_{LR} approximations in Fig. 7.11.

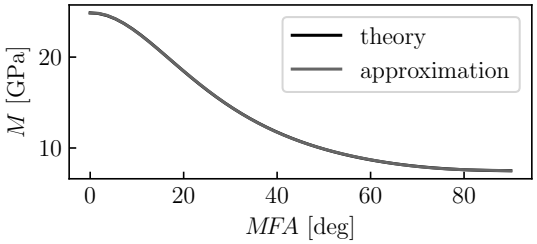

Figure 7.13: Comparison of the values of M obtained from anisotropic theory of indentation with corresponding polynomial approximation

The meaning of all quantities mentioned above is summarized in Table 7.5. Note that the model considers a separate value microfibril angle MFA_i for each specimen which – together with known volume fraction of earlywood $f_{\mathrm{EW},i}$ – explains the mechanical properties E_i, ν_i and M_i.

Table 7.5: Quantities and their roles in the hierarchical Bayesian model.

Explanatory variables	$\varepsilon_{\mathrm{L},ij}$, $\varepsilon^{\mathrm{ic}}_{\mathrm{L},ij}$, $f_{\mathrm{EW},i}$
Explained variables	$\sigma_{\mathrm{L},ij}$, $\sigma^{\mathrm{ic}}_{\mathrm{L},ij}$, $\varepsilon^{\mathrm{ic}}_{\mathrm{R},ij}$, M_{ij}
Top-level parameters	$s_{\sigma,i}$, s^{ic}_{σ}, $s^{\mathrm{ic}}_{\varepsilon}$, s_{ν}, s_M, α_m, β_m, $\Delta\overline{M}$, a_i, b_i, c_i
Parameters	$\overline{\sigma}_{\mathrm{L},ij}$, $\overline{\sigma}^{\mathrm{ic}}_{\mathrm{L},ij}$, $\overline{\varepsilon}^{\mathrm{ic}}_{\mathrm{R},ij}$, $\overline{M}_i$, $E_{\mathrm{L},i}$, $\nu_{\mathrm{LR},i}$, $\overline{\nu}_{\mathrm{LR},i}$, MFA_i , m_i

7.5.3 Prior distribution of top-level parameter

Bayesian inference requires specifying the prior distribution of the top-level model parameters. For all standard deviations of measurement errors, i.e. for $s_{\sigma,i}$, s^{ic}_{σ}, $s^{\mathrm{ic}}_{\varepsilon}$, s_{ν}, and s_M, we adopted the gamma distribution with scale $\alpha = 0.001$ and rate $\beta = 0.001$. These values are commonly chosen to define a vaguely informative prior for positive parameters. For unbounded parameters $\Delta\overline{M}$, a_i, b_i and c_i we assumed normal distribution with $\mu = 0$ and $\sigma = 10$. Finally, for parameters α_m and β_m in Eq. (7.17) we accept again the gamma distribution with scale $\alpha = 1$, and rate $\beta = 0.001$. This is because, when combined with Eq. (7.16), such a choice renders approximately a uniform prior distribution of *MFA* on its assumed range $(0, MFA_{\max})$, see ahead Figure 7.16(c).

7.5.4 Application and results

Having defined the hierarchical stochastic model in Section 7.5.2 and 7.5.3 we can examine the posterior distribution by drawing samples from the generated Markov chains. In particular, the model has been implemented in PyMC3 package [37] and two chains each of 1000 samples were generated using the No-U-Turn sampler [38] based on Hamiltonian Monte Carlo method. The marginal posterior distribution of each parameter is best presented by plotting its kernel density estimate (KDE), i.e. PDF estimated from the generated samples[11].

We first explore the distributions of measurement errors plotted in Fig. 7.14. It can be seen that standard deviations of all assumed errors are quite conclusively inferred from the measured data and their distributions are relatively narrow. A little less certain are the values of standard deviations of measurement errors associated with standard tensile tests, Fig. 7.14(a). Recall that separate values of standard deviation of the measurement error were assumed for individual specimens. This choice now seems justifiable, because some of the KDEs in Fig. 7.14(a) do not practically overlap indicating that the measurement noise on these specimens probably differs.

The systematic error in measured indentation modulus $\Delta\overline{M}$ is also clearly identified with a narrow posterior distribution centered around -7 GPa, see Fig. 7.14(f). This correction compensates relatively small values obtained from nanoindentation measurements, Fig. 7.9(a), which would otherwise be incompatible with the expected values of *MFA*.

Figure. 7.15(a) shows the posterior distribution of microfibril angle of each specimen.

[11] The kernel density estimate can also be seen as a smoothed histogram.

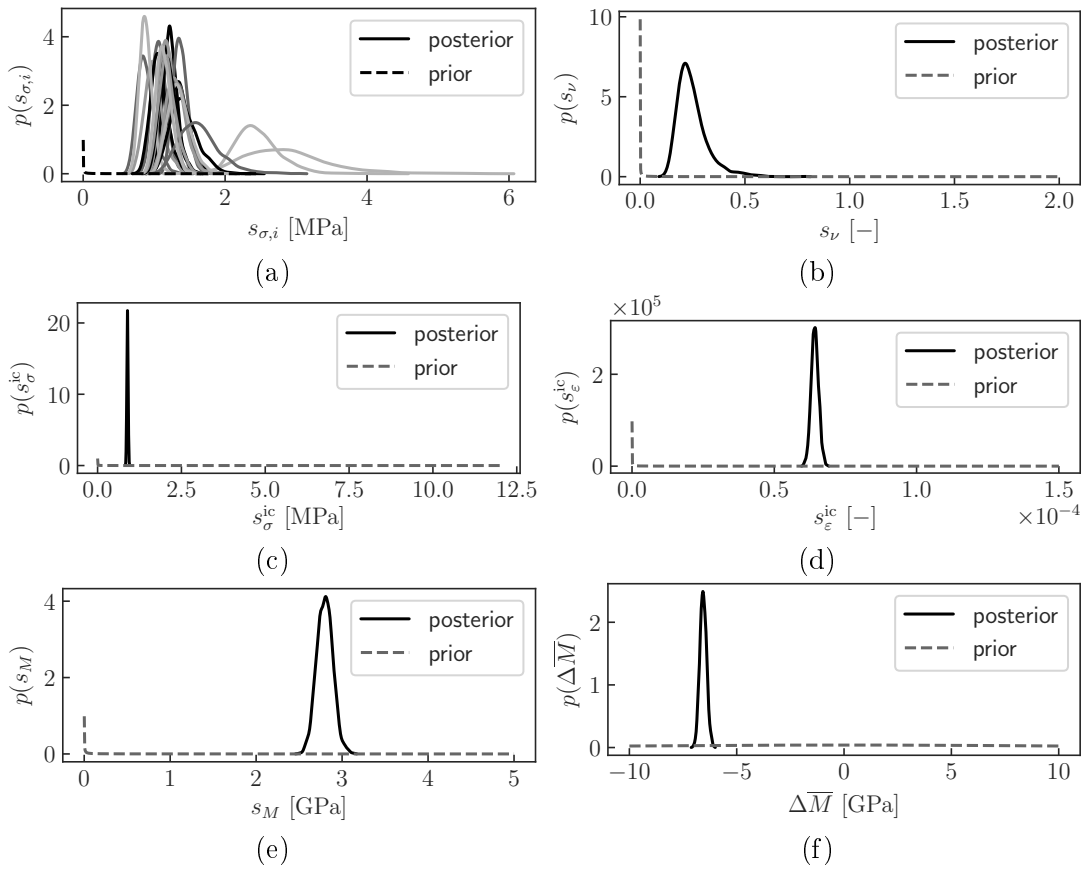

Figure 7.14: Posterior distributions of standard deviations of measurement and modeling errors of a) stress s_σ^{ic} in the standard tensile test, b) Poisson ratio s_ν in the DIC measurements, c) stress s_σ^{ic} in DIC, d) radial strain $s_\varepsilon^{\mathrm{ic}}$ in DIC, e) nanoindentation measurements s_M and f) posterior distribution of systematic error of measured indentation modulus $\Delta\overline{M}$

The transformed marginal distributions of quantities E_{L}, ν_{LR} and $\overline{M}$ are plotted for individual specimens in Figs. 7.15(b-d). Remember that they depend deterministically on *MFA* through Eqns (7.15), (7.22) and (7.25). Relatively narrow posterior distributions associated with majority of specimens indicate that the value of *MFA* and subsequently the values of E_{L}, ν_{LR} and M were inferred from the measured data with quite a low uncertainty. On the other hand, the locations of these distributions are quite dispersed suggesting a significant variability of these quantities from specimen to specimen. In terms of uncertainty categories, the width of each distribution characterizes the epistemic uncertainty of MFA_i on the i-th specimen, which could possibly be reduced by increasing the number of measured data and/or by modifying the model. On the other hand, the variability of the locations of the posterior distribution shows the aleatory (irreducible) uncertainty of *MFA* of a given specimen. This uncertainty is described in the model with the beta distribution scaled to the maximum acceptable value of $MFA_{\max} = 50°$, recall

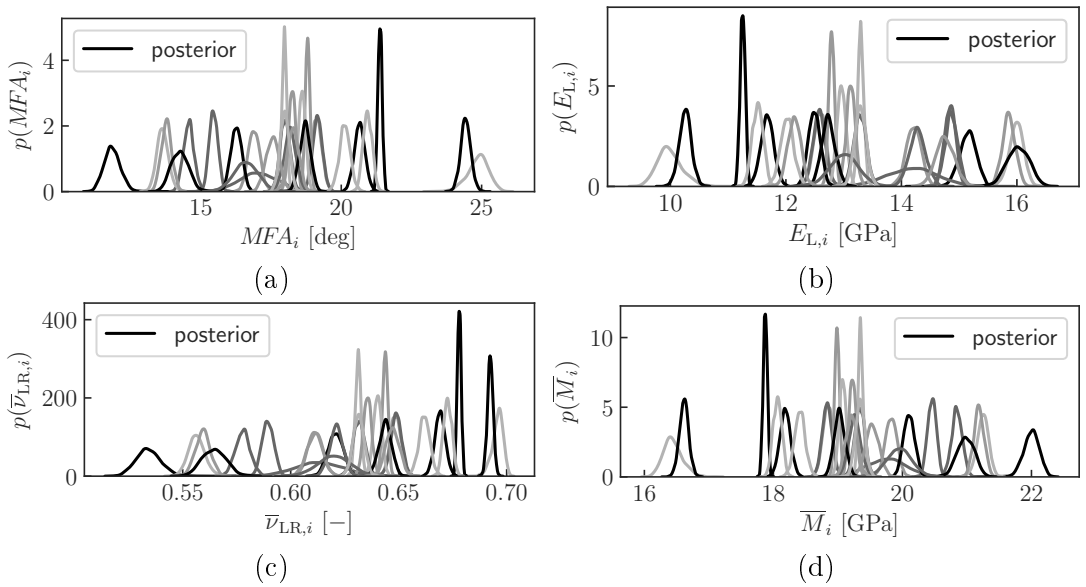

Figure 7.15: Posterior distribution of a) microfibril angle, b) longitudinal elastic modulus, c) Poisson's ratio, d) indentation modulus of each tested specimen

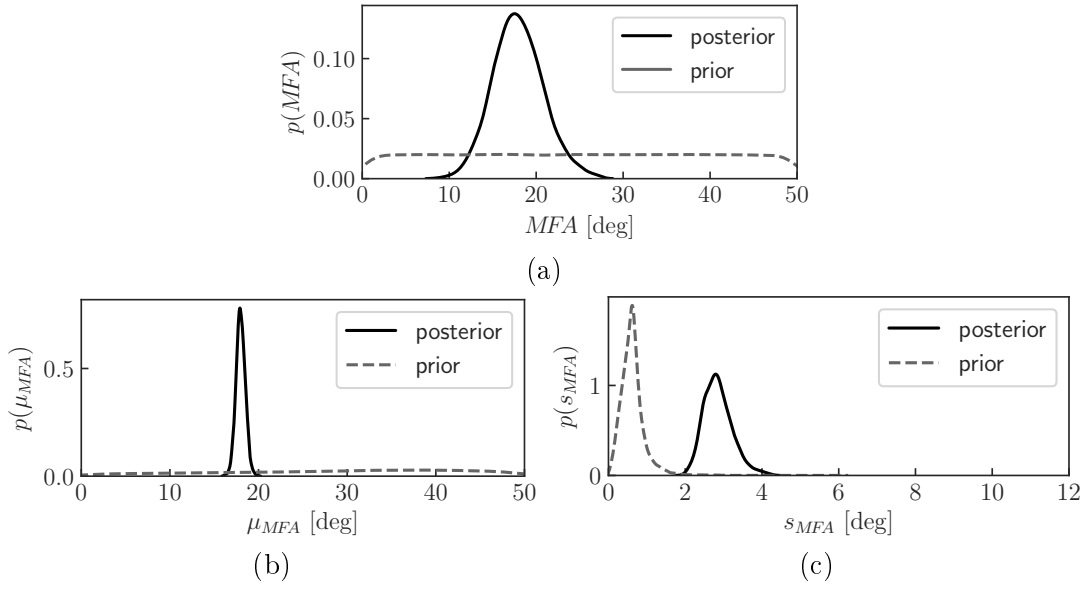

Figure 7.16: Posterior distribution of microfibril angle related parameters: a) MFA, b) expected value μ_{MFA}, c) standard deviation s_{MFA}

Eqns. (7.16) and (7.17). The prior and the posterior marginal distribution of *MFA* is plotted in Fig. 7.16(a). This distribution quantifies jointly the aleatory and epistemic uncertainty of *MFA* in the tested spruce wood. On the contrary, the distributions of its mean value, Fig. 7.16(b), and standard deviation, Fig. 7.16(c), which are computed directly from the top-level parameters α_m and β_m, describe only the epistemic uncertainty attributed to a limited number of measured data and simplifications adopted in the forward hierarchical model.

7.6 Conclusions

Small scale laboratory experiments are often used to provide inputs to a theoretical model subsequently adopted in the prediction of the response of large structural elements. However, if such experimental data are of low credibility, which might be difficult to see directly, the theory will provide inadmissible predictions regardless of its accuracy. Two particular examples are presented in this contribution in support of derivating the effective stiffness matrix of spruce via homogenization:

- The first approach grounds on the application of nanoindentation to estimate the microfibril angle to give reduced properties of wood at cell wall level. Adopting the present results without scrutiny would significantly underestimate the actual macroscopic stiffness of the examined wood, recall relatively low values of indentation moduli in Fig. 7.8(a) inconsistent with the measured macroscopic stiffness in Table 7.3.

- The second approach, although not specifically mentioned in the previous discussions, may start from macroscopic measurements of elastic modulus and Poisson's ratio to estimate the microfibril angle from inverse analysis. The macroscopic stiffnesses would be then provided in analogy to the first approach. This path may eventually lead to inability of finding a unique MFA which would provide effective properties matching both the measured elastic modulus and Poisson ratio. The main cause would be an unacceptable level of inaccuracy of the measured radial strains associated with the deviation of grains from the radial direction assumed in theoretical predictions, recall Figs. 7.5(a,b).

Identifying the measurement error, if experimental uncertainty may prove significant, is therefore of paramount importance. In the present study, the Bayesian inference was exploited to uncover this, initially hidden, information.

To recapitulate, we have formulated hierarchical stochastic model in order to track down the variation of the microfibril a angle among specimens of spruce wood. This material property is of essential interest since it – together with volume fraction of early wood – theoretically defines all components of macroscopic stiffness matrix. Beside the sought distribution of MFA, the model identifies wide range of errors contributing to the randomness of observed data. In particular, a systematic difference between the measured

indentation modulus and the theoretical value obtained via the theory of anisotropic indentation was identified. Quite significant error in the measured Poisson ratio was also found suggesting that either the particular setup of the DIC measurement of transverse strain is far from optimal or that the current model formulation ignores some relevant phenomenon. Either way, the Bayesian inference proved to be flexible tool for identification of these uncertainties.

Acknowledgment

We are thankful for financial support provided by the Czech Grant Agency, project No. 18-05791S.

Apendix A – Construction of posterior distribution

The posterior probability density function $p(\theta|y)$ can be unambiguously constructed from the hierarchy of stochastic and deterministic relations that define the forward model. However, this is commonly done automatically under the hood of the Bayesian modeling software. The software usually accepts a model described in a domain specific language that is very similar to Eqns. (7.13)–(7.25). Nevertheless, we feel useful to provide a simple yet illustrative example on how the posterior PDF is constructed.

For simplicity, consider N specimens made of the same material each subjected to a displacement-control tensile test to yield M_i stress-strain pairs $(\varepsilon_{ij}, \sigma_{ij})$ for each specimen i. The model is then formulated as

$$\sigma_{ij} \sim \text{Normal}(\overline{\sigma}_{ij} = E_i\varepsilon_{ij}, s_\sigma) \quad \text{for } i = \{1 \dots N\},\ j = \{1 \dots M_i\}, \tag{7.26}$$

$$E_i \sim \text{Normal}(\mu_E, s_E) \quad \text{for } i = \{1 \dots N\}, \tag{7.27}$$

where μ_E, s_E, s_σ, and E_i are the model parameters, ε_{ij} are the explanatory variables and σ_{ij} are the data. Recall that the normal distribution denoted as $\text{Normal}(\mu, s)$ and parameterized by mean μ and standard deviation s reads

$$p(y|\mu, s) = f_{\text{N}}(y, \mu, s) = \frac{1}{\sqrt{2\pi s^2}} e^{-\frac{(y-\mu)^2}{2s^2}}. \tag{7.28}$$

A series of K statistically independent and normally distributed variables $\boldsymbol{y}$ provides

$$p(\boldsymbol{y}|\mu, s) = \prod_{k=1}^{K} f_{\text{N}}(y_k, \mu, s). \tag{7.29}$$

Using the rule of conditional probability, the posterior distribution of all model parameters given the measured data is written as

$$p(\boldsymbol{E}, \mu_E, s_E, s_\sigma|\boldsymbol{\sigma}) = \frac{p(\boldsymbol{\sigma}, \boldsymbol{E}, \mu_E, s_E, s_\sigma)}{p(\boldsymbol{\sigma})} \propto p(\boldsymbol{\sigma}, \boldsymbol{E}, \mu_E, s_E, s_\sigma). \tag{7.30}$$

Applying the chain rule of conditional probability and considering Eqns. (7.26) and (7.27) gives

$$p(\boldsymbol{\sigma}, \boldsymbol{E}, \mu_E, s_E, s_\sigma) = p(\boldsymbol{\sigma}|\boldsymbol{E}, s_\sigma)p(\boldsymbol{E}|\mu_E, s_E)p(\mu_E)p(s_E)p(s_\sigma) \tag{7.31}$$

$$= \prod_{i=1}^{N}\prod_{j=1}^{M_i} f_{\mathrm{N}}(\sigma_{ij}, \overline{\sigma}_{ij} = E_i\varepsilon_{ij}, s_\sigma) \prod_{i=1}^{N} f_{\mathrm{N}}(E_i, \mu_E, s_E)p(\mu_E)p(s_E)p(s_\sigma), \tag{7.32}$$

where $p(\mu_E)$, $p(s_E)$ and $p(s_\sigma)$ are the prior distributions of the top-level parameters.

Apendix B – Model hierarchy

The relation between the quantities in the statistical model can be represented in the form of graph. The elliptical nodes in Fig. 7.17 are parameters, the rectangular nodes are quantities computed deterministically from the parent values, and the gray nodes represent the observed data. The nodes contained in rectangles with rounded corners are array quantities. The number in the lower right corner specifies the length of these arrays. Explanatory variables are not shown.

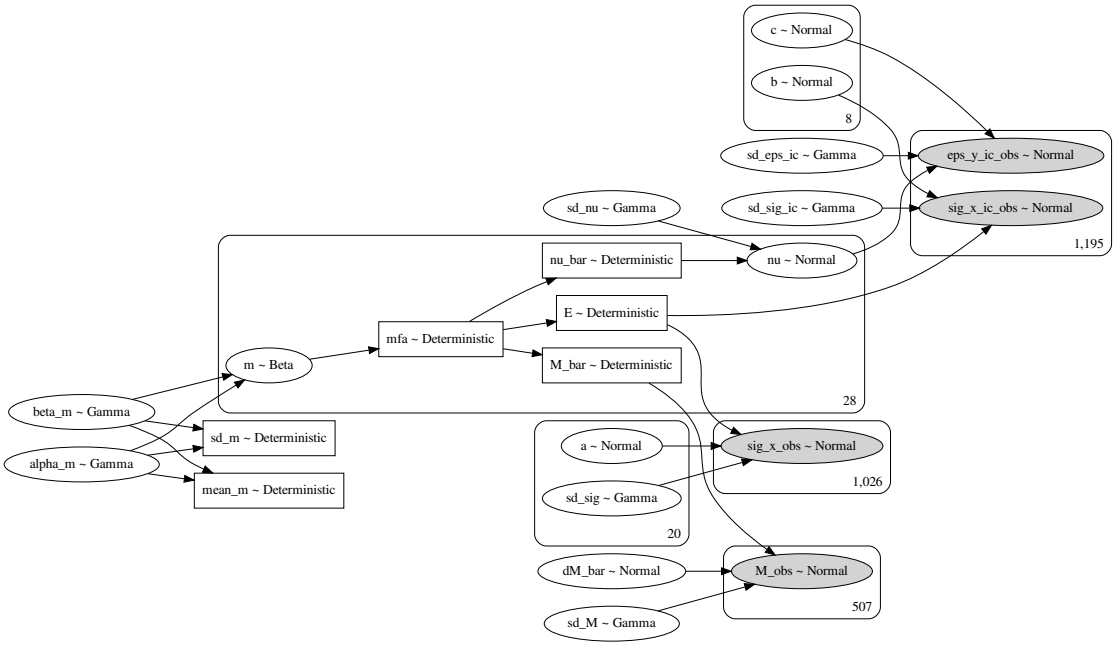

Figure 7.17: Hierarchy of the model represented in form of directed graph

Bibliography

[1] T. Janda, J. Šejnoha, M. Šejnoha, Hierarchical stochastic model of terrain subsidence during tunnel excavation, IOP Conference Series: Materials Science and Engineering 236 (2017).

[2] T. Janda, M. Šejnoha, J. Šejnoha, Applying Bayesian approach to predict deformations during tunnel construction, International Journal for Numerical and Analytical Methods in Geomechanics 42 (2018) 1765–1784.

[3] A. De Falco, M. Mori, G. Sevieri, Bayesian updating of concrete gravity dams parameters using static measurements, in: 6th European Conference on Computational Mechanics (ECCM 6), 11-15 June, Glasgow, UK, 2018, pp. 1–12.

[4] J. Köhler, J. D. Sorensen, M. H. Faber, Probabilistic modeling of timber structures, Structural Safety 29 (2007) 255–267.

[5] M. Šejnoha, T. Janda, L. Melzerová, V. Nežerka, J. Šejnoha, Modeling glulams in linear range with parameters updated using Bayesian inference, Engineering Structures 138 (2017) 293–307.

[6] K. Persson, Micromechanical Modelling of Wood and Fibre Properties, Ph.D. thesis, Lund University (2000).

[7] K. Hofstetter, Ch. Hellmich, J. Eberhardsteiner, Development and experimental validation of a continuum micromechanics model for the elasticity of wood, European Journal of Mechanics - A/Solids 24 (6) (2005) 1030–1053.

[8] M. Šejnoha, T. Janda, L. Kucíková, P. Padevět, Combining homogenization, indentation and Bayesian inference in estimating the microfibril angle of spruce, Procedia Engineering 190 (2017) 310–317.

[9] M. Šejnoha, J. Sýkora, J. Vorel, L. Kucíková, J. Antoš, J. Pokorný, Z. Pavlík, Moisture induced strains in spruce from homogenization and transient moisture transport analysis, Computers and structures 0 (2018) 0–0.

[10] J. Konnerth, Ch. Buksnowitz, W. Gindl, K. Hofstetter, A. Jäger, Full Set of Elastic Constants of Spruce Wood Cell Walls Determined by Nanoindentation, in: International Convention of Society of Wood Science and Technology and United Nations Economic Commission for Europe – Timber Committee, 11-14 October, Geneva, Switzerland, 2010, pp. 1–9.

[11] A. Jäger, Th. Bader, K. Hofstetter, J. Eberhardsteiner, The relation between indentation modulus, microfibril angle, and elastic properties of wood cell walls, Composites Part A: Applied Science and Manufacturing 42 (6) (2011) 677–685.

[12] J. Vlassak, W. Nix, Measuring the elastic properties of anisotropic materials by means of indentation experiments, Journal of the Mechanics and Physics of Solids 42 (8) (1994) 1223–1245.

[13] J. Vlassak, M. Ciavarella, J. Barber, X. Wang, The indentation modulus of elastically anisotropic materials for indenters of arbitrary shape, Journal of the Mechanics and Physics of Solids 51 (9) (2003) 1701–1721.

[14] N. Siu, D. Kelly, Bayesian parameter estimation in probabilistic risk assessment, Reliability Engineering and System Safety 62 (1998) 89–116.

[15] D. Kelly, C. Smith, Bayesian inference in probabilistic risk assessment - The current state of the art, Reliability Engineering and System Safety 94 (2009) 628–643.

[16] Ch. P. Robert, G. Casella, Monte Carlo Statistical Methods, 2nd Edition, III, Springer-Verlag, 2004.

[17] J. D. Eshelby, The determination of the elastic field of an ellipsoidal inclusion and related problems, Proceeding of Royal Society, Series A 241 (1957) 376–396.

[18] R. Hill, Elastic properties of reinforced solids - Some theoretical principles, Journal of the Mechanics and Physics of Solids 11 (1963) 357–372.

[19] Y. Benveniste, A new approach to the application of Mori-Tanaka theory in composite materials, Mechanics of Materials 6 (1987) 147–157.

[20] J. Zeman, M. Šejnoha, From random microstructures to representative volume elements, Modelling and Simulation in Materials Science and Engineering 15 (4) (2007) S325–S335.

[21] J. Dvorak, Micromechanics of Composite Materials, Dordrecht : Springer, 2013.

[22] M. Šejnoha, J. Zeman, Micromechanics in Practice, WIT Press, Southampton, Boston, 2013.

[23] L. Kucíková, Micromechanical study of spruce wood, Master's thesis, Czech Technical University in Prague (2018).

[24] J. C. Michel, H. Moulinec, P. Suquet, Effective properties of composite materials with periodic microstructure: A computational approach, Computer Methods in Applied Mechanics and Engineering 172 (1999) 109–143.

[25] G. W. Milton, The Theory of Composites, Cambridge Monographs on Applied and Computational Mathematics, Cambridge University Press, 2002.

[26] H. Lu, P. Cary, Deformation measurements by digital image correlation: Implementation of a second-order displacement gradient, Experimental Mechanics 40 (2000) 393–400.

[27] B. Pan, H. Xie, Z. Wang, Equivalence of digital image correlation criteria for pattern matching, Applied Optics 49 (2010) 5501–5509.

[28] B. Pan, Z. Lu, H. Xie, Mean intensity gradient: An effective global parameter for quality assessment of the speckle patterns used in digital image correlation, Optics and Lasers in Engineering 48 (2010) 469–477.

[29] V. Nežerka, Ncorr-post: DIC Post-Processing Tool, Tech. rep., http://mech.fsv.cvut.cz/ nezerka/dic/index.htm (2014).

[30] V. Nežerka, Ncorr-post-CSTool: ...DIC Post-Processing Tool to Display Strains along Cross-Section, Tech. rep., http://mech.fsv.cvut.cz/ nezerka/dic/index.htm (2015).

[31] W. Gindl, T. Schöberl, The significance of the elastic modulus of wood cell walls obtained from nanoindentation measurements, Composites Part A: Applied Science and Manufacturing 35 (11) (2004) 1345–1349.

[32] W. T. Y. Tze, S. Wang, T. G. Rials, G. M. Pharr, S. S. Kelley, Nanoindentation of wood cell walls: Ccontinuous stiffness and hardness measurements, Composites: Part A 38 (2007) 945–953.

[33] J. Konnerth, N. Gierlinger, J. Keckes, W. Gindl, Actual versus apparent within cell wall variability of nanoindentation results from wood cell walls related to cellulose microfibril angle, Journal of Material Science 44 (2009) 4399–4406.

[34] W. Oliver, G. Pharr, An improved technique for determining hardness and elastic modulus using load and displacement sensing indentation experiments, Journal of materials research 7 (06) (1992) 1564–1583.

[35] J. R. Barber, Determining the contact area in elastic-indentation problems, Journal for strain analysis for engineering design 9 (1974) 230–232.

[36] A. Gelman, J. Carlin, H. Stern, D. Dunson, A. Vehtari, D. Rubin, Bayesian Data Analysis, Third Edition, Chapman & Hall/CRC Texts in Statistical Science, Taylor & Francis, 2013.

[37] J. Salvatier, T. Wiecki, C. Fonnesbeck, Probabilistic Programming in Python using PyMC (Jul. 2015). arXiv:1507.08050, doi:10.48550/arXiv.1507.08050.

[38] M. D. Hoffman, A. Gelman, The No-U-Turn Sampler: Adaptively Setting Path Lengths in Hamiltonian Monte Carlo, Journal of Machine Learning Research 15 (2014) 1593–1623. doi:10.48550/arXiv.1111.4246.

Chapter 8

Conclusions

The presented research demonstrates the broad applicability of Bayesian inference to various problems and tasks in civil engineering. This approach allows for learning about unobservable quantities or model parameters from observable data while systematically accounting for uncertainties inherent in the data acquisition process.

Two key strengths of the Bayesian approach deserve particular emphasis:

- Hierarchical Bayesian models naturally and efficiently consolidate the information about the parameters, even when the data come from different sources and are influenced by distinct errors. This capability enables robust modeling in complex engineering contexts where data variability and measurement discrepancies are common.
- Bayesian inference is especially valuable in situations where the colloquial rule of thumb – "at least 30 data points are needed for a good sample size" – might discourage statistical analysis. By combining a well-chosen prior distribution with any amount of observed data, Bayesian methods produce a meaningful posterior distribution, enabling robust analysis even with limited data.

Despite its strengths, Bayesian inference also presents challenges that require careful consideration.

- The concept of prior distribution can be contentious as there is no universally rigorous method for its selection, leading to concerns about subjectivity. Although this is a valid critique, many engineering problems already depend on expert judgment. Bayesian methods provide a systematic way to integrate expert knowledge with empirical data, making this subjectivity an asset rather than a drawback when handled appropriately.
- Large-scale deterministic simulations are often integral to probabilistic models in engineering problems. However, the inclusion of computationally expensive functions within the likelihood expression poses challenges to efficient sampling. In such cases, two primary strategies can be employed, each with its own limitations:

- Evaluating the simulation at each MCMC step can be computationally expensive, particularly for high-dimensional problems. Additionally, many simulations do not provide gradients, restricting the use of more efficient Hamiltonian Monte Carlo methods.
- Creating a surrogate model introduces approximation errors, adding another source of uncertainty to the problem. This approach may also struggle with complex simulations that involve a large number of parameters.

The studies presented in this thesis illustrate how Bayesian statistics enhance our ability to quantify uncertainty and make data-informed decisions about unobservable model parameters, but also provides a structured framework for predictions of yet unobserved quantities.

Future research can further expand the utility of Bayesian methods, particularly in refining selection strategies for prior distribution and integrating large-scale engineering simulations into probabilistic models.